UNIVERSITY OF OXFORD

ATMOSPHERIC, OCEANIC AND PLANETARY PHYSICS

DPhil in Atmospheric, Oceanic and Planetary Physics

Unravelling the isotopic imprints of Martian CO_2 and H_2O using solar occultation observations from the Atmospheric Chemistry Suite onboard ExoMars Trace Gas Orbiter

Juan Alday

juan.aldayparejo@physics.ox.ac.uk

Abstract

Numerous lines of geomorphological and mineralogical evidence suggest that liquid water was once abundant on Mars' surface, which might also be indicative of a more hospitable environment for life to grow. The presence of large amounts of liquid water on the surface require climatic conditions very different from those enabled by the dry and thin atmosphere Mars has today. In fact, it is still not well understood how the past Martian atmosphere was able to produce sufficient greenhouse warming to sustain liquid water on the surface, nor what drove the transition of the climate to the one we observe today. Enrichment in the heavy isotopes of atmospheric species such as hydrogen, nitrogen or the noble gases with respect to Earth suggest that this transition was driven by the escape of a large portion of the atmosphere to space. Isotope ratios can provide constraints on the amount of atmosphere that existed in the past, but require a very detailed knowledge of the present day isotopic ratios and the relative rates by which the different isotopologues of each species escape to space.

To this aim, we monitor the isotopic composition of H, C and O in carbon dioxide and water vapour using sensitive infrared solar occultation measurements made by the mid-infrared channel of the Atmospheric Chemistry Suite (ACS MIR) onboard the ExoMars Trace Gas Orbiter (TGO), which makes measurement in a spectral range between 2.3 and 4.2 μm. The modelling and inversion of the spectral data is performed using the NEMESIS radiative transfer and retrieval algorithm, which is adapted to model the particularities of the measurements of ACS MIR, and retrieve the isotopic ratios along with other atmospheric parameters such as the pressure and temperature profiles.

The developed retrieval scheme is applied in three instances to constrain different aspects of the isotopic composition of the Martian atmosphere. First of all, eight solar occultation observations made during the first months of operations of the ExoMars TGO are used to measure, for the first time, the vertical distribution of the oxygen isotope ratios in H_2O ($^{18}O/^{16}O$ and $^{17}O/^{16}O$). These results show that the O isotope ratios in H_2O are enriched with respect to their primordial sources, which is consistent with fractionation during the escape of the Martian atmosphere into space throughout history. In the second place, more than a

full Martian Year of observations are used to understand the variability of D/H and $^{18}O/^{16}O$ in water and estimate how its dissociation products are fractionated. These measurements show that while the variations of the D/H ratio in H_2O are mainly driven by condensation-induced fractionation, the differential photolysis of HDO and H_2O is a more important factor in determining the isotopic composition of the dissociation products (OH and H). Finally, observations encompassing strong absorption bands of carbon dioxide are used to measure the carbon and oxygen isotopic composition ($^{13}C/^{12}C$, $^{18}O/^{16}O$ and $^{17}O/^{16}O$) of carbon dioxide at high altitudes aiming to understand how the isotope ratios in the upper atmosphere relate to those measured on the surface. This analysis shows that the C and O isotopic ratios are on average consistent with those found on Earth. The vertical distribution of the C and O isotope ratios shows a decrease above the homopause which is consistent with the expectations from diffusive separation, although some orbits also show an increase in the O isotopic ratios in the lower thermosphere which we conclude may be due to photochemical fractionation.

The measurements of the isotopic ratios presented in this thesis, as well as their interpretation in context with other atmospheric parameters, provide a significant contribution to our understanding of the isotopic composition of the Martian atmosphere, which in turn allow a better understanding of the history and evolution of the atmosphere of Mars.

Acknowledgements

First and foremost, I would like to thank my supervisors **Patrick Irwin** and **Colin Wilson** for their support and guidance throughout these years. You have been excellent supervisors. Not only you have gone above and beyond in supporting my academic development, but also you have made me enjoy every second of this DPhil journey. It has been great to work with you, and I really hope we continue to do so in the future. Thank you very much for everything.

I would also like to express my gratitude to my collaborators: **Kevin Olsen**, **Sasha Trokhimosvkiy**, **Lucio Baggio**, **Denis Belyaev**, **Franck Montmessin**, **Franck Lefèvre**, **Anna Fedorova**, **Oleg Korablev** and the rest of the ACS Team. It has been a pleasure to be a part of this team and I have deeply enjoyed the time with you in all meetings and conferences around the world.

Huge thanks to all my colleagues and friends here at Oxford: **Daniel Toledo**, **Ryan Garland**, **Ashwin Braude**, **Sophie Bauduin**, **Jean-Loup Baudino**, **Arjuna James**, **Jack Dobinson**, **Jingxuan Yang**, **Charlotte Alexander**, and especially to **Jake Taylor**. It has been great to share all these years with you, in AOPP, and in the pubs nearby!

I owe a huge thanks to **María**, who has immensely supported me. You and Pepi together have made these awful lockdowns turn into a wonderful time. Thank you very much for the acting plays, the piano rehearsals, the trips, the days of eating and Netflix, and for being with me.

It is not possible to describe my life in the last years without mentioning everybody from La Katacumbia, Los Puchitos and 11 Iffley Rd. **Pablete**, **Mario**, **Adri**, **Alvarito**, **Jorge**, **Recio**, **Miguel**, **Gauthier**, **Sam**, **Erika**, **Felix**, **Andrea**, **Laura**, **Javi** and many more, you have made these years in Oxford a truly enjoyable experience that I will never forget.

Lastly, the biggest thank you of all goes to my family, especially my siblings, **Bego** and **Rafa**, for continuously supporting me, even if it is at a distance. I know we will always be there for each other. I also can't go without mentioning my grandparents, **Miren**, **Elías**, **Ana** and **Juan**, whom I think would have been very proud.

I dedicate this thesis to my parents, ***Rafa*** *and* ***María Jesús****. If I have written this thesis, it is because of all you have given me. I will always be thankful and love you.*

Contents

List of Figures

List of Tables

Chapter 1

Introduction

Mars, named after the Roman God of War, is the fourth planet in its distance to the Sun, and the closest to the Earth. Observed as a red dot in the night sky, Mars has always drawn attention throughout history, even before telescopes were ever invented. The occasional retrograde motion of Mars in the sky helped our ancestors to realise planets were orbiting around the Sun, and not around the Earth as it was previously thought. The use of telescopes allowed a more detailed analysis of the Red Planet, allowing the observation of features like the seasonal polar caps, or changes in the atmosphere attributed to clouds. Nowadays, Mars remains one of the main targets of the space exploration, being observed by ground-based telescopes, spacecraft orbiting around it, or even rovers taking *in situ* measurements.

Mars is not only the closest planet to the Earth in terms of distance, but it is also the one that most closely resembles it. The rotation rate of Mars leads to a 24h 37m day, comparable to the 23h 56m one of the Earth. In addition, the obliquity of Mars, of approximately 25° with respect to the ecliptic, makes the planet experience four seasons, as the Earth does. On the other hand, the greater distance from the Sun, the smaller size, and the different atmospheric conditions (see Table 1.1), make Mars experience a different environment than the Earth, but with some similarities that make scientists wonder about the past and present habitability of the planet.

Life, as we know it from Earth, appears to be closely related to the presence of an essential ingredient, liquid water. Mars' thin atmosphere is characterised by a low surface pressure, of approximately 6.3 mbar, and low temperatures, of about -58°C. In this range of temperatures

Table 1.1: Planetary parameters for Earth and Mars

	Earth	Mars
Distance from Sun (AU)	0.98 - 1.02	1.38 - 1.67
Orbital eccentricity	0.017	0.093
Planetary obliquity (°)	23.93	25.19
Solar day, sol (hours)	24	24.66
Year length (Earth days)	365.24	686.98
Equatorial radius (km)	6378	3396
Polar radius (km)	6357	3376
Surface gravity (m s^{-2})	9.81	3.72

and pressures, water on the surface can just be found as ice or vapour, but not liquid, which makes present atmospheric conditions to be inhospitable for life to grow. However, numerous lines of evidence suggest that liquid water might have been flowing on the Martian surface four billion years ago. These lines of evidence include:

- **Geomorphological evidence.** In the past decades, several spacecraft have provided high-resolution images of the Martian surface, revealing the presence of river valleys and lake basins in many areas, which require liquid fluid to have flown on the surface in the past (Carr and Clow, 1981; Baker et al., 1991; Head et al., 1999). Several studies explored the possibility of different fluids to have caused these surface features, such as erosion by lava (Carr, 1974), liquid hydrocarbons (Yung and Pinto, 1978) or liquid CO_2 (Sagan et al., 1973), although the most plausible candidate appears to be liquid water (Carr and Clow, 1981; Carr, 1995).

- **Mineralogical evidence.** The Martian surface is predominatly made of basalt, which, if reacting with liquid water, can produce a number of so-called "aqueous minerals" such as carbonates, hydrated silica, phyllosilicates or sulfates, among others (Haberle et al., 2017). These minerals have been detected on the Martian surface by means of spacecraft or surface landers (Murchie et al., 2009), and are therefore indicative of the presence of liquid water on the Martian surface.

- **Isotopic evidence.** The isotopic composition of the Martian atmosphere in species such as Ar, H, Xe or N is enriched in the heavier isotope with respect to that on Earth. This enrichment in the heavier isotopes is understood as indirect evidence of the escape of the atmosphere into space, which leaves the remaining atmosphere enriched in the

heavier isotope (e.g., Jakosky (1991)). The implication for the climate of early Mars is that the atmosphere was thicker than it is today, and perhaps thick enough to create the required conditions for sustaining liquid water on the surface.

Although all this evidence suggests the presence of liquid water on Mars in the past, it is still not clear what climatic conditions permitted it, especially since the luminosity of the Sun was approximately 25% less four billion years ago than it is today (Gough, 1981). Attempts to reconcile the presence of liquid water on the Martian surface with the "faint young Sun" usually invoke atmospheres with a composition and mass different from the present one, in order to provide enough greenhouse warming. For instance, Pollack et al. (1987) suggested that the greenhouse warming produced by a 5 bar CO_2 atmosphere was sufficient to sustain the required temperatures, but later work by Kasting (1991) realised that much of the CO_2 in such an atmosphere would condense into clouds, and then precipitate. The clouds would increase the planetary albedo, causing the surface to cool, and eventually leading the CO_2 to accumulate on the surface, and decreasing the total pressure of the atmosphere. Other theories have also been suggested, invoking the presence of other gases which nowadays are present just in trace quantities, but which might have been much more abundant in the past, when an increased volcanic activity was expected (e.g., Johnson et al. (2008)). One interesting theory is the one proposed by Wordsworth et al. (2013), which does not require sustained global warming, but only episodic events of volcanism, impacts or spin axis/orbital perturbations to generate enough liquid water to erode the valleys.

Methods for estimating the climate of early Mars and its evolution rely on constraints imposed by measurements of the isotope ratios. In particular, as the atmosphere escapes to space, it is expected to leave the remaining fraction enriched in the heavier isotopes, as described by the Rayleigh distillation equation

$$R_i(t) = R_i(t=0) \cdot x(t)^{f-1}, \tag{1.0.1}$$

where R_i is the atmospheric isotope ratio, x is the fraction of remaining fluid, and f is the fractionation factor relating the efficiency of escape of the heavy isotope with respect to that of the lighter one. Therefore, with estimations of the past and present isotopic ratios representative of the Martian atmosphere (i.e., $R_i(t)$ and $R_i(t=0)$) and the fractionation

factor f, one can estimate the fraction of atmosphere that has escaped to space from time $t = 0$ to time t. However, some difficulties may arise when estimating these input values:

- The isotopic composition of the present-day atmosphere can be constrained using remote sensing techniques (e.g., Owen et al. (1988); Villanueva et al. (2015)), or *in situ* measurements (e.g., Nier et al. (1976); Webster et al. (2013)). However, it must be noted that the isotope ratios inferred from localised measurements are subject to climatological processes that might affect the isotopic composition of the sample. Therefore, in order to estimate the isotopic ratios representative of the Martian atmospheric reservoir outside of any fractionating processes (i.e., R_i in equation 1.0.1), one must understand the several processes that might fractionate the isotope ratios, to what extent, and how they vary. It must be noted that indeed the present-day Martian atmospheric reservoir is fractionated relative to their primordial sources. However, unless explicitly stated, the term non-fractionated in this thesis will refer to the isotopic ratios representative of the Martian atmospheric reservoir at present.

- The fractionation factor f describes the relative efficiency of escape between the heavier and lighter isotopes. It is defined as

$$f = \frac{\phi_{i_1}/\phi_{i_2}}{R_{i,0}}, \tag{1.0.2}$$

  where ϕ_{i_1} and ϕ_{i_2} are the fluxes of escaping atoms of the two isotopologues, and $R_{i,0}$ represents the isotopic ratio representative of the near-surface atmospheric reservoir (Yung et al., 1989). As previously stated, this factor represents the efficiency of escape of the heavy isotope with respect to the light one. If the ratio of escaping fluxes in the upper atmosphere is the same as the ratio representative of the near-surface atmospheric reservoir, then $f = 1$, meaning that the atmospheric isotopic ratio will not evolve with time as the atmosphere escapes. On the other hand, when the heavy isotope has a low efficiency of escape with respect to the lighter one ($f \to 0$) the atmospheric isotope ratios will largely increase as the atmosphere escapes into space (Cangi et al., 2020). In order to estimate the ratio of escaping fluxes, one must understand the physical and chemical pathways by which the near-surface atmospheric reservoir is decomposed and transported to the upper atmosphere, where escape occurs, and how these processes

might fractionate the isotopic ratios.

Using this approach, based on measurements of the $^{13}C/^{12}C$ ratio in CO_2, Jakosky (2019) estimates that 1-2 bars of CO_2 escaped to space, although this estimate is a lower limit, since other processes like the formation of carbonates or the condensation onto a permanent polar cap deplete the atmosphere in the heavier isotope. Similarly, using measurements of the D/H ratio, Alsaeed and Jakosky (2019) estimate that the ancient reservoir of water on Mars was 40 to 170-m water global equivalent layer (1-m GEL = 1.45×10^{17} kg of water), which, combining the 5 to 100-m GEL outgassed and 20 to 220-m GEL lost to space, lead to the current water reservoir of 20 to 50-m GEL. Therefore, these calculations allow to get an insight of the climate of early Mars and to better understand if our neighbouring planet was hospitable for life to grow.

In this project, we use sensitive infrared solar occultation observations made with the Atmospheric Chemistry Suite (ACS) onboard the ExoMars Trace Gas Orbiter (TGO) to constrain the vertical structure of the isotope ratios in H_2O and CO_2. In particular, we aim to answer the following questions from the data:

- What is the non-fractionated isotope composition of H_2O and CO_2 in the Martian atmosphere?

- Does the isotopic composition of atmospheric H_2O and CO_2 vary? If so, what are the main drivers of variation, and to what extent do the isotope ratios fractionate?

- Are the different isotopes in H_2O and CO_2 fractionated as they are decomposed into lighter species, affecting the escape fractionation factor f?

The rest of this chapter is devoted to provide a detailed introduction of the Martian atmosphere, focusing on the behaviour of CO_2 and H_2O. Then, we review the current knowledge about the isotope composition of these species, including the results from previous measurements, as well as the expectations from several fractionation processes.

1.1 Mars atmosphere

1.1.1 Thermal structure and composition

In the last decades, several orbiting spacecraft, surface landers and modelling efforts have provided an in-depth understanding of the Martian atmosphere, showing how it is perhaps the closest to Earth in terms of weather and climate, and how some of its characteristics are best explained in comparison with Earth.

On Earth, the atmosphere is typically divided in several layers: the lowest layer is the troposphere, where the atmosphere is efficiently mixed by turbulence and temperature decreases with altitude following an adiabatic behaviour; above the troposphere, separated by the tropopause at approximately 13 km, lies the stratosphere, where temperature increases due to the absorption of ultraviolet (UV) sunlight in the ozone layer; higher up, in the mesosphere, at approximately 50-60 km, temperature decreases again due to the absence of ozone, until it increases again in the thermosphere (∼80-100 km), where the extreme UV radiation is absorbed; above the thermosphere, at approximately 600 km, lies the exosphere, where the atmosphere meets the interplanetary space. On Mars, the atmosphere is instead divided into the "lower", "middle" and "upper" atmospheres. The lower atmosphere expands from the surface to approximately 50 km, where temperatures decrease with height. The middle atmosphere expands from approximately 50 to 100 km, and is characterised by high variability of temperatures driven by the influence of tides and waves. Above 100 km lies the upper atmosphere, in which the temperature increases with height due to the absorption of extreme UV sunlight. It must be noted that Mars does not have a stratosphere, as the Earth does, due to the absence of an ozone layer (e.g., Read et al. (2015); Smith et al. (2017)).

The variations of the thermal structure in the lower Martian atmosphere also present several similarities with those on Earth, given the similar obliquity of the rotation axis with respect to the ecliptic (see Table 1.1). However, in addition to the summer and winter seasons caused by the obliquity of the planet, Mars' seasonal variations are also influence by the orbital eccentricity, which makes the distance to the Sun 20% smaller at perihelion than at aphelion, receiving approximately 40% greater solar insolation during the perihelion season. Currently, perihelion occurs at a solar longitude (i.e., angular distance of Mars around the Sun, with

0° defined at the vernal equinox in the northern hemisphere) of $L_S = 251°$, and the closer distance to the Sun increases the radiative heating of the atmosphere during this season, which reinforces the heating of the summer season in the southern hemisphere (see Figure 1.1).

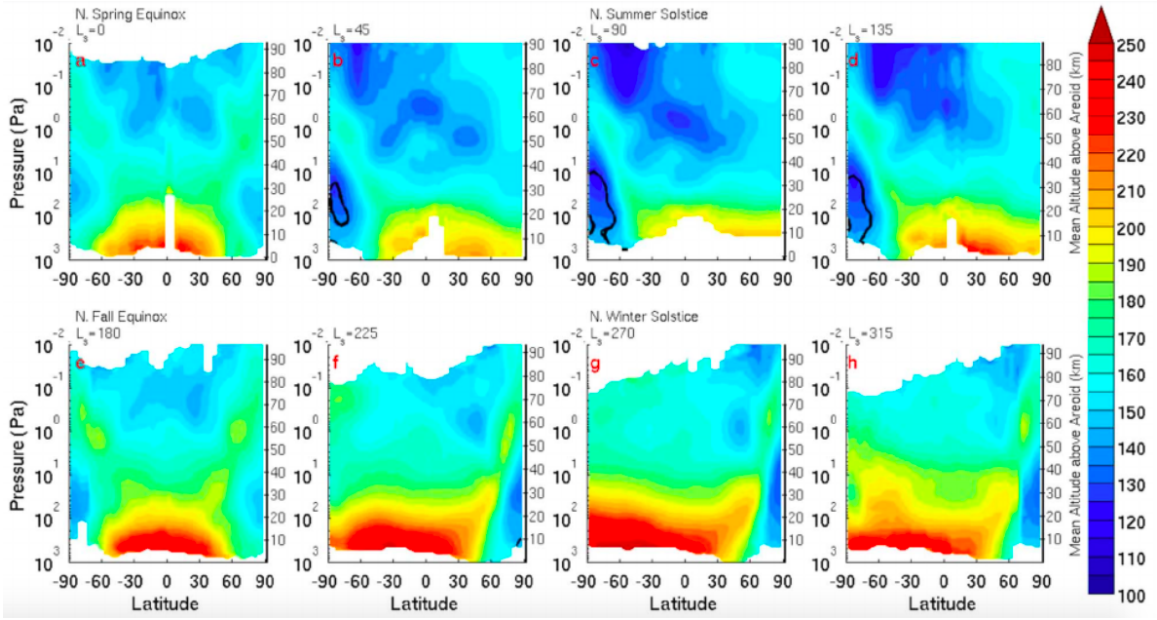

Figure 1.1: Zonal average temperatures in the lower and middle atmosphere measured by the Mars Climate Sounder onboard the Mars Reconnaissance Orbiter (MCS/MRO) during MY29. The black contours indicate the CO_2 frost point. Figure from McCleese et al. (2010).

Apart from the seasonal and latitudinal variations caused by the eccentricity of the orbit and the obliquity of the planet, which establish the solar insolation of the atmosphere, the thermal structure of the Martian atmosphere cannot be properly understood without the presence of dust particles suspended in the atmosphere (Gierasch and Goody, 1972; Madeleine et al., 2011). Figure 1.2 shows the climatology of zonal average temperatures at 0.5 mbar, as well as the dust and water ice opacities as observed by the Planetary Fourier Spectrometer onboard Mars Express (PFS/MEx) from Martian Year (MY) 26 to MY33. As shown in the Figure, dust storms are common in Mars, occurring usually at high southern latitudes between L_S 210 and 270°, and affecting the atmospheric radiative forcing and circulation (e.g., Smith et al. (2001); Giuranna et al. (2019)). In 2018 (MY34), almost coinciding with the start of the science operations of the ExoMars TGO, there was a Global Dust Storm (GDS) starting in the northern hemisphere at $L_S = 184.9°$ (Sánchez-Lavega et al., 2019). This is the first case of a GDS starting in the northern hemisphere, and at a time unusual for most GDSs. The evolution of the MY34 GDS was recorded by several instruments, reporting its influence

in the atmospheric structure and composition (e.g., Smith (2019); Fedorova et al. (2020b); Gkouvelis et al. (2020)).

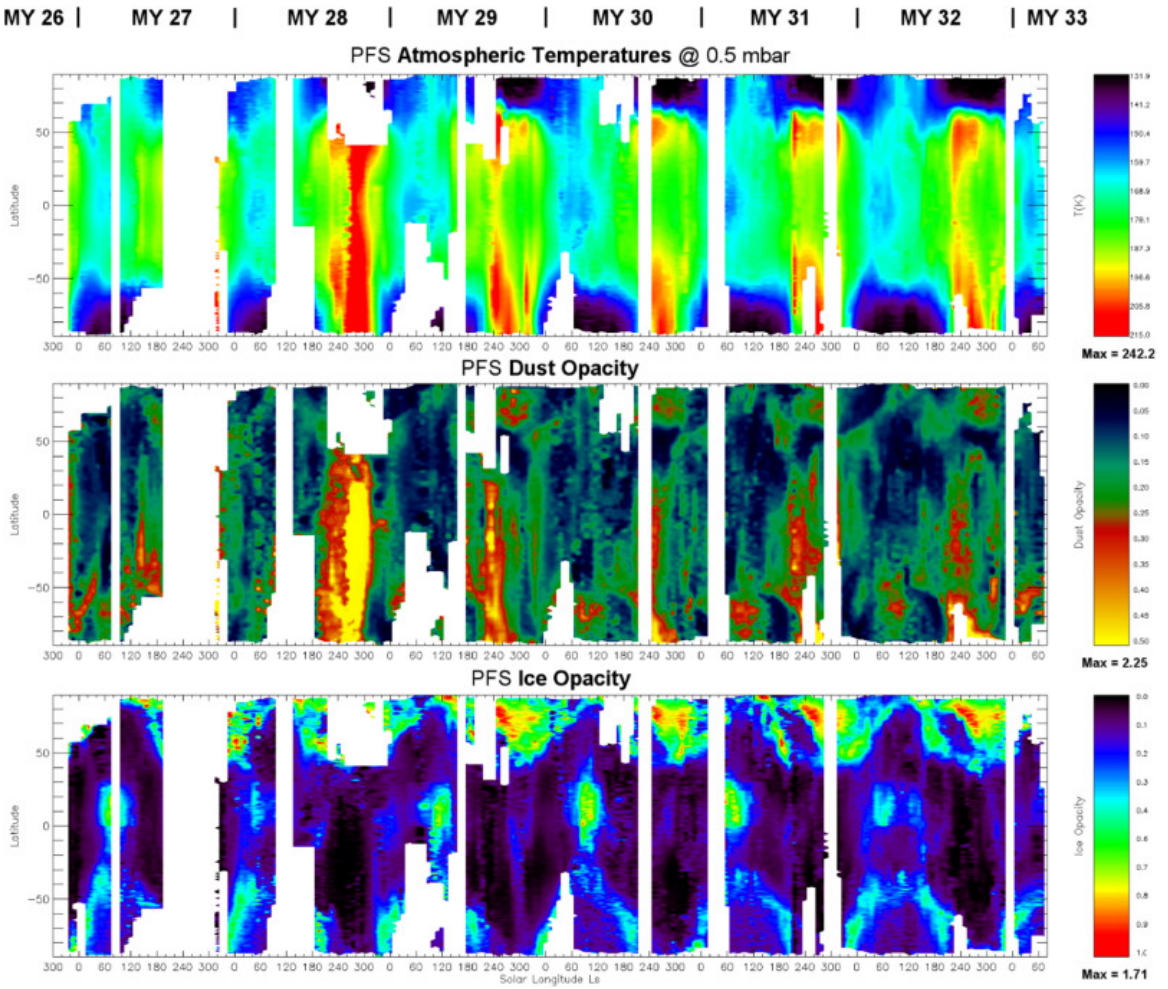

Figure 1.2: Climatology of temperature at 0.5 mbar (top), dust opacity (middle) and water ice opacity (bottom) as observed by the Planetary Fourier Spectrometer onboard Mars Express (PFS/MEx) from MY26 to MY33. Figure from Giuranna et al. (2019).

One of the main differences between the Earth's and Mars' atmospheres lies in regards of their composition. While Earth's atmosphere is primarily a mixture of N_2 and O_2, the majority of the Martian atmosphere is in the form of CO_2 (96%), with smaller amounts of N_2 (1.9%) and Ar (1.9%) (e.g., (Mahaffy et al., 2013)). Of the gases that build up the composition of the Martian atmosphere (see Table 1.2), CO_2 and H_2O are the only condensible species. However, as carbon dioxide condenses onto the polar caps, it drives large seasonal variations in the atmospheric pressure and density, driving variations of the volume mixing ratio of the non-condensible species. Apart from the measured species shown in Table 1.2, there are other gases which have not yet been detected in the atmosphere, but whose presence is expected

from models. These gases are expected to be present in very low abundances, created by the dissociation of the major species (C, O, H, N) and in posterior chemical reactions (e.g., HO_x, C_xH_x, NO_x).

Table 1.2: Composition of the Martian atmosphere. Adapted from Smith et al. (2017).

Gaseous species	Average abundance	Reference
CO_2	0.9513	Owen et al. (1977)
N_2	0.027	Owen et al. (1977)
	0.019	Mahaffy et al. (2013)
Ar	0.016	Owen et al. (1977)
	0.019	Mahaffy et al. (2013)
O_2	0.0014	Hartogh et al. (2010)
CO	800 ppmv	Smith et al. (2009)
H_2O	15-1500 ppmv	Smith (2004)
H_2	15 ppmv	Krasnopolsky and Feldman (2001)
Ne	2.5 ppmv	Owen et al. (1977)
Kr	0.3 ppmv	Owen et al. (1977)
Xe	0.08 ppmv	Owen et al. (1977)
O_3	10 - 350 ppbv	Perrier et al. (2006)
H_2O_2	10 - 40 ppbv	Encrenaz et al. (2004)
CH_4	0-40 ppbv	Mumma et al. (2004)
HCl	1 - 4 ppbv	Korablev et al. (2021)

1.1.2 The H_2O cycle

The role of water in the present Martian climate is not as negligible as one may think based on the low abundances in which it is found in the atmosphere. Observations show that water follows a seasonal cycle, in which water variations are controlled by exchanges with the different reservoirs (e.g., Jakosky and Farmer (1982); Smith (2002)). The three main reservoirs of water on Mars are the atmosphere, the surface and the subsurface. Current estimations suggest that if these reservoirs were to be condensed or melted, they would form a layer of 20-50 m along the whole Martian surface (Lasue et al., 2013; Alsaeed and Jakosky, 2019).

The pattern followed by the atmospheric reservoir has been studied during several consecutive Martian years, with the use of observations from the different Mars missions (e.g., Smith et al. (2018); Sindoni et al. (2011); Trokhimovskiy et al. (2015)). Figure 1.3 shows the averaged water column between Martian years 27 to 31, as a function of latitude and solar longitude, as observed by the SPICAM instrument on Mars Express (Trokhimovskiy et al., 2015). The

atmospheric water content in the Martian atmosphere varies with season, due mainly to the sublimation and condensation of the polar caps. The annual maximum of water content in the atmosphere is found in the early summer northern hemisphere (L_S = 120° - 130°), after the sublimation of the northern polar cap. After this season the abundance in the northern polar cap rapidly decreases, balanced by transport to the equatorial region, which has a peak at approximately L_S = 150° at 30°N, and the condensation of the atmospheric water vapour on the polar cap. Similarly, the maximum water column density in the southern hemisphere occurs during the southern summer, but in this case the peak value is twice as weak as for the northern maximum. This asymmetry is in part caused by the formation of water ice clouds at low latitudes (∼10°S-30°N), which prevents water vapour from being transported to the southern hemisphere. In turn, the warmer conditions of the southern hemisphere summer do not favour the formation of water ice clouds, resulting in a positive net flux of water vapour from the southern to the northern hemisphere (Montmessin et al., 2004).

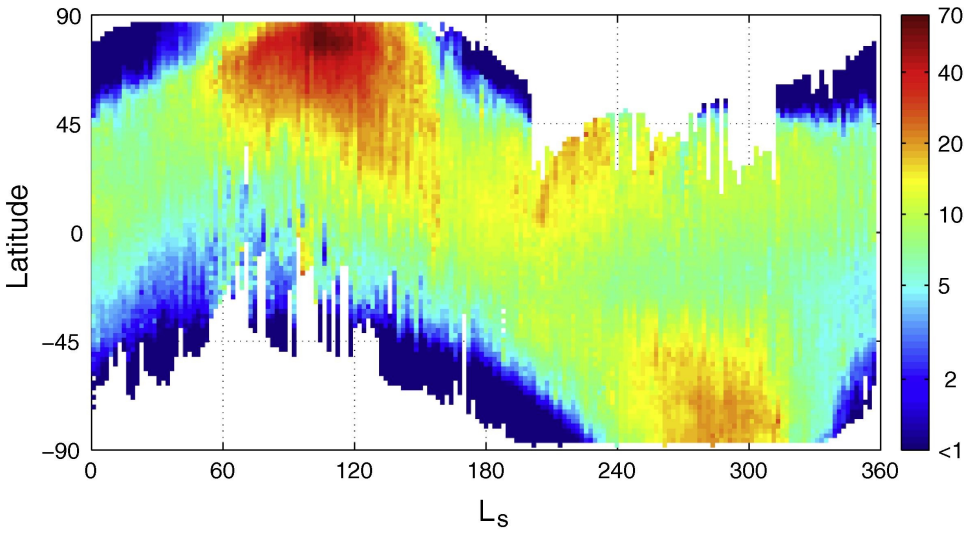

Figure 1.3: Water column in pr. μm (1 pr. μm = 3.34 × 10^{18} cm^{-2}) averaged over Martian years 27 to 31, as observed by SPICAM. Figure from Trokhimovskiy et al. (2015).

The vertical distribution of the water vapour is also important for understanding phenomena such as mixing of the atmosphere, atmosphere-surface interactions, cloud formation and escape processes. One of the major factors controlling the vertical distribution of water vapour is the saturation. At the altitude at which saturation level reaches one, known as the hygropause, water vapour can be transformed into the solid state, and therefore cloud formation is enabled. At the hygropause, water vapour condenses, and the volume mixing ratio suddenly drops with

altitude, making most of the water content to be confined below this altitude. The altitude of the hygropause is controlled by the thermal structure of the atmosphere: during the northern hemisphere spring, the planet is close to aphelion, and average temperatures reach the annual minimum, which sets low altitudes for the condensation level of H_2O, of approximately 10 km. On the other hand, during the southern hemisphere spring, the planet is close to perihelion, and the warmer temperatures raise the hygropause upwards to higher altitudes, of about 40-60 km (Clancy et al., 1996). Maltagliati et al. (2011) reported the presence of supersaturated water vapour, using observations by SPICAM onboard Mars Express. This was attributed to the absence of dust particles acting as condensation nuclei, as the threshold saturation ratio for homogeneous nucleation on Mars exceeds 1000 (Montmessin, 2002). However, Fedorova et al. (2020b) recently confirmed the high levels of supersaturation on Mars even in the presence of dust and ice crystals, which is speculated to be due to a longer timescale for condensation compared with rapid drops in temperature and/or rises in water concentration.

The most sensitive observations of the vertical distribution of water vapour have been reported using observations by the NOMAD and ACS instruments onboard the ExoMars TGO (Aoki et al., 2019; Fedorova et al., 2020b). Figure 1.4 shows the vertical distribution of temperature, water vapour, saturation ratio, and aerosols as observed by ACS (Fedorova et al., 2020b). The observations show that dust storms (GDS between L_S = 193-220° and regional dust storm between L_S = 320-335°) increase the atmospheric temperature, rising the hygropause up to high altitudes. In addition, high altitude water is also observed around the perihelion season. Unlike the effect of dust storms, whose effect on rising the altitude of the hygropause is sporadic, upwelling of water vapour in the perihelion season is recurrent every year, and has likely governed the escape of water to space over geological time scales (Fedorova et al., 2020b).

Water vapour condenses to form water ice clouds in the Mars' atmosphere. Cloud formation also appears to have distinctive seasonal variations, following two major patterns. The *Aphelion Cloud Belt* forms at low latitudes (∼10°S-30°N) during northern spring and summer, as a result of the north-south circulation. As previously mentioned, this condensation near the equator has consequences on the general transport of water vapour in the atmosphere during this season, as this process prevents some of the water vapour from reaching the southern

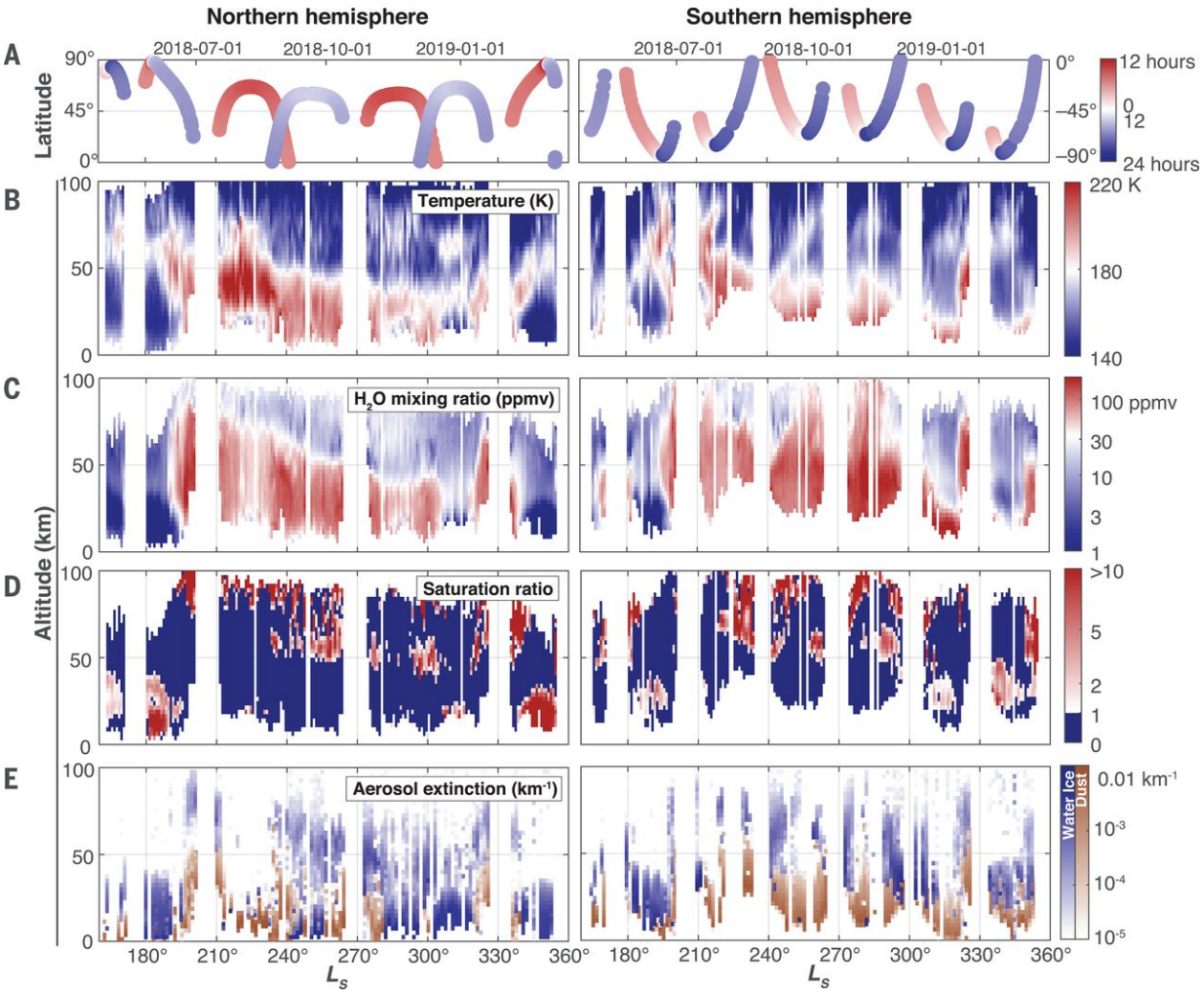

Figure 1.4: Atmospheric properties during the dusty season of MY34 as measured by ACS NIR onboard ExoMars TGO. Each panel shows the data value in colour, plotted as functions of L_S and altitude, with the northern hemisphere on the left and the southern hemisphere on the right. A) Distribution of solar occultation measurements. B) Atmospheric temperature. C) Water vapour volume mixing ratio. C) Saturation ratio of water vapour. D) Water ice and dust aerosol extinctions. Figure from Fedorova et al. (2020b).

hemisphere (Clancy et al., 1996). During southern spring and summer this equatorial cloud belt does not form, as it is slightly warmer on average (Read et al., 2015). The second major pattern in which water ice is observed in the Martian atmosphere is in the so-called *Polar Hoods*, which form over both poles during autumn and winter seasons (Benson et al., 2010, 2011).

Surface ice represents the major reservoir of water on Mars. In particular, most of the surface water ice is stored in the permanent northern polar cap, which extends asymmetrically until 80°N-85°N, with a thickness up to a few km (Zuber, 1998). In contrast, the southern polar cap is mostly composed by CO_2 ice, with an amount of perennial water ice approximately 20 times lower than the perennial water ice in the north (Bibring et al., 2004). This asymmetry in the polar caps explains the north-south asymmetry found in the atmospheric water content. In the north polar cap, the ice is directly exposed to sunlight, while at high-southern latitudes the water ice is protected by the CO_2 seasonal ice until very late in summer. Polar layer deposits, observed as horizontal layers of ice and dust at both poles, are attributed to the different deposition during climate cycles driven by variations on the obliquity of Mars orbit (Milkovich and Head, 2005).

Subsurface ice has also been shown to be present on Mars, holding information about past Martian climates. These subsurface deposits are expected to be produced by two main sources: direct deposition of ice throughout Martian history that was subsequently consolidated, and deposition on the subsurface on the present from the vapour phase, that travels through the voids between soil grains (Schorghofer and Forget, 2012). The water content in the Martian subsurface has been primarily determined from neutron detectors on orbital spacecraft, that take advantage of the interaction of cosmic rays with hydrogen. The hydrogen-rich regions inferred from these observations are correlated with regions where ice is predicted to be stable, and therefore suggesting that the hydrogen is hosted by subsurface ice (Boynton et al., 2002; Feldman et al., 2002). The polar regions host high water abundances (20-100% water-equivalent hydrogen), that extend up to 50° in latitude. The deposits at low latitudes range between 2 and 10% in water content, with two localized maximums near the Arabia Terra region, situated at 25°N latitude (Feldman et al., 2004).

1.1.3 The CO_2 cycle

Like water vapour, carbon dioxide acts as a volatile species in the Martian atmosphere, involving cyclic interactions between the atmosphere and surface. Approximately 25-30% of the atmospheric CO_2 is sublimed and refrozen from the seasonal ice deposits every year (e.g., Tillman et al. (1993); Kelly et al. (2007)), although a perennial carbon dioxide deposit exists in the southern hemisphere (Kieffer, 1979). As CO_2 represents approximately 95% of the Martian atmosphere (see Table 1.2), these seasonal patterns generate large variations in the overall surface pressure, as measured by several landers (Hess et al., 1977; Harri et al., 2014). Numerous studies have demonstrated that the global climate of Mars is controlled by the optical properties (i.e., albedo and emissivity) of solid CO_2, but in turn these properties depend on a number of parameters, such as contamination by dust and H_2O ice, solar phase or atmospheric circulation (Haberle et al., 2008; Piqueux et al., 2015).

In the atmosphere, carbon dioxide can also be found in its solid state, mainly in low-altitude clouds in the polar regions, and high-altitude mesospheric clouds (Clancy and Sandor, 1998; Montmessin et al., 2006a; Clancy et al., 2007). The clouds in the polar regions have been historically difficult to observe, as they usually form in the darkness of the polar night, and nadir-viewing infrared observations struggle to differentiate the clouds from surface frost (Forget et al., 1995). The polar CO_2 ice clouds appear in the lower atmosphere, during the winter nights in both poles, with particle sizes of several tens or hundreds of micrometers (Pettengill and Ford, 2000; Colaprete and Toon, 2002; Hayne et al., 2012). These CO_2 ice particles precipitate and are deposited on the surface, contributing between 3% and 20% by mass to the seasonal deposits at high latitudes (Hayne et al., 2014). The mesospheric clouds have been observed by several instruments in different missions (e.g., McConnochie et al. (2010); Vincendon et al. (2011); Montmessin et al. (2006a); Aoki et al. (2018)). These types of clouds appear at low latitudes ($\pm 30°$), in mainly two different circumstances: daytime clouds form between 60 and 85 km, with particle sizes of 0.5-3 μm (Montmessin et al., 2007; Määttänen et al., 2010); night-time clouds form between 80 and 100 km with particle sizes around 0.1 μm (Montmessin et al., 2006a; Jiang et al., 2019).

The vertical distribution of CO_2 gas is mainly controlled by the dissociation of carbon dioxide by UV photons, which break the CO_2 molecules apart to form CO and O. This process produces a decrease of the CO_2 volume mixing ratio in the upper atmosphere, while in the lower altitudes the atmosphere is approximately well-mixed (see Figure 1.5). The altitude above which the CO_2 volume mixing ratio decreases is driven by the solar UV flux, the atmospheric column above and the solar zenith angle (SZA). For instance, close to perihelion, the solar insolation is about 40% higher than close to aphelion, which would lead to UV photons penetrating to lower altitudes. However, the increase of the surface pressure (i.e., atmospheric column density) due to the sublimation of the southern polar cap, and the increase atmospheric mixing due to the intensified Hadley circulation make the atmosphere to be well-mixed up to high altitudes, while during aphelion ($L_S = 71°$) there is a sharp decrease of the CO_2 mixing ratio at approximately 75-100 km. In the near-surface atmosphere, some variations of the CO_2 abundance occur due to the condensation and sublimation of the seasonal polar caps.

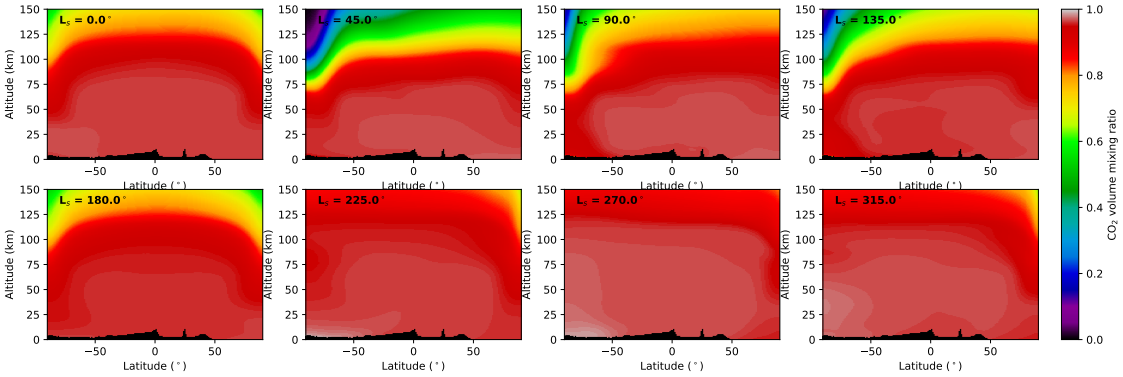

Figure 1.5: Evolution of the volume mixing ratio of carbon dioxide in the Martian atmosphere at noon as predicted by the Mars Climate Database (Forget et al., 1999) as a function of altitude, latitude and solar longitude.

For a long time, the stability of carbon dioxide in the Martian atmosphere remained a puzzle, since the rate of dissociation of CO_2 molecules into CO and O was much faster than the recombination by the inverse reaction, which is spin-forbidden. This process should in principle lead to a large buildup of CO and O in the Martian atmosphere, rather than a CO_2-dominated atmosphere (Lefèvre and Krasnopolsky, 2017). In turn, the stability of CO_2 in the Martian atmosphere appears to be controlled by the "odd-hydrogen" species (H, OH, HO_2), which are produced in the photodissociation of water vapour. These odd-hydrogen

species, although found in the atmosphere in just trace amounts, can catalytically convert CO into CO_2 at a much faster rate than the inverse reaction of CO_2 dissociation (McElroy and Donahue, 1972; Parkinson and Hunten, 1972). As a by-product of this catalysis, molecular hydrogen is also formed and stabilised in the atmosphere.

1.1.4 Atmospheric escape

Atmospheric escape into space is one of the key processes for understanding the evolution of the Martian atmosphere throughout history. In this section, we introduce the current knowledge describing the physical and chemical pathways by which H, C and O are lost from the Martian atmosphere.

H escape

The escape of hydrogen in the Martian atmosphere is thought to occur mainly in the form of thermal escape of atomic hydrogen (Jakosky et al., 2018). Traditionally, the main source of escaping H atoms in the Martian atmosphere was thought to be molecular hydrogen: H_2O molecules, confined to the lowest altitudes due to the natural barrier created by the formation of water ice clouds, are photodissociated in the atmosphere giving rise to odd-hydrogen species (e.g., OH, HO_2), which catalyse the recombination of CO_2, forming stable H_2 as a by-product (McElroy and Donahue, 1972; Lefèvre et al., 2004). The H_2 molecules are allowed to migrate to the upper atmosphere, where they can recombine with CO_2^+, giving rise to HCO_2^+ and H. These H atoms in the upper atmosphere have velocities following a Maxwell-Boltzmann distribution, which depends on the mass of the atoms and the temperature. At typical temperatures in the exobase, the atoms in the tail of the Boltzmann distribution will have velocities exceeding the escape velocity, and will escape the gravitational bound of the planet due to the absence of sufficient collisions in the exosphere (Jakosky et al., 2018).

Ultraviolet observations of the Martian atmosphere made with the Hubble Space Telescope and Mars Express revealed an unexpected variability in the density of atomic hydrogen, which was found to peak during the perihelion season (Chaffin et al., 2014; Bhattacharyya et al., 2015; Halekas, 2017). These sudden seasonal variations were found not to be consistent with the supply from long-lived H_2, which gives rise a steady production of hydrogen throughout the year. Using simulations from a photochemical model, Chaffin et al. (2017) showed that

these seasonal variations in the upper-atmospheric H density could be explained by the presence of H_2O molecules between 40-100 km, which can be readily photolysed, giving rise to enhancements of the atomic hydrogen abundance and its escape rate in a timescale of weeks, providing an explanation for the observed variations. Using observations from MCS/MRO, Heavens et al. (2018) showed that not only the density of atomic hydrogen increases during the perihelion season, but also correlates with the presence of dust storms, which raise the level of the hygropause to 80 km above the Martian surface and enabling the direct production of atomic hydrogen. Recent photochemical models have also suggested another mechanism for the seasonal production of atomic hydrogen in the Martian atmosphere (Krasnopolsky, 2019; Stone et al., 2020). Instead of being the direct photolysis of H_2O the main source for the production of H, these models suggest that it is the dissociation of H_2O by ions producing the observed variations of atomic hydrogen.

O escape

As opposed to the case of atomic hydrogen, the escape of oxygen from the Martian atmosphere is not dominated by thermal escape. Instead, the escape of O is dominated by non-thermal processes involving reactions with ions. The mechanisms governing the escape of oxygen escape can be classified in three types:

- Dissociative recombination, by which ions produced by solar UV photons recombine with an electron and are rapidly dissociated into neutral molecules which might have sufficient energy to overcome the Martian gravity. In principle, this type of escape mechanism occurs in a variety of oxygen-containing ions, such us O_2^+, CO_2^+, CO^+ or NO^+, but the most important of these appears to be the dissociative recombination of O_2^+.

- Ion escape, by which ionospheric ions are accelerated by an electric field with enough kinetic energy to overcome the gravity of Mars and ultimately escape to space. The electric field may be produced by different processes, such as by the moving magnetic field of the solar wind or plasma pressure gradients in the ionosphere (e.g., Jakosky et al. (2018)).

- Sputtering, reaction by which the ions in the ionosphere are accelerated by the solar

wind electric field and, instead of escaping the planet, impact with other neutrals in the atmosphere and eject them into space. This loss mechanism is believed to be dominant in the removal of heavy and inert gases such as Ar (Jakosky et al., 2017), but can eject atoms of any species.

The relevance of each of these mechanisms to the overall loss of oxygen from the Martian atmosphere was estimated by Jakosky et al. (2018) using a combination of observations from several instruments on the MAVEN spacecraft. Their estimations suggest that the most important mechanism for the escape of oxygen is dissociative recombination, followed by ion escape and sputtering, with present-day loss rates of 5×10^{25}, 5×10^{24} and 3×10^{24} s^{-1}, respectively.

C escape

The mechanisms governing the escape of carbon from the Martian atmosphere and their respective rates still remain unclear, mainly because they have not yet been constrained with measurements from the MAVEN spacecraft (Jakosky, 2019). Therefore, the pathways by which carbon escapes from the Martian atmosphere are mainly constrained using photochemical models (e.g., Gröller et al. (2014); Lo et al. (2020)). These models suggest that, while carbon can be lost from the Martian atmosphere in different ways, such as CO_2^+ ion escape and sputtering or CO sputtering (Barabash et al., 2007; Leblanc, 2002), their contribution to the total amount of carbon lost to space appears to be much lower than the loss of hot atomic carbon (Gröller et al., 2014; Cui et al., 2019; Lo et al., 2020).

The loss of atomic C from the Martian atmosphere can in turn be produced by several mechanisms. Early studies suggested that the main source of escaping carbon was the dissociative recombination of CO^+ ($CO^+ + e^- \rightarrow C + O$) (McElroy, 1972), although further analyses revealed that it was indeed the photodissociation of CO molecules that is the dominant process in the production of atomic C (Fox and Bakalian, 2001; Gröller et al., 2014; Cui et al., 2019). Recently, Lo et al. (2020) have incorporated a series of new measurements of the photodissociation cross sections of CO_2 and CO into a 1-D photochemical model to produce the latest estimations of the production rates of atomic C in the Martian atmosphere. These new measurements include the photodissociation cross sections of CO_2 into $C + O_2$ (Lu et al.,

2014), a reaction that was not incorporated in previous models, which predicted $CO_2 + h\nu \rightarrow CO + O$. Figure 1.6 shows the major mechanisms governing the production and destruction of atomic carbon in the Martian atmosphere, which are dominated by the direct production of atomic C from the photolysis of CO_2 and the recombination of these products ($C + O_2$), respectively.

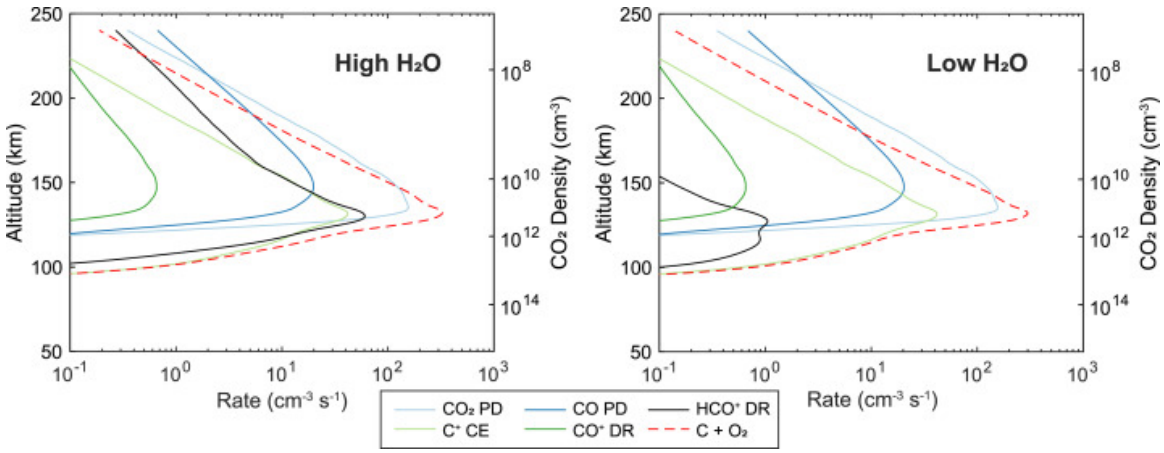

Figure 1.6: Major production (solid lines) and loss (dashed lines) mechanisms of atomic C when using high and low H_2O density profiles. PD stands for photodissociation, DR for dissociative recombination and CE for charge exchange. Figure from Lo et al. (2020).

However, it must be noted that the study of Lo et al. (2020) focuses on the overall production of atomic C in the Martian atmosphere, rather than on the production of hot atomic carbon (i.e., production of C atoms with sufficient kinetic energy to overcome the gravity of Mars). Therefore, while the photolysis of CO_2 appears to be the major mechanism for the production of C in the atmosphere, it might not be as relevant as the photodissociation of CO and the dissociative recombination of CO^+ for the escape of carbon from the Martian atmosphere.

1.1.5 Isotope composition

Isotope ratios provide important constraints on the evolution of planetary atmospheres. In the atmosphere of Mars, several measurements have revealed the enrichment in the heavier isotopes of several species with respect to those on Earth, which is thought to be an indirect evidence of the atmospheric escape throughout the Martian history and the presence of a much denser atmosphere four billion years ago. Isotopic enrichments were first measured at Mars using mass spectrometers on the Viking landers, measuring ratios of $^{15}N/^{14}N = 1.7$ and $^{40}Ar/^{36}Ar = 10.3$ with respect to Earth (Owen et al., 1977). Mahaffy et al. (2013) reported

a ratio of $^{40}Ar/^{36}Ar = 6.5$ as compared to Earth, using the Quadrupole Mass Spectrometer (QMS) on the Curiosity Rover. This value, even if considerably smaller than the measurement performed with the Viking Lander, shows a large enrichment with respect to the telluric ratio. Using measurements of the upper atmospheric $^{38}Ar/^{36}Ar$ ratio with the Neutral Gas and Ion Mass Spectrometer (NGIMS) onboard the Mars Atmosphere and Volatile Evolution (MAVEN) spacecraft, Jakosky et al. (2017) estimated that 66% of atmospheric argon was lost to space.

Enrichment of the heavier isotope has also been observed in the isotopologues of H_2O and CO_2, providing more evidence of the importance of atmospheric escape in the evolution of the Martian atmosphere. Not only the isotope ratios show the importance of atmospheric escape, but also measurements of the isotope ratios in different species allow to constrain the size of the ancient reservoir of each species, providing clues on the composition of the past climate of Mars. For instance, based on measurements of the $^{13}C/^{12}C$ ratio in CO_2, Jakosky (2019) estimate that 1-2 bars of CO_2 escaped to space. Similarly, measurements of the D/H ratio have been used to constrain the size of the ancient water reservoir on Mars (e.g., Kurokawa et al. (2014); Alsaeed and Jakosky (2019)). However, the isotopic composition does not only vary in geologic timescales, but also gets fractionated in processes happening in the present-day climate. Therefore, in order to understand the evolution of the Martian atmosphere from its isotopic composition, one must first understand the variations of the isotope ratios in today's atmosphere, in order to disentangle the isotopic composition of the bulk of the atmosphere, and that measured in localised measurements.

In the literature, isotopic ratios are usually expressed as a factor of the measured ratio R with respect to a standard ratio R_s representative of the Earth (e.g., $^{18}O/^{16}O$, D/H), or as a deviation of the measured ratio with respect to the standard (e.g., $\delta^{18}O$, δD) in units of ‰, given by $\delta^{18}O = (R/R_s - 1) \times 1000$. Table 1.3 presents the standard ratios for the H, O and C isotopes. From now on, unless explicitly mentioned, the isotope ratios will be given with respect to the standards, either as a factor or deviation.

In this section, we review the current knowledge of the isotope composition of H_2O and CO_2 in the Mars' atmosphere, including the results from past measurements, and the processes that might fractionate them in short and long timescales. This information provides a context

Table 1.3: Standard isotope ratios of the H, O and C isotopes measured in this thesis, as given by the Vienna Standard Mean Ocean Water (VSMOW) and the Vienna Pee Dee Belemnite (VPDB).

Isotope ratio	Standard	Value
D/H	VSMOW	1.558×10^{-4}
$^{18}O/^{16}O$	VSMOW	2.005×10^{-3}
$^{17}O/^{16}O$	VSMOW	3.799×10^{-4}
$^{13}C/^{12}C$	VPDB	1.124×10^{-2}

for the results of this thesis, allowing the comparison and validation with past measurements, and understanding the potential sources of variation in the measured isotope ratios.

1.1.5.1 Previous measurements

H isotopes

The first measurement of the D/H ratio in the present Martian atmosphere was reported by Owen et al. (1988), using the Fourier transform spectrometer at the Canada-France-Hawaii 3.6-meter telescope, and observing an enrichment in the heavier isotope of a factor of 6 ± 3, with respect to VSMOW. In the following years, different means of Earth-based spectroscopy allowed the measurement of the D/H ratio (5.2 ± 0.2, Bjoraker et al. (1989); 5.5 ± 2, Krasnopolsky et al. (1997)), which were consistent with that reported by Owen et al. (1988).

The first indication of variability in the D/H ratio was reported in a conference abstract by Mumma et al. (2003), in which they measured the latitudinal distribution of H_2O and HDO using the CSHELL mapping spectrometer at the NASA Infrared Telescope Facility (IRTF). After that, variations of the D/H ratio have been measured using different observatories on Earth. The most relevant measurements of the atmospheric D/H ratio in H_2O are:

- Using the same observational setup as Mumma et al. (2003), Novak et al. (2011) measured latitudinal maps of the D/H ratio during mid-spring in the northern hemisphere ($L_S = 50°$), observing peak values of 6.9 ± 0.2 near the subsolar point, decreasing to 3.8 ± 0.3 towards the polar regions.

- The first *in situ* measurements of the Martian D/H ratio were reported by Webster et al. (2013) using the Sample Analysis at Mars (SAM)'s tunable laser spectrometer

(TLS) on the Curiosity Rover. They measured an enrichment in deuterium of a factor of 6 ± 1 VSMOW over the first 100 days of operations. These localised measurements are representative of that specific location and time, but the contribution from expected seasonal cycling is unknown.

- Krasnopolsky (2015) reported measurements of the spatially-resolved D/H ratio on Mars using CSHELL at the NASA IRTF in eight observing sessions from 2007 to 2014. In these observations, Mars was at a solar longitude of L_S = 110°, 42°, 20°, 70°, 60°, 110°, 89° and 145°. The global mean observed D/H ratio was 4.6 ± 0.7. In four of these observing sessions, Krasnopolsky (2015) found mild variations of the D/H ratio. However, in two other sessions, strong variations in the latitudinal distribution of D/H were found, and they appeared strongly correlated with the temperature. Krasnopolsky (2015) argues that the correlation with temperature is consistent with the temperature dependence of HDO/H_2O fractionation between water vapour and ice, which could be indicative of the source of the variations in the isotope ratio.

- Aoki et al. (2015) used coordinated observations from the Infrared Camera and Spectrograph (IRCS) of the Subaru telescope and PFS on Mars Express to determine the latitude distribution of D/H at the middle of northern spring (L_S = 52°) and beginning of northern summer (L_S = 96°) of MY31. They found a significant variation of the D/H ratio between these two observing sessions in the polar region (70-80°N), from 2.4 ± 0.6 at L_S = 52° to 5.1 ± 0.7 at L_S = 96°, which is consistent with the expectations from condensation/sublimation processes (see section 1.1.5.2). However, the latitudinal mean values did not show any evidence of significant variation (D/H = 4.1 ± 1.4 at L_S = 52° and D/H = 4.4 ± 1.0 at L_S = 96°).

- Villanueva et al. (2015) created maps of the atmospheric D/H using several ground-based high-resolution spectrographs (CRIRES at the Very Large Telescope, CSHELL at NASA IRTF, and NIRSPEC at the Keck telescope) between 2008 and 2014 (see Figure 1.7). These maps show great variability of atmospheric D/H with latitude and season. In addition, the observations show a strong correlation with topography, showing large values of the D/H ratio (>7) over orographic depressions, whereas much lower values (1 to 3) are found in high-altitude regions. The observed latitudinal variability

is in general consistent with the predictions from condensation/sublimation processes accounted in the model of Montmessin et al. (2005). However, the strong local variations observed across the planet require a more realistic model that includes more fractionating processes.

- Encrenaz et al. (2016) created maps of the D/H ratio during the northern hemisphere summer ($L_S = 113°$) in 2014, using the Echelle Cross Echelle Spectrograph (EXES) instrument aboard the Stratospheric Observatory for Infrared Astronomy (SOFIA) facility. They observe a disk-integrated D/H value of 4.4 (+1, -0.6), with a significant enhancement from 3.5 in the southern hemisphere to 6 in the northern latitudes, which is consistent with the predicted variations by the model of Montmessin et al. (2005). Later on, Encrenaz et al. (2018) used the same observational setup as in 2016 and 2017 to create similar maps as in 2014, when Mars was at solar longitudes of $L_S = 127°$ and $L_S = 304°$, respectively. The disk-integrated values they observed were 4 (+0.8, -0.6) and 4.5 (+0.7, -0.6), respectively, consistent with the measurements of Encrenaz et al. (2016). Nevertheless, in these occassions, there was not evidence of strong local variations in the D/H ratio nor for seasonal variations in the global D/H ratio between northern summer and southern summer, which is in contrast with the latitudinal variability observed by Encrenaz et al. (2016) during the northern hemisphere summer.

- Khayat et al. (2019) used CSHELL at the NASA IRTF to measure the D/H during the northern summer ($L_S = 126°$) in 2016, at a similar time than the observations made by Encrenaz et al. (2018). In this case, Khayat et al. (2019) find a significant increase in the D/H ratio from southern to northern latitudes, similar to the one observed during this season by Encrenaz et al. (2016), but in contrast with the results of Encrenaz et al. (2018). However, globally, the D/H measurements presented by Khayat et al. (2019) are consistent with those reported by Encrenaz et al. (2016, 2018), Aoki et al. (2015) and Krasnopolsky (2015), but lower than those reported by Novak et al. (2011) and Villanueva et al. (2015).

Apart from the D/H ratio in water vapour, the isotope ratio has been estimated by looking at the Lyman-α emission of atomic hydrogen and deuterium. These measurements have important implications to our understanding of the escape of H and D, and therefore to

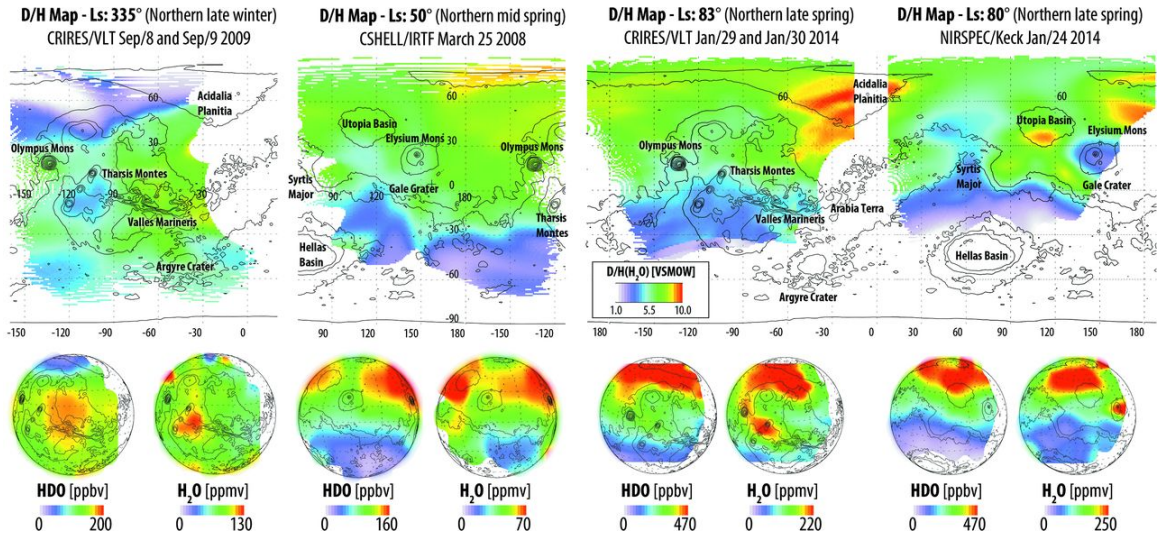

Figure 1.7: Deuterium/hydrogen maps obtained from ground-based telescope observations of H_2O and HDO from March 2008 to January 2014. The units of the D/H ratio are expressed as a factor relative to the Earth's ocean water, represented by the Vienna Standard Mean Ocean Water (VSMOW). Figure from Villanueva et al. (2015).

relate the measurements of the present-day HDO/H_2O to the water reservoir in the past. Krasnopolsky et al. (1998) detected the Lyman-α emission of deuterium in the upper atmosphere of Mars using the Goddard high-resolution spectrograph (GHRS) onboard the Hubble Space Telescope (HST). Using photochemical models, they estimated that the isotope ratio in molecular hydrogen (HD/H_2) was approximately a factor of 2.5 lower than that in water vapour (Krasnopolsky, 2002).

In addition, the Lyman-α emission of H and D has been frequently measured by the Imaging Ultraviolet Spectrograph (IUVS) instrument onboard the Mars Atmosphere Volatile EvolutioN (MAVEN) spacecraft (Clarke et al., 2017; Mayyasi et al., 2019). Clarke et al. (2017) measured the variations of the brightness of the Lyman-α emission over the course of a martian year. Although they did not provide actual values of the D/H ratio, they observed large variations of the brightness, which require variations of the number densities of both H and D by an order of magnitude, and not always in sync with each other (Clarke et al., 2017). Mayyasi et al. (2019) reported the seasonal variability of deuterium in the upper atmosphere, which appears to have pronounced variations of the number density of D, increasing with Mars' proximity to the Sun and peaking near southern summer solstice, during the dusty season. These results suggest that the number density of D (and H) increase when water vapour is provided to the upper atmosphere during the perihelion and dusty seasons (Mayyasi et al.,

2019; Fedorova et al., 2020b).

C and O isotopes

In contrast to the large volume of measurements constraining the variations of the D/H ratio in H_2O, there is little information about variability of the C and O isotope composition of the Martian atmosphere. The first measurements of the isotope composition of the Martian atmosphere were obtained from ground-based observations by Connes et al. (1969), providing measurements of the $^{13}C/^{12}C$ and $^{18}O/^{16}O$ isotope ratios in CO_2 (Young, 1971) and CO (Kaplan et al., 1969), which were found to be terrestrial within an uncertainty of 15%. Later on, Nier and McElroy (1977) reported measurements of the isotope composition of C and O in CO_2, using upper atmospheric measurements from the mass spectrometers on the Viking entry probes. These measurements showed an isotopic composition of C and O indistinguishable from the terrestrial one within the 5% measurement uncertainty ($\delta^{13}C = 0 \pm 50‰$ and $\delta^{18}O = 0 \pm 50‰$). For the oxygen isotopic composition, Nier and McElroy (1977) actually derive a value of $\delta^{18}O = 20‰$, but conclude that it is essentially terrestrial within the measured uncertainties (Jakosky, 1991). These measurements posed some challenges for interpreting the history of the Martian atmosphere, given the measured enrichment in the heavy isotopes in N or Ar, which was absent in the isotopologues of CO_2. This was interpreted to be due to the presence of a large reservoir that mitigates the effect of escape of oxygen and carbon atoms into space (Jakosky, 1997).

Early ground-based high resolution spectroscopic measurements revealed a depletion of the ratios in CO_2 with respect to Earth ($\delta^{13}C$ = -73 ± 58 ‰; $\delta^{18}O$ = -40 ± 130 ‰, Schrey et al. (1986); $\delta^{13}C$ = -73 ± 58 ‰; $\delta^{18}O$ = -130 ± 80 ‰, Krasnopolsky et al. (1996)) but more recent observations showed only marginal deviations with respect to the standard ($\delta^{13}C = 0 \pm 110$ ‰, Encrenaz et al. (2005); $\delta^{13}C$ = -22 ± 20 ‰; $\delta^{18}O$ = 18 ± 18 ‰, Krasnopolsky et al. (2007)). In addition, in a conference abstract Bjoraker et al. (1989) reported depletion of the heavier isotopes of H_2O ($\delta^{18}O$ = -100 ± 30 ‰ and $\delta^{17}O$ = -50 ± 10 ‰), using observations made with the Fourier Transform Spectrometer on the Kuiper Airborne Observatory.

The most precise measurements of the C and O isotope composition in the Martian atmosphere were made by the Phoenix Lander and Curiosity Rover, but observing non-overlapping

values within the measured uncertainties. Niles et al. (2010) found carbon dioxide to be enriched in ^{18}O but not ^{13}C (δ^{13}C = -2.5 ± 4.3 ‰; δ^{18}O = 31 ± 5.7 ‰) using measurements with the Thermal Evolved Gas Analyzer (TEGA) mass spectrometer on the Phoenix Lander. However, reconsideration of these data suggest that the lack of measured enrichment in ^{13}C may be a measurement artifact (Livengood et al., 2020). On the other hand, Webster et al. (2013) reported similarly enriched ^{13}C and ^{18}O with respect to telluric values (δ^{13}C = 46 ± 4 ‰; δ^{18}O = 48 ± 5 ‰) using measurements made with SAM/TLS on the Curiosity Rover. Webster et al. (2013) also measure an enrichment in the ^{17}O/^{16}O isotope ratio (δ^{17}O = 24 ± 5 ‰), consistent with the expectations from mass-dependent fractionation (δ^{17}O ∼ 0.53 × δ^{18}O). In addition, Webster et al. (2013) also measured the isotope composition of ^{18}O in H_2O (δ^{18}O = 84 ± 10 ‰), which appears to be more enriched than that in CO_2, which suggests that the oxygen in atmospheric water vapour is not in equilibrium with the crust (Urey, 1947; Jakosky, 1991).

The only evidence of variability in δ^{18}O was reported by Livengood et al. (2020), using ground-based heterodyne spectroscopic observations from the NASA Infrared Telescope Facility (IRTF). Looking at different longitudes at the subsolar latitude, representative of the local time, diurnal variations of δ^{18}O in CO_2 were measured, varying from δ^{18}O = -92 ± 23 ‰ to δ^{18}O = 71 ± 18 ‰, over a temperature increase from 266.9 to 275.4 K, suggesting a correlation between the isotopic fractionation and the surface temperature (see Figure 1.8). In addition, Livengood et al. (2020) re-analysed the measurements from the TEGA instrument on the Phoenix Lander, comparing the measured δ^{18}O against δ^{13}C, finding a positive correlation between both ratios (δ^{18}O = 1.3 × δ^{13}C), and suggesting that the observed dispersion of the measurements was indeed variability of the isotopic ratios.

1.1.5.2 Fractionation processes

Condensation/sublimation processes

Isotopic fractionation during condensation and sublimation processes occurs due to the slight differences between the vapour pressures of the different isotopologues, with the heavy isotope generally having a lower vapour pressure (Fouchet and Lellouch, 2000). In Mars, these processes are expected to have an effect in two ways: the condensation and sublimation of

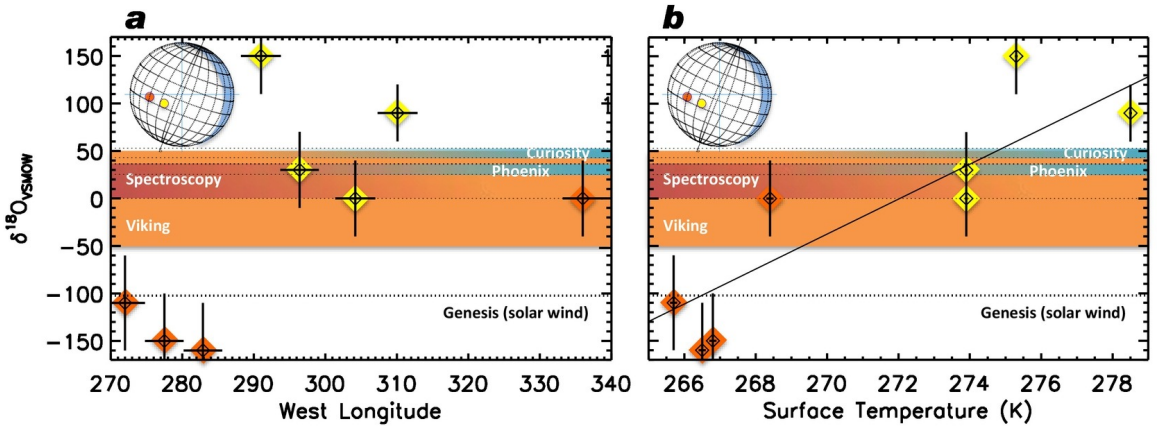

Figure 1.8: Measured deviations of $\delta^{18}O$ in CO_2. The orange dots correspond to measurements on the subsolar point, while the yellow ones correspond to the subsolar latitude, but with a shift of 20° towards the planetary east, which corresponds to 1.33 hours of local time. Figure from Livengood et al. (2020).

the polar caps, and the condensation onto ice clouds.

Bertaux and Montmessin (2001) studied the Vapour Pressure Isotopic Effect (VPIE) in water ice cloud formation for $H_2^{16}O$ and $HD^{16}O$ in order to explain the lower value of the D/H ratio in the upper atmosphere of Mars, compared to the lower altitudes, as measured by Krasnopolsky et al. (1998). They suggested that at the level of the hygropause, if icy grains are formed, these will be enriched in $HD^{16}O$ compared to $H_2^{16}O$. Then, when the icy grains fall and resublimate at lower altitudes, they will preferentially transport $HD^{16}O$ downwards, leaving the atmosphere enriched in the lighter isotope at higher altitudes, where photochemical reactions can occur. This process provides an efficient mechanism for the atmosphere to retain D over H close to the surface. If the hygropause is located below the photolysis region, then this process will deplete the products of H_2O photodissociation in deuterium.

Montmessin et al. (2005) studied the behavior of the D/H ratio in H_2O using a 3-D General Circulation Model (GCM) for the Martian atmosphere. Figure 1.9 shows the calculated latitudinal and seasonal distribution of the D/H ratio from the model, which predicts a relative enrichment of the heavy isotope during the sublimation of the polar caps (northern cap at $L_S = 90°$ and southern polar cap at $L_S = 270°$), and a relative depletion of the heavy isotope in the atmosphere during the condensation of the polar caps (southern at $L_S = 90°$ and northern at $L_S = 270°$), following closely the seasonal behaviour of atmospheric water vapour. The model of Montmessin et al. (2005) predicts the general latitudinal and seasonal trends observed by

ground-based telescopes (see section 1.1.5.1), although some of the observed strong variations are not well described by the model (Villanueva et al., 2015; Krasnopolsky, 2015).

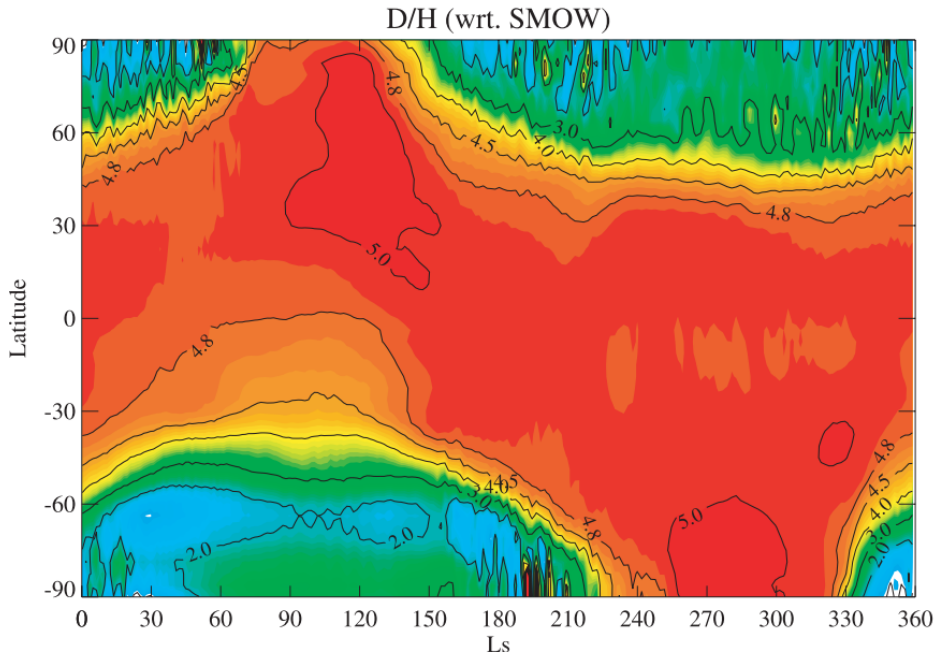

Figure 1.9: Latitudinal and seasonal distribution of the D/H ratio, as predicted from the model of Montmessin et al. (2005).

Although these models have not been applied to study the effect of the VPIE in the oxygen isotope ratios in water vapour in the Martian atmosphere, we can provide some constraints on the expected variability, as compared to the variability in the D/H ratio, from the isotopic studies performed on Earth. Laboratory studies about the isotope fractionation from the condensation of water vapour onto ice were performed mainly in the 70s. Merlivat and Nief (1967) measured the equilibrium fractionation factor of the D/H ratio during the condensation of water vapour onto water ice, between 230 K and 273 K. On Mars, temperatures relevant to the condensation of water vapour onto ice are lower, and the expression of Merlivat and Nief (1967) is usually extrapolated. In order to expand the range of temperatures of the measurements, Lamb et al. (2017) measured the equilibrium fractionation between vapour and ice from 190 K to 230 K, which is more relevant to Martian temperatures, but showing just small discrepancies with respect to the results of Merlivat and Nief (1967). The expression of the fractionation factor α_D derived from the measurements by Lamb et al. (2017) is given by

$$\alpha_D = \frac{(\mathrm{HD^{16}O/H_2^{16}O})_{\mathrm{ice}}}{(\mathrm{HD^{16}O/H_2^{16}O})_{\mathrm{vap}}} = \exp\left(\frac{13525}{\mathrm{T}^2} - 5.59 \times 10^{-2}\right), \tag{1.1.1}$$

where T is the temperature in K. Similarly, Majoube (1970) measured the equilibrium fractionation factor for the $^{18}O/^{16}O$ ratios in H_2O, which is given by

$$\alpha_{^{18}O}(\mathrm{H_2O}) = \exp\left(\frac{11.83}{\mathrm{T}} - 28.224 \times 10^{-3}\right). \tag{1.1.2}$$

To first order, and ignoring the temperature effect, the relation between δD and δ^{18}O during condensation follows the meteoric line ($\delta\mathrm{D} = 8 \times \delta^{18}\mathrm{O}$, Dansgaard (1964)), and the deuterium excess is only very slightly modified (d-excess = δD - 8 δ^{18}O). Nevertheless, given the different temperature dependence of the fractionation factor for the $^{18}O/^{16}O$ and D/H ratios, the slope of the δD - δ^{18}O relation increases as temperature decreases (Majoube, 1971), leading to the existence of a d-excess (see Figure 1.10a). In addition to the effect of temperature at which condensation occurs, laboratory measurements enabled to observe strong departures from the relation expected for isotopic fractionation at equilibrium conditions, which depicted the presence of kinetic effects occurring due to the different diffusivities of the isotopologues while condensing (Jouzel and Merlivat, 1984). Although there is a rather large discrepancy in the estimations of the diffusion coefficients of different water isotopes in air (Merlivat, 1978; Cappa et al., 2003; Luz et al., 2009), the effect of kinetic fractionation lowers the slope of the δD - δ^{18}O relation (see Figure 1.10a). In particular, the kinetic effects are of the same order of magnitude for both δD and δ^{18}O. However, as the equilibrium fractionation factor is much larger for δD, the relative importance of kinetic effects in isotopic fractionation of water ice clouds is greater for δ^{18}O (Casado et al., 2016).

Similarly as there is an equilibrium line in the δD - δ^{18}O relation, there is too for δ^{17}O - δ^{18}O, which is given by $\ln(\delta^{17}\mathrm{O} + 1) = 0.528\ \ln(\delta^{18}\mathrm{O} + 1)$ (Barkan and Luz, 2005; Landais et al., 2008). Nevertheless, unlike for the d-excess, temperature does not appear to have a strong effect on the equilibrium ^{17}O-excess (^{17}O-excess = $\ln(\delta^{17}\mathrm{O} + 1)$ - $0.528\ \ln(\delta^{18}\mathrm{O} + 1)$) (Van Hook, 1968). Although temperature does not have an effect on the relative equilibrium fractionation factors between δ^{17}O and δ^{18}O, kinetic effects will lower the slope of the δ^{17}O - δ^{18}O relation, creating a ^{17}O-excess, which is larger as the kinetics effects become more important (Casado et al., 2016).

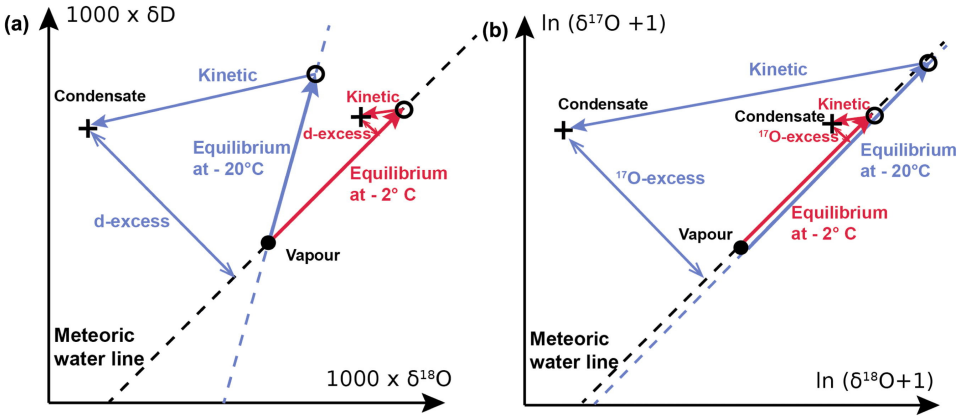

Figure 1.10: a) Theoretical evolutions of δD and $\delta^{18}O$ during condensation of water vapour onto water ice at different temperatures, and showing the effects of kinetic fractionation. b) Theoretical evolutions of $\delta^{17}O$ and $\delta^{18}O$ during condensation of water vapour onto water ice at different temperatures, and showing the effects of kinetic fractionation. Figure from Casado et al. (2016).

With this information, one can make some estimations for the predicted variability of the water isotope ratios in the Martian atmosphere in condensation processes. Considering the expressions for the equilibrium fractionation factors of Merlivat and Nief (1967) and Majoube (1970) for δD and δ^{18}O respectively, and considering that condensation occurs following Rayleigh distillation, the δD - δ^{18}O relation varies with temperature as shown in Figure 1.11. With these assumptions, one may expect variations in δ^{18}O to be approximately a factor of 15 lower than in δD. However, it must be noted that this estimation is subject to the relative importance of kinetic effects in the Martian atmosphere, that might be relevant given the cold temperatures and high levels of supersaturation observed in the atmosphere (Fedorova et al., 2020b; Casado et al., 2016). Regarding the potential variations of δ^{17}O, as the relation of δ^{17}O and δ^{18}O in equilibrium does not appear to vary with temperature, one might expect variations following the meteoric line. However, kinetic effects might also be important in shaping the oxygen isotope composition during condensation.

Carbon dioxide also acts as a volatile species in the Martian atmosphere, and can therefore get fractionated during condensation on CO_2 ice clouds or on the polar caps. The isotopic fractionation during the condensation of carbon dioxide into ice was measured by Eiler et al. (2000), looking at the $^{18}O/^{16}O$ and $^{13}C/^{12}C$ ratios. They concluded that while the C isotope ratio did not show any significant fractionation, the oxygen isotope fractionation factor followed the relation

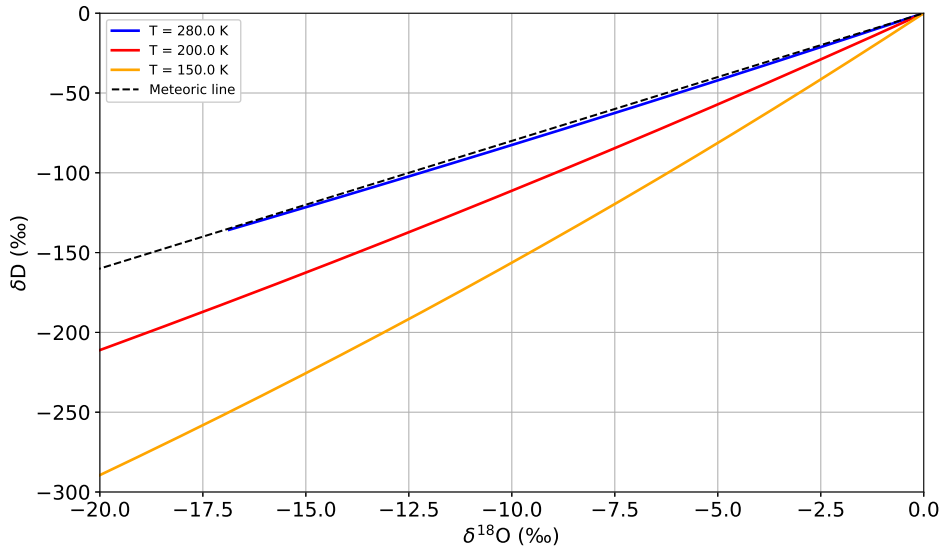

Figure 1.11: Estimated relation between the equilibrium fractionation of δD and $\delta^{18}O$ during condensation at different temperatures, as estimated using the fractionation factors of Merlivat and Nief (1967) and Majoube (1970), and assuming Rayleigh distillation.

$$\alpha_{^{18}O}(CO_2) = \exp\left(\frac{2.826}{\mathrm{T}} - 14.5 \times 10^{-3}\right). \tag{1.1.3}$$

where T is the temperature in K. Eiler et al. (2000) estimate that the atmospheric volumes subject to high extents of condensation may have variations of $\delta^{18}O$ in CO_2 up to tens of per mil.

Gas adsorption in the regolith

The regolith is an important reservoir of volatiles on Mars, storing substantial amounts of H_2O and CO_2 adhered by physical adsorption (Fanale and Cannon, 1974). Adsorption and desorption of the regolith is mainly driven by solar insolation, which creates large variations of the surface temperature that strongly affect the adsorption coefficient of the gases. Therefore, adsorption is expected to vary in a diurnal basis, although it also experiences seasonal variability (e.g., Zent et al. (1993)).

Isotopic fractionation in adsorption is caused by the different adsorption diffusivities of the different isotopologues (Moores et al., 2011). Hu (2019) modelled the diurnal variation of the D/H ratio caused by atmospheric exchange with the regolith. Their model predicts the diurnal variations to show a drop of the near-surface atmospheric D/H ratio in the early

morning (∼6 am), then an increase that yields the peak D/H value during the daytime (∼ 12-14 pm), and finally another decrease during the late afternoon and evening (see Figure 1.12). The model predicts diurnal variations of 300-1400 ‰ near the surface. However, it also predicts these variations to be approximately a factor of 5 smaller at 100 m above the surface (Hu, 2019). Similarly, the oxygen isotopes in H_2O might experience fractionation during the adsorption process, but the extent of it is unknown, since there have not been laboratory studies measuring the fractionation factors.

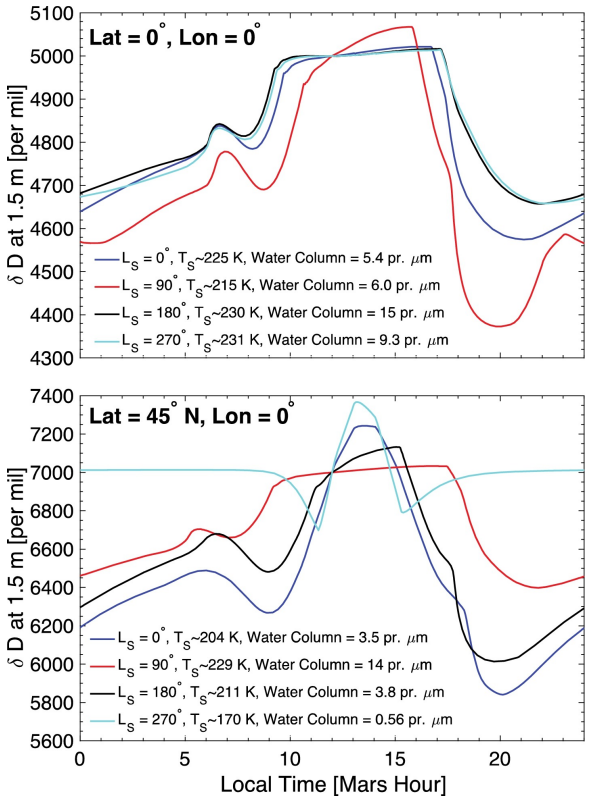

Figure 1.12: Diurnal variation of the D/H ratio predicted by the model of Hu (2019) at the equator and mid-latitudes, as a function of solar longitude.

Apart from water, the Martian regolith exchanges substantial amounts of CO_2, and can therefore fractionate its isotopic composition. Rahn and Eiler (2001) investigated the isotope fractionation of CO_2 adsorption on mineral surfaces relevant to Mars. They found that adsorption can actually enrich the atmosphere in ^{13}C relative to ^{12}C, which is in contrast to the common expectation that the condensed phase should be enriched in the heavy isotopes. In the case of the $^{18}O/^{16}O$ ratio, the atmosphere is depleted in the heavy isotope due to the adsorption process, but just to a modest extent, being approximately a factor of four lower than the fractionation due to condensation (Eiler et al., 2000; Rahn and Eiler, 2001).

Livengood et al. (2020) measured substantial variations in the $^{18}O/^{16}O$ ratio (see Figure 1.8), being correlated with the surface temperature. This correlation with temperature could be indicative of fractionation due to the adsorption and desorption of CO_2. However, Livengood et al. (2020) note that a large fraction of the atmospheric CO_2 would have to be trapped on the regolith at night to produce these large variations, given the experimental constraints of Rahn and Eiler (2001).

It must be noted that, although the adsorption and desorption of CO_2 on the Martian regolith can produce variations of the isotope composition of H_2O and CO_2, these processes occur at the surface, while the lowest altitude above the surface observed in solar occultations is typically about 5 km, depending on the dust abundance (see Figure 1.4). Although convective motions rapidly mix the atmosphere vertically from the surface to the top of the planetary boundary layer, which is usually located at an altitude between 6 and 10 km in the daytime (Korablev et al., 2019; Temel et al., 2019), it is unlikely that at the altitude range sampled in solar occultations we find diurnal variations representative of adsorption processes.

Photochemical reactions

Fractionation in photo-induced reactions occurs due to the small difference in the zero point energy (ZPE) between the different isotopologues and the contraction of the wave function of the system due to the substitution of a light atom with a heavier one. These differences create a difference in the reaction cross section and can therefore fractionate the isotopes (Liang et al., 2004). In addition, isotopic fractionation can also occur in some chemical reactions, due to the different reaction rate constants.

The photo-induced fractionation effect (PHIFE) has important implications in the connection between the D/H ratio in water vapour and in hydrogen. Cheng et al. (1999) measured the absorption cross sections of H_2O, HDO and D_2O, and observed that they showed some significant variations (see Figure 1.13a). In addition, they computed the photolysis rates of H_2O using the photochemical model of Nair et al. (1994). In order to highlight the difference of the PHIFE, they re-computed the dissociations rates of H_2O, but now using instead the cross sections of HDO (see Figure 1.13b). On a per-molecules basis, at high altitudes, the photolysis rates of H_2O and HDO are about the same, as most of the photons at these alti-

tudes are absorbed near 170 nm. However, at low altitudes the photolysis of HDO is about 2-3 times less efficient than that of H_2O, because most of the absorption takes place near 190 nm, due to the UV shielding by CO_2. Krasnopolsky et al. (1998) measured the D/H ratio in H_2 to be approximately 2.5 times lower than in H_2O, which appears to be explained by a combination of the PHIFE and the VPIE (Cheng et al., 1999; Bertaux and Montmessin, 2001).

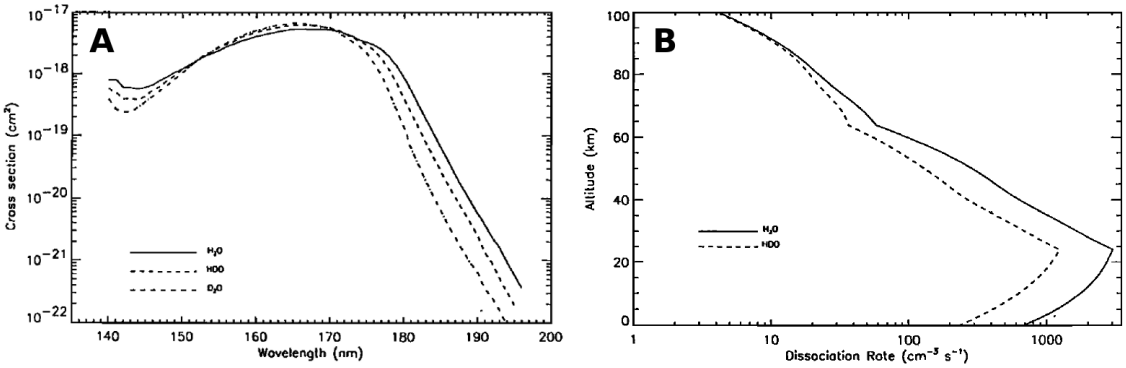

Figure 1.13: A) Laboratory measurements of the cross sections of H_2O, HDO and D_2O. B) Comparison of the photolysis rates of H_2O and the relative rate of HDO in the atmosphere of Mars based on the model of Nair et al. (1994). Figure from Cheng et al. (1999).

The photolysis cross sections of the oxygen isotopologues of water vapour have not been measured in the laboratory. Miller and Yung (2000) presented a theoretical method for the analysis of the PHIFE, computing the absorption cross sections for the different isotopologues of water vapour. Figure 1.14 shows the difference in the absorption cross sections of several isotopologues of water vapour with respect to that of $H_2^{16}O$ (e.g., $(\epsilon(\lambda) = (\sigma_{HDO}(\lambda)/\sigma_{H2O}(\lambda)$ - 1) $\cdot$ 100)). The results of Cheng et al. (1999) showed that a factor of 2-3 was expected due to the difference in the absorption cross sections in the long-wave tail near 190 nm ($\nu = 52630$ cm^{-1}). At these wavelengths, the D/H, $^{18}O/^{16}O$ and $^{17}O/^{16}O$ all have lower cross sections than $H_2^{16}O$. However, while the difference in the cross section with HDO reach values of about 60%, these differences are only of the order of 2.5 and 1.5% for $H_2^{18}O$ and $H_2^{17}O$, respectively. Therefore, the fractionation for the oxygen isotopes ($\delta^{18}O$ and $\delta^{17}O$) is expected to be lower than that of the D/H ratio.

As with water vapour, the photodissociation of CO_2 fractionates the isotopic composition of the parent molecule and the products (CO and O). The first evidence of fractionation due to the photodissociation of CO_2 molecules was investigated in a series of experiments, showing

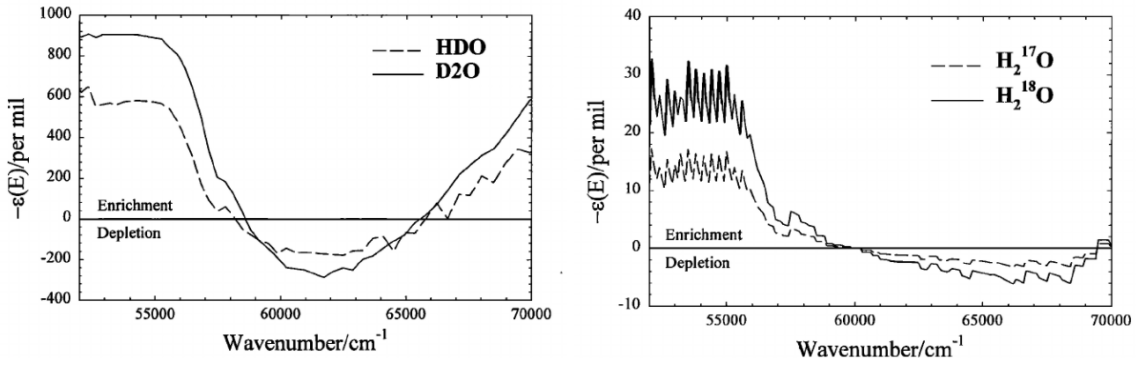

Figure 1.14: a) Percentual difference of the photodissociation cross sections of HDO and D_2O with respect to $H_2^{16}O$, as measured by Cheng et al. (1999). b) Percentual difference of the photodissociation cross sections of $H_2^{18}O$ and $H_2^{17}O$ with respect to $H_2^{16}O$, as predicted by the ZPE-method of Miller and Yung (2000). Figure from Miller and Yung (2000).

that $^{17}O^{12}C^{16}O$ was anomalously enriched in the dissociation products at $\lambda = 184.9$ nm, not following a mass-dependent fractionation, which was attributed to a spin-forbidden process (Bhattacharya et al., 2000; Mahata and Bhattacharya, 2009b,a). However, Schmidt et al. (2013) challenged these results, suggesting they could be the result of an experimental bias. Schmidt et al. (2013) calculated the absorption cross sections for the different isotopologues of carbon dioxide, as shown in Figure 1.15. The results of Schmidt et al. (2013) predict that the $^{12}C^{16}O_2$ molecules are preferentially photolysed with respect to the heavier isotopologues, producing a relative enrichment in $\delta^{13}C$, $\delta^{18}O$ and $\delta^{17}O$ in the remaining CO_2. Similarly, one might expect the isotope fractionation of the products to be depleted in the heavy isotopes, consistent with observations in the Earth's atmosphere (Beale et al., 2016).

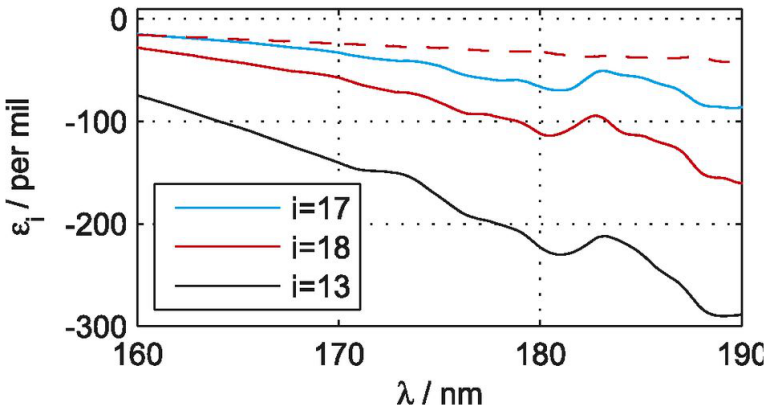

Figure 1.15: Difference in the absorption cross sections of $^{12}C^{16}O_2$ and $^{13}C^{16}O_2$ (black), $^{18}O^{12}C^{16}O$ (red) and $^{17}O^{12}C^{16}O$ (blue), as predicted by Schmidt et al. (2013). The red dashed line represents the different in absorption cross section predicted by the ZPE-method of Miller and Yung (2000). Figure from Schmidt et al. (2013).

Apart from the fractionation associated with the photodissociation of H_2O and CO_2 molecules, the isotope composition of these two species might also be affected by fractionation in reactions of the H, C and O chemistry in other species, which then transfer this fractionation when recombined to form H_2O and CO_2. For instance, stratospheric ozone on Earth is greatly enriched in heavy oxygen (∼400‰) in a mass-independent way, with approximately equal $\delta^{18}O$ and $\delta^{17}O$ enrichments (Thiemens, 1999). Similarly, stratospheric CO_2 also shows mass-independent fractionation, which could be related to the isotopic exchange between carbon dioxide and ozone (Yung et al., 1991). Understanding the fractionation of H_2O and CO_2 in the atmosphere can therefore be subject to several reactions and processes.

Atmospheric escape

Fractionation during atmospheric escape into space might occur due to the greater ease of the lighter isotopes to escape relative to the heavier ones. In principle, the mechanisms governing the escape of the different isotopologues are the same. However, these mechanisms may not affect all isotopologues at the same rates due to their slightly different properties, which gives rise to isotopic fractionation as the atmosphere escapes into space. It must be noted that, unlike the other fractionating processes introduced in this section, atmospheric escape does not produce variations measurable in the present-day atmosphere, but instead changes the isotope composition of the atmospheric reservoir over long timescales. Therefore, understanding the role of fractionation during atmospheric escape is essential to understand the evolution of the Martian atmosphere.

The escape of deuterium, as it is for hydrogen, is dominated by thermal escape (see section 1.1.4). However, due to the heavier mass of D with respect to H, the escape rates of the two atoms will be different, mainly because of two effects:

- At the homopause, the atmosphere transitions from a state of strong turbulence and mixing to a molecular-diffusion-dominated one above it, where the scale heights of the different isotopologues are different, leading to the diffusive separation of the isotopes. Taking into account that escape processes occur at the exobase, which is above the homopause, diffusive separation between the homopause and exobase will lead to a lower density of the heavy isotopes. Therefore, diffusive separation will lead to a fractionation

given by

$$f = \exp\left(\frac{-\Delta m \cdot g \cdot \Delta z}{k_B \cdot T}\right) \tag{1.1.4}$$

where Δm is the mass difference between the two isotopologues (1 amu for D/H, $^{13}C/^{12}C$ or $^{17}O/^{16}O$, and 2 amu for $^{18}O/^{16}O$), g is the gravity, Δz is the altitude difference between the homopause and exobase, k_B is Boltzmann's constant, and T is the temperature (see Figure 1.16a).

- Thermal escape occurs due to the presence of atoms with a thermal velocity greater than the escape velocity of Mars (e.g., Chaffin et al. (2014)). The velocity distribution of the atoms at a given temperature follows the Maxwell-Boltzmann distribution functions, which is given by

$$f(v)\mathrm{d}v = \left(\frac{m}{2\pi k_B T}\right)^{3/2} \cdot 4\pi v^2 \cdot \exp\left(\frac{-mv^2}{2k_B T}\right) \cdot \mathrm{d}v \tag{1.1.5}$$

where m is the mass of the particle. The escape velocity is given by

$$v_e = \sqrt{\frac{2GM}{(R+z)}}, \tag{1.1.6}$$

where G is the gravitational constant ($G = 6.67 \times 10^{-11}$ m^3 kg^{-1} s^{-2}), M is the mass of Mars ($M = 6.4171 \times 10^{23}$ kg), R is the radius of Mars ($R = 3389.5$ km) and z is the altitude above the surface. Considering an exobase altitude of 200 km, the escape velocity of Mars is 4.8 km/s. Figure 1.16b shows the velocity distributions of H and D atoms assuming an exospheric temperature of 220 K (Forbes et al., 2008). Because of the mass difference between D and H atoms, while the probability of a H atom to have a velocity greater than the escape velocity is $p_H = 0.0044$, the probability for D atoms is only $p_D = 8.66 \times 10^{-6}$.

These processes reveal a greater ease of H atoms to escape as compared to D atoms. Therefore, as the atmosphere escapes into space, the remaining gas bound to Mars is expected to get enriched in the heavy isotope, following the Rayleigh fractionation law (Jakosky et al., 1994). In particular, diffusive separation between both species yields a fractionation factor of

D/H of $f = 0.83$, which implies that almost the totality of water was lost from the Martian atmosphere to leave the remaining atmosphere with a D/H ratio of 5 with respect to the primordial isotopic ratios (see Figure 1.16c). However, it must be noted that the fractionation by diffusive separation occurs on top of any other fractionating processes that might influence the efficiency of H and D-bearing species to be converted into atomic H and D atoms. Indeed, estimations of the fraction of water reservoir lost to space require the definition of a net escape fractionation factor f that encompasses the effects of all fractionating processes from the start as H_2O and HDO molecules, until they are lost in the form of H and D atoms (see equation 1.0.2).

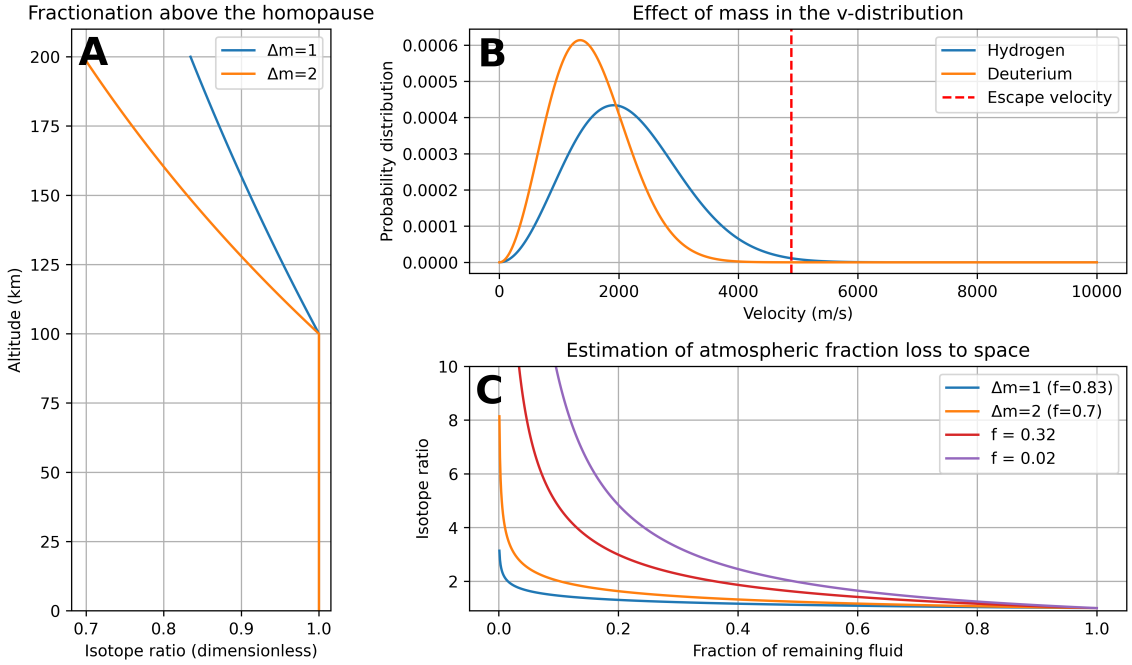

Figure 1.16: A) Vertical variations of the isotope ratios due to diffusive separation above the homopause. The homopause is considered to be at 100 km, with an upper-atmospheric temperature of T = 220 K. B) Estimated velocity distributions of H and D atoms assuming an exospheric temperature of 220 K. The red-dashed line indicates the escape velocity at 200 km above the surface. C) Factor of enrichment in the isotopic ratio of the remaining bulk abundance, as a function of the fraction of fluid that remains bound to the planet, considering different values of the escape fractionation factor f. The blue and orange lines indicate the fractionation factor associated with diffusive separation. The purple and red lines are calculated using the estimated values by Yung et al. (1988) and Krasnopolsky (2002).

Estimations of this escape fractionation factor have been mainly performed using photochemical models which treat the H and D-bearing species independently, allowing to estimate the relative efficiency of escape between H and D atoms. In this way, Yung et al. (1988) estimated a fractionation factor of $f = 0.32$, suggesting a lower efficiency of D atoms to reach

the upper atmosphere. Krasnopolsky (2002) estimated the fractionation factor taking into account both thermal and non-thermal escape mechanisms, considering several scenarios for the solar activity, and derived values ranging from 0.055 to 0.167. Recently, Cangi et al. (2020) explored the sensitivity of the fractionation factor f with respect to other atmospheric parameters, such as the water vapour abundance or the atmospheric temperature. Their results yielded values of f ranging from 10^{-1} to 10^{-5} when considering only thermal escape. However, although they do not fully model the fractionation in non-thermal escape processes, they estimated that the fractionation factor when including both thermal and non-thermal processes ranges from 0.03 to 0.1 instead (see Figure 1.17).

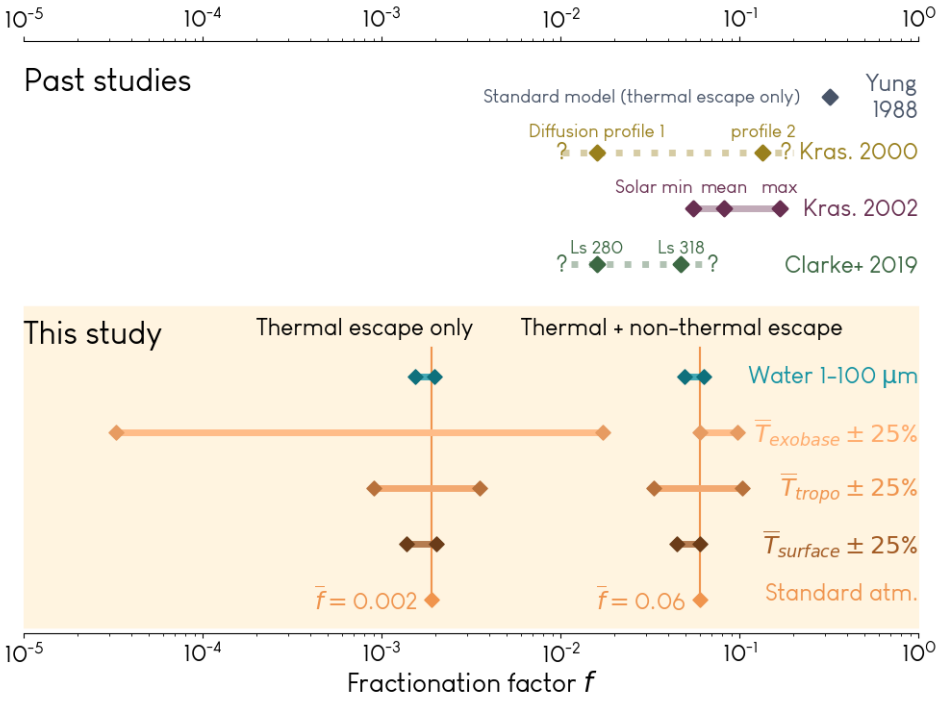

Figure 1.17: Net escape fractionation factors of the D/H ratio estimated from the models of Yung et al. (1988), Krasnopolsky (2000), Krasnopolsky (2002), Clarke et al. (2019) and Cangi et al. (2020). Figure from Cangi et al. (2020).

In the case of oxygen, the mechanism dominating its escape into space is the dissociative recombination of O_2^+ ions (see section 1.1.4). Fox and Hać (2010) modelled the isotope effect inherent in this mechanism using Monte Carlo simulations. They derive a ratio of the escape probability of ^{18}O to that of ^{16}O of approximately 0.4, and therefore predict an enrichment of ^{18}O relative to ^{16}O as the atmosphere escapes. Another important source of escape of oxygen from the Martian atmosphere is ion sputtering (see section 1.1.4). In this case, the accelerated

ions provide enough energy to eject any isotopologue from the atmosphere, regardless of their mass. However, as this process is most effective above the exobase, the fractionation factor will be given by the diffusive separation of the isotopes between the homopause and the exobase ($f \sim 0.7$ for $^{18}O/^{16}O$ and $f \sim 0.83$ for $^{17}O/^{16}O$), as shown in Figure 1.16 (Jakosky, 2019). However, it must be noted that, as discussed for the D/H ratio, estimations of the amount of gas lost to space require the definition of a escape fractionation factor that includes all processes from the start as $H_2^{16}O$ and $H_2^{18}O$ until they finally escape. Besides, unlike hydrogen, whose main source comes from the Martian water reservoir, the oxygen atoms in water vapour are expected to interact with those from the CO_2 reservoir and minerals in the crust, which make the estimations of the escape fractionation factor more complex.

Finally, in the case of carbon, the relevance of each mechanism for its overall escape remains unclear. The isotope effect inherent in some of the mechanisms discussed in section 1.1.4 can be estimated as:

- Fox and Hać (1999) used Monte Carlo simulations to calculate the velocity distributions of ^{12}C and ^{13}C produced by the dissociative recombination of CO^+. They estimated that the fraction of ^{12}C atoms with velocities greater than the escape velocity was 0.62-0.66, while from ^{13}C the fraction is only 0.47-0.48. These results suggest that the isotope fractionation factor from this mechanism lies in the range 0.72-0.77.

- As discussed for the case of oxygen, sputtering itself does not fractionate the isotope composition of the atmosphere, but it depends on the relative abundance of each isotopologue near the exobase, which can be estimated using the expectations from diffusive separation between the homopause and the exobase. This estimation is approximately $f \sim 0.83$ in the case of the $^{13}C/^{12}C$ isotopic ratio, as shown in Figure 1.16 (Jakosky, 2019) (see Figure).

- Hu et al. (2015) estimated the isotope fractionation factor associated with the photodissociation of CO taking into account the velocity distributions of the dissociation products (C + O), yielding a fractionation factor of approximately 0.6.

It must be noted that, unlike for the D/H ratio, there have not been any modelling attempts to characterise the net escape fractionation factor for the C and O isotopic ratios,

including all processes from their start as CO_2 and H_2O molecules, until they escape into space. Therefore, although an enrichment in the heavy isotopes is expected from atmospheric escape, the total amount of atmospheric loss for the O and C reservoirs remains uncertain. In addition, it must be noted that, although the overall enrichment in heavy isotopes in the atmosphere provides indirect evidence of atmospheric escape, other processes could also have impacted the isotope composition of the Martian atmosphere over long timescales, including:

- Condensation of H_2O and CO_2 on permanent polar caps could have depleted the atmosphere in the heavy isotopes, given their preferential condensation onto ice, as given by equations 1.1.1, 1.1.2 and 1.1.3 (Jakosky, 2019; Krasnopolsky, 2015).

- Volcanic out gassing throughout the Martian history would partially reset the atmospheric isotopic ratios with their primordial values (Greeley and Schneid, 1991; Grott et al., 2011; Alsaeed and Jakosky, 2019; Jakosky, 2019).

- Atmospheric escape by impact ejection could have ejected part of the atmosphere to space. However, this process is expected to leave the isotopic composition of the remaining atmosphere untouched.

- Impacting objects during accretion and up through a possible late heavy bombardment (LHB) can supply volatiles to Mars, mixing the isotope composition of the Martian atmosphere with that of the impacting objects (Bogard et al., 2001; Fox and Hać, 2010).

1.2 Summary

This chapter has summarised key aspects about the Martian atmosphere relevant to understand the isotopic composition of H_2O and CO_2 in the atmosphere, as well as its potential variability. In particular, we have provided a detailed overview of the CO_2 and H_2O atmospheric cycles, explaining how they exchange with other reservoirs on the surface and subsurface and how they escape to space. In addition, we have provided an extensive overview of the previous measurements that have been made to constrain the isotopic composition of CO_2 and H_2O in the atmosphere of Mars, as well as the expectations of isotopic fractionation in the several processes that might affect H_2O and CO_2 in the atmosphere. This information

is relevant to understand the results derived from the ACS measurements and relate them to our original research questions stated at the beginning of this chapter.

In Chapter 2, we provide a brief introduction to the ExoMars programme, and then a more detailed description of the ACS instrument and the data. Chapter 3 explains the physics behind the observations made with ACS, what information these spectra can provide about the isotopic composition of Mars' atmosphere, and how it can be inverted using the NEMESIS radiative transfer and retrieval algorithm to obtain the vertical profiles of the isotope ratios. Chapters 4, 5 and 6 present the main results of the thesis, presenting the first vertical profiles of the isotope ratios in H_2O and CO_2, as well as their variations with season, latitude and local time. Finally, chapter 7 summarises the main points of the thesis, addressing our original research questions and provides some research lines for future work.

Chapter 2

ACS onboard the ExoMars TGO

The ExoMars programme emerged as a collaboration between the European Space Agency (ESA) and the Russian Space Agency (Roscosmos). This programme, apart from the demonstration of a number of flight and *in situ* technologies, has a number of scientific objectives to better understand the Martian environment, which include the search for signs of past and present life, the characterisation of trace gases in the atmosphere, and the investigation of the variations of the water and geochemical environment. ExoMars will accomplish these objectives with a two-stage mission, launching in 2016 and 2022 (Vago et al., 2015).

The first stage of the programme comprises a Trace Gas Orbiter (TGO) and an Entry, Descent and Landing Demonstrator Module (EDM) known as Schiaparelli. Both were launched on March 2016, arriving to Mars seven months later on October 2016. Schiaparelli, whose main objective was to test the technology for a controlled and successful landing on the surface of Mars, was ejected from TGO on October 16, descending into the Martian atmosphere. During the descent, an anomaly in the navigation system made the deceleration systems operate as if Schiaparelli had already landed, while it was at an altitude of 3.7 km, leading ultimately to the crash of the lander. TGO was inserted into a high-elliptical orbit around Mars. After a different set of manoeuvres and an aerobraking phase, TGO lowered its altitude into the final 400 km circular orbit on March 2018, starting the science operation phase.

The second part of ExoMars will most likely launch in 2022, arriving to Mars on 2023, and comprises the Rosalind Franklin Rover and the Kazachok Surface Platform. The main objective of the rover will be the search of biosignatures. As the atmosphere of Mars offers

little protection to radiation and photochemistry at the surface, the ExoMars rover is equipped with a drill, which will enable the search for biomarkers down to a maximum depth of 2 m. On the other hand, the Kazachok surface platform will analyse the environment and surface of the landing site, allowing for a long-term monitoring of the climate.

The Trace Gas Orbiter is the most important part of the mission for the goals of this project. Since March 2018, it has been orbiting Mars in an almost circular orbit, with a mean altitude of 400 km, but with altitude variations between 380 and 432 km. The orbital plane lies at an angle of 74° with respect to the equator, and the orbital period is approximately two hours, which implies about 12 revolutions in 1 Martian sol (see Figure 2.1). The scientific payload onboard of TGO performs observations in both nadir and solar occultation modes. The ground track of TGO covers latitudes ±74°, as constrained by the inclination of the orbit. For consecutive orbits, the observed latitude advances about 30°, and after 7 sols the planet is completely mapped (Korablev et al., 2018). Regarding the solar occultation coverage, the 2-hour orbit implies approximately 24 solar occultations per day, 12 at ingress and 12 at egress.

The payload of the ExoMars TGO comprises four different instruments for the accomplishment of the scientific goals:

- ACS (Atmospheric Chemistry Suite) consists of three different infrared spectrometers, covering a wavelength range between 0.7 and 17 μm. ACS operates in both nadir and solar occultation modes, enabling the detection of trace species in the Martian atmosphere, the characterisation of high vertical resolution profiles of already detected species, and the continuous monitoring of the Martian climate (Korablev et al., 2018).

- The NOMAD (Nadir and Occultation for MArs Discovery) instrument is a spectrometer suite with three different channels, two covering the infrared (2.2-4.3 μm) for solar occultation and nadir-viewing observations, and the other covering the ultraviolet-visible (UVIS 0.2-0.65 μm). NOMAD complements ACS on the search for trace gases in the infrared, and also allows the detection of other gases such as ozone, and the characterization of aerosols with the UVIS channel (Vandaele et al., 2018).

- CaSSIS (Colour and Stereo Surface Imaging System) is a high-resolution colour and

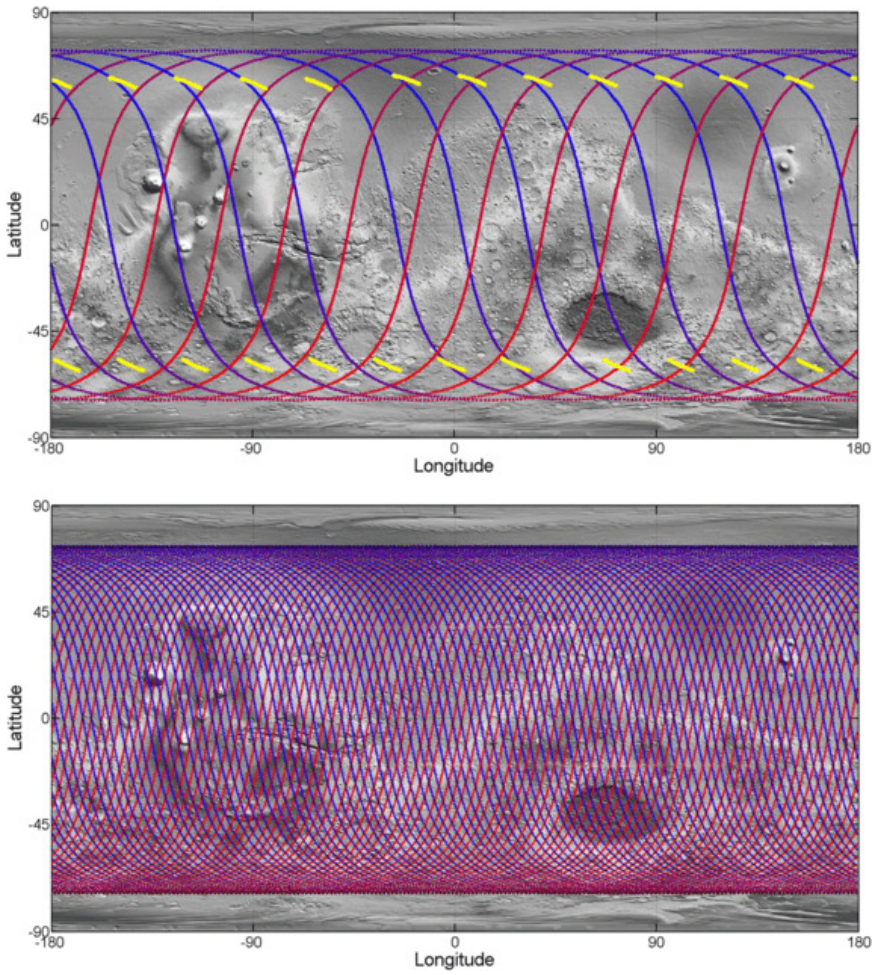

Figure 2.1: TGO ground track for 1 sol (top) and for 7 sols (bottom). The red lines indicate dayside passes, while the blue color indicates nightside passes. Yellow lines represent occultation events, with the projection of the tangent height ranging from 0 to 200 km. Source: (Korablev et al., 2018)

stereo camera, with a pixel resolution of approximately 5 m at the surface of Mars. CaSSIS allows the construction of accurate digital elevation models of the surface, as well as the investigation of interesting geological formations, providing context for sources and sinks of trace gases potentially measured by ACS and NOMAD (Thomas et al., 2017). In addition, CaSSIS provided context for the selection of the ExoMars 2022 landing site, which was decided to be Oxia Planum.

- FREND (Fine Resolution Epithermal Neutron Detector) is a neutron detector that allows the detection of hydrogen in the form of water or water-containing minerals from the Martian surface up to a metre down. This investigation follows that initiated by NASA's Mars *Odyssey* mission, but providing a higher spatial resolution, thanks to the introduction of a collimation module that limits the field of view of the detector (Mitrofanov et al., 2018).

In this chapter, an in-depth description of the ACS instrument is provided, focusing on the mid-infrared channel, which is the most relevant for the purposes of this work. In particular, the following sections describe the design of the instrument, as well as the measurements it makes, in context with the operational constraints of the spacecraft.

2.1 ACS Design

The Atmospheric Chemistry Suite is one of the Russian contributions to the scientific payload of the ExoMars TGO, and was built by the Space Research Institute (IKI) in Moscow, Russia. ACS consists of four main blocks (see Figure 2.2A), three of which are infrared spectrometers designed to establish a detailed inventory of the trace gases in the Martian atmosphere: a spectrometer combining an acousto-optic tunable filter (AOTF) with an echelle grating in the near infrared (NIR), an echelle cross-dispersion spectrometer in the middle infrared (MIR), and a Fourier Transform spectrometer for the thermal infrared (TIRVIM), covering a total wavelength range from 0.7 to 17 μm (Korablev et al., 2018).

The NIR channel is designed as a combination of an echelle spectrometer with an AOTF for the selection of diffraction orders within a total wavelength range of 0.73 to 1.6 μm. This concept was initially proposed for measurements in the terrestrial atmosphere (Korablev et al.,

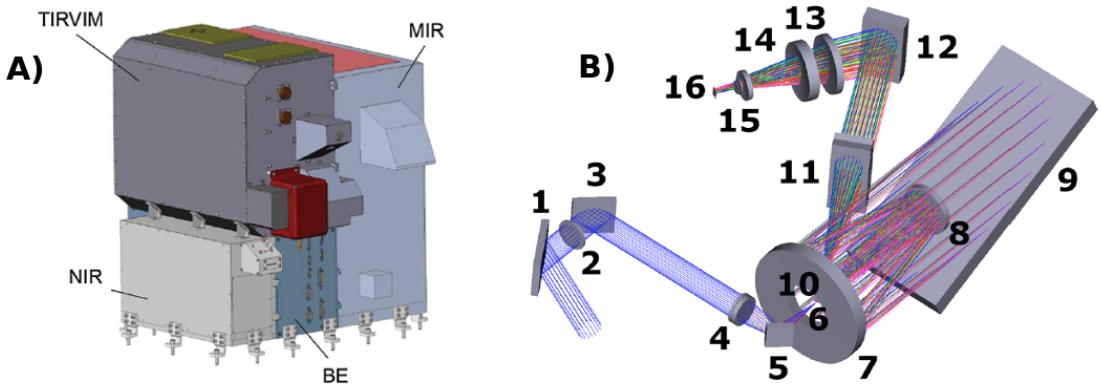

Figure 2.2: (A) ACS architecture design, showing the four blocks it consists of: the NIR, MIR and TIRVIM channels, and the block of electronics (BE). (B) Optical design of ACS MIR. The numbers indicate the different elements of the instrument, standing for: 1,3,5 - Folding mirrors; 2 - Blocking filter; 4 - Entry telescope; 6 - Slit; 7,8 Primary and secondary collimator mirrors; 9 - Echelle diffraction grating; 10 - Folding convex mirror; 11 - Collimator of the secondary grating; 12 - Steerable secondary grating; 13,14 - Focusing lenses; 15 - Cold filter; 16 - Detector array. Source: (Korablev et al., 2018)

2002), and has been used for other space missions such as SPICAV on Venus Express (Nevejans et al., 2006) and SPICAM-IR on Mars Express (Korablev et al., 2006). The wavelength range covered by the NIR channel encompasses absorption bands of CO_2, H_2O, CO and O_2. Fedorova et al. (2020b) used NIR's solar occultation observations to measure the climatology of pressure, temperature, and water vapour, monitoring the effects of the Global Dust Storm (GDS) in the atmospheric state and composition, observing high levels of supersaturation in water vapour, and depicting the perihelion season as an enhancing mechanism for the transport of water vapour to the upper atmosphere.

TIRVIM is a double-pendulum Fourier-transform spectrometer (FTS) that operates in a wavelength range between 1.7 and 17 μm, with a spectral resolution finer than 1 cm^{-1}. The capabilities of the design of TIRVIM are confirmed from several Fourier-transform spectrometers designed at IKI (Formisano et al., 1993; Korablev et al., 2009). TIRVIM can also operate both in nadir and solar occultation modes. The role of TIRVIM's nadir mode is to characterise the main climatic parameters in space and time, such as the vertical profiles of temperature from the CO_2 band at 15 μm, dust and ice opacity. This role follows the continuous monitoring developed by other instruments such as the Thermal Emission Spectrometer on the Mars Global Surveyor (TES/MGS, Smith et al. (2004)), the Mars Climate Sounder on the Mars Reconnaissance Orbiter (MCS/MRO, Kleinböhl et al. (2009)), or the Planetary Fourier Spectrometer onboard Mars Express (PFS/MEx, Giuranna et al. (2019)). On the solar occul-

tation mode, TIRVIM's wide spectral range makes it especially suitable to study the vertical distribution of aerosol density and particle size, for both dust silicates and water ice clouds (Luginin et al., 2020).

Lastly, the MIR channel, which is the most relevant for the purposes of this project, is an echelle cross-dispersion spectrometer operating in a wavelength range between 2.3 and 4.2 μm (2380 - 4347 cm^{-1}). The MIR channel is a new concept designed for obtaining high spectral resolution ($\lambda/\Delta\lambda \sim$ 30000-50000) in a reasonably wide instantaneous spectral range (0.09–0.27 μm), as opposed to the narrow instantaneous spectral range provided by echelle-AOTF spectrometers (e.g., $\sim$0.016 μm for NIR), allowing the simultaneous detection and mapping of several atmospheric species. To date, ACS MIR has proved its capabilities in characterising the atmospheric composition of the Martian atmosphere. First results from the MIR channel reported the non detection of methane in the Martian atmosphere, setting upper limits as low as 0.012 ppbv (Korablev et al., 2019), which is orders of magnitude below the background methane detections by the Curiosity Rover (Webster et al., 2018). ACS MIR also measured the isotopic composition of H_2O (Vandaele et al., 2019), and the effect of the GDS in the vertical distribution of CO (Olsen et al., 2021). Later on, further refinement of the calibration pipeline depicted fine spectroscopic features in the spectral range where methane absorbs, including the detection of a previously unknown magnetic dipole CO_2 band (Trokhimovskiy et al., 2020), and a faint infrared signature of O_3 never detected on Mars before (Olsen et al., 2020). Finally, Korablev et al. (2021) reported the first detection of HCl in the Martian atmosphere, whose abundance appears to be correlated with the onset of the GDS.

2.1.1 ACS MIR Optical Design

The optical design of the MIR channel is sketched in Figure 2.2B. The beam of light enters the instrument through the periscope, and is then directed to the telescope through the entry optics, which comprise a blocking filter and the folding mirrors. The telescope projects the image on to the slit, whose size determines the field-of-view (FOV) of the instrument, which is 0.3 $\times$ 4.1 mrad (1 $\times$ 14 arc min), partially covering the apparent size of the solar disk (20 arc min). The light beam then reaches the echelle grating, which splits the beam into several diffraction orders. The main difference of ACS MIR with other spectrometers is that

the diffraction orders are then directed into a secondary movable grating, which allows the selection of the diffraction orders. This secondary grating consists actually of two diffraction gratings of 361 and 180 grooves per mm respectively, mounted back-to-back, and connected to a motor that allows different positions of the system. Depending on relative angle of the secondary grating, from 7 to 17 diffraction orders can be selected for simultaneous recording on to a 512 $\times$ 640 pixel detector.

The steerable motor can change the angle of the secondary grating in 1.8° steps, and also allows a fast 180° turn to switch between the echelle gratings. The wavenumber range covered for each of the secondary positions is shown in Table 2.1. In addition, the motor is able to switch between contiguous positions with a characteristic time of approximately 0.1 seconds, allowing the possibility to perform a broader spectral scan in the observations. However, occultations with more than one secondary grating position have not yet been performed due to the complexity of the calibration of these observations.

Table 2.1: Wavenumber coverage of ACS MIR as a function of the secondary grating position.

Echelle grating	Position	Relative angle	Diffraction orders	Wavenumber range (cm^{-1})
1 (361)	3	7.5°	206 - 214	3453 - 3601
1 (361)	4	5.7°	216 - 225	3604 - 3769
1 (361)	5	3.9°	226 - 237	3789 - 3987
1 (361)	6	2.1°	238 - 251	3990 - 4222
1 (361)	7	0.3°	250 - 265	4191 - 4456
2 (180)	9	-3.3°	141- 152	2362 - 2560
2 (180)	10	-5.1°	151 - 164	2529 - 2761
2 (180)	11	-6.9°	162 - 178	2713 - 2996
2 (180)	12	-8.7°	174 - 194	2915 - 3265
2 (180)	13	-10.5°	188 -213	3149 - 3585

Once the light is diffracted on the secondary grating, it is projected onto the detector, such that the x-axis represents the spectral dimension, while the selected diffraction orders are split along the y-axis. The width of each diffraction order along the y-axis is determined by the projection of the slit's FOV on the detector, each row representing a given tangent height above the Martian surface. Figure 2.3 shows observations of the clear Sun made with ACS MIR during the Mid-Cruise Check-up (MCC) campaigns on June 2016. These measurements are indicative of the behaviour of the signal-to-noise ratio (SNR) on the detector frame, which peaks close to the center, and decreases towards the edges.

ACS MIR on-board software was designed to be as versatile as possible, and allows the selection of specific rows on the detector frame (i.e., diffraction orders). Partial framing on ACS MIR observations is not only used to reduce the downlink volume, but also to increase the number of measured frames in a given occultation and consequently increase the vertical resolution, always complying with data volume constraints imposed by the spacecraft (Korablev et al., 2018).

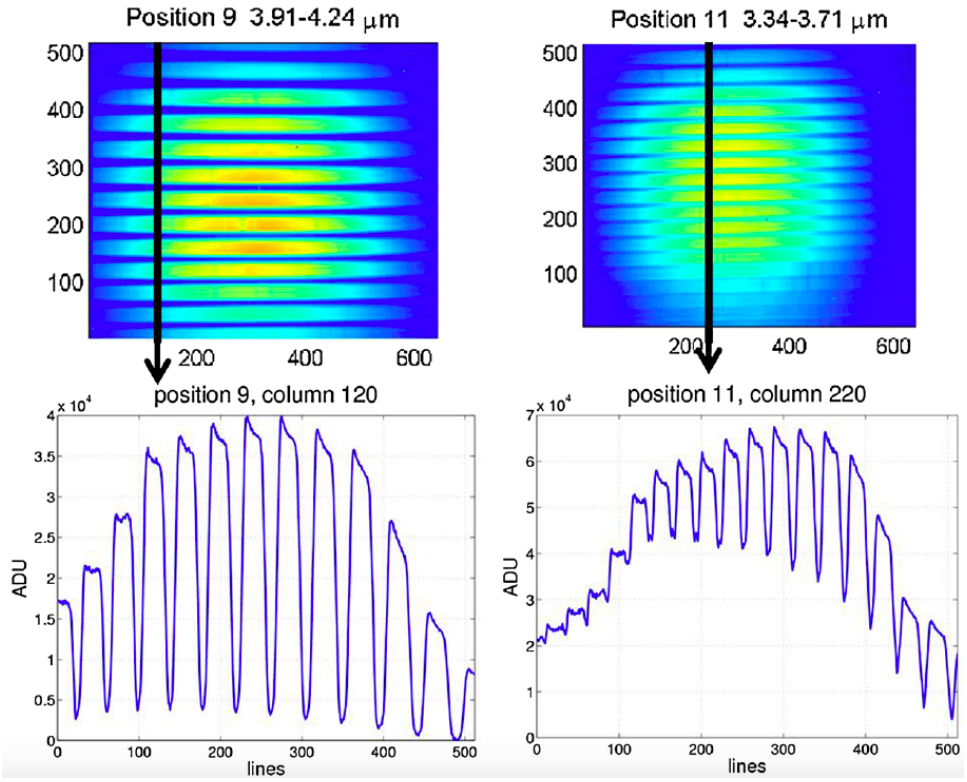

Figure 2.3: Example of two ACS MIR frames (Position 9 - diffraction orders 141 to 152; Position 11 - diffraction orders 162 to 178) obtained from a Sun observation during the MCC campaigns on June 2016. The lower figures represent a vertical cut across the detector, showing the spacing between the different diffraction orders in the detector. Source: Korablev et al. (2018).

2.1.2 ACS Boresight alignment

The boresight pointing of the spectrometers on ACS during solar occultation observations was selected such that the three channels could operate simultaneously, taking advantage of their combined capabilities. Figure 2.4A shows the boresight FOV of the NOMAD and ACS instruments for an ACS-driven solar occultation. MIR's slit is oriented perpendicularly to the Martian surface, and is just partially illuminated by the Sun. The partial illumination of the slit not only allows the simultaneous observations by ACS NIR, whose FOV also intersects

with the Sun, but also avoids overlapping of the diffraction orders in the detector frame, which is undesirable for calibration purposes (see Figure 2.4B). In solar occultations, TIRVIM's FOV encompasses the whole disk of the Sun, and can therefore operate simultaneously with the other two channels.

Figure 2.4A shows that during solar occultation observations, the slits of the NOMAD instrument and ACS MIR cannot be simultaneously illuminated due to the apparent size of the Sun being smaller than the separation of the two boresight directions, which means they cannot operate at the same time. Therefore, solar occultations need to be either ACS or NOMAD-driven, although it must be noted that the NIR and TIRVIM channels on ACS can also operate during NOMAD-driven observations. A compromise between the ponting of both instruments was agreed, such that 10 occultations per day are ACS-driven, while the remaining 14 occultations are performed using NOMAD's optimal pointing.

The geometrical parameters of the measurement in each acquisition made by ACS MIR during one occultation are calculated using the SPICE kernels provided by ESA's Science Operations Centre (SOC) (Costa, 2018). These kernels are processed at the Space Research Institute (IKI), generating three ASCII files with the geometry of the observation corresponding to the line-of-sight at the slit edges and centre. For each acquisition, these parameters include the latitude, longitude and local time of the tangent point, as well as the tangent altitude above the Martian surface. On ACS MIR's detector frame, the slit is projected over 10-20 pixels along the y-axis, visible as several stripes corresponding to the several diffraction orders (see Figure 2.4). Interpolation of the observational parameters in the three files allows the computation of the geometry for each spectrum recorded in the different detector rows.

2.2 ACS MIR Measurements

2.2.1 ACS MIR solar occultations

From a spacecraft orbiting around a planet such as the ExoMars TGO, one can potentially look at the nadir, at the limb, or at an external source of light, such as the Sun or other stars. Nadir-viewing observations have the advantage of providing a good horizontal resolution, but they can provide just a limited amount of information about the vertical structure. On

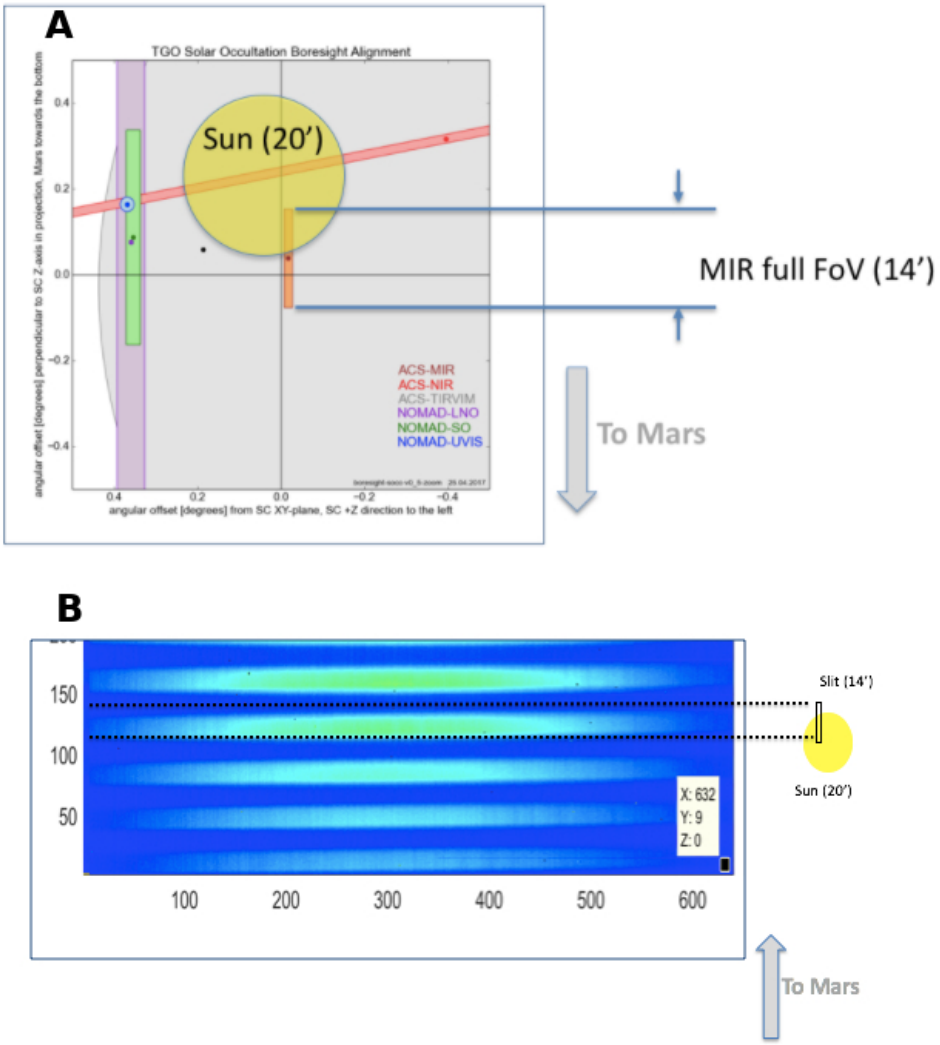

Figure 2.4: A) TGO solar occultation boresight alignment for an ACS-driven observation. B) Projection of the partially-illuminated slit on MIR's detector. Credit: Alexander Trokhimovkiy.

the other hand, limb-viewing observations provide precise vertical constraints. However, the line-of-sight covers a large range of latitudes and longitudes, and therefore provides poorer horizontal resolution.

The MIR channel on ACS operates in solar occultation mode. Geometrically, solar occultation observations are comparable to limb-viewing observations, in the sense that a long path along a large range of latitudes and longitudes is observed. However, the pointing in this case is directed to the Sun, or other stars in the case of star occultations. Solar occultation observations are especially suitable for the measurement of trace gases due to the great brightness of the Sun, which results in high signal-to-noise ratio (SNR) spectra, and the long observed path length, which results in an observed air mass about 10 times greater than when observing the nadir.

Figure 2.5 shows a sketch of the observational setup of ACS MIR solar occultations. ACS MIR observes the Sun from 0 to 270 km above the Martian surface within 3–6 min. In each individual acquisition, 200 consecutive frames are stacked together on-board. The integration time of a single frame is 3 or 6 ms, depending on the selected secondary grating position, but each of the 200 readouts from the detector takes approximately 10 ms, with one acquisition lasting 2.1 s. In each occultation, the uppermost heights are averaged to obtain a reference solar spectrum, which is then used to generate the transmission spectra. The reference height for calculating the reference solar spectrum is somewhat arbitrary, depending on the observed spectral range, but must be high enough so that there is no atmospheric contamination. On the other hand, a dark signal, combination of the detector dark current and the surrounding thermal background emission, is estimated from the lowermost observations, where the Sun is completely concealed by the Martian surface, and refined in dedicated observations of open space. The spectral calibration of the measurement is performed using solar lines and comparing them to the ACE-FTS solar atlas (Hase et al., 2010). Then, it is further refined using observed atmospheric absorption lines of CO_2 and H_2O.

2.2.2 ACS MIR observation coverage

The 2-hour orbital period of the ExoMars TGO allows 24 solar occultations observations per day (12 ingresses and 12 egresses), 10 of which are made using ACS' optimal boresight align-

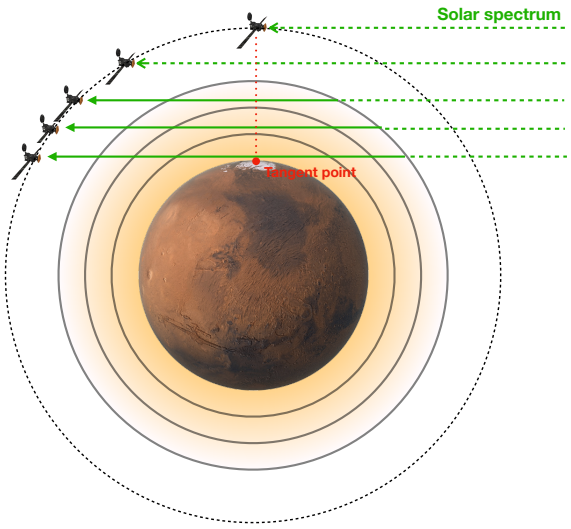

Figure 2.5: Sketch of the observational setup during a solar occultation observation.

ment, in which all three channels on ACS can simultaneously operate, and the remaining 14 observations are NOMAD-driven, in which ACS MIR does not operate. Other constraints for the observations include limitations in the downlink volume, and the unavailability of occultations due to geometric constraints. Available downlink volume is variable throughout the science mission, as it depends on the availability of ground stations, as well as on the distance between the Earth and Mars. In order to comply with the downlink volume limitations, MIR observations are made either using partial framing, in which only the most interesting diffraction orders for each secondary grating position are selected and sent to Earth, or decreasing the vertical resolution of the observation. The unavailability of solar occultations for the ExoMars TGO is best described by the β-angle, which is defined as the angle between the orbit plane and the Sun direction vector. The β-angle varies throughout the science operation phase in cycles of approximately seven weeks. When $\beta > 63°$, the Sun is not concealed by the body of Mars, and full occultations therefore do not occur (Geiger et al., 2018).

TGO science operations started in March 2018, when Mars was at $L_S = 163°$ in Martian Year 34 (MY34). Up to February 2021, ACS MIR has made 4506 observations, probing the atmosphere for more than a full Martian year, at a broad range of locations and local times (see Figure 2.6). The latitudinal coverage of ACS observations spans a broad range of latitudes between 90°S and 88°N. During a single day, the occultation tangent points are evenly distributed in longitude, at fixed latitudes in the northern and southern hemisphere,

as indicated with yellow dots in Figure 2.1.

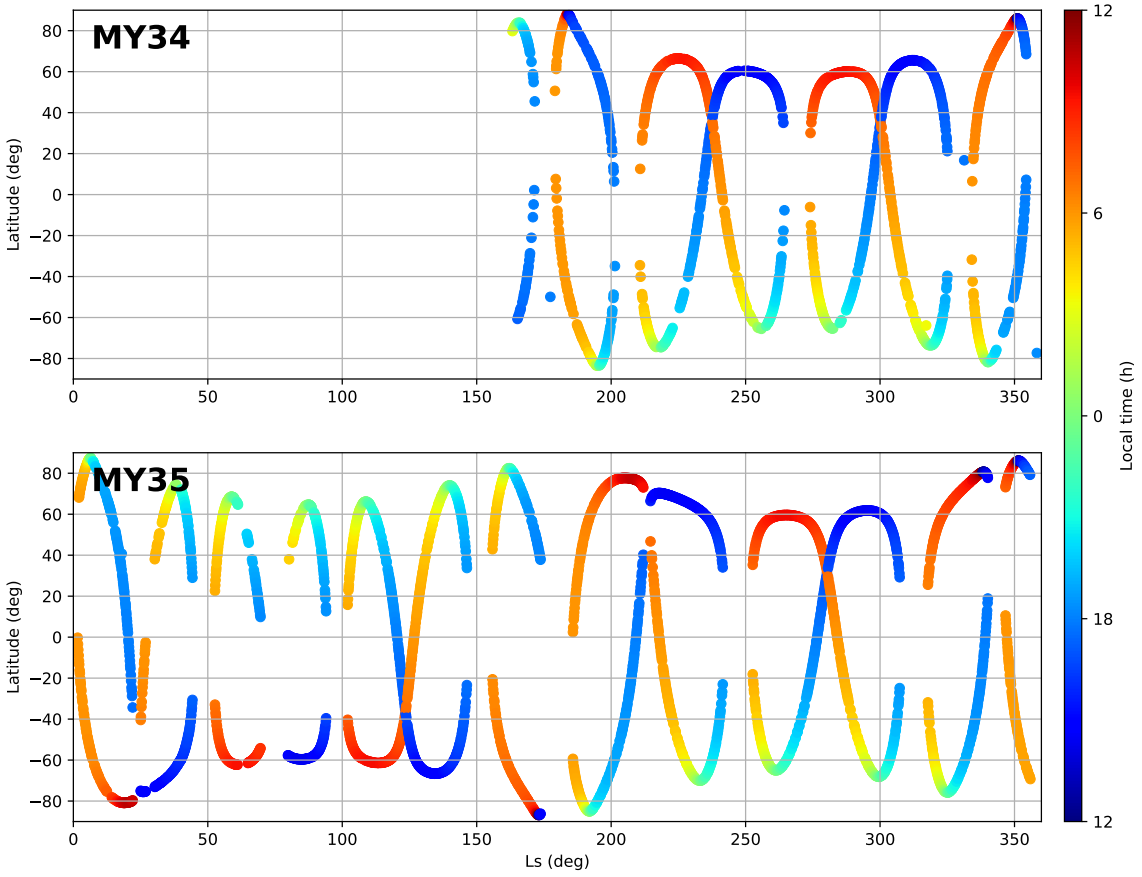

Figure 2.6: ACS MIR solar occultation coverage as a function of latitude and solar longitude, from March 2018 to March 2020. The colorbar represents the local time of the observations.

It can be observed in Figure 2.6 that there are occultation-free periods approximately every 50° of solar longitude, which correspond to periods in which the β-angle is greater than 63°. The β-angle not only affects the availability of occultations, but also the characteristics of the occultations. For instance, occultations with $\beta < 60°$ from 200 km to the surface typically occur within 2-4 minutes, while an occultation with $\beta = 61$ ° takes approximately 8 minutes (Korablev et al., 2018). Long-lasting occultations are characterised by a denser vertical resolution, but the tangent point moves in latitude during the course of an occultation, which can affect the analysis of the measurements if there is horizontal variability in the atmosphere.

2.2.3 ACS MIR double image

Early on after the start of the ExoMars TGO's nominal science phase, comparison between the measured and modelled transmission spectra revealed a doubling of the absorption lines. Indeed, further investigation of this feature made it clear that it was the whole detector image being doubled, with an offset of approximately 5 and 2 pixels in the vertical and horizontal directions respectively. The cause of this doubled-image is unknown, although it is presumably the result of a partial fracture in one of the lenses broken during launch. An accurate understanding of the doubled-image is essential for understanding the sensitivity of the ACS MIR spectra and carefully disentangling the impact of the atmospheric parameters from the instrumental effects.

The nature and magnitude of the doubled image is complex, varying throughout the detector array, and making a potential rectification of the fault difficult. Figure 2.7 illustrates the behaviour of the doubled image for the upper and lower portions of the detector frame, by comparing images of the same diffraction order, but observed in different positions of the secondary grating. In particular, diffraction order 250 is observed both when using secondary grating positions 6 and 7 (see Table 2.1), but while this order is situated in the lower part of the detector in position 6, it is situated in the upper portion in position 7. While the transmission image for this diffraction order is neat in position 6 (panel D), the same diffraction order is blurred in position 7 (panel E), caused by the superposition of two doubled images.

Variations of the magnitude of the doubled image are observed not only in different parts of the detector, but also in different rows within a diffraction order. Figure 2.8 shows the spectra measured in the rows corresponding to the slit edge and centre in diffraction orders 217 and 225, when using secondary grating position 4. In diffraction order 217, the spectrum measured at the slit centre shows absorption lines with two peaks, caused by the doubling of the image. At the slit edge, the spectrum shows single peaks for each absorption line instead. In addition, as previously illustrated in Figure 2.7, the magnitude of the doubled image varies in different parts of the detector. While the measured spectra shows clear differences between the doubling at the slit centre and edge in diffraction 217, these differences are milder for diffraction order 223, which is situated at the bottom part of the detector frame. All the

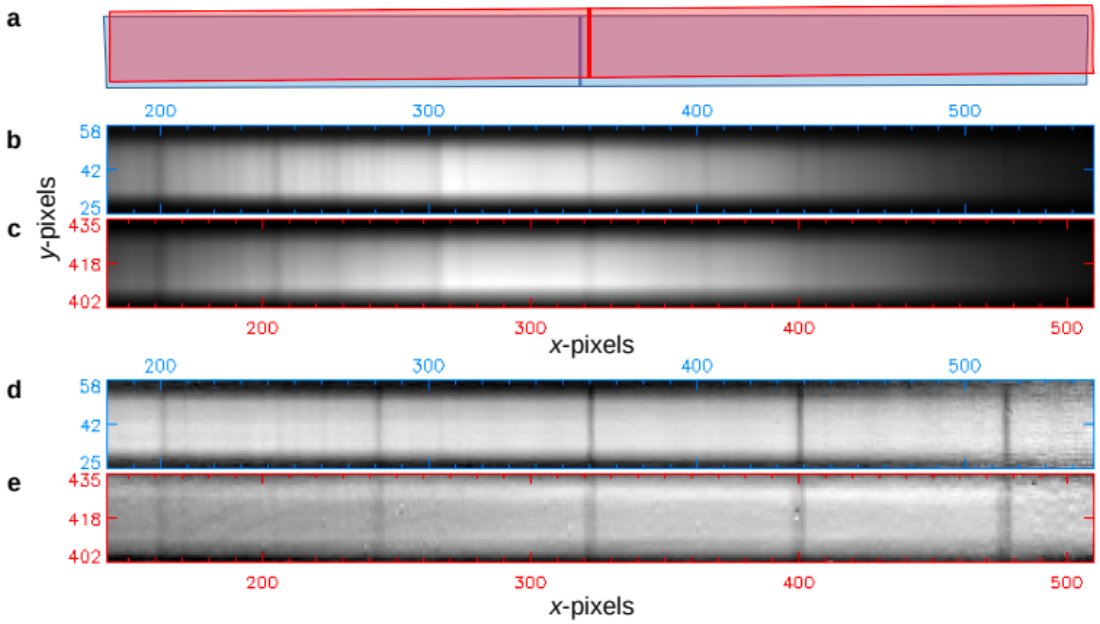

Figure 2.7: Illustration of doubled image in an ACS MIR detector frame. a) schematic representing two offset and overlapping images, b) the lower-portion of a position 6 detector image of intensity featuring order 250, c) the upper-portion of a position 7 intensity image featuring order 250, d) the lower-portion of a position 6 transmission image with order 250, e) the upper-portion of a position 7 transmission image with order 250. Figure from Olsen et al. (2021).

variability of the doubled image impedes the correction of the detector images. Instead, the doubling of the absorption lines needs to be accounted for in the radiative transfer model (see Section 3.4.4).

2.3 Summary

In the previous chapter, we introduced the key aspects of the Martian atmosphere relevant to understand the measurements of the isotope ratios in CO_2 and H_2O. In this chapter, we have provided a detailed overview of the ExoMars mission, the Trace Gas Orbiter, and in particular of the middle infrared channel of the Atmospheric Chemistry Suite, which is the one we use to measure the isotopic ratios. ACS MIR has the primary goal of providing a detailed inventory of the trace gases present in the Martian atmosphere. In order to achieve the highest sensitivity to the trace gases, ACS MIR combines an advanced optical design that allows high spectral resolution measurements ($\lambda/\Delta\lambda \sim$ 30000-50000), with the enhanced sensitivity to trace gases achieved with solar occultation observations. ACS MIR's optical design is characterised by the use of two echelle gratings, one of which can rotate to separate the diffraction orders. Depending on which of the twelve positions the secondary grating is

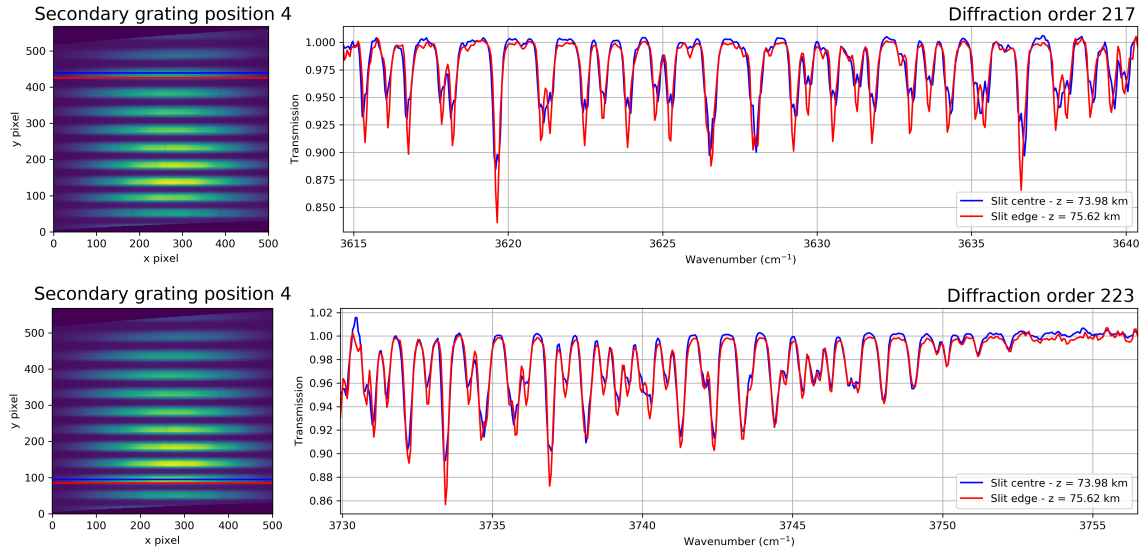

Figure 2.8: ACS MIR spectra measured using secondary grating position 4. The two panels on the left show the measured detector frames, highlighting the rows corresponding to the slit edge and centre in diffraction orders 217 and 223, whose corresponding spectrum is shown in the righthand panels.

rotated to, the instrument can access different spectral ranges within the total spectral range of the instrument (2.3 - 4.2 μm or 2380 - 4347 cm^{-1}).

In the next chapter, we explain how the ACS MIR measurements are modelled based on the atmospheric vertical profiles and discuss the most suitable spectral ranges and secondary grating positions to study the isotopic composition of CO_2 and H_2O in the atmosphere of Mars with ACS MIR spectra. In the following chapters, we then apply these methods to derive the isotope ratios from the ACS MIR solar occultation observations.

Chapter 3

Atmospheric retrievals in ACS MIR solar occultations

Apart from *in situ* atmospheric measurements, the best way to analyse planetary atmospheres is to observe their electromagnetic spectra, which incorporates the absorption, emission and reflection of light. In particular, the infrared part of the spectrum is especially interesting as it allows us to constrain temperatures, gas and aerosol abundances.

In order to obtain information about the structure and composition of an atmosphere from its spectrum, we need a radiative transfer forward model that relates the atmospheric parameters to the observed spectrum. A retrieval tool is then used in order to solve the inverse problem, in which the properties of the atmosphere are retrieved from the comparison of the model and the measurement.

In this project, we use the Non-linear Optimal Estimator for MultivariatE Spectral analySIS (NEMESIS) code, developed by Irwin et al. (2008). The code was initially developed to analyse spectra from the Cassini spacecraft, but constructed to be generally applicable to any planetary atmosphere and observation geometry. NEMESIS has been already applied to many different atmospheres from ground-based telescope and spacecraft, in both nadir and limb-viewing observations (e.g., Irwin et al. (2008); Sefton-Nash et al. (2013)). In this case, we will apply it to solar occultation measurements for the first time.

In this chapter, we explain the main equations describing the radiative transfer model and the retrieval tool. We then give an overview of the the isotope studies that can be performed using ACS MIR, and finally explain the specific retrieval scheme adopted for ACS MIR solar occultation observations.

3.1 Radiative transfer in solar occultation observations

The main purpose of any radiative transfer code is to calculate a synthetic spectrum for a given atmosphere, which is computed solving the radiative transfer equation. This equation states that the propagation of radiation is affected by emission, absorption and scattering. For the purposes of these project, given the spectral range observed with ACS MIR and the range of temperatures on Mars, thermal emission is negligible. In addition, given the small field of view of the instrument and the fact that we are looking directly at the Sun, we assume that the contribution by scattering will also be negligible and thus do not account for it. Therefore, in this context the radiative transfer equation simplifies to

$$\frac{dI_\nu}{ds} = -I_\nu k_\nu(s) n(s), \tag{3.1.1}$$

where I_ν is the spectral intensity of the radiation beam, k_ν is the absorption coefficient in cm^2, n is the number density in cm^{-3} and s is the distance along the path in cm. Upon integration equation 3.1.1 gives

$$I_\nu = I_{\nu_0} \cdot e^{-\tau_\nu} \tag{3.1.2}$$

where τ_ν is the optical depth defined as $\tau_\nu = \int k_\nu(s) n(s) ds$. The absorption coefficient and the density are continuous functions of the path length s, whose integration is not analytically solvable in a general case. Therefore, the optical depth is computed numerically, discretising the atmosphere into a finite number of layers. In the case of solar occultation observations, the observed intensity I_ν is usually normalised with the out-of-atmosphere measured solar intensity I_{ν_0}, in order to obtain a transmission spectrum T_ν.

Absorption of photons from the solar flux in the Martian atmosphere will be caused by either gases or aerosols. In the case of the gaseous absorption, the monochromatic absorption

coefficient k_ν for a given transition is given by

$$k_\nu(p,T) = S(T)\phi_\nu(p,T), \tag{3.1.3}$$

where S is the line strength of the transition and ϕ is the function describing the broadening of the line. The strength at a reference temperature ($T_0 = 296$ K) of the line transitions of the various gases in the Martian atmosphere are tabulated in spectroscopic line databases, such as the 2016 edition of the HITRAN database (Gordon et al., 2017). Then, the intensity at any other temperature is calculated by

$$S(T) = S(T_0)\frac{Q(T_0)}{Q(T)}\frac{e^{-hcE''/k_BT}}{e^{-hcE''/k_BT_0}}\frac{(1-e^{hc\nu/k_BT)}}{(1-e^{hc\nu/k_BT_0})} \tag{3.1.4}$$

where $Q(T)$ is the partition function at temperature T, h is the Planck constant, c is the speed of light, k_B is the Boltzmann constant and E'' is the lower state energy, which is also tabulated in the HITRAN database. The internal partition function, which describes the statistical properties of a gas in thermodynamic equilibrium, are computed using the 2017 edition of the TIPS database created by Gamache et al. (2017).

The spectral lines are not totally monochromatic, but they rather occur over a finite range of wavenumbers. Various physical processes can give rise to the broadening of a spectral line, such as natural broadening, Doppler broadening and pressure broadening, with the last two being dominant in the majority of planetary atmospheres. Doppler broadening, as its name suggests, is produced by the Doppler effect from the thermal motion of the molecules in a gas. In local thermodynamic equilibrium (LTE), the velocity distribution is given by the Maxwell-Boltzmann distribution, and the broadening of the line is described by a Gaussian profile, with a half-width at half-maximum (HWHM) given by

$$\alpha_D = \frac{\nu_0}{c}\sqrt{\frac{2N_Ak_BTln(2)}{M}} \tag{3.1.5}$$

where ν_0 is the central wavenumber of the transition, N_A is the Avogadro constant and M is the molar mass of the molecule.

Pressure broadening is related to the effect of collisions in the characteristic lifetime of the emission or absorption process. This type of broadening is described by a Lorentzian

profile and its width is related to the frequency of the collisions. The HWHM γ of this profile is usually tabulated in spectroscopic databases at a reference pressure (p_0 = 1 atm) and a reference temperature (T = 296 K) in the cases for self-broadening and air-broadening, and can be calculated at any other pressure and temperature using

$$\gamma(p,T) = \frac{\gamma_{air}(p_0,T_0)(p-p_{gas}) + \gamma_{self}(p_0,T_0)p_{gas}}{p_0}\left(\frac{T_0}{T}\right)^n \tag{3.1.6}$$

where p_{gas} indicates the partial pressure of the emitting or absorbing gas and n is the temperature exponent coefficient, also tabulated in the database.

Traditionally, the temperature dependence of the pressure-broadening coefficient γ has been modelled using an exponential function as described in equation 3.1.6. Recently, Gamache and Vispoel (2018) developed a new expression that correctly models the temperature dependence of γ over a large range of temperatures, using a Double Power Law (DPL) given by

$$\gamma(p,T) = \frac{p}{p_0}\cdot\left[c_1\left(\frac{T_0}{T}\right)^{n_1} + c_2\left(\frac{T_0}{T}\right)^{n_2}\right] \tag{3.1.7}$$

where c_1, c_2, n_1 and n_2 are coefficients tabulated in the spectroscopic line databases. Gamache and Vispoel (2018) compared the performance of equations 3.1.6 and 3.1.7 in more than 100 thousand transitions, and in all cases the DPL gave better results than the standard power law. Currently, the HITRAN database provides the relevant parameters for the standard power law, but it is foreseen that the spectroscopic databases will start tabulating the parameters relevant to the DPL in the near future.

The values for γ_{air} tabulated in the HITRAN database are representative of Earth-like atmospheres (i.e., N_2 combined with O_2). However, the Martian atmosphere is dominated by CO_2, and both the pressure broadening coefficient γ_{air} and the temperature exponent n depend on the gas environment. In the past years, great modelling and laboratory efforts have been made in order to estimate the pressure broadening coefficients for CO_2-dominated atmospheres, and there are public results for some gases such as SO_2, NH_3, HF, HCl, OCS and C_2H_2 (Wilzewski et al., 2016).

In the case of water vapour, previous studies on Mars have often applied a constant scaling of 1.67 with respect to the air-broadened coefficients in an Earth-like atmosphere (N_2 + O_2) derived by Brown et al. (2007) to simulate the effect of a CO_2-dominated atmosphere. Nevertheless, Brown et al. (2007) point out that the measured ratio of CO_2 to air-broadened coefficients shows large variability around the mean value of 1.67 (0.95–3.07), and therefore the "simple scaling of the coefficients for N_2 broadening does not provide a reliable set for CO_2 broadening of water" (Brown et al., 2007). Gamache et al. (2016) published a spectral line list for the water isotopologues, which simulates the line shape parameters using the Modified Complex Robert–Bonamy formalism (MCRB), which in general yields to average uncertainties of ∼5% and should provide a more accurate representation than a constant scaling factor. This spectroscopic linelist for H_2O in a CO_2-dominated atmosphere was improved by Devi et al. (2017b,c,a) for $HD^{16}O$ using laboratory measurements. More recently, Régalia et al. (2019) made laboratory measurements using a CO_2 gas cell to constrain the line parameters for the three first oxygen isotopologues of water vapour ($H_2^{16}O$, $H_2^{18}O$, $H_2^{17}O$), in combination with MCRB calculcations. Régalia et al. (2019) point out that while their MCRB calculations and measurements are in good agreement in the 2.7μm-band, they are not in such a good agreement with the calculations of Gamache et al. (2016), due the effects of neglecting the vibrational dependence for the line widths. In addition, Régalia et al. (2019) use the DPL parameterisation of Gamache and Vispoel (2018) for the characterisation of the temperature dependence of the CO_2-broadening coefficients, which should yield more accurate results. In conclusion, for the purpose of this project, the spectroscopic linelist of Régalia et al. (2019) is used for the three main oxygen isotopologues ($H_2^{16}O$, $H_2^{18}O$, $H_2^{17}O$), while the laboratory measurements of Devi et al. (2017b,c,a) are used to constrain the abundances of $HD^{16}O$.

Another source of removal of photons from the solar intensity is the extinction by aerosols suspended in the atmosphere. NEMESIS calculates the extinction coefficient of the aerosols using Mie Theory, which models the particles as dielectric spheres with a uniform refractive index. The main aerosol population in the Martian atmosphere are silicate mineral dust particles, which are modelled using the complex refractive indices of Wolff et al. (2006). Water and CO_2 ice clouds may also form under the right atmospheric conditions, which can be modelled using the refractive indices of Warren and Brandt (2008) and Hansen (1997), respectively.

In order to calculate the opacity along the line of sight for a given measurement, the absorption coefficients of the aerosols and gases must be combined with the information about the reference atmospheric profiles and the geometry of the observation. The path length along the line of sight in each of the layers is calculated using the cosine rule in a spherically symmetric atmosphere, as shown in Figure 3.1. Once the geometry of each layer has been determined, the line-of-sight column densities are computed by integrating the number density of each layer along the path. In addition, effective temperatures and pressures for each of the layers are also computed for an accurate representation of the spectroscopic parameters (e.g., equation 3.1.7). To perform this calculation, each layer is split into 101 points along the path, and the effective temperatures and pressures are calculated by means of a weighted average, where the weights are given by the density in each of the points. Once the line-of-sight column densities and effective temperatures and pressures are calculated, one can compute the opacity and transmission along the path (see equation 3.1.2).

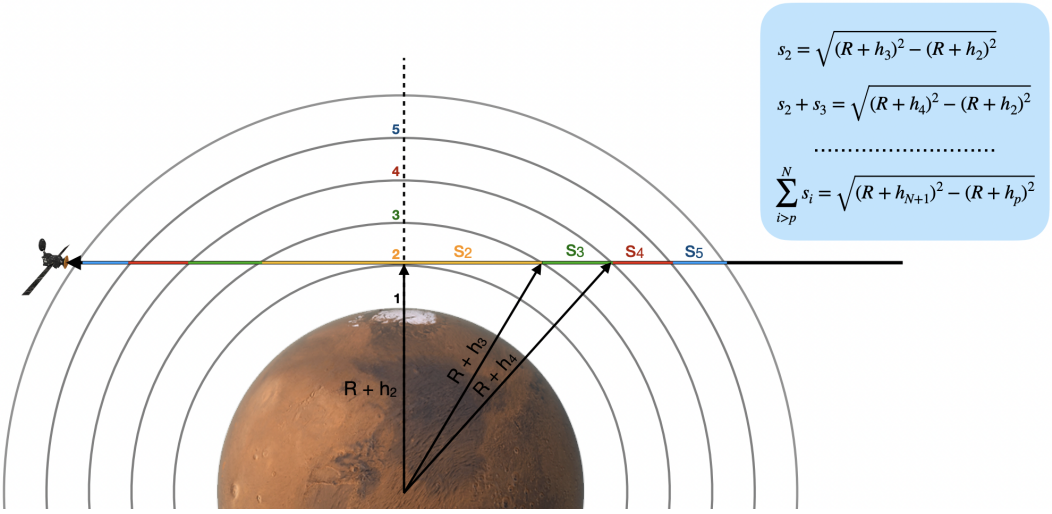

Figure 3.1: Sketch describing the calculations of the path lengths in each of the layers for a solar occultation measurement. In the figure, R represents the radius of Mars, h_i is the bottom altitude of the layer, and s_i represents the path length along each of the layers.

Another important aspect to consider in the radiative transfer analysis of solar occultation measurements involves the sensitivity of the spectra along the path. In general, the line-of-sight opacity peaks at the tangent point due to the exponential decrease of the atmospheric density with altitude. Therefore, the sensitivity of the spectrum typically peaks at the tangent point. However, when the absorption lines are strong, they can saturate before the light beam reaches this point. In this case, the sensitivity of the spectrum peaks at an altitude

level different from that of the tangent point. Figure 3.2 shows an example of how the transmission varies along the path in a wavelength range covering the centre and edge of a strong band of CO_2. It is shown that while for the highest wavenumbers (i.e., weaker absorption lines), the transmission level decreases rapidly at the tangent point, this transition occurs at a point further from the observer for the stronger lines. This varying sensitivity of the spectra along the line of sight might pose some challenges in the interpretation of retrieved gaseous abundances, especially if there are strong horizontal gradients along the line of sight, where the assumption of a spherically symmetric atmosphere breaks down.

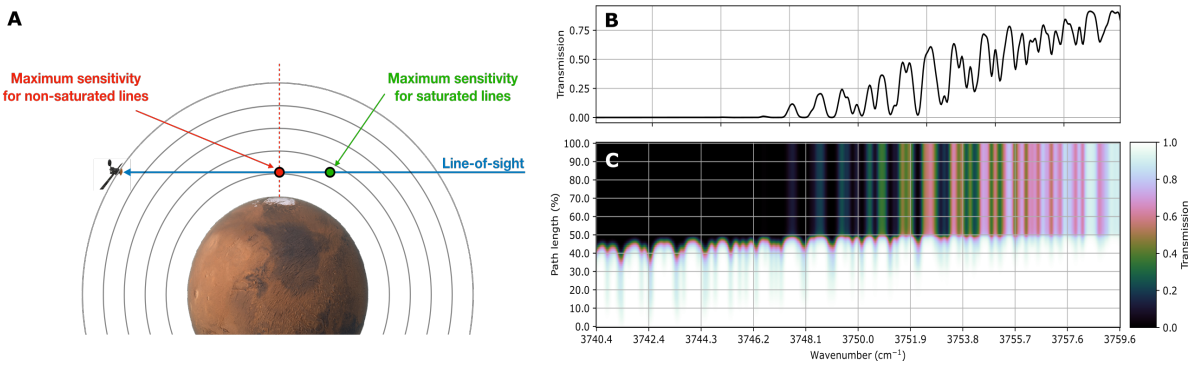

Figure 3.2: A) Sketch of the sensitivity of solar occultation measurements along the line of sight. B) Synthetic transmission spectrum of CO_2 in the atmosphere of Mars at a tangent altitude of 10 km. C) Evolution of the transmission along the path, where 50% represents the tangent point of the observation.

3.2 Isotopic studies using ACS MIR

The radiative transfer model allows us to generate synthetic spectra for a given input set of atmospheric parameters. In this section, we generate synthetic spectra to provide an overview of the isotope studies that can be performed using ACS MIR, and which spectral ranges and secondary grating positions are more suitable to do so. For the purpose of this project, we provide an overview for H_2O and CO_2. Nevertheless, it must be noted that ACS MIR also allows the characterisation of the chlorine isotopic composition of HCl (Trokhimovskiy et al., 2021) from secondary grating positions 11 and 12, and the carbon and oxygen composition of CO from positions 6 and 7 (Olsen et al., 2021).

3.2.1 H_2O isotopes

Figure 3.3 shows a synthetic spectrum covering the full spectral range of ACS MIR (2360 to 4460 cm^{-1}), using a Gaussian instrument lineshape with a FWHM of 0.15 cm^{-1}, and at a tangent height of 10 km using the temperature and pressure profiles from the Mars Climate Database (Forget et al., 1999) at noon at 0°N and 0°W at $L_S = 0°$. In this section, these same atmospheric profiles are used for generating all the spectra unless otherwise stated. The spectrum in Figure 3.3 shows the contribution from CO_2, as well as from the four main water vapour isotopologues ($H_2^{16}O$, $H_2^{18}O$, $H_2^{17}O$, $HD^{16}O$), using a constant H_2O volume mixing ratio of 100 ppmv, the standard Earth-like fractionation for the oxygen isotopologues, and a value of 5 with respect to Earth for the D/H ratio. The main aspects describing the suitability of each grating position to constrain the isotope composition of water vapour are:

- Secondary grating positions 7 and 9 do not include any absorption features of water vapour, and are therefore not suitable for retrieving the isotope composition of H_2O.

- Secondary grating positions 6, 12 and 13 show measurable absorption of $H_2^{16}O$, but lack of any measurable absorption lines of any other isotopologue.

- Secondary grating positions 10 and 11 show measurable absorption of $HD^{16}O$. The absorption lines in these positions are very suitable for the retrieval of vertical profiles of $HD^{16}O$, since they are not contaminated by the absorption of other species. However, position 10 lacks of absorption lines of $H_2^{16}O$, required to determine the D/H ratio, and position 11 only includes few weak lines of $H_2^{16}O$, which are not observable as high as the $HD^{16}O$ ones (see Figure 3.4). In this cases, in order to constrain the D/H ratio, one may use vertical profiles of $H_2^{16}O$ from the ACS NIR channel (Fedorova et al., 2020b).

- Secondary grating position 3 shows measurable lines of $H_2^{16}O$, but only weak ones for the rest of the isotopologues. In addition, this position includes a strong band of CO_2 which masks the weaker absorption of the H_2O isotopologues, which makes this position not optimal for isotope studies.

- Secondary grating position 4 includes some of the strongest lines of the four main isotopologues of H_2O. Unfortunately, as shown in Figures 3.3 and 3.4, most of these absorption lines are completely masked by very strong CO_2 bands. However, the spectral

range covered by diffraction order 224 lies outside the CO_2 absorption band, and includes absorption lines of several water isotopologues.

- Secondary grating position 5 includes measurable absorption lines for all four main isotopologues of H_2O. In the case of the oxygen isotopes ($H_2^{18}O$ and $H_2^{17}O$), these are the strongest lines observed within the spectral range of ACS MIR. In the case of $HD^{16}O$, although the lines are not as strong as in secondary grating position 4, they can be measured in at least diffraction orders 226 and 227, which allows the simultaneous measurement of the three isotope ratios (D/H, $^{18}O/^{16}O$ and $^{17}O/^{16}O$).

In summary, secondary grating positions 4 and 5 are found to be the most suitable to constrain the isotope composition of H_2O, as all isotope ratios can be simultaneously measured. Secondary grating positions 10 and 11 include very clean absorption lines of $HD^{16}O$, but lack of strong enough $H_2^{16}O$ lines, which would require to use vertical profiles from ACS NIR instead.

In the first Martian year of operations, no measurements have been made that include the combination of several grating positions. In the case these measurements are made in the future, the optimal setup for measuring the D/H ratio would be to combine secondary grating positions 11 and 12, which include many absorption lines of similar optical depth. In the case of the oxygen isotope ratios, secondary grating position 5 alone provides the best selection of absorption lines.

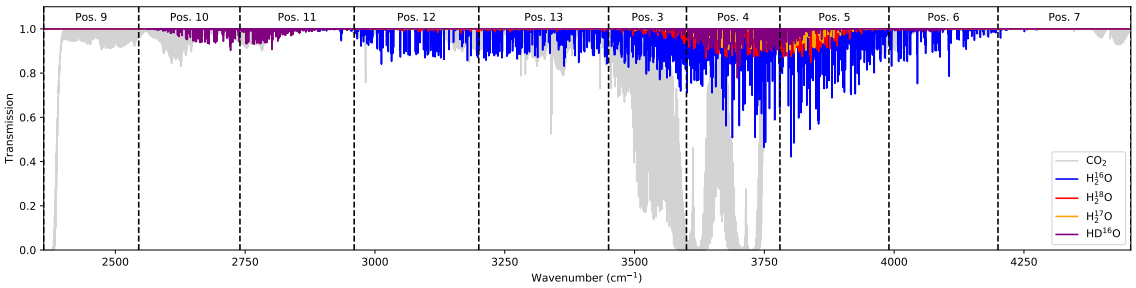

Figure 3.3: Synthetic spectrum relevant for Martian conditions, covering the full spectral range of ACS MIR, with an instrument lineshape described by a Gaussian function with a FWHM of 0.15 cm^{-1}. The contribution from CO_2 and the H_2O isotopes is shown, following the colours in the legend.

In this thesis, we first use data from secondary grating position 5 to constrain, for the first time, the vertical profiles of the O isotopic ratios in H_2O. Then, the analysis of the

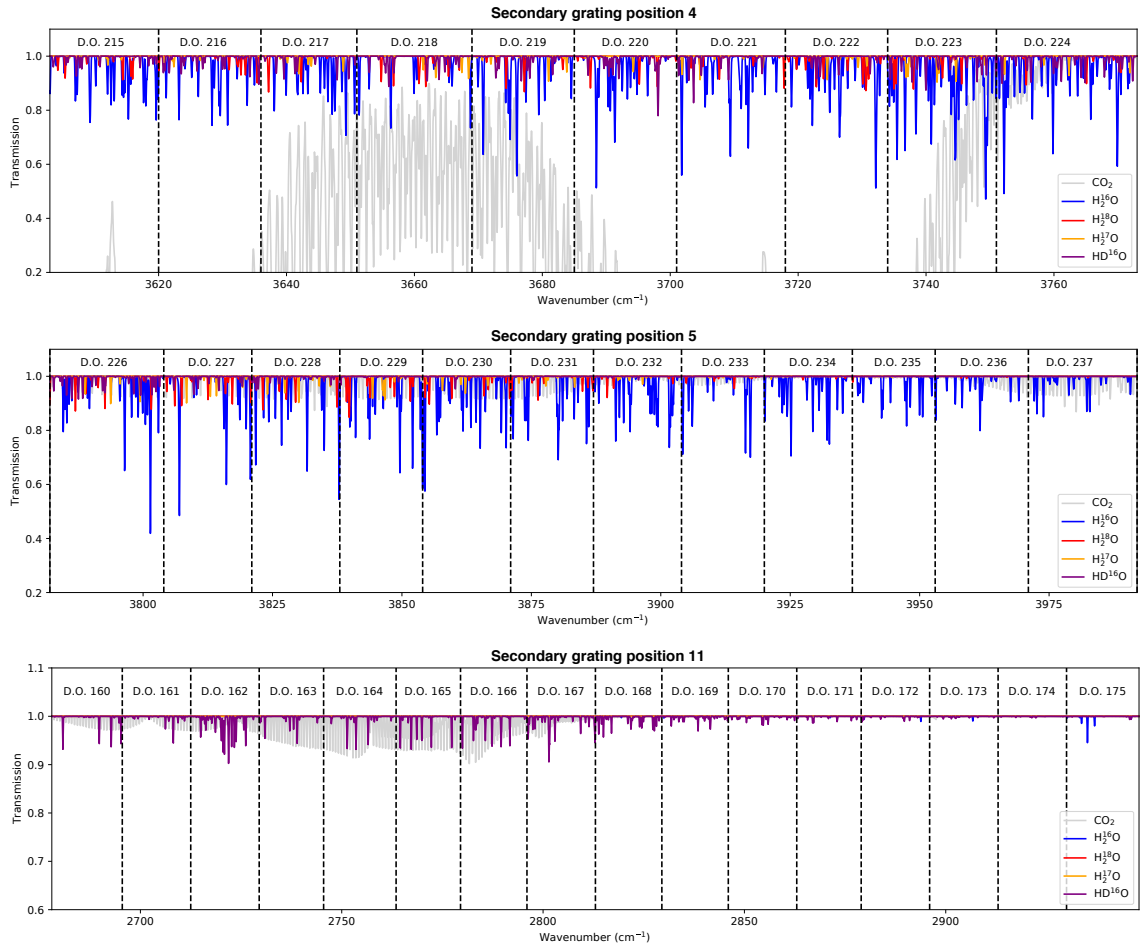

Figure 3.4: Synthetic spectrum relevant for Martian conditions, in the spectral range covered by ACS MIR when operating in secondary grating positions 4, 5 and 11, with an instrument lineshape described by a Gaussian function with a FWHM of 0.15 cm^{-1}. The contribution from CO_2 and the H_2O isotopes is shown, following the colours in the legend. The spectral coverage of each of the diffraction orders observed with each secondary grating position is also indicated in the figure.

isotopic composition of H_2O is extended to more than a full Martian year of observations using secondary grating position 4 to constrain the variability of the D/H and $^{18}O/^{16}O$ ratios.

3.2.2 CO_2 isotopes

Figure 3.5 shows an analogue synthetic spectrum to the one shown in Figure 3.3, but in this case highlighting the contribution from the main four isotopologues of CO_2 ($^{12}C^{16}O_2$, $^{13}C^{16}O_2$, $^{18}O^{12}C^{16}O$, $^{17}O^{12}C^{16}O$), assuming they follow the same isotope fractionation as on Earth. The main aspects describing the suitability of each grating position to constrain the isotope composition of carbon dioxide are:

- Secondary grating position 9 includes measurable absorption bands of the three main oxygen isotopes of CO_2. In addition, in the lowest wavenumber range, it includes a strong band of $^{12}C^{16}O_2$, which allows us to constrain the CO_2 absorption up to approximately 200 km. In this part of the spectral range, there is also a strong band of $^{17}O^{12}C^{16}O$. Nevertheless, retrievals of the $^{17}O/^{16}O$ ratio using these strong bands are complicated, as the absorption lines of the main isotopologue mask those of $^{17}O^{12}C^{16}O$.

- Secondary grating positions 10 and 11 include weak bands of $^{18}O^{12}C^{16}O$ and $^{17}O^{12}C^{16}O$, but not of $^{12}C^{16}O_2$.

- Secondary grating position 12 includes weak bands of $^{12}C^{16}O_2$, $^{13}C^{16}O_2$ and $^{18}O^{12}C^{16}O$, which allow the retrieval of the isotope ratios in the lower atmosphere.

- Secondary grating position 13 includes weak and strong bands for all main four isotopologues (see Figure 3.6). Note that the spectral ranges in Figure 3.5 are approximate, since the ranges covered by different grating positions partially overlap (see Table 2.1). The weak bands may be used to constrain the ratios at low altitudes, where the strong lines saturate. At high altitudes, where the weak bands disappear, one may use the strong absorption bands to generate vertical profiles of the isotope ratios from the lower to the upper atmosphere.

- Secondary grating positions 3 and 4 include strong bands for all main four isotopologues (see Figure 3.6). Indeed, the strong bands in secondary grating position 3 are the same as those observed in secondary grating position 13, as the spectral ranges acquired with

the two positions overlap. These bands allow the measurement of the isotope ratios up to altitudes of approximately 120 km.

- Secondary grating positions 5 and 6 include weak bands of the three main oxygen isotopes of CO_2 (see Figure 3.6). Secondary grating position 5 includes two absorption bands to constrain the $^{18}O/^{16}O$ ratio, situated in different parts of the spectral range. The redundancy of these bands is convenient, since they are projected in different parts of the detector frame, and may be used to cross-validate the results, since the calibration of the data might be slightly different in different parts of the detector.

- Secondary grating position 7 only includes a weak band of $^{12}C^{16}O_2$, and is therefore not suitable for isotope studies.

In summary, secondary grating position 13 is found to be the most suitable for retrieving the isotope composition of CO_2, as it includes both weak and strong absorption bands for all main four isotopologues, which allows the simultaneous characterisation of the $^{13}C/^{12}C$, $^{18}O/^{16}O$ and $^{17}O/^{16}O$ isotope ratios, from the lower to the upper atmosphere. However, in practice, in the fist Martian year of operations, secondary grating position 13 calibrated data has not been released. This is because of the large number of diffraction orders acquired with this position, which are not sufficiently separated on the detector frame, partially overlapping, and complicating the calibration procedure. Therefore, in this thesis, we use ACS MIR observations made with secondary grating position 4 to constrain the C and O isotopic ratios in CO_2.

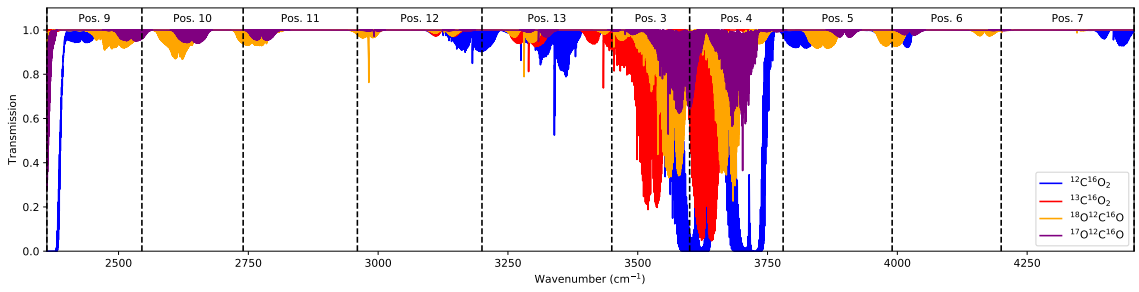

Figure 3.5: Synthetic spectrum relevant for Martian conditions, covering the full spectral range of ACS MIR, with an instrument lineshape described by a Gaussian function with a FWHM of 0.15 cm^{-1}. The contribution from the CO_2 isotopes is shown, following the colours in the legend.

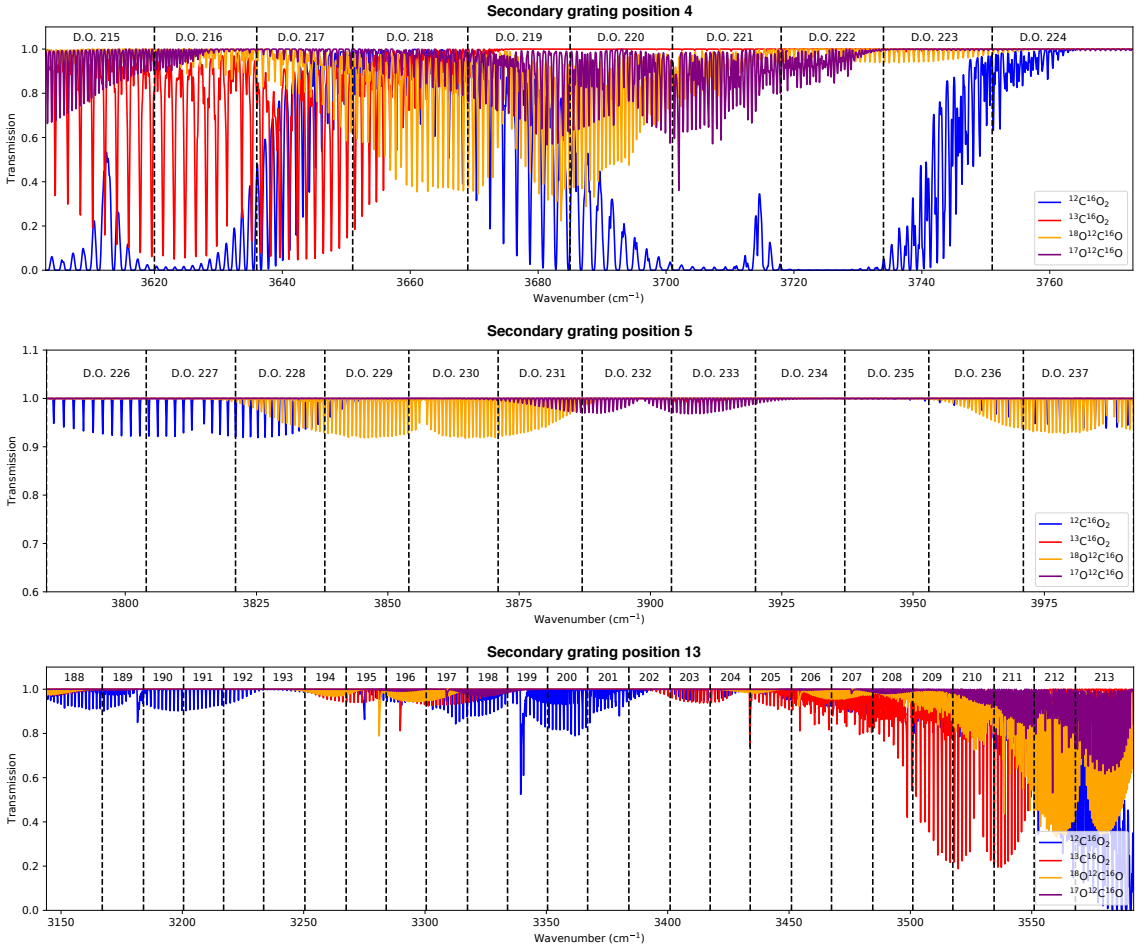

Figure 3.6: Synthetic spectrum relevant for Martian conditions, in the spectral range covered by ACS MIR when operating in secondary grating positions 4, 5 and 13, with an instrument lineshape described by a Gaussian function with a FWHM of 0.15 cm^{-1}. The contribution from the CO_2 isotopes is shown, following the colours in the legend. The spectral coverage of each of the diffraction orders observed with each secondary grating position is also indicated in the figure.

3.3 NEMESIS retrieval algorithm

The main purpose of any retrieval algorithm is to solve the inverse problem, which consists in calculating the set of atmospheric parameters that provides the best fit to the observational data, in our case the transmission spectra. NEMESIS uses the non-linear optimal estimator formalism, which minimises the difference between the modelled and measured spectra, subject to a minimum departure from an *a priori* state of the atmosphere, by minimizing the cost function

$$\phi = (\mathbf{y}_m - \mathbf{y}_n)^T \mathbf{S}_\epsilon^{-1} (\mathbf{y}_m - \mathbf{y}_n) + (\mathbf{x}_n - \mathbf{x}_0)^T \mathbf{S}_x^{-1} (\mathbf{x}_n - \mathbf{x}_0) \tag{3.3.1}$$

where $\mathbf{y}_m$ is the measured spectrum, $\mathbf{y}_n$ is the synthetic spectrum calculated using the forward model, $\mathbf{x}_n$ is the state vector, which includes the atmospheric parameters to be retrieved, $\mathbf{S}_\epsilon$ is the measurement covariance matrix, $\mathbf{x}_0$ is the *a priori* state vector and $\mathbf{S}_x$ is the *a priori* covariance matrix.

For atmospheric sounding in the Earth's atmosphere, climatology provides good statistics about the *a priori* state vector and covariance matrix. However, for planetary atmospheres no such statistical record exists, and in that case the diagonal elements of the *a priori* covariance matrix are set to the square of the estimated errors in the *a priori* state vector. In the case of retrieving continuous vertical profiles, the values at different altitudes are assumed to be correlated, and the off-diagonal terms of $\mathbf{S}_x$ are then set to follow

$$S_{ij} = \sqrt{S_{ii} S_{jj}} \cdot \exp\left(-\frac{|\ln p_i / p_j|}{L_c} \right) \tag{3.3.2}$$

where p_i represents the pressure at the ith level and L_c is the correlation length, equivalent to the number of scale heights over which the continuous profile is assumed to be correlated (Rodgers, 2000).

The retrieval procedure NEMESIS applies to minimise the cost function in equation 3.3.1 is to calculate the state vector in the next iteration as

$$\mathbf{x}_{n+1} = \mathbf{x}_0 + \mathbf{S}_x \mathbf{K}_n^T (\mathbf{K}_n \mathbf{S}_x \mathbf{K}_n^T + \mathbf{S}_\epsilon)^{-1} (\mathbf{y}_m - \mathbf{y}_n - \mathbf{K}_n (\mathbf{x}_0 - \mathbf{x}_n)) \tag{3.3.3}$$

where $\mathbf{K}_n$ is the Jacobian matrix at the nth iteration, which represents the derivatives of transmission spectra at each wavenumber with respect to each of the elements in the state vector. However, the convergence of the retrieval using equation 3.3.3 can be unstable due to the great variability of $\mathbf{K}_n$ over iterations. Instead, NEMESIS uses a scheme based on the Marquardt–Levenberg principal, in which the state vector at the next iteration is modified so that it follows

$$\mathbf{x}'_{n+1} = \mathbf{x}_n + \frac{\mathbf{x}_{n+1} - \mathbf{x}_n}{1 + \lambda}, \tag{3.3.4}$$

where λ is initially set to 1. If the spectrum calculated using $\mathbf{x}'_{n+1}$ reduces the cost function in equation 3.3.1, then $\mathbf{x}'_{n+1}$ is used as $\mathbf{x}_n$ in the next iteration, and λ is multiplied by 0.3. In the opposite case, in which $\mathbf{x}'_{n+1}$ actually increases the cost function, then $\mathbf{x}_n$ is kept and the value of λ is multiplied by 10. As the code converges, $\lambda \longrightarrow 0$ and $\mathbf{x}_n$ tends to the optimal estimate.

The error in the optimal estimate is estimated to be the result of two main contributions. The first contribution is the smoothing error $\mathbf{S}_s$, which can be regarded as the effect in which the observing system smooths the profile. In such a case, the retrieval can be regarded as an estimate of the smoothed state rather than an estimate of the true state, or what is equivalent, an estimate of the true state, but with an error contribution due to smoothing (Rodgers, 2000). This contribution to the retrieved error can be calculated as:

$$\mathbf{S}_s = (\mathbf{K}^T\mathbf{S}_\epsilon^{-1}\mathbf{K} + \mathbf{S}_x^{-1})^{-1}\mathbf{S}_x^{-1}(\mathbf{K}^T\mathbf{S}_\epsilon^{-1}\mathbf{K} + \mathbf{S}_x^{-1})^{-1}. \tag{3.3.5}$$

The second contribution to the retrieved uncertainty comes from the propagation of the measurement error to the state vector. The covariance matrix of the retrieval noise can be calculated as

$$\mathbf{S}_m = (\mathbf{K}^T\mathbf{S}_\epsilon^{-1}\mathbf{K} + \mathbf{S}_x^{-1})^{-1}\mathbf{K}^T\mathbf{S}_\epsilon^{-1}\mathbf{K}(\mathbf{K}^T\mathbf{S}_\epsilon^{-1}\mathbf{K} + \mathbf{S}_x^{-1})^{-1}. \tag{3.3.6}$$

In NEMESIS, the measurement error covariance matrix $\mathbf{S}_\epsilon$ is assumed diagonal, with each of the diagonal elements corresponding to the measured instrument noise equivalent transmission units. In addition, NEMESIS also allows the introduction of a forward modelling

error (e.g., can be used to incorporate uncertainties in the line databases) to the measurement error covariance matrix, to set how well we think we can fit the spectra.

These two main contributions form the total retrieved uncertainty in the state vector, which is given by

$$\mathbf{S}_t = \mathbf{S}_m + \mathbf{S}_s = (\mathbf{K}^T \mathbf{S}_\epsilon^{-1} \mathbf{K} + \mathbf{S}_x^{-1}). \tag{3.3.7}$$

3.4 Retrieval scheme for ACS MIR observations

Previous sections have dealt with the theory of radiative transfer in solar occultations and the optimal estimation formalism, as well as an overview of the most suitable grating positions of the ACS MIR spectrometer to perform isotope studies. In this section, we talk about the specific retrieval scheme applied to ACS MIR solar occultation measurements.

In principle, isotope ratios can be constrained by measuring the equivalent width of an absorption line for each isotopologue, and calculating the ratio, taking into account the line strengths of each of the lines. This approach is convenient because of a number of reasons: it requires more simple calculations than a full radiative transfer computation; the equivalent width is not influenced by inaccurate estimations of the line broadening parameters (e.g. Doppler and pressure broadening), and the instrument line shape. However, in practice, this approach is difficult to implement because of two main reasons: lack of a substantial amount of absorption lines not coincident with lines of other species; accurate calculations of the equivalent width require an accurate estimation of the temperature field, as the line strength of any absorption line depends on temperature (see equation 3.1.4), which requires a full retrieval algorithm.

In this project, we use a full radiative transfer algorithm and a two-step retrieval scheme, first retrieving the pressure and temperature vertical profiles, and then the volume mixing ratio profiles for the different isotopologues, which allow the calculation of the isotope ratios. In addition, the instrument lineshape is also retrieved, due to the need of a complex parameterisation required to model the doubling of the absorption lines (see section 2.2). In this section, we first explain in detail the parameterisation of all variables retrieved from

the spectra, which are applicable to any ACS MIR retrieval. Finally, we discuss the error quantification in section 3.4.5.

3.4.1 Retrievals of pressure and temperature profiles

Retrieving vertical profiles of atmospheric temperature and pressure is not only important for our purposes to understand how the isotopic ratios vary in context with other parameters, but also it is essential to retrieve accurately the gaseous number densities, given that the strength of some absorption lines is very dependent on the temperature (see equation 3.1.4). Retrieving vertical profiles of temperature in the atmosphere from solar occultation measurements is not straightforward, especially considering that at the spectral region covered by ACS MIR, atmospheric thermal emission is not observed. For this purpose, there are two main approaches that can be applied.

The first approach exploits the dependence with temperature of the absorption lines within a rotational band of CO_2. In a rotational band, each absorption line corresponds to a rotational transition J, and the line strength is dependent on the temperature, as expressed in equation 3.1.4. In particular, if the temperature of the gas changes, the maximum absorption in the rotational bands will be shifted. Therefore, evaluating the relative absorption of the lines within a rotational band might allow us to simultaneously retrieve temperature and gas density. Mahieux et al. (2010) applied this approach for the retrieval of high-altitude (70 to 170 km) temperature profiles in the Venusian atmosphere using the SOIR instrument on Venus Express. However, this approach did not get the retrieval to converge due to the modulation that the AOTF bandpass function created on the measured spectrum, which obscured the dependency of the absorption at different lines on temperature (Mahieux et al., 2012).

The second approach, which is the one we establish for our retrieval scheme, is based on the assumption of a well-known CO_2 mixing ratio, and the hydrostatic relation between density and pressure. This technique was applied in stellar occultation observations using SPICAM on Mars Express (Quémerais et al., 2006; Montmessin et al., 2006b; Forget et al., 2009). In those analyses, the CO_2 absorption is used to retrieve a vertical profile of CO_2 partial number density $n_{CO_2}(z)$. Then, assuming a known profile of CO_2 volume mixing ratio $\mathrm{VMR}_{CO_2}(z)$ the pressure and temperature can be estimated using

$$n(z) = n_{CO_2}(Z)/\mathrm{VMR}_{CO_2}(z) \tag{3.4.1}$$

$$dP(z) = -\rho(z) \cdot g(z) \cdot dz = -n(z) \cdot M(z) \cdot g(z) \cdot dz \tag{3.4.2}$$

$$P(z) = P(z_{max}) + \int_z^{z_{max}} n(\bar{z}) \cdot M(\bar{z}) \cdot g(\bar{z}) \cdot d\bar{z} \tag{3.4.3}$$

$$T(z) = \frac{P(z)}{n(z)k_B} \tag{3.4.4}$$

where P is the pressure, T is the temperature, k_B is the Boltzmann constant ($k_B = 1.3806 \times 10^{-23}$ J/K) and M is the molecular mass of the atmosphere, which is estimated from the Mars Climate Database (MCD).

NEMESIS does not allow direct retrievals on number density, but it rather calculates the densities from the pressure and temperature using the ideal gas law in equation 3.4.4. Instead, the retrieval scheme we adopt is to retrieve a continuous profile of temperature $T(z)$, and the pressure at a given tangent height $P(z_r)$. Then the pressure levels at all heights $P(z)$ are computed assuming hydrostatic equilibrium using

$$P(z) = P(z_r) \cdot \exp\left(-\int_{z_r}^{z} \frac{g(\bar{z})M(\bar{z})}{T(\bar{z})k_B} d\bar{z}\right). \tag{3.4.5}$$

This retrieval scheme has the advantage of updating the temperature field in each iteration as opposed to the methods used for SPICAM (e.g. Quémerais et al. (2006); Montmessin et al. (2006b)), which do not change the temperature field during the retrieval, and which might yield systematic correlations between the assumed temperature and the retrieved densities. In addition, the retrieval of temperature and pressure profiles from the hydrostatic equilibrium assumption has the advantage of requiring fewer spectral points than the retrieval from the temperature dependence of the absorption lines, which require the analysis of several absorption lines. On the other hand, the adopted approach has the disadvantage of requiring a good knowledge of the CO_2 volume mixing ratio profile. While in the lower atmosphere the volume mixing ratio of CO_2 is accurately estimated by models, like the Mars Climate Database, at high altitudes the CO_2 mixing ratio decreases as the molecules are photodissociated by UV photons, which might produce variations not captured by the average climatology estimated

with models (see Figure 1.5).

The convergence of this retrieval parameterisation was tested using synthetic retrievals. Forward models were generated for different scenarios of pressure and temperature, using a set of random parameters from the MCD, and random noise were added to the spectra considering a signal-to-noise ratio (SNR) of 1000. Then, these synthetic spectra were retrieved using the same *a priori* state vector. The results from these tests were satisfactory, showing good convergence within five iterations, and retrieving the vertical profiles used to generate the synthetic spectra. In addition, a validation of the retrieved temperature and pressure profiles from ACS MIR spectra has been performed by comparing them with those simultaneously retrieved by Fedorova et al. (2020b) using measurements by ACS NIR, although this comparison is presented in Chapter 5.

3.4.2 Retrievals of gaseous volume mixing ratios profiles

The second step of the retrieval scheme we adopt is to retrieve the gas abundances once the temperature and pressure have been fixed, and therefore the total number density $n(z)$ is assumed to be known. The absorption in each line allows the retrieval of vertical profiles of number density for each gas $n_{gas}(z)$, which in turn allows the retrieval of the volume mixing ratio profiles using

$$\mathrm{VMR}_{gas}(z) = \frac{n_{gas}(z)}{n(z)}. \tag{3.4.6}$$

Similarly as performed for the retrieval of pressure and temperature profiles, the convergence of the retrieval of volume mixing ratio profiles was verified using synthetic spectra, generated using random input parameters for H_2O and CH_4 vertical profiles. Although the convergence was tested for these two gases, the retrieval scheme is analogous for other gases, and the results are therefore applicable for the retrieval of other trace gases or isotopologues in the Martian atmosphere.

Once the VMR profiles from different isotopologues are retrieved, the isotope ratios in H_2O and CO_2 may be derived considering the total number of isotopes in the species. For example, the D/H and $^{18}O/^{16}O$ isotopic ratios in water vapour can be calculated as

$$\mathrm{D/H} = \frac{\mathrm{D\ from\ HD^{16}O}}{\mathrm{H\ from\ HD^{16}O + H\ from\ H_2^{16}O}} = \frac{[\mathrm{HD^{16}O}]}{[\mathrm{HD^{16}O}] + 2[\mathrm{H_2^{16}O}]} \approx \frac{[\mathrm{HD^{16}O}]}{2[\mathrm{H_2^{16}O}]}, \tag{3.4.7}$$

$$^{18}\mathrm{O}/^{16}\mathrm{O} = \frac{^{18}\mathrm{O\ from\ H_2^{18}O}}{^{16}\mathrm{O\ from\ H_2^{16}O} + {}^{16}\mathrm{O\ from\ H_2^{16}O}} = \frac{[\mathrm{H_2^{18}O}]}{[\mathrm{H_2^{18}O}] + [\mathrm{H_2^{16}O}]} \approx \frac{[\mathrm{H_2^{18}O}]}{[\mathrm{H_2^{16}O}]}, \tag{3.4.8}$$

where $[X]$ represents the isotopologues' volume mixing ratio. The isotopic ratios in carbon dioxide can be calculated analogously, taking into account the number of each of the atoms within the molecule. The corresponding uncertainties in the measured isotopic ratios can be calculated taking into account the uncertainties of each of the retrieved isotopologues. For example, the uncertainty of the D/H ratio can estimated as

$$\sigma_{\mathrm{D/H}} = \mathrm{D/H} \cdot \sqrt{\left(\frac{\sigma_{[\mathrm{HD^{16}O}]}}{[\mathrm{HD^{16}O}]}\right)^2 + \left(\frac{\sigma_{[\mathrm{H_2^{16}O}]}}{[\mathrm{H_2^{16}O}]}\right)^2}, \tag{3.4.9}$$

where $\sigma_{[\mathrm{HD^{16}O}]}$ and $\sigma_{[\mathrm{H_2^{16}O}]}$ are the uncertainties associated with the measurements of $\mathrm{HD^{16}O}$ and $\mathrm{H_2^{16}O}$ respectively. The procedure by which these uncertainties are calculated is explained in detail in section 3.4.5.

3.4.3 Retrievals of the aerosol opacity

Apart from the absorption of the gaseous species, which allows the retrieval of the pressure, temperature and gaseous mixing ratio profiles, aerosols suspended in the Martian atmosphere will also contribute to the removal of photons from the light beam. NEMESIS allows the calculation of aerosol extinction coefficients using Mie Theory, which requires information about the complex refractive indices as an input. Figure 3.7 shows the line-of-sight opacity of dust and water ice particles assuming the opacity is $\tau = 1$ at 3500 $\mathrm{cm^{-1}}$, and using the refractive indices of Wolff et al. (2006) and Warren and Brandt (2008) for dust and water ice particles, respectively. The analysis of the spectra obtained with secondary grating positions 12, 13 and 3 allows the retrieval of and differentiation between water ice and dust particles (Stcherbinine et al., 2020). However, the analysis of aerosol populations is much better constrained using TIRVIM, which provides measurements with lower spectral resolution than MIR, but in a much broader spectral range (1.7 - 17 μm) (Luginin et al., 2020).

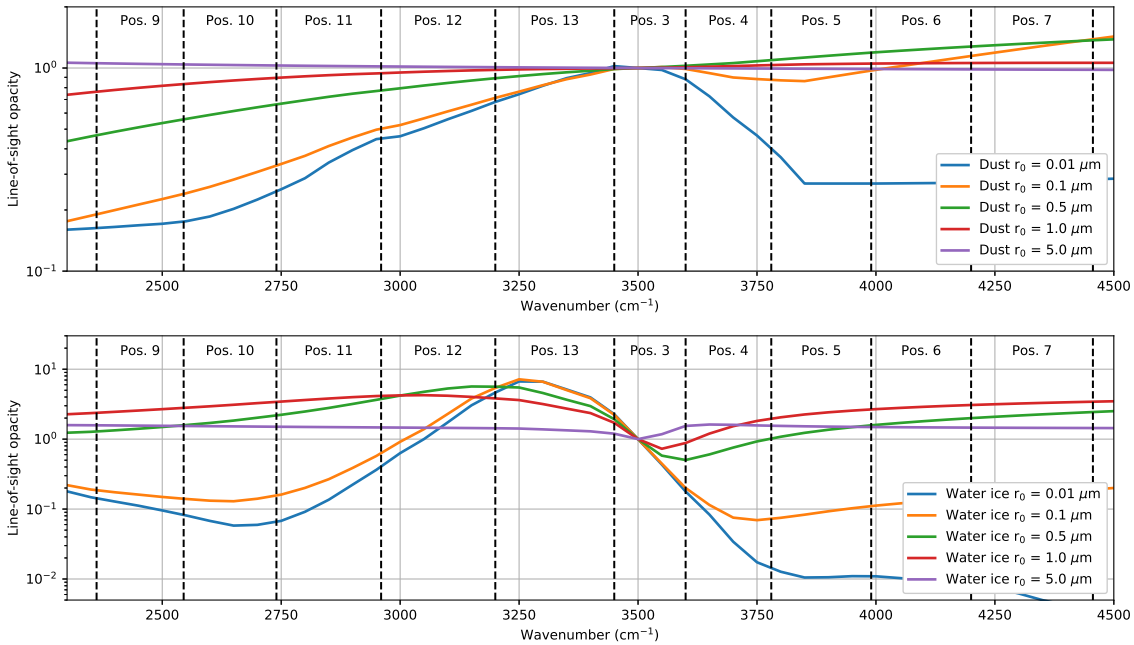

Figure 3.7: Dust (top) and water ice (bottom) line-of-sight opacity within the spectral range covered by ACS MIR assuming the dust opacity at 3500 cm^{-1} is $\tau = 1$. The different colours represent the opacity of different particle size distributions, modelled using a log-normal distribution $f(r) = \frac{1}{r\sigma\sqrt{2\pi}} \exp\left(-\frac{(\ln r - \ln \mu)^2}{2\sigma^2}\right)$, with $\sigma^2 = 0.25$ and μ given by the numbers in the legend (r_0). The spectral range covered by each of ACS MIR's secondary grating positions is also highlighted.

In principle, NEMESIS allows the retrieval of vertical profiles of aerosol density as well as the particle size distributions. However, such a study is out of the scope of this thesis, and we use a much simpler parameterisation of the aerosol contribution instead. The aerosol extinction in this thesis is retrieved by fitting the aerosol line-of-sight opacity at a given wavenumber $\tau(\nu_0)$ and assuming a linear relation with the wavenumbers given by

$$\tau(\nu) = \tau(\nu_0) + b \cdot (\nu - \nu_0), \tag{3.4.10}$$

where b is the slope of the function. The linear relation between the aerosol opacity at different wavenumbers is valid as long as the spectral range of the measurement is narrow enough not to include non-linear spectral features by particles. In the specific case of this thesis, all spectral windows used to retrieve the isotopic composition of CO_2 and H_2O from ACS MIR spectra only cover a few wavenumbers (<10 cm^{-1}) and can therefore be accurately modelled using this parameterisation.

3.4.4 Retrievals of the instrument line shape

Apart from the retrieval of the atmospheric parameters, which are of most interest for the purposes of this thesis, the instrument line shape (ILS) is also retrieved in order to compensate for the doubling of the absorption lines, as explained in section 2.2. In this work the spectra are fitted using an ILS consisting of a superposition of two Gaussian functions in order to model the doubling of the absorption lines. The relative depth of the two Gaussians varies depending on the selected row on the detector frame, with wavenumber, and in different observations. For each occultation and spectral window, the parameters describing the ILS are fitted using the following assumptions. First of all, the full width at half maximum (FWHM) of the two Gaussians is the same, and is constant in wavelength units. Secondly, the relative offset of the centre of the two Gaussians does not vary with wavenumber. In the third place, the relative depth of the two Gaussians is linearly varying with wavenumber. Lastly, the same parameters apply to all acquisitions during one solar occultation.

Figure 3.8 shows an example of the results from the ILS fit in one ACS MIR solar occultation observation made with secondary grating position 4. In particular, we show the results from the best fits obtained when using the spectra from the detector rows corresponding to the slit centre and slit edge. It is shown that the parameterisation used to model the ILS provides good convergence, allowing to perform an accurate fit of the measured data. In particular, this approach provides accurate fits of the data for every row within the detector frame, from the slit centre, where the best fit is obtained with a double-Gaussian ILS with nearly equal amplitudes, to the slit edge, where the second Gaussian is just about 10% of the main one.

In principle, one could investigate a parameterisation to describe the behaviour of the spectral resolution and doubling throughout the detector frame, in order to not fit the ILS in every occultation, but fix it prior to the retrieval instead. However, this is not possible due to the varying behaviour of the ILS with time. Figure 3.9 shows the evolution of the fitted ILS FWHM from the start of the science phase in March 2018 to October 2020. It is shown that the spectral resolution of the instrument has been slightly worsening with time, with the FWHM of approximately 0.16 cm^{-1} ($\lambda/\Delta\lambda \sim 23500$) at the start of the science phase increasing towards 0.18 cm^{-1} ($\lambda/\Delta\lambda \sim 21000$) in the observations made in October

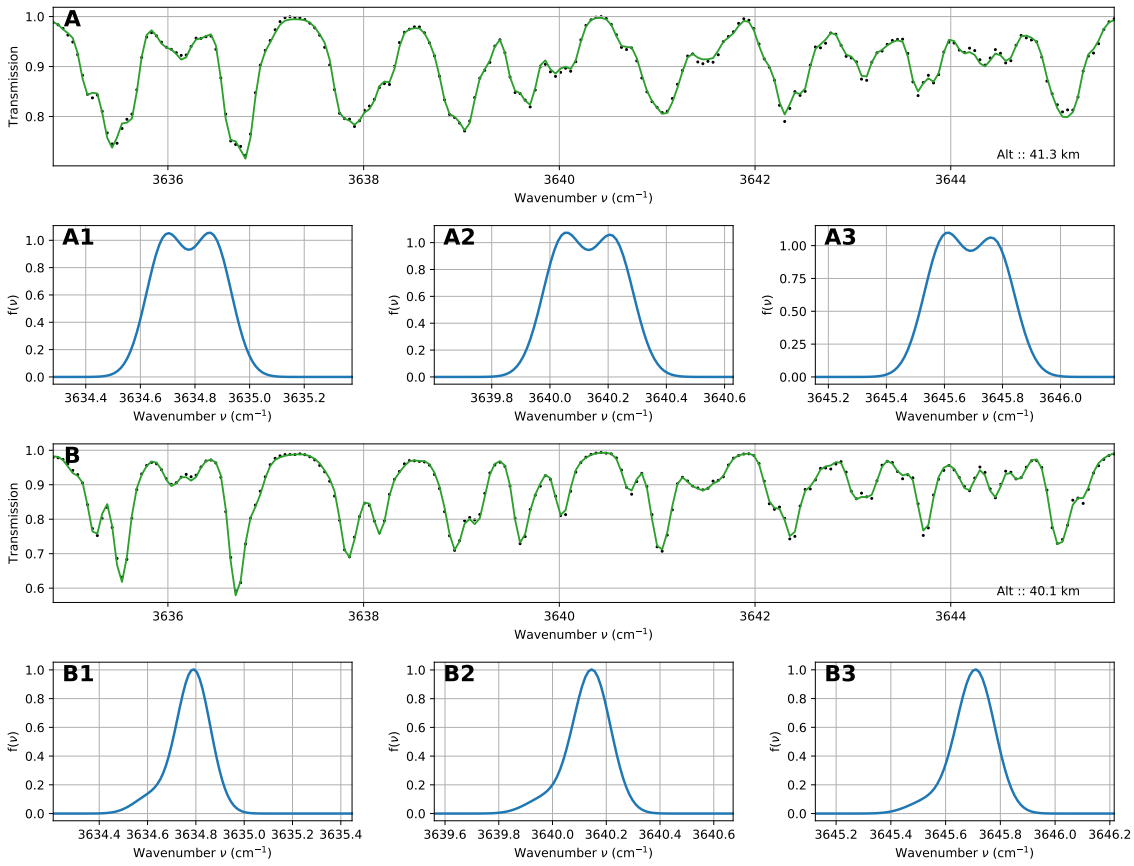

Figure 3.8: ACS MIR transmission spectrum for diffraction order 217 measured in the solar occultation made using secondary grating position 4 in orbit 1849. Panels A and B show the measured transmission spectra and best fit to the data when using the detector rows corresponding to the slit centre (A) and slit edge (B). The rest of the panels show the ILS function fitted at the first (1), middle (2) and last (3) spectral points of the measurement, for both the slit centre and edge.

2020. This varying behaviour of the ILS requires a fitting approach that enables an accurate description of the instrument function for any given observation.

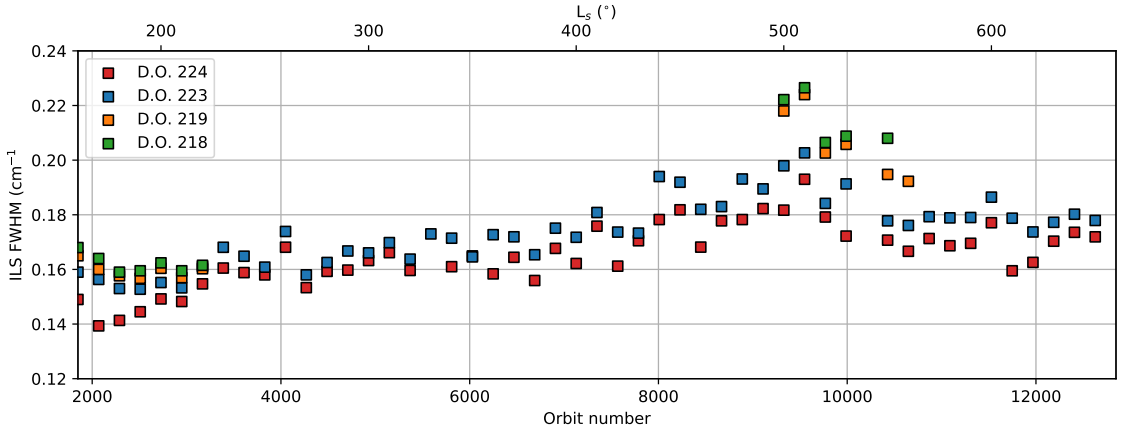

Figure 3.9: Evolution of the FWHM of the ACS MIR instrument function from the start of the science operations in March 2018 until October 2020. The different colours show the results of the fitted ILS FWHM for the spectral windows in diffraction orders 218, 219, 223 and 224 in secondary grating position 4, binned into points with 10° of solar longitude.

3.4.5 Error analysis

The optimal estimation formalism works on the basis of finding a solution that replicates the measured spectrum with a solution that is closest to an *a priori* state of the atmosphere. The *a priori* state vector is accompanied with its covariance matrix $\mathbf{S}_x$, which represents the uncertainty in the system prior to the retrieval. The retrieved uncertainties are expressed on the basis of this matrix, given by

$$\mathbf{S}_t = (\mathbf{K}^T \mathbf{S}_\epsilon^{-1} \mathbf{K} + \mathbf{S}_x^{-1})^{-1}, \tag{3.4.11}$$

where $\mathbf{S}_t$ is the retrieved covariance matrix, $\mathbf{S}_\epsilon$ is the measurement covariance matrix, representing the uncertainty in the spectra, and $\mathbf{K}$ is the Jacobian matrix (i.e., the rate of change of the transmission spectra with respect to each element in the state vector). The noise in the transmission spectra is adjusted, after a first retrieval, to be consistent with the magnitude of the observed residuals (the difference between the observed and modelled spectra). Then, the retrieval is repeated using this adjusted measurement uncertainty.

In the case in which there is no information contained in the spectra for some element of the state vector (i.e., $\mathbf{K}^T \mathbf{S}_\epsilon^{-1} \mathbf{K} = 0$), then the retrieved uncertainty would be equal to the

a priori. This approach might be misleading in some cases. If, for example, one specifies a 20% uncertainty in the *a priori* profile, then the retrieved profile will have an uncertainty of 20% even at altitudes where the observation provides no constraint. One solution would be to increase the uncertainties in the *a priori*. However, when not enough constraint is applied in the *a priori*, the retrieval might get *ill-conditioned*, leading to highly unrealistic vertical oscillations in the retrieved profiles (Irwin et al., 2008).

In order to mitigate the effect of the *a priori* uncertainty in the retrieval errors, we introduce a correcting factor. This factor, applied before by Irwin et al. (2019), is given by

$$\sigma(i) = \frac{1}{\sqrt{\frac{1}{\mathbf{S}_t(i,i)} - \frac{1}{\mathbf{S}_x(i,i)}}}, \tag{3.4.12}$$

where $\sigma(i)$ is the corrected uncertainty of the ith element of the state vector. On the basis of retrievals on synthetic spectra, this approach is found to provide a more reliable estimation of the uncertainties (i.e., those that reflect the true uncertainty with respect to the state vector used to generate the synthetic spectra), and provides a reliable representation of where the retrieval is sensitive to the observation.

This approach provides a reliable representation of the impact of random errors in the retrieved profiles. However, it must be noted that some of the uncertainties in the system might be systematic (e.g., spectroscopy or doubling of the absorption lines). Systematic uncertainties are generally more difficult to characterise than random errors, and can drive the retrieved estimate away from the true solution always in the same direction, as opposed to random errors, which generate discrepancies around the true value. For example, if a retrieval is performed looking at a single absorption line, and the line strength of the line is overestimated in the spectroscopic database, the inversion of the spectra will always yield a lower atmospheric abundance than there actually is, leading to an unrealistic solution which is not accurately represented in the retrieved covariance matrix.

In order to mitigate the effect of the systematic uncertainties, we opt for combining multiple retrievals performed independently in different spectral windows spreading in different diffraction orders, if possible, and in different rows from the detector frame. The use of several

spectral windows allows the use of different absorption lines for the different species, minimising the impact of spectroscopic uncertainties. The use of several rows from the detector frame for a given spectral window allows the characterisation of the uncertainty in the ILS and the doubling of the absorption lines, which vary from the slit centre to the slit edge (see Figure 3.8).

The retrieved vertical profiles from each of the spectral windows or detector rows can be combined using a weighted average, in which the weights are given by the inverse of the variance at each altitude ($\sigma(\mathrm{z})^{-2}$), which is calculated using equation 3.4.12. Figure 3.10 shows an example of the retrieved $H_2^{16}O$ volume mixing ratio vertical profiles in different spectral windows from an ACS MIR solar occultation observation made with secondary grating position 5 in orbit 2520. Standard error propagation of the retrieved uncertainties in the averaged vertical profile (see panel A in Figure 3.10) does not appear to reflect the true uncertainty of the retrieval, as it is smaller than the variation of the retrieved profiles in each spectral window. In contrast, the uncertainty shown in panel B is calculated as the weighted standard deviation of all profiles. This approach appears to give a better representation of the retrieved uncertainty. Nevertheless, it underestimates the uncertainties in regions where there is no information in the spectra, as they all tend to the *a priori* state. Error bars shown in panel C show the combination of the two previous approaches, selecting the one that provides a higher value. This approach may be analogously applied for the combination of retrieved profiles from different detector rows. We consider this method to provide a more accurate representation of the true uncertainty of the retrieval, reflecting the systematic uncertainties from the variation of the several spectral windows, as well as the lack information in the spectra.

3.5 Summary

In the previous chapter, we introduced the main characteristics of ACS MIR, explaining the observational characteristics of the solar occultation observations as well as the main features of the optical design of the instrument. The optical scheme of ACS MIR was designed to obtain high spectral-resolution measurements in a portion of the spectral range accessed by the instrument.

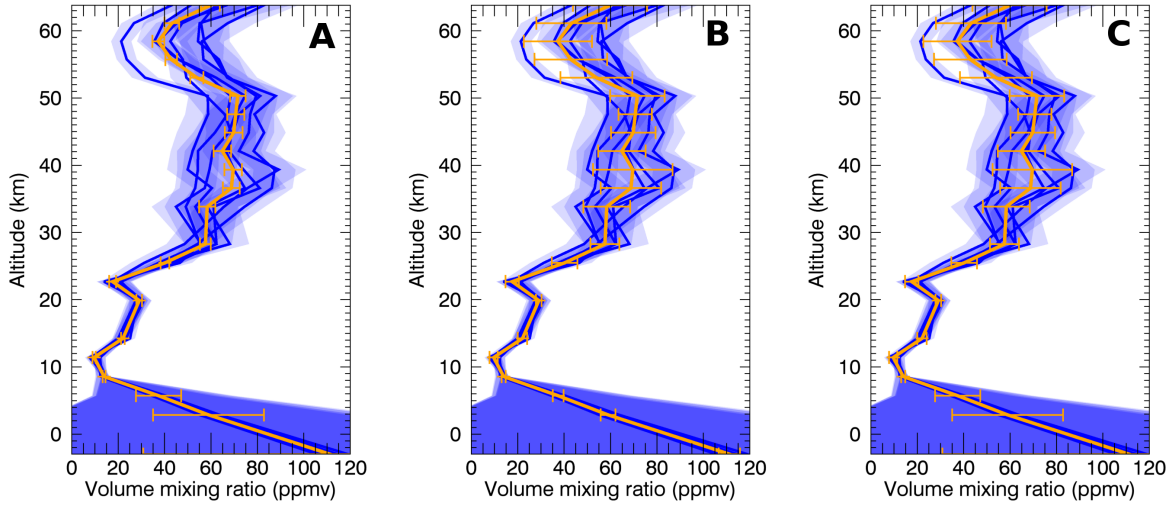

Figure 3.10: Retrieved $H_2^{16}O$ vertical profiles from different spectral windows (blue lines) in the observation performed using secondary grating position 5 during orbit 2520, as well as the weighted-averaged profile (orange line). Uncertainties in the averaged profile in panel A are derived from the propagation of errors from each retrieved profile. Uncertainties in panel B are calculated as the weighted standard deviation from all the profiles. Panel C shows the combination of the two previous panels, selecting the larger of the two methods.

In this chapter, we have provided a detailed explanation of the radiative transfer calculations required to model the ACS MIR measurements. Using the NEMESIS algorithm, we have determined which ACS MIR secondary grating positions are most suitable for the characterisation of the isotopic ratios in H_2O and CO_2. In particular, secondary grating positions 4, 5 and 11 are found to be best for retrieving the isotopic ratios in H_2O, while grating positions 4 and 13 are best for the retrieval of the CO_2 isotope ratios. In addition, we have introduced the optimal estimation retrieval framework utilised by the NEMESIS algorithm, which is used to solve the inverse problem and estimate the atmospheric parameters from the spectral measurements. In particular, we have explained how the NEMESIS algorithm has been adapted for the retrieval of temperature, pressure, gaseous mixing ratios, aerosol line-of-sight opacity, and the instrument line shape from the ACS MIR spectra.

In the next chapters, we explain how this retrieval scheme is applied to the ACS MIR measurements to characterise the isotopic composition of CO_2 and H_2O. Chapter 4 describes an initial analysis of observations made using secondary grating position 5 to constrain, for the first time, the O isotope ratios in H_2O. In order to extend the analysis of the isotopic composition of H_2O to a climatological study and to include the D/H ratio in the retrievals, the analysis of the data in Chapter 5 is switched to secondary grating position 4, which allows

us to constrain the variability of D/H and $^{18}O/^{16}O$ for more than a full Martian year. Finally, a climatological study of the C and O isotopic ratios in CO_2 is presented in Chapter 6 using observations from secondary grating position 4.

Chapter 4

Oxygen isotopic ratios in H_2O from grating position 5

Unlike the D/H ratio, which has been the subject of a large number of observing campaigns, the isotopic composition of oxygen in water vapour has only been constrained at the surface with the Curiosity Rover ($\delta^{18}O = 84 \pm 10$ ‰; Webster et al. (2013)). Although the precision of the observation is good, the contribution from seasonal cycling to this measurement is unknown. Therefore, the measured value might be subject to climatological isotopic fractionation which may occur, for instance, during condensation onto water ice or adsorption and desorption processes on the regolith (see Section 1.1.5.2). The $^{17}O/^{16}O$ isotopic ratio of water vapour in the Martian atmosphere has not been determined to date. Together, both oxygen isotope ratios provide important constraints about the evolution of the oxygen reservoirs on Mars. In particular, the distinct isotopic signature that the different processes leave in the atmospheric reservoir might reveal the nature of the mechanisms that have affected it throughout history (see Section 1.1.5).

In addition, while the present-day D/H ratio is about five times more enriched in deuterium with respect to that of ancient Mars (Usui et al., 2012), evidence of the atmospheric escape into space, the oxygen isotope ratios in both CO_2 and H_2O show a milder enrichment in the heavy isotope. Oxygen, as hydrogen does, escapes from the Martian atmosphere to space, and it is expected to leave the remaining atmosphere enriched in the heavy isotope (Jakosky et al., 2018; Fox and Hać, 2010). This mild enrichment in the oxygen isotopic composition

of the Martian atmosphere is interpreted to be due to the presence of a large reservoir that mitigates the effect of escape of oxygen atoms into space (Jakosky, 1997).

In the present chapter we measure, for the first time, the vertical distribution of the oxygen isotopic composition in water vapour, aiming to confirm the measurements of Webster et al. (2013) of the $^{18}O/^{16}O$ isotopic ratio, and understand how it relates to $^{17}O/^{16}O$, which has never been measured before. We perform this analysis by applying the methodology presented in Chapter 3, which was developed to be applicable for the retrieval of the atmospheric abundance of any gas in the Martian atmosphere, to ACS MIR solar occultation observations, which were introduced in Chapter 2. In particular, we use the observations made using ACS MIR secondary grating position 5, which cover a spectral range between 3789-3987 cm^{-1}.

In the following sections, we explain how the previously introduced measurements and methods are applied to constrain the oxygen isotopic composition of H_2O in the Martian atmosphere. In section 4.1 we provide a detailed overview of the ACS MIR measurements made secondary grating position 5. In section 4.2, we explain how the methods presented in Chapter 3 are applied to the analysis of these data. Finally, in section 4.3 we present the main results of the study and discuss about their implications to our understanding of the evolution of the Martian atmosphere.

The analysis described in this chapter of the thesis has been peer-reviewed and published in *Astronomy & Astrophysics* (Alday et al., 2019). Although that publication has a number of coauthors, all work presented in this chapter was performed by me, except for the calibration of the ACS MIR transmission spectra, which was performed by Lucio Baggio at LATMOS and Alexander Trokhimovskiy at the Space Research Institute (IKI).

4.1 ACS MIR observational dataset

The dataset used in this study is assembled using ACS MIR observations made with secondary grating position 5 during the first months of operations. In particular, eight solar occultation observations are selected from the dataset because of the clarity of the absorption lines of the minor oxygen isotopologues ($H_2^{18}O$ and $H_2^{17}O$), which allows a careful validation of the retrieved profiles and the spectral fits. These observations were made during the first three

months of operations, expanding approximately 50° in L_S and sampling both northern and southern hemispheres, as well as the morning and evening terminators, as shown in Figure 4.1. In addition, Table 4.1 also shows the orbital characteristics of the observations used in this study.

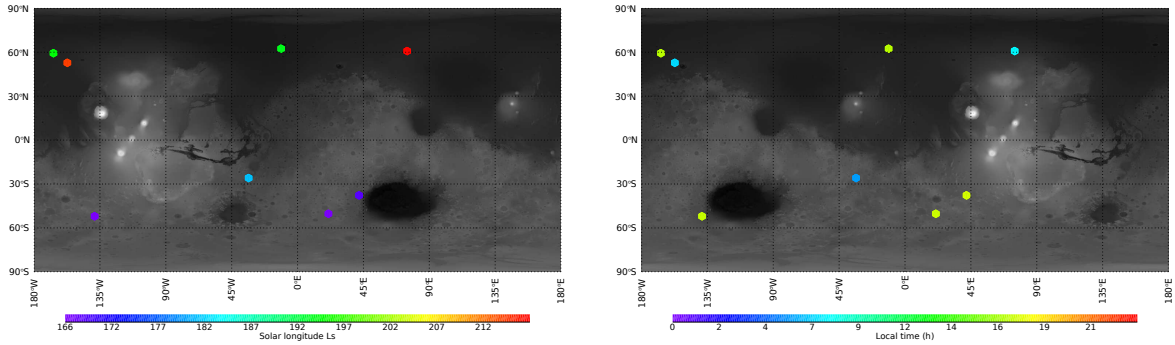

Figure 4.1: Observational coverage of the ACS MIR measurements made with secondary grating position 5 used to constrain the oxygen isotopic composition of water vapour. The two panels show the tangent point of the solar occultations on top of a map of Mars, with the colour of the points representing the solar longitude (left) and local time (right) of the observations.

Table 4.1: Orbital parameters for the ACS MIR observations selected for the analysis of the isotopic composition of H_2O from secondary grating position 5.

Orbit	Ingress/Egress	Date (UTC)	Latitude (°)	Longitude (°)	Ls (°)	Local time
1917	Ingress	2018-04-29	-52	-139	167	17
1924	Ingress	2018-04-29	-50	21	167	18
1961	Ingress	2018-05-02	-37	42	169	18
2233	Egress	2018-05-24	-25	-33	181	6
2502	Ingress	2018-06-15	62	-11	194	17
2520	Ingress	2018-06-17	59	-167	195	17
2929	Egress	2018-07-20	53	-157	215	7
2984	Egress	2018-07-25	61	75	218	8

The data from secondary grating position 5 includes twelve diffraction orders (226-237) expanding over a wavenumber range between 3789 and 3987 cm^{-1}. Absorption lines of the main isotopologue of water vapour are observed in all orders, but the clearest lines of the minor oxygen ones are just observed in the uppermost portion of the detector, which corresponds to diffraction orders 226 to 229 (see Section 3.2). Diffraction order 226 includes some of the clearest absorption lines for the minor isotopologues, as well as lines from the main isotopologue of CO_2, which are used for the derivation of the pressure and temperature profiles. Unfortunately, this diffraction order is in the uppermost part of the detector, and part of the

slit for this diffraction order is projected just outside the detector frame (see Figure 4.2) and the full spectral range cannot be accessed for some detector rows. Because of this, the analysis of the data from secondary grating position 5 is performed in the row corresponding to the slit edge, which apart from minimising the effect of the doubled-image, allows the use of diffraction order 226 in the retrieval scheme.

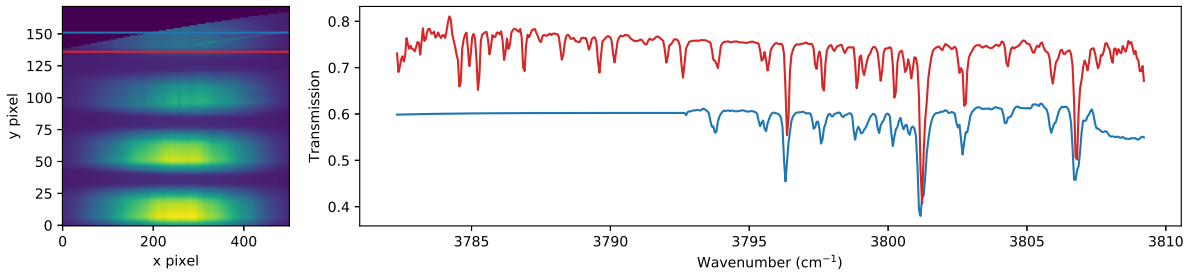

Figure 4.2: Example of the uppermost portion of an ACS MIR detector frame made using secondary grating position 5. The left panel shows an example of the uppermost part of the detector frame made with grating position 5, corresponding to diffraction orders 226 to 229. The right panel shows the measured spectra recorded at the detector rows of diffraction order 226 corresponding to the slit edge and slit centre.

In order to perform the retrievals, seven spectral windows expanding from diffraction orders 226 to 231 are selected, which include absorption lines of the three main oxygen isotopologues in water vapour ($H_2^{16}O$, $H_2^{18}O$ and $H_2^{17}O$) and carbon dioxide (see Figure 4.3). Isotopic signatures in carbon dioxide can also be measured using this secondary grating position, but the profiling of these species is not performed in this chapter, but using observations made with secondary grating position 4 (see Chapter 6).

4.2 Retrieval scheme

The retrieval of the atmospheric parameters from the ACS MIR solar occultation spectral measurements is performed using the scheme presented in Section 3.4 with the NEMESIS retrieval algorithm (Irwin et al., 2008). In particular, the retrieval of the isotopic ratios is performed in two steps. First of all, the volume mixing ratio of the several water isotopologues along with the pressure and temperature profiles are retrieved from the spectral windows in diffraction orders 226, 227 and 228, which include absorption lines of $^{12}C^{16}O_2$ (see Table 4.2). In the second step, the retrieved pressure and temperature profiles are fixed in the reference atmosphere, and the volume mixing ratio profiles of the water vapour isotopologues

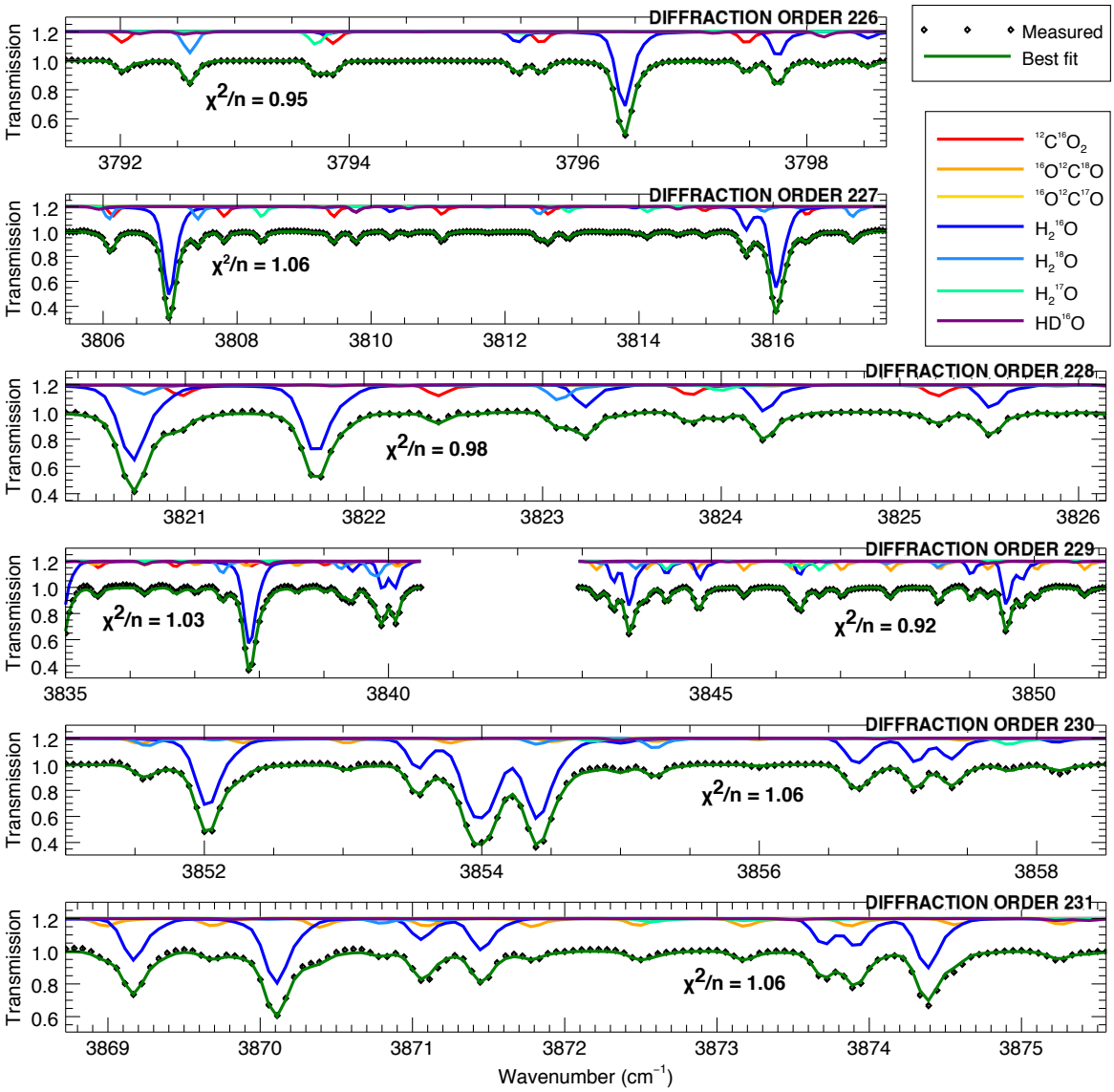

Figure 4.3: ACS MIR normalised transmission spectra obtained at tangent height of 16.8 km above martian ellipsoid in the observation made in orbit 2233, using spectral windows from diffraction orders 226–231. The green line is the best fit to the data, while the coloured lines represent the contribution to the absorption from each gas. The contribution from each gas is shifted by 0.2 for the clarity of the figure.

are retrieved using all spectral windows, including those used in the first step. However, in this case, instead of using profiles from the Mars Climate Database as the *a priori* estimate of the water abundance, the previously retrieved profile of $H_2^{16}O$ in the first step is used, and scaled for the minor isotopologues using the Earth-like fractionation (i.e., $^{18}O/^{16}O$ and $^{17}O/^{16}O$ = 1 VSMOW) at all altitudes.

Table 4.2: Summary of the spectral windows and retrieval scheme used to derive the pressure, temperature and water vapour isotope ratio profiles from secondary grating position 5.

Spectral Window	Diffraction Order	Wavenumber range (cm^{-1})	Retrieved Parameters
1	226	3791.5 - 3798.7	p, T ($^{12}C^{16}O_2$) $H_2^{16}O$, $H_2^{18}O$, $H_2^{17}O$
2	227	3805.4 - 3817.7	p, T ($^{12}C^{16}O_2$) $H_2^{16}O$, $H_2^{18}O$, $H_2^{17}O$
3	228	3820.3 - 3826.2	p, T ($^{12}C^{16}O_2$) $H_2^{16}O$, $H_2^{18}O$
4	229	3835.3 - 3840.5	$H_2^{16}O$, $H_2^{18}O$
5	229	3842.9 - 3851.2	$H_2^{16}O$
6	230	3851.0 - 3858.5	$H_2^{16}O$
7	231	3868.7 - 3875.6	$H_2^{16}O$

This approach, in which the *a priori* estimates of the volume mixing ratio of the different water isotopologues are updated after the first step, has been chosen to minimise errors in the derivation of the isotopic ratios given the nature of the optimal estimation formalism. In this retrieval framework, the algorithm tries to find the parameters that while fitting the data, are closest to the *a priori* estimate (see equation 3.3.1). Water vapour in the Martian atmosphere is highly variable and it might show large departures from model predictions, especially in the presence of dust storms. If the sensitivity of the spectra to different isotopes is very different, the effect of the *a priori* estimate for the retrieval of different species might also be impacted, giving rise to systematic errors in the derivation of the isotope ratios. However, variations of the isotopic ratios in the atmosphere are much milder than those in the water vapour abundance. When updating the *a priori* estimate with the previously retrieved $H_2^{16}O$ abundance, which provides the highest sensitivity of all water isotopes, and consider the minor isotopologues follow Earth-like fractionation, the effect of the *a priori* estimate on the retrieval

is mitigated.

The atmospheric vertical profiles are retrieved from each spectral window along with the parameters defining the instrument lineshape (ILS), following the double Gaussian parameterisation presented in Section 3.4.4. In the particular case of these retrievals, given that the spectra are taken close to the slit edge, where the impact of the doubled-image is minimised, the strength of the second Gaussian function does not typically exceed 25% of the main one (see Figure 4.4). Typical values of the ILS FWHM range from 0.12-0.15 cm^{-1}, which correspond to a spectral power in the range of $\lambda/\Delta\lambda$ = 25000-32000. The application of the double Gaussian parameterisation to define the ILS of ACS MIR was first published in this study (Alday et al., 2019), and has been later applied to other analyses of the ACS MIR observations (e.g., Olsen et al. (2020); Trokhimovskiy et al. (2020)).

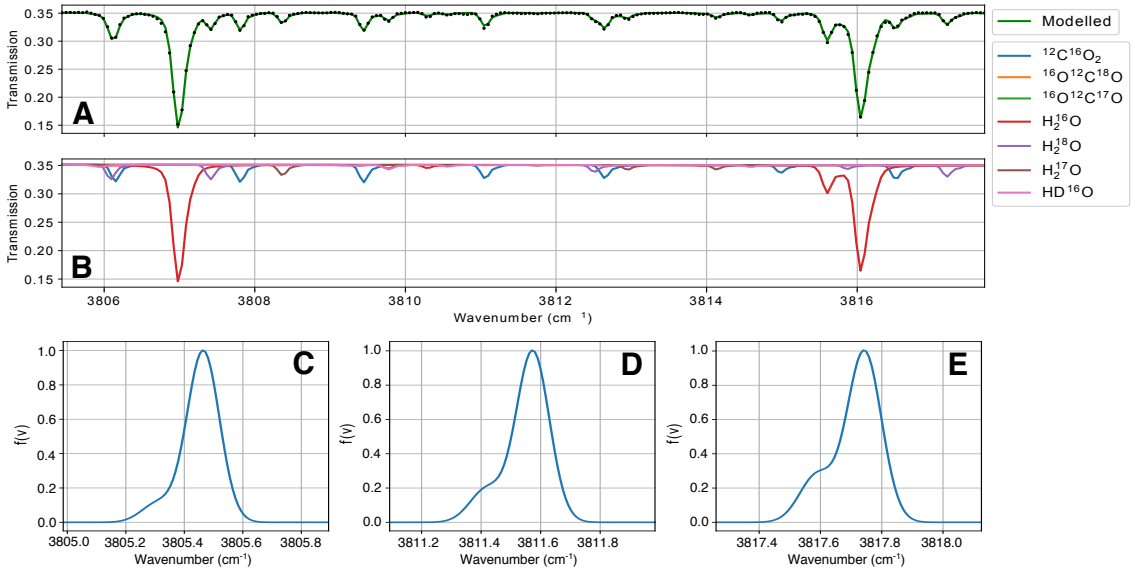

Figure 4.4: ACS MIR transmission spectrum for diffraction order 227 obtained at tangent height of 11.4 km above the martian ellipsoid in the observation made in orbit 2520. (A) Measurement and best fit to the data. (B) Contribution from each gas to the spectrum. (C), (D) and (E) show the ILS function used at the first, middle, and last spectral point of the spectrum.

Once the atmospheric vertical profiles are independently retrieved from each spectral window, they are combined using the procedure presented in Section 3.4.5 (see Figures 4.5 and 3.10). This approach provides a good representation of the true uncertainty of the retrieval, since it not only includes the random uncertainties propagated from the spectra, but also the differences between the retrieved profiles from different spectral windows. Indeed, these differences are in certain instances larger than the uncertainties associated with each of the

individual profiles derived from the measurements errors, suggesting the presence of systematic biases. The source of these systematic uncertainties is unknown, but could be related to imperfections in the calibration pipeline, in the spectroscopic parameters used to model the absorption lines, or uncertainties rising from the simultaneous derivation of the parameters defining the ILS and the atmospheric profiles. We take the dispersion between the independent retrievals as being representative of the systematic uncertainties and providing a realistic estimation of the true uncertainty of the retrieval.

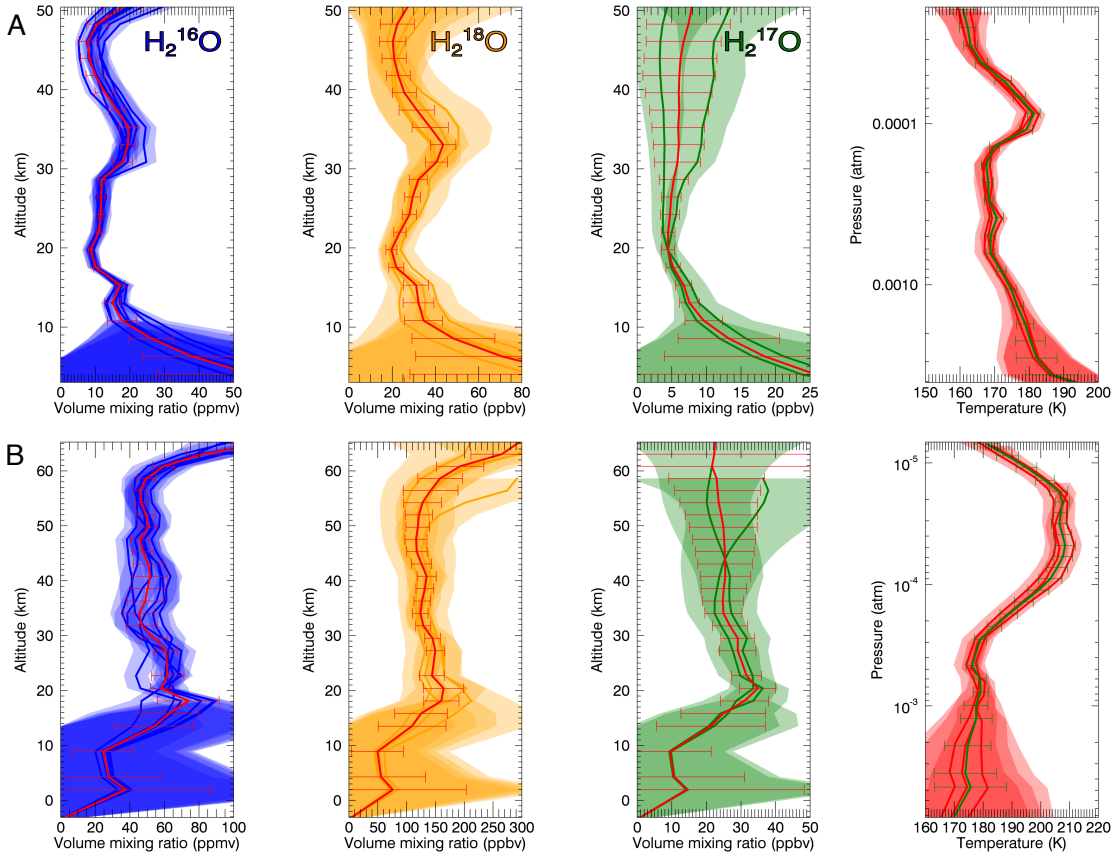

Figure 4.5: Retrieved vertical profiles of temperature and volume mixing ratios of $H_2^{16}O$, $H_2^{18}O$ and $H_2^{17}O$, for the observations made in orbits 1924 (A) and 2929 (B). The retrieved profiles from several spectral windows are shown, as well as the derived averaged profile.

4.3 Results

The retrieval scheme introduced in Section 4.2 is applied to the eight observations made with secondary grating position 5 selected for the characterisation of the oxygen isotopic composition of water vapour in the Martian atmosphere (see Table 4.1). In order to validate

the measurements and methods, the retrieved temperature profiles are compared to those retrieved from the NIR channel on ACS, which performs simultaneous measurements with ACS MIR. The NIR profiles are measured exploiting the temperature dependence of the CO_2 rotational band at 1.57 μm (Fedorova et al., 2020b), which is a different method than the one applied in this work, which exploits the assumption of hydrostatic equilibrium (see Section 3.4.1). In addition, we search for collocated observations made with the Mars Climate Sounder (MCS) onboard Mars Reconnaissance Orbiter (MRO), applying criteria on location ($\pm 1°$ latitude and longitude), local time (± 2 hours), and solar longitude ($\pm 0.5°$). We find one MCS observation (Latitude = 64°; Longitude = 12°W; L_S = 194°; Local time = 15 h) fulfilling the criteria as compared to ACS MIR observation made in orbit 2502 (see Table 4.1). Figure 4.6 shows the comparison between the NIR, MIR and MCS pressure-temperature profiles, exhibiting a good agreement between the different datasets, and increasing the confidence of the measurements and methods.

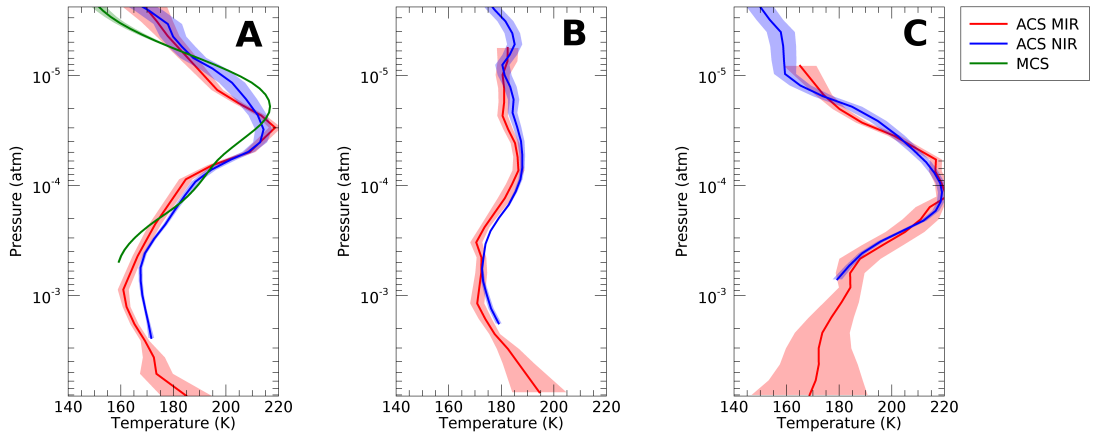

Figure 4.6: Retrieved temperature and pressure profiles measured by the MIR and NIR channels in the solar occultation observations performed in orbits 2502 (A), 2520 (B) and 2984 (C). Panel A also shows the retrieved temperature and pressure profile from one MCS observation made in similar conditions as in ACS orbit 2502 (see text).

The volume mixing ratio profiles of the different isotopologues allow the derivation of the oxygen isotope ratios, which are calculated using $R(^xO) = [H_2^xO]/[H_2^{16}O]$, where ^xO stands for ^{18}O and ^{17}O, and then normalised using Earth's standard isotopic fractionation (see Table 1.3). Figure 4.7 shows the retrieved profiles for all observations in Table 4.1 as well as the resulting isotopic ratios in H_2O. The oxygen isotope composition of water vapour in the Martian atmosphere is generally enriched in the heavy isotope with respect to Earth. Despite

the rather different conditions found in the atmosphere in terms of water abundance and temperature in these eight observations, the retrieved profiles of the oxygen isotope ratios do not appear to show differences greater than the level of uncertainties.

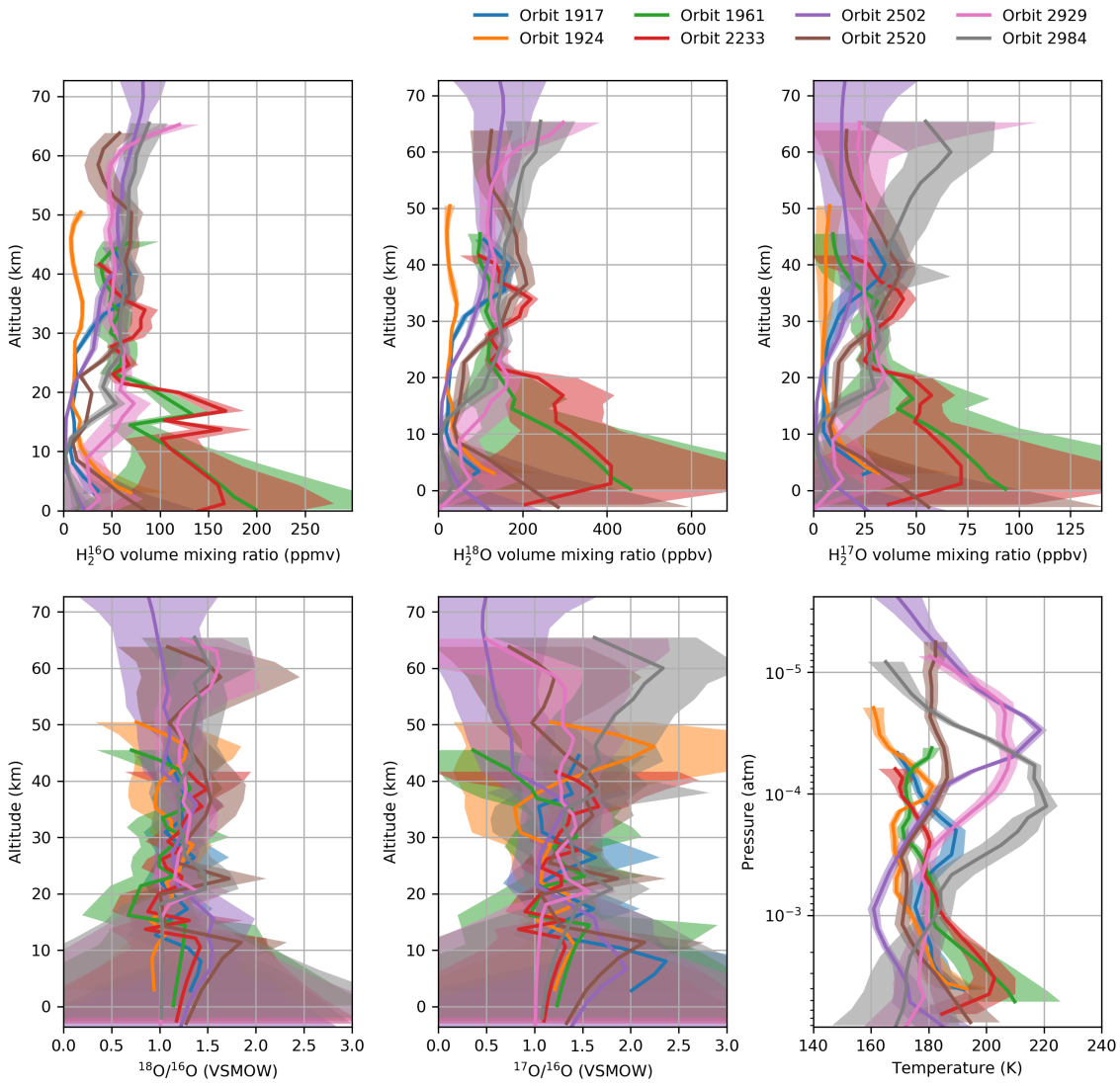

Figure 4.7: Retrieved vertical profiles obtained for each of the processed ACS MIR secondary grating position 5 observations listed in Table 4.1. The isotopic ratios are in units of VSMOW, which represents Earth-like isotopic fractionation.

Spatial, seasonal and vertical variations of the O isotopic ratios in water vapour due to evaporation and condensation processes are expected to follow similar trends as predicted for the D/H ratio, but with a smaller amplitude (Merlivat and Nief, 1967; Majoube, 1970). The amplitude of the variations of the $^{18}O/^{16}O$ ratio with respect to D/H depend on the temperature at which condensation occurs and the impact of kinetic fractionation, but one

may expect these variations not to exceed approximately ∼0.1 VSMOW (see Section 1.1.5.2). Given that condensation-induced fractionation for the oxygen isotopes is mass-dependent, these variations would not exceed ∼0.05 VSMOW for the $^{17}O/^{16}O$ ratio. The magnitude of the observed uncertainties is larger than the expected variations, and therefore does not rule out the possibility of variations due to condensation processes. The largest variations of the isotope ratios are expected to occur during the condensation of the polar caps during the winter season. However, in that case it might be challenging to obtain reliable measurements of the isotope ratios, since the water abundance drops by orders of magnitude during this season, which directly impacts the retrieved uncertainties.

In order to reduce the retrieved uncertainties and get an insight of the overall trends of the ratios, we express all vertical profiles in the same altitude grid, and calculate the weighted average over all analysed observations, as shown in Figure 4.8. Both the $^{18}O/^{16}O$ and $^{17}O/^{16}O$ ratios appear to be relatively constant in the altitude range where ACS MIR is most sensitive. The $^{18}O/^{16}O$ ratio might show a slight enrichment with altitude, but this is within the order of the uncertainties. Assuming the isotope ratios are well mixed, it is possible to calculate an average value for all altitudes, which is $^{18}O/^{16}O = 1.20$ VSMOW and $^{17}O/^{16}O = 1.23$ VSMOW.

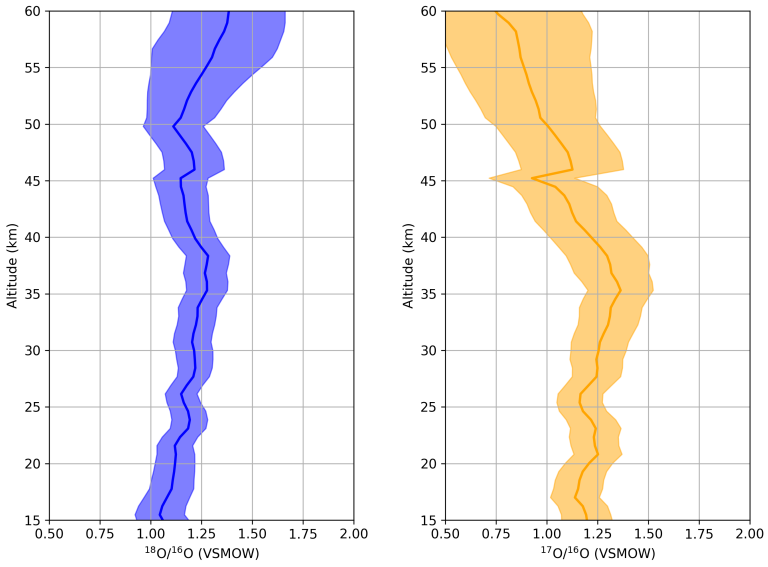

Figure 4.8: Weighted-averaged vertical profiles of the oxygen isotopic ratios in water vapour, with respect to the VSMOW. The shaded areas represent the uncertainties associated to the average profiles, which are calculated using the propagation of errors from the different profiles. Altitudes are defined with respect to the Martian ellipsoid.

In the publication where the work described in this chapter of the thesis was presented (Alday et al., 2019), the uncertainties associated with the averaged values were calculated to be $^{18}O/^{16}O = 1.20 \pm 0.08$ VSMOW and $^{17}O/^{16}O = 1.23 \pm 0.11$ VSMOW, which correspond to the errorbars derived at the most constrained altitude in Figure 4.8. However, in order to be consistent with the methodology applied in Chapters 5 and 6, the uncertainties associated with the average isotopic ratios are here revised. Figure 4.9 shows a histogram of the measured $^{18}O/^{16}O$ and $^{17}O/^{16}O$ isotopic ratios in all observations, as well as the associated uncertainties. Most derived uncertainties of the $^{18}O/^{16}O$ ratio lie within 0.2-0.3 VSMOW, while most of the corresponding ones for the $^{17}O/^{16}O$ ratio lie within 0.25-0.55 VSMOW. We calculate the uncertainties associated with the average isotopic ratios to be $^{18}O/^{16}O = 1.20 \pm 0.20$ VSMOW and $^{17}O/^{16}O = 1.23 \pm 0.25$ VSMOW, which correspond to the lower bound of the typical measured uncertainties.

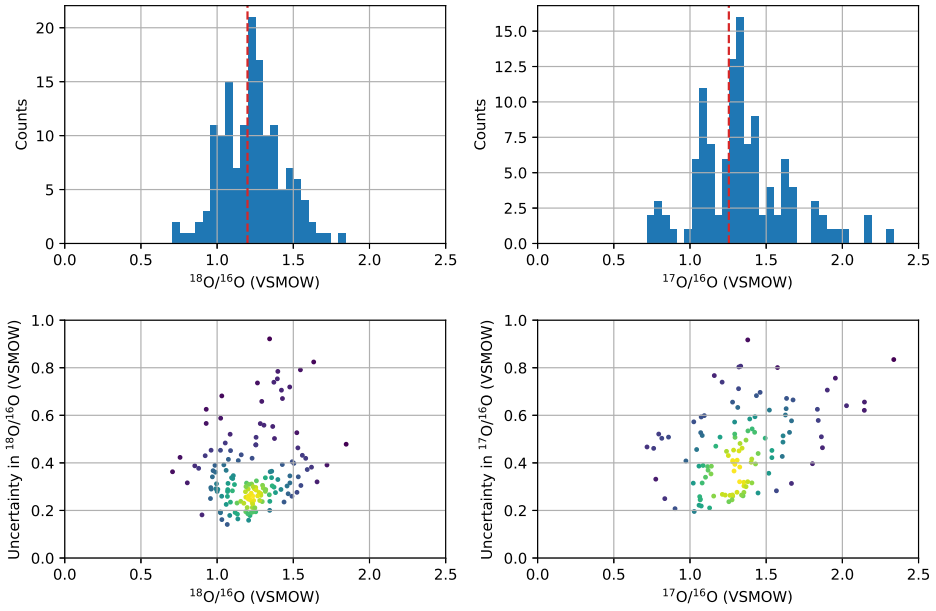

Figure 4.9: Histogram of the measured $^{18}O/^{16}O$ and $^{17}O/^{16}O$ isotopic ratios (top) and the associated retrieved uncertainties (bottom). The red dashed lines in the top panels represent the average isotopic ratios. The colour of the points on the plots in the bottom panels represents the density of measured points.

The derived value of the $^{18}O/^{16}O$ isotope ratio in water vapour is more enriched in the heavy isotope than that measured by the Curiosity Rover ($^{18}O/^{16}O = 1.08 \pm 0.01$ VSMOW; Webster et al. (2013)), although both measurements are consistent within the reported uncertainties. The nature of this difference is unknown, although it might be related to climatological frac-

tionation due to condensation and adsorption/desorption processes, which will be enhanced near the surface, where Curiosity makes its measurements (see section 1.1.5.2).

We find both oxygen isotope ratios in water vapour to be enriched in the heavy isotope, which might be indicative of atmospheric loss to space throughout the Martian history, which preferentially enriches the remaining atmosphere bound to the planet in the heavy isotope (e.g., Jakosky (1991)). While the enrichment in the heavy isotopes might be indicative of atmospheric loss, estimating the amount of oxygen lost throughout history is not straightforward, since it requires accurate knowledge about the escape fractionation factor f (see equation 1.0.2). Fox and Hać (2010) estimate that the fractionation factor inherent in the escape mechanism by dissociative recombination of O_2^+ is approximately 0.4 for $^{18}O/^{16}O$, meaning that the remaining atmosphere is efficiently enriched in ^{18}O as oxygen escapes. However, this factor just represents the fractionation inherent in that particular mechanism, but does not include the fractionation factor of the mechanisms by which the oxygen atoms in the different reservoirs are transformed into O_2^+. In addition, unlike hydrogen, whose main reservoir is Martian water, oxygen atoms in H_2O are expected to interact with those from CO_2 and minerals on the surface, which complicates the connection between water escape and enrichment in the heavy isotopes of oxygen in water vapour.

Interestingly, the enrichment in the heavy isotope of both oxygen isotope ratios with respect to Earth is found to be similar (i.e., $\delta^{18}O \sim \delta^{17}O$). Most terrestrial and lunar materials (e.g., clouds and rain, tropospheric CO_2 and O_2, bulk of silicates on Earth) follow mass-dependent oxygen fractionation, by which $\delta^{18}O \sim 0.52 \cdot \delta^{17}O$ (Thiemens, 1999). Mauersberger (1981) measured an enrichment of $\delta^{18}O = \delta^{17}O = 400$ ‰ in stratospheric ozone, confirming previous indications that ozone might be formed in a mass-independent process from molecular oxygen (Thiemens and Heidenreich, 1983). Later on, more atmospheric species were found to be enriched in a mass-independent way (e.g., stratospheric CO_2, nitrates, sulfates), in particular those reacting with ozone in the atmosphere (Brinjikji and Lyons, 2021). The measurement of mass-independent oxygen fractionation in Martian water vapour might therefore be indicative of photochemical reactions with other oxygen-bearing species.

4.4 Summary

In the previous chapters, we provided a detailed overview of the ACS MIR measurements and the methods by which these can be modelled and analysed. In this chapter, we have applied these retrieval techniques to eight solar occultation observations made during the first months of operations using secondary grating position 5 in order to constrain, for the first time, the vertical distribution of the $^{18}O/^{16}O$ and $^{17}O/^{16}O$ isotopic ratios in water vapour.

We have found that the oxygen isotopic composition of water vapour is enriched in the heavy isotopes with respect to Earth, which might be indicative of atmospheric loss to space. In addition, we have found that both isotope ratios are indeed similarly enriched with respect to Earth and do not follow the expectations from mass-dependent fractionation, which might be indicative of interactions of the water vapour isotopologues with those from other oxygen-bearing species through photochemical reactions.

Despite the rather different conditions found in the atmosphere in terms of pressure, temperature and atmospheric water content in the eight observations analysed in this chapter, the retrieved profiles for the oxygen ratios do not appear to show differences greater than the level of uncertainties. In order to look for variability in the isotopic composition of water vapour, in Chapter 5 we extend the analysis of the ACS MIR solar occultations to a climatological study encompassing more than a Martian Year of observations. However, in order to include simultaneous profiles of the D/H ratio, this climatological analysis applies the retrieval techniques to ACS MIR measurements made with secondary grating position 4.

Chapter 5

Isotopic composition of H_2O from grating position 4

In the previous chapter, we explained how we used a reduced number of observations from ACS MIR secondary grating position 5 to constrain, for the first time, the oxygen isotopic composition of H_2O in the Martian atmosphere. In this chapter, we use a similar approach but now aiming to characterise the variations of the H_2O isotope ratios in space and time. Variations of the D/H ratio are expected to be larger than those of the O isotopologues and therefore easier to characterise from the measurements. Although secondary grating position 5 includes some absorption lines of $HD^{16}O$, these are weaker than those in secondary grating position 4. Therefore, in order to include the D/H ratio in the analysis of the variations of the isotope ratios, we use ACS MIR observations made with secondary grating position 4, which allow us to study the evolution of the vertical profiles of both D/H and $^{18}O/^{16}O$. In addition, aiming to understand how the water isotopologues are fractionated as they are decomposed into lighter species, we combine the ACS measurements with calculations of the photolysis rates of H_2O and HDO, which provides an insight of the isotopic fractionation in the process that ultimately leads to the escape of the different isotopologues.

In sections 5.1 and 5.2 we present the measurements and methods used to measure the climatology of the D/H and $^{18}O/^{16}O$ from secondary grating position 4. The results are then presented in section 5.3. We describe the observed variations of the isotope ratios in H_2O in section 5.3.1. In section 5.3.2, we explain how we estimate the average non-fractionated

values of the isotope ratios using the global statistics of the measurements from the whole dataset. Finally, in section 5.3.3 we explain how we estimate the isotopic ratio of the photolysis products of water vapour (OH and H) using a combination of the ACS measurements and the photolysis rates of H_2O and HDO.

The analysis described in this chapter of the thesis has been peer-reviewed and published in *Nature Astronomy* (Alday et al., 2021a). Although that publication has a number of coauthors, all work presented in this chapter was performed by me except for the calibration of the ACS MIR transmission spectra, which was performed by Alexander Trokhimovskiy at the Space Research Institute (IKI), and the calculation of the photolysis cross-sections of H_2O and HDO, which were calculated by Franck Lefèvre at LATMOS.

5.1 ACS MIR observational dataset

The dataset assembled for this study comprises all available secondary grating position 4 observations from the start of the science operations in March 2018 to the observations made in February 2021. These include 627 secondary grating position 4 solar occultation measurements, which account for approximately 14% of all available ACS MIR observations, covering more than a full Martian year of measurements and including more than half of Martian Year 34 (MY34) (L_S = 160-360°) and most of MY35 (L_S = 0-356°), as shown in Figure 5.1. In solar occultation measurements, the Sun is observed during the sunrise and sunset at a given location on Mars, so that the local time of the observation varies given the latitude of the tangent point, the solar longitude of Mars around the Sun, and whether it is the morning or evening terminator that is observed (see top panel in Figure 5.1). Given the orbit of the ExoMars TGO, the majority of the solar occultations take place at high northern and southern latitudes between approximately 40 and 80°, although some occultations occur close to the equator (see bottom panel in Figure 5.1).

The data from secondary grating position 4 includes ten diffraction orders (215-224) expanding over a wavenumber range between 3604 and 3769 cm^{-1}. This spectral range encompasses absorption bands of several isotopologues of H_2O and CO_2 observed across several diffraction orders (see Figure 3.4 and Figure 3.6). However, absorption by CO_2 in this spectral region is

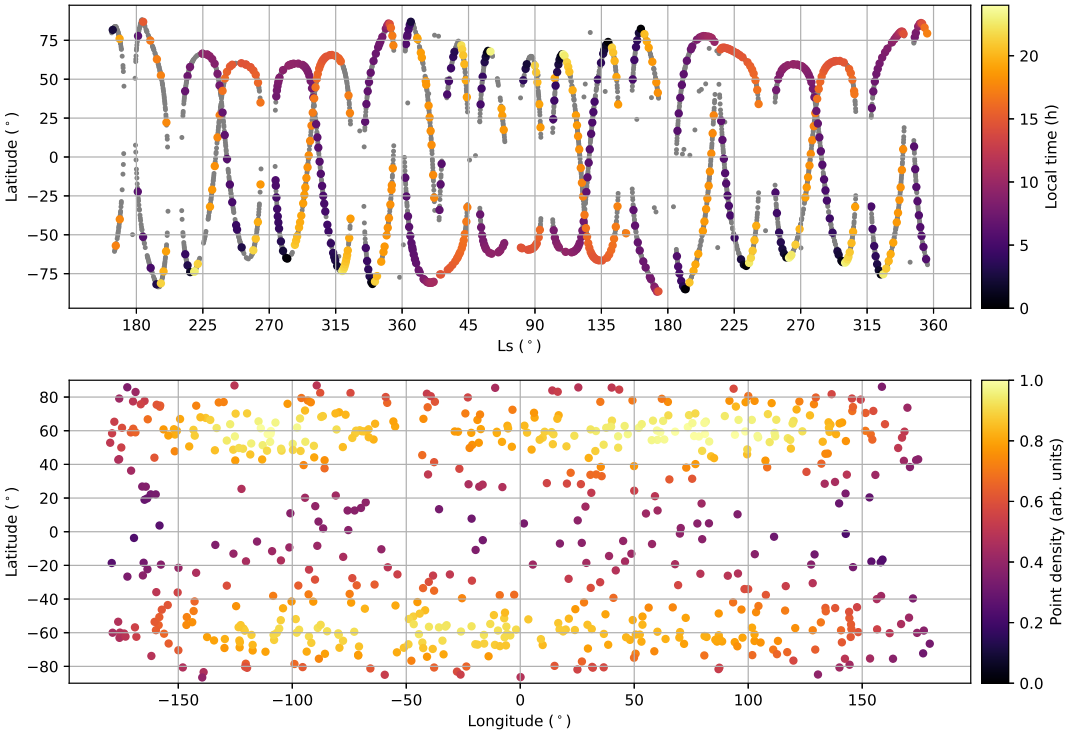

Figure 5.1: Observational coverage of ACS MIR secondary grating position 4 solar occultation observation. Top) Evolution of the latitude of the observations as a function of solar longitude. The grey dots represent all ACS MIR solar occultation observations, while the coloured dots are those made using secondary grating position 4. The colour of the dots represents the local time of the observation. Bottom) Latitude and longitude of the tangent point of all available grating position 4 observations. The colour of the dots represents the density of occultations.

so strong that it masks the much weaker absorption lines of the H_2O isotopes across most of the diffraction orders, impeding the achievement of high sensitive measurements of the isotopic ratios in water vapour (see Figure 5.2). Diffraction order 224 lies just outside the strong absorption band of CO_2, enabling a better characterisation of the water vapour absorption lines, and the derivation of the isotope ratios. It must be noted that, although the strong absorption by CO_2 complicates the analysis of the isotope ratios, it allows the derivation of pressure and temperature vertical profiles from the near-surface up to 180 km, demonstrating the unprecedented capabilities of the ACS instrument.

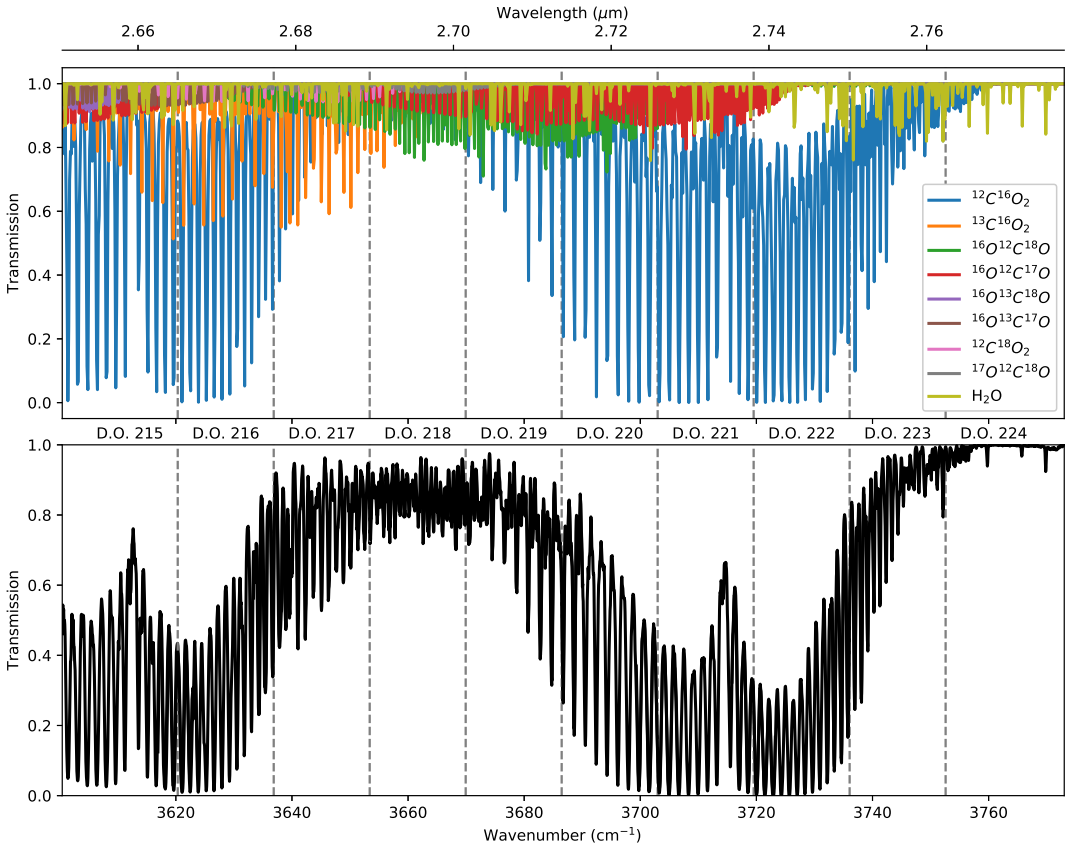

Figure 5.2: Top) Synthetic spectrum for the wavelength range covered by ACS MIR secondary grating position 4, showing the contribution from CO_2 isotopologues and H_2O to the spectrum. Bottom) ACS MIR secondary grating position 4 measurement at a tangent height of 30 km made in the solar occultation during orbit 1849. The vertical dashed lines indicate the spectral range encompassed by each of the diffraction orders acquired in this grating position.

The analysis of this chapter is therefore based on the spectra measured with diffraction orders 223 and 224. These two orders are situated in the lowermost part of the detector frame, where the effect of the doubled-image is minimised (see Section 2.2.3). In particular, two spectral windows are selected within these orders, used to sample both absorption by

CO_2 and the isotopes of H_2O (see Figure 5.2). The spectral window in diffraction order 223 samples the edge of the strong CO_2 band centered at 3715 cm^{-1}, with lines strong enough to be cover the altitude range in which water lines are visible, and therefore allowing the derivation of gaseous volume mixing ratios that otherwise would not be reliable. The spectral window in diffraction order 224 includes several absorption lines of $H_2^{16}O$, some of which can be measured up to 120 km in certain instances. This spectral window also includes some absorption lines of $HD^{16}O$, and one absorption line of $H_2^{18}O$ and $H_2^{17}O$. The absorption line of $H_2^{18}O$ (~3865 cm^{-1}) is clear and not contaminated by other species, which allows greater sensitivity for the derivation of the $^{18}O/^{16}O$ isotopic ratio. On the other hand, the observable absorption line of $H_2^{17}O$ (~3862.3 cm^{-1}) coincides with absorption by $H_2^{16}O$, which impedes the derivation of valuable vertical profiles of the $^{17}O/^{16}O$ ratio.

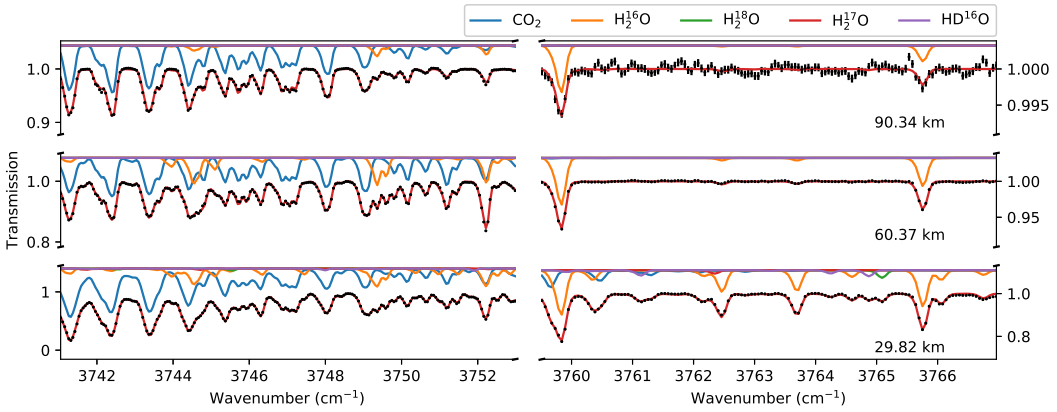

Figure 5.3: ACS MIR spectra measured during orbit 4124 within the spectral windows in diffraction orders 223 (left) and 224 (right) selected for the derivation of the pressure, temperature and H_2O isotopic ratio profiles at three different tangent heights. The black dots represent the measured spectra, while the red line shows the best fit to the data. The contribution from the different absorbing species is shown and shifted for the clarity of the figure, with the colours representing each of the species following the legend on top.

5.2 Retrieval scheme

The retrieval scheme adopted for this work follows the same logic as that used for the characterisation of the oxygen isotope ratios from secondary grating position 5 (see Chapter 4). However, while the analysis of grating position 5 spectra exploited the availability of absorption lines of the gaseous species in different diffraction orders to derive reliable quantities and uncertainties, spectra from secondary grating position 4 allows us to measure only a limited number of absorption lines, and a slightly different approach must be used. In this case, we

exploit the capabilities of the ACS MIR observations by combining several rows from the detector frame.

The analysis of the data is performed with a two-step scheme, which is summarised in Figure 5.4. First of all, vertical profiles of pressure and temperature are retrieved from CO_2 absorption in diffraction order 223, along with the vertical distribution of the $H_2^{16}O$ volume mixing ratio from diffraction order 224. Secondly, the retrieved pressure and temperature profiles are fixed, and the $H_2^{16}O$ volume mixing ratio is used as an *a priori* estimate to retrieve from diffraction order 224 the volume mixing ratios of $H_2^{16}O$, $H_2^{18}O$ and $HD^{16}O$, assuming an *a priori* isotopic composition of $^{18}O/^{16}O = 1$ and $D/H = 5$ with respect to VSMOW, and using a spectral window suitable for the derivation of the isotopic ratios.

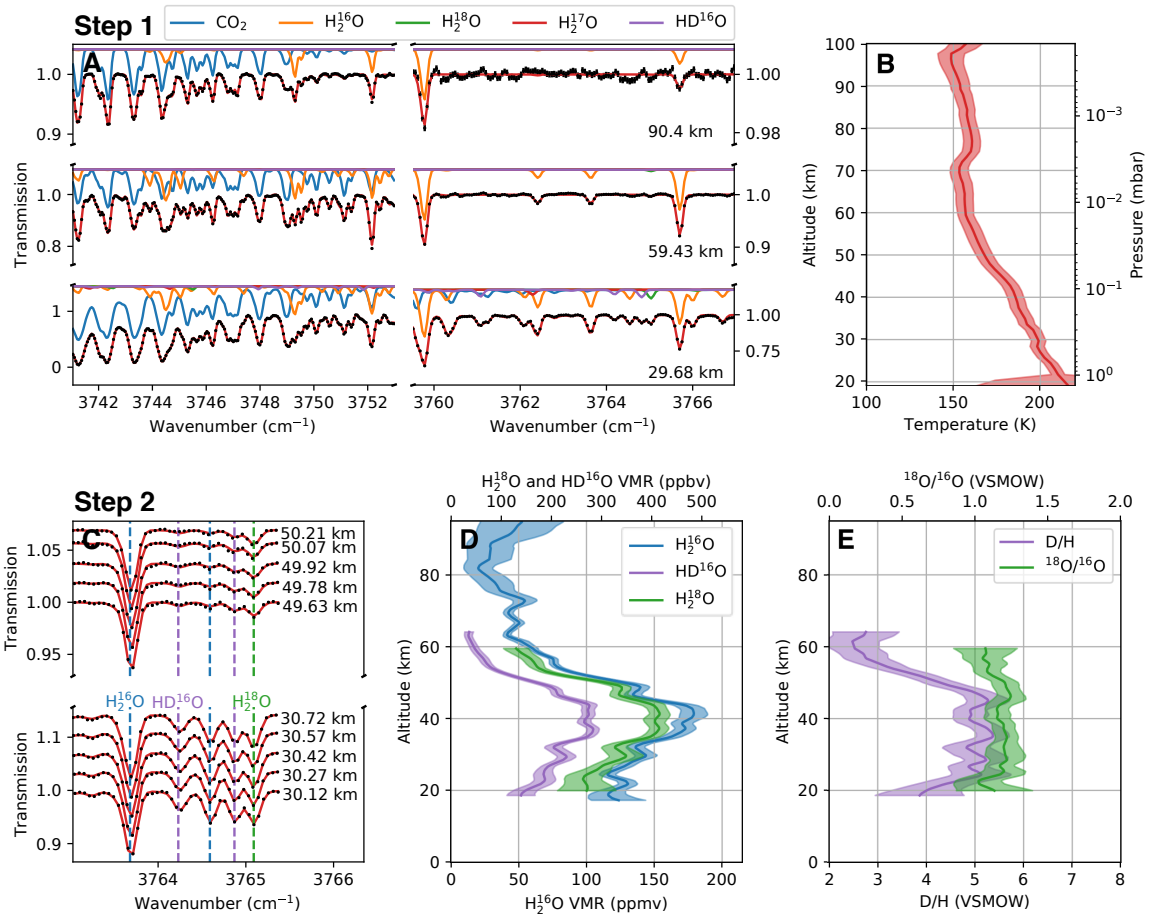

Figure 5.4: Example of ACS MIR spectra and summary of the retrieval scheme. ACS MIR spectra shown in this figure was obtained in orbit 4409 (A) (Latitude = 42° S, L_S = 291°, Local time = 19h). In step 1 of the retrieval scheme, pressure and temperature based on the absorption of CO_2 (B), and $H_2^{16}O$ volume mixing ratio profiles are retrieved from one detector row in diffraction orders 223 and 224 (A). In step 2, spectra from five different detector rows (C) are independently used to retrieve the volume mixing ratios of $H_2^{16}O$, $H_2^{18}O$ and $HD^{16}O$ (D) from the spectral window in diffraction order 224, which allow the derivation of the D/H and $^{18}O/^{16}O$ isotope ratios (E).

The retrieval of the pressure and temperature profiles is performed using the scheme introduced in section 3.4.1 and applied for the analysis of secondary grating position 5 spectra. In this case, the profiles are retrieved using the spectral window in diffraction order 223 taken from the row corresponding to the stripe centre, where the signal intensity is maximum, and which therefore yields the highest signal-to-noise ratio (SNR). The initial retrieval of the vertical distribution of $H_2^{16}O$ volume mixing ratio is also performed using the maximum-intensity row, but now in the spectral window of diffraction order 224 (see Figures 5.3 and 5.4). Comparison of the retrieved $H_2^{16}O$ profiles with those derived from simultaneous measurements by ACS NIR in the 1.38-μm band (Fedorova et al., 2020b) revealed a bias between the retrieved water vapour abundance using both datasets when observing high water vapour densities (see Figure 5.5). This bias is presumably related to the saturation of the water vapour absorption lines, which impact the sensitivity of the line along the line-of-sight. In order to reconcile the retrievals from both datasets, we select a smaller spectral window (3763-3765.4 cm^{-1}) including weaker absorption lines of $H_2^{16}O$. In this case, the retrievals are in good agreement with those retrieved from ACS NIR spectra at low altitudes (see Figure 5.5).

The retrieval of the D/H and $^{18}O/^{16}O$ isotope ratios is performed using the spectral window between 3763 and 3765.4 cm^{-1} in diffraction order 224. However, in this case, given the smaller number and strength of the absorption lines, five different rows from the detector frame are independently retrieved and later combined, increasing the effective vertical resolution of the measurements, as well as the confidence of the retrievals. The combination of the retrieved profiles and the uncertainty estimation from the different detector rows is performed using the same method as was described in section 3.4.5 and later applied for the analysis of grating position 5 data (see section 4.2). However, in this case, instead of combining profiles from different spectral windows, it is the profiles from the same spectral window in different detector rows that are combined (see Figure 5.6).

The combination of the different detector rows is essential for the reliability of the results as it would otherwise be very complicated to differentiate between real variations in the retrieved profiles and oscillations caused by spurious signatures in the ACS MIR data. These spurious signatures appear in some observations and generally have low amplitude, but their impact might be important when the actual absorption lines are weak. In some cases, if one of these

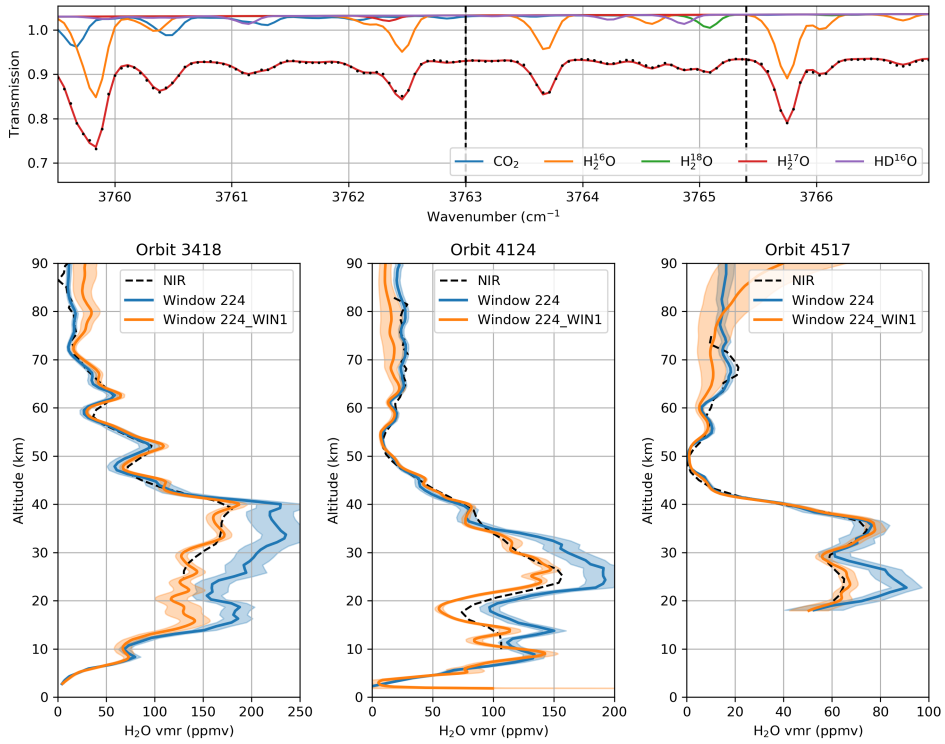

Figure 5.5: Characterising biases in the retrievals by comparing with simultaneous ACS NIR measurements. The top panel shows an ACS MIR transmission spectrum (black dots), the best fit to the data (red line), as well as the contribution from different gases to the spectra, following the different colours shown on the legend. The lower three panels show the retrieved profiles from ACS NIR spectra (black dashed lines - Fedorova et al. (2020b)), as well as the retrieved profiles from ACS MIR when using the whole spectral window shown in the top panel (blue lines) and the spectral range shown between the black dashed lines in the top panel (orange lines). The three observations shown here correspond to the observations made during orbits 3418 (Lat = 50° N, L_S = 240°, Local time = 16h), 4124 (Lat = 49° N, L_S = 276°, Local time = 8h) and 4517 (Lat = 55° N, L_S = 296°, Local time = 8h).

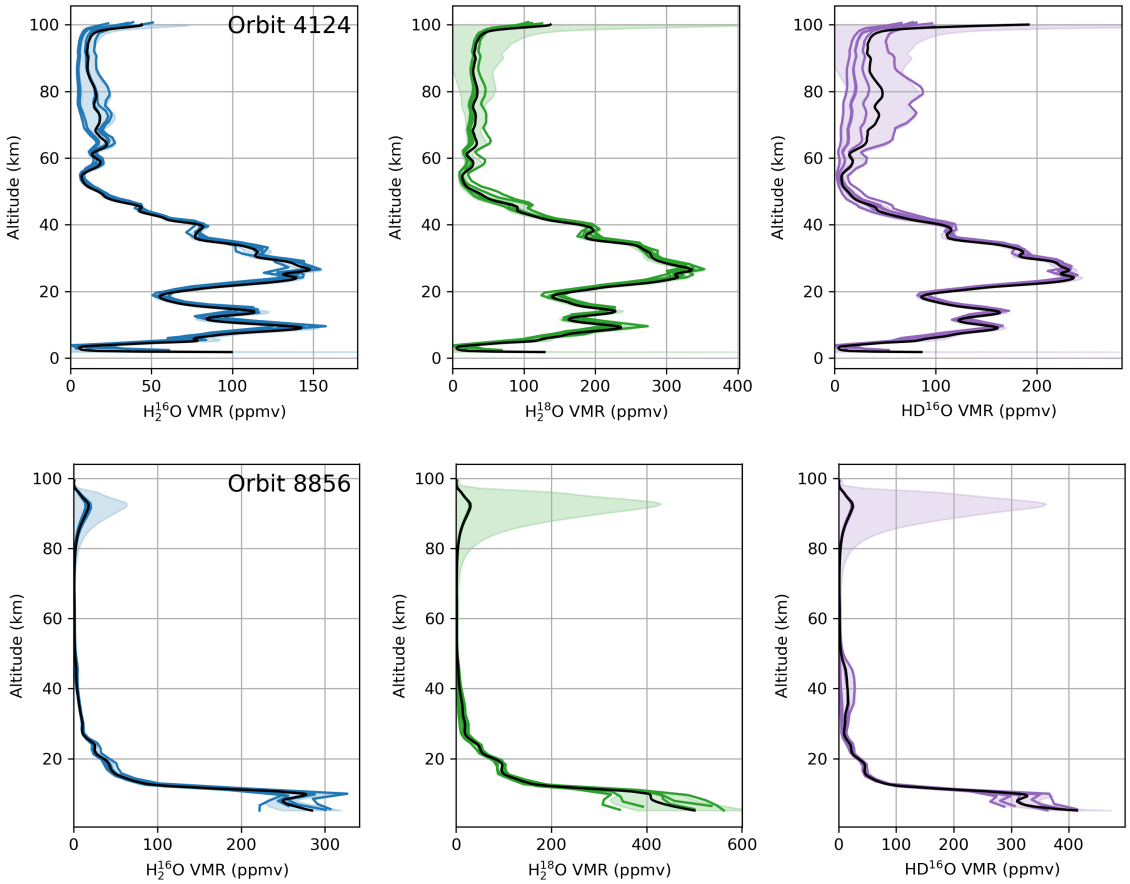

Figure 5.6: Calculation of the averaged profiles and uncertainties in the combination from several detector rows. The different panels show the vertical profiles of $H_2^{16}O$, $H_2^{18}O$ and $HD^{16}O$ retrieved independently from several detector rows. The uncertainties in the weighted-averaged profiles (black lines) are calculated using the maximum between the propagation of errors from the different profiles and the dispersion from the independent profiles from the mean. The profiles on the top panels correspond to the observation made in orbit 4124 (Lat = 49° N, Ls = 276°, Local time = 8h) and the ones at the bottom to the observation made in orbit 8856 (Lat = 66° N, Ls = 108°, Local time = 0h).

spurious signatures coincides with the position of an absorption line, the retrieval algorithm will try to fit the spurious artifact with an actual gaseous contribution, producing unreal oscillations in the retrieved profiles, as shown in the profiles above 70 km in Figure 5.7. In this analysis, where few absorption lines are used, this effect can have a strong impact on the retrieved profiles and it is therefore essential to identify them and include their impact on the retrieved uncertainties. The combination of several rows from the detector proves to be a good approach for overcoming this effect, as the retrieved profiles from each of these rows agree when lines are clear, but clearly differ when spurious signatures are present on the data. Therefore, this approach provides reliable results, with associated errorbars representative of the true uncertainty of the retrieval.

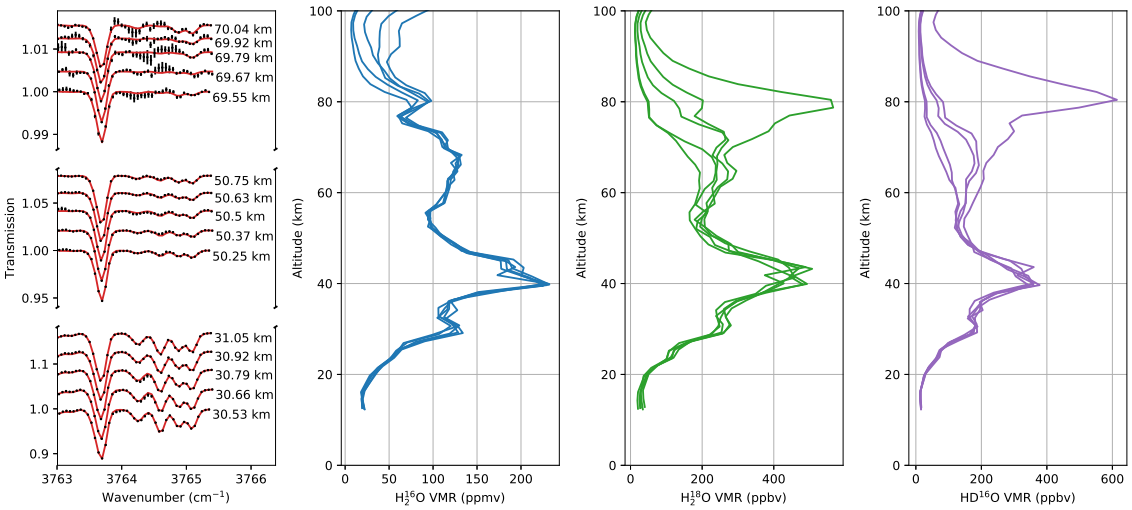

Figure 5.7: Comparison of the retrieved profiles of the H_2O isotope volume mixing ratio profiles when using different rows from the detector frame. The left panel shows the measured data (black dots) and best fit (red lines) in three different acquisitions obtained from different detector rows in the observation made during orbit 2593. The three right panels show the retrieved profiles of $H_2^{16}O$, $H_2^{18}O$ and $HD^{16}O$ obtained from the different detector rows.

In order to test the reliability of the retrieval scheme and the accuracy of the results, the retrieved profiles are compared with vertical profiles retrieved from the ACS NIR channel, which makes simultaneous observations of the Martian atmosphere sampling the CO_2 band at 1.57 μm and the H_2O band at 1.38 μm (Fedorova et al., 2020b). As shown in Figure 5.8, both analyses are found to follow the same altitude trends in different seasons and locations. In Figure 5.9 we make a comparison of all the retrieved values with uncertainties less than 50% from both channels in the observations made during MY34. We calculate that the differences are on average 18.3% for the retrieved H_2O number density, and 7.5 K for the retrieved

temperature. Assuming both instruments are similarly sensitive to these parameters ($\sigma_{NIR} = \sigma_{MIR}$), we estimate a 12.9% uncertainty in the H_2O density and an uncertainty of 5.3 K in the temperature field ($\sigma_{NIR} = \sigma_{MIR} = \sigma_{diff}/\sqrt{2}$).

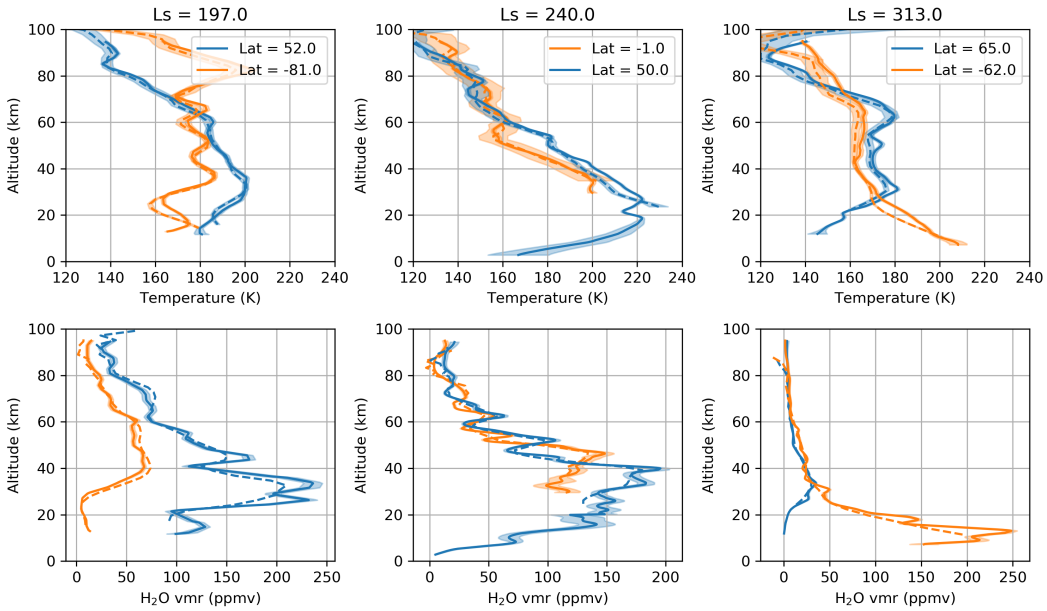

Figure 5.8: Validation of the retrieved vertical profiles of temperature and water vapour mixing ratio from ACS MIR and ACS NIR. The different panels show the retrieved profiles of temperature and water vapour volume mixing ratio from simultaneous observations made by ACS MIR (solid lines - this study) and ACS NIR (dashed lines - Fedorova et al. (2020b)) in different latitudes and seasons.

Unfortunately, the ACS NIR channel does not include any absorption bands of the minor water isotopologues (i.e., $H_2^{18}O$ and $HD^{16}O$), and the retrievals of the isotope ratios cannot be validated with simultaneous measurements. In order to validate these, we perform retrievals of the D/H ratio using secondary grating position 11, using the pressure and temperature fields retrieved by ACS NIR. In particular, we retrieve the $H_2^{16}O$ and $HD^{16}O$ mixing ratios from diffraction orders 175 and 162 (see Figure 3.4), using spectral windows between 2932 and 2938 cm^{-1}, and 2719 and 2725 cm^{-1}, respectively. Even though the observations made with secondary grating positions 4 and 11 are not simultaneous, the derived vertical profiles of D/H ratio from both spectral ranges show similar behaviours when observing similar seasons, confirming the retrievals derived from secondary grating position 4 (see Figure 5.10).

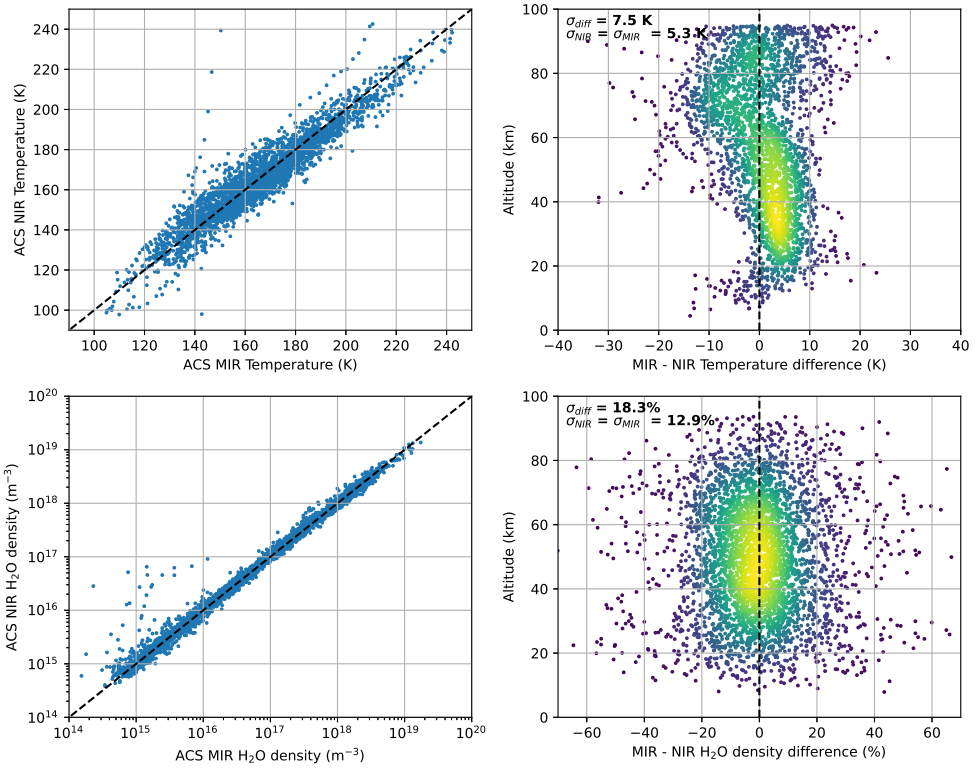

Figure 5.9: Validation of the retrieved vertical profiles of temperature and water vapour mixing ratio from ACS MIR and ACS NIR. The panels on the left show the retrieved temperature and H_2O density using ACS MIR against those retrieved by ACS NIR (Fedorova et al., 2020b) for all the observations made during MY34. The black dashed line in these panels indicates the expected trend if the retrievals from both channels were equal. The panels on the right show the differences in the retrieved parameters from both channels as a function of altitude.

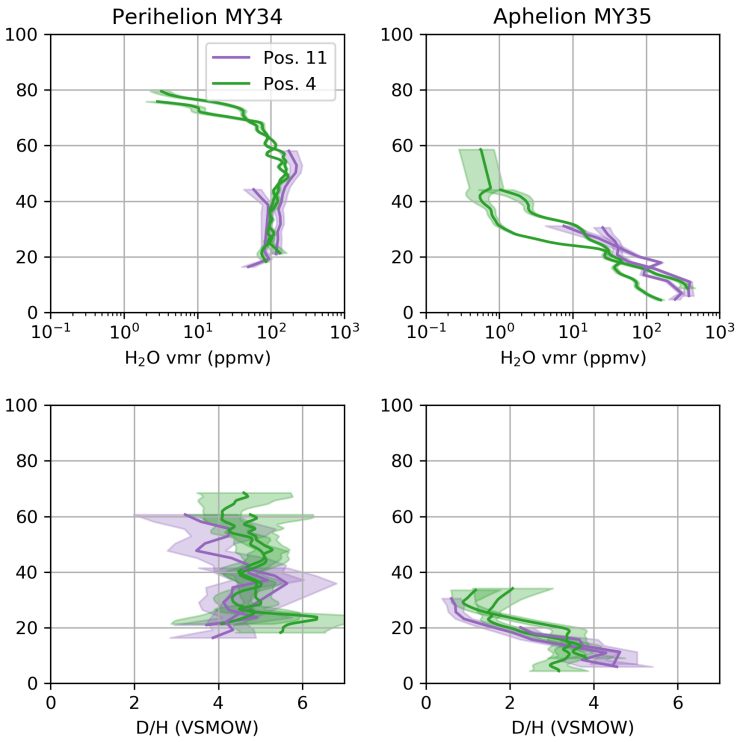

Figure 5.10: Validation of the retrieved vertical profiles of D/H using ACS MIR observations with secondary grating positions 4 and 11. The different panels show the retrieved profiles of water vapour mixing ratio and D/H ratio for observations taken during the perihelion season of MY34 and the aphelion season of MY35 when observing with secondary grating positions 4 (green) and 11 (purple). The observations made with position 11 were performed during orbits 3550, 3553, 8358 and 8381. The observations made with position 4 were performed during orbits 3564, 3576, 8355 and 8401.

5.3 Results

The retrieval scheme developed for the analysis of ACS MIR secondary grating position 4 data was applied to all available observations from the start of the science operations in March 2018 to February 2021, corresponding to 627 solar occultation observations spanning 1.55 Martian years, as described in section 5.1. This analysis allows the monitoring of the vertical profiles of pressure, temperature, and volume mixing ratio of $H_2^{16}O$, $H_2^{18}O$ and $HD^{16}O$, which in turn allow the derivation of the D/H and $^{18}O/^{16}O$ isotope ratios. In addition, the simultaneous characterisation of the pressure, temperature, and H_2O density fields allows the calculation of the water vapour saturation ratio following

$$S = \frac{p_w}{p_{sat}}, \tag{5.3.1}$$

where p_w is the partial pressure of water vapour, and p_{sat} is the water vapour saturation vapour pressure over ice, which can be calculated at a given temperature using the Goff-Gratch equation given by

$$\begin{aligned} \log_{10}(p_{sat}) = -9.09718 \cdot \left(\frac{273.16}{T} - 1\right) - 3.56654 \cdot \log_{10}\left(\frac{273.16}{T}\right) \\ +0.876793 \cdot \left(1 - \frac{T}{273.16}\right) + \log_{10}(6.1071), \end{aligned} \tag{5.3.2}$$

where the temperature T is given in K and p_{sat} is in hPa.

The results derived from the analysis of the ACS MIR secondary grating position 4 data are summarised in Figure 5.11, which shows the evolution or climatology of the retrieved atmospheric parameters. In the following subsections, these results are classified and displayed to highlight the aspects of the data most relevant for the purposes of this thesis, aiming to constrain the initial research questions stated in Chapter 1. In section 5.3.1, we analyse the seasonal evolution of the retrieved atmospheric parameters, focusing on the variations of the isotopic ratios. Section 5.3.2 deals with the estimation of the average non-fractionated isotopic ratios representative of the Martian atmosphere, which must be accurately measured for making reliable estimations of the evolution of water vapour on Mars. Finally, section 5.3.3 aims to constrain the relation between the isotope ratios in H_2O and the dissociation species, which is relevant for understanding the relative escape of the several isotopes.

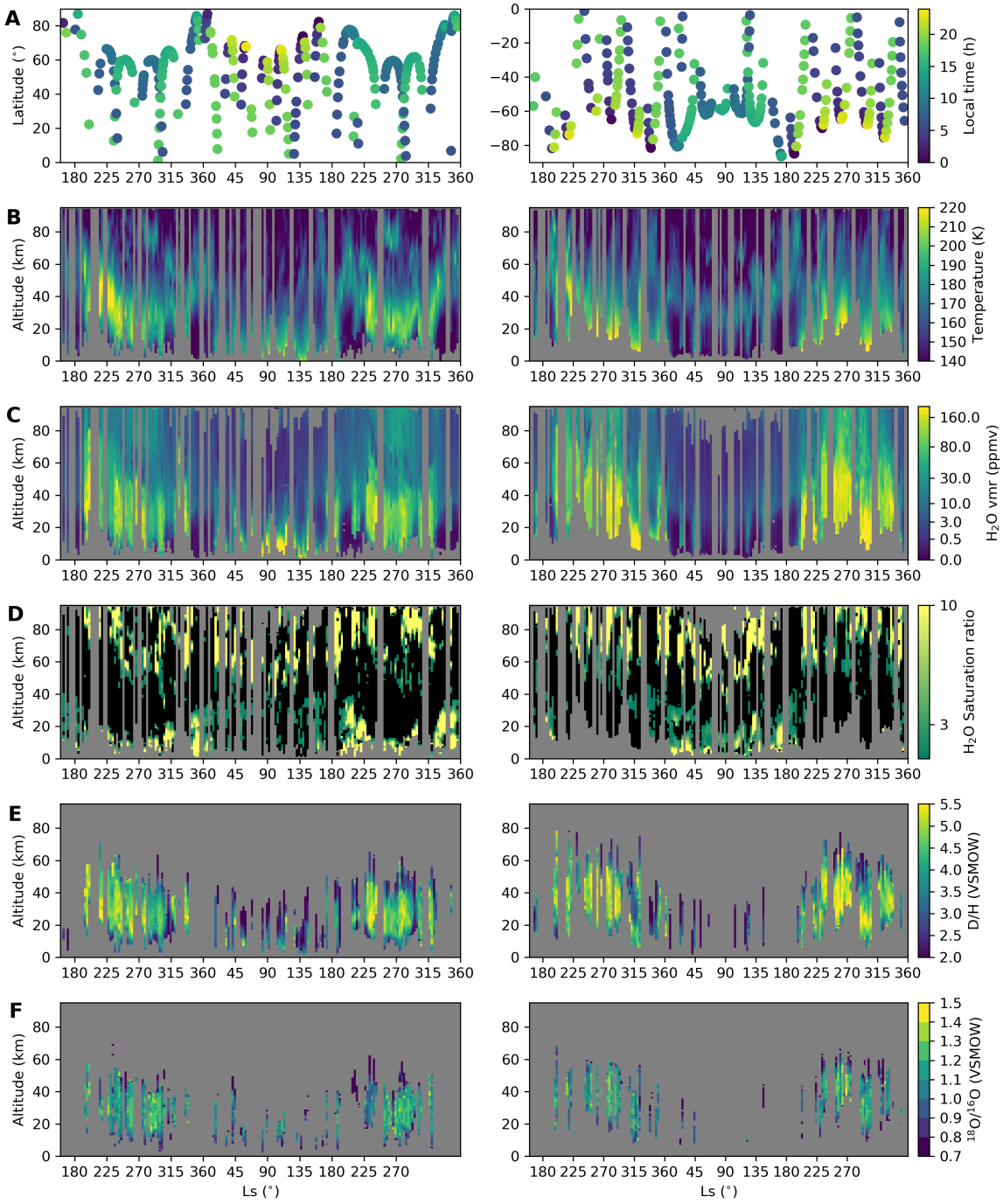

Figure 5.11: Climatology of the retrieved atmospheric parameters. The panels show the values of the retrieved parameters as a function of altitude and solar longitude for the northern (left) and southern (right) hemispheres. A) Distribution of ACS MIR solar occultation observations, with the local time represented by the colour bar. B) Atmospheric temperature. C) Water vapour volume mixing ratio. D) Saturation ratio of water vapour, with black representing all the values <1, and the values >1 following the colour bar E) D/H ratio in water vapour with uncertainties lower than 1 VSMOW. F) $^{18}O/^{16}O$ ratio in water vapour with uncertainties lower than 0.2 VSMOW.

5.3.1 Climatology of the retrieved atmospheric parameters

The evolution of the retrieved parameters in Figure 5.11 shows large variations as a function of time. Due to the nature of the Sun-synchronous near-polar orbit of the ExoMars TGO, the latitudinal coverage of the ACS solar occultation observations varies with time, as shown in the top panels of Figure 5.11. Therefore, it must be noted that some of the variations observed in the climatology are related to latitude changes rather than seasonal ones.

During the observed period, both temperature and H_2O volume mixing ratio profiles show drastic seasonal and latitudinal changes. During the Southern Hemisphere (SH) spring and summer seasons (L_S = 180° and L_S = 270°) in both MY34 and MY35, Mars is close to perihelion (L_S = 251°), and the greater dust heating and proximity to the Sun intensify the Hadley circulation, allowing warmer temperatures to expand to the middle atmosphere in both the northern and southern hemispheres. These greater temperatures move the hygropause (i.e., level at which water vapour saturates) upwards to higher altitudes, allowing water vapour to migrate to the middle and upper atmospheres, and reaching values greater than 50 ppmv as high as 100 km. The ascension of water vapour to the middle atmosphere also occurs during the Global Dust Storm (GDS) in MY34 (L_S = 190-220°), when the hygropause is moved to approximately 80 km in both hemispheres. This behaviour is not observed during the same period in MY35, when the altitude of the hygropause is set around 40-50 km at mid-latitudes (see Figure 5.11). This difference shows the impact of dust storms, which increase the dust heating and prevent the condensation of water vapour (Neary et al., 2020). During the Northern Hemisphere (NH) spring and summer seasons (L_S = 0° and L_S = 90°), although high water vapour abundances ($>$ 150 ppmv) are observed in the NH, these are confined to altitudes below ∼20 km. At high southern latitudes ($>$ 60°S), during this time, very low water vapour abundances ($<$ 1 ppmv) and temperatures ($<$ 150 K) are observed. These seasonal trends are in agreement with other observations (Aoki et al., 2019; Fedorova et al., 2020b,a) and with the expectations from the simulations of a General Circulation Model (GCM) (Montmessin et al., 2004).

The evolution of the D/H ratio is closely linked to that of the H_2O abundance, showing some strong differences between the summer seasons in the northern and southern hemispheres (see

Figures 5.11 and 5.12). During the SH summer in MY34 and MY35, the intensified Hadley circulation raised the hygropause to higher altitudes, allowing water vapour and its minor isotopologues to expand into the middle atmosphere until they reach the saturation level where the volume mixing ratio starts decreasing. During this period, the D/H ratio in the NH lies within 4-5 VSMOW up to 30-40 km, where it starts decaying towards 2-4 VSMOW in the 40-50 km range, in agreement with the expectations based on condensation-induced fractionation, which predict a preferential condensation of $HD^{16}O$ over $H_2^{16}O$ (Bertaux and Montmessin, 2001; Montmessin et al., 2005). A similar behaviour is observed in the SH during this period, with values of 5-6 VSMOW up to 50-60 km, where they decrease down to 2-4 VSMOW at 60-70 km. During the NH summer, the presence of isotopic fractionation in condensation processes is even clearer, showing a steady decrease of the D/H ratio from 4-5 VSMOW at 10 km down to 2-3 VSMOW at 20-30 km, due to a lower altitude of the hygropause. During this period, the water vapour content in the SH is very low, and only a few observations yield low uncertainties in the D/H ratio, which indicate values of approximately 2 VSMOW between 10 and 30 km.

The variations observed in the water vapour D/H ratio appear to be consistent with the expectations from condensation-induced fractionation, which were modelled by Montmessin et al. (2005) using a GCM. Recently, the team from the Laboratoire Atmosphères, Observations Spatiales (LATMOS) has generated a data product with the GCM results using the same observational constraints as ACS solar occultations, allowing a comparison between the observed and modelled variations of the D/H ratio (see Figures 5.11, 5.12 and 5.13) (Montmessin et al., 2005; Rossi et al., 2021). The modelled vertical profiles, as well as the measured ones, show a decrease of the D/H ratio above the hygropause. In addition, during the winter seasons in both the northern and southern hemispheres ($L_S \sim 270°$ and $L_S \sim 90°$), both the model and the measurements reveal low values of the D/H ratio below 15 km, which correspond to the condensation of water on the polar caps. Therefore, to first order, the observed variability of the D/H ratio agrees with the predictions from the GCM, which is consistent with the hypothesis that the main driver of isotopic fractionation in Martian water vapour is condensation-induced fractionation. In the future, a more quantitative comparison is required for obtaining an in-depth understanding of the fractionation mechanism and to understand, for example, the effects of supersaturation and kinetic fractionation in the

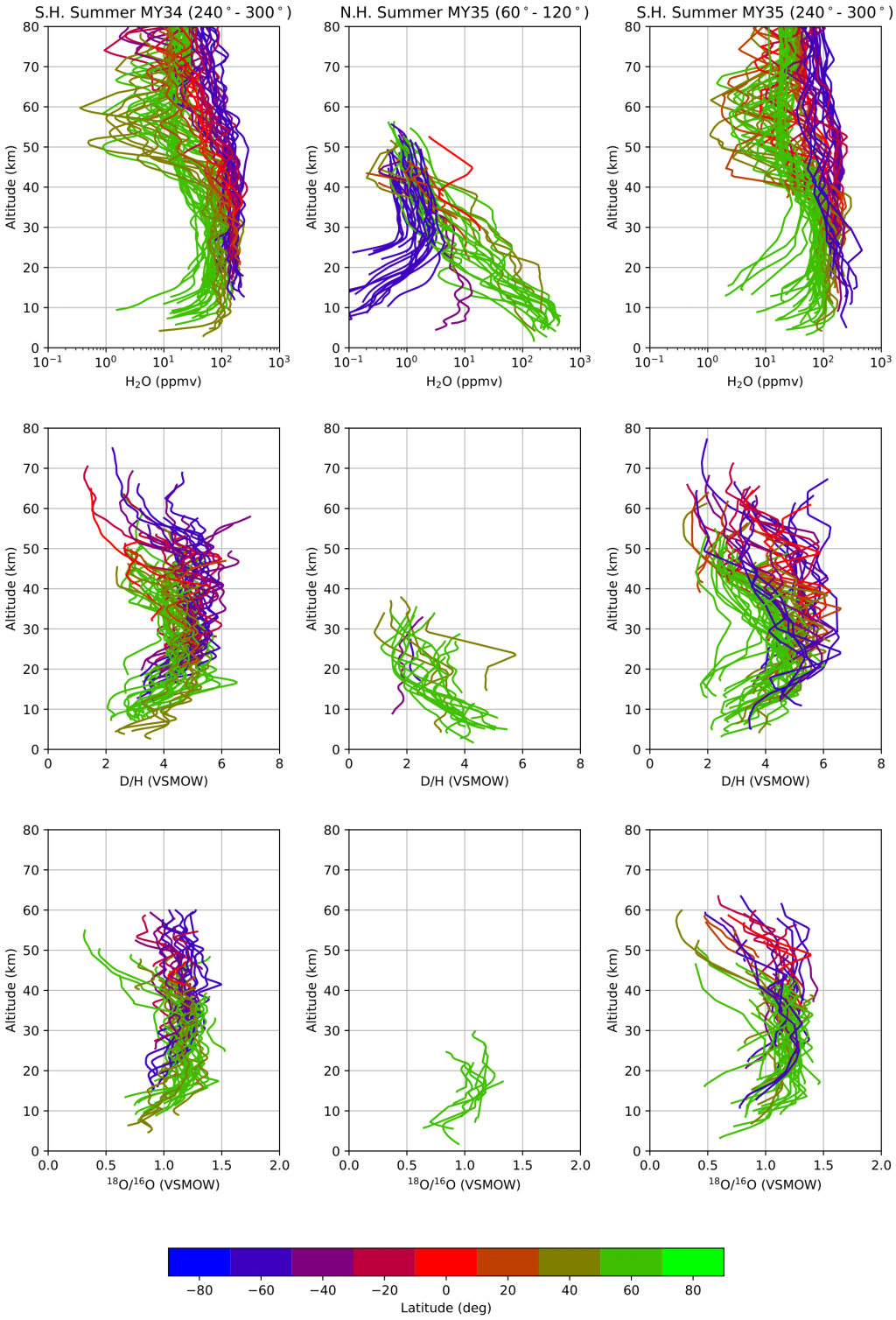

Figure 5.12: Evolution of the water vapour mixing ratio and the D/H and $^{18}O/^{16}O$ isotopic ratios in the perihelion and aphelion seasons of MY34 and MY35. The different panels show the retrieved profiles separated in different seasons, with the colour of the lines representing the latitude of the observations. For the clarity of the figure, only the points with uncertainties of D/H < 1 VSMOW and $^{18}O/^{16}O$ < 0.13 VSMOW are shown.

differentiation between H_2O and HDO during the formation of water ice clouds (see Section 1.1.5.2).

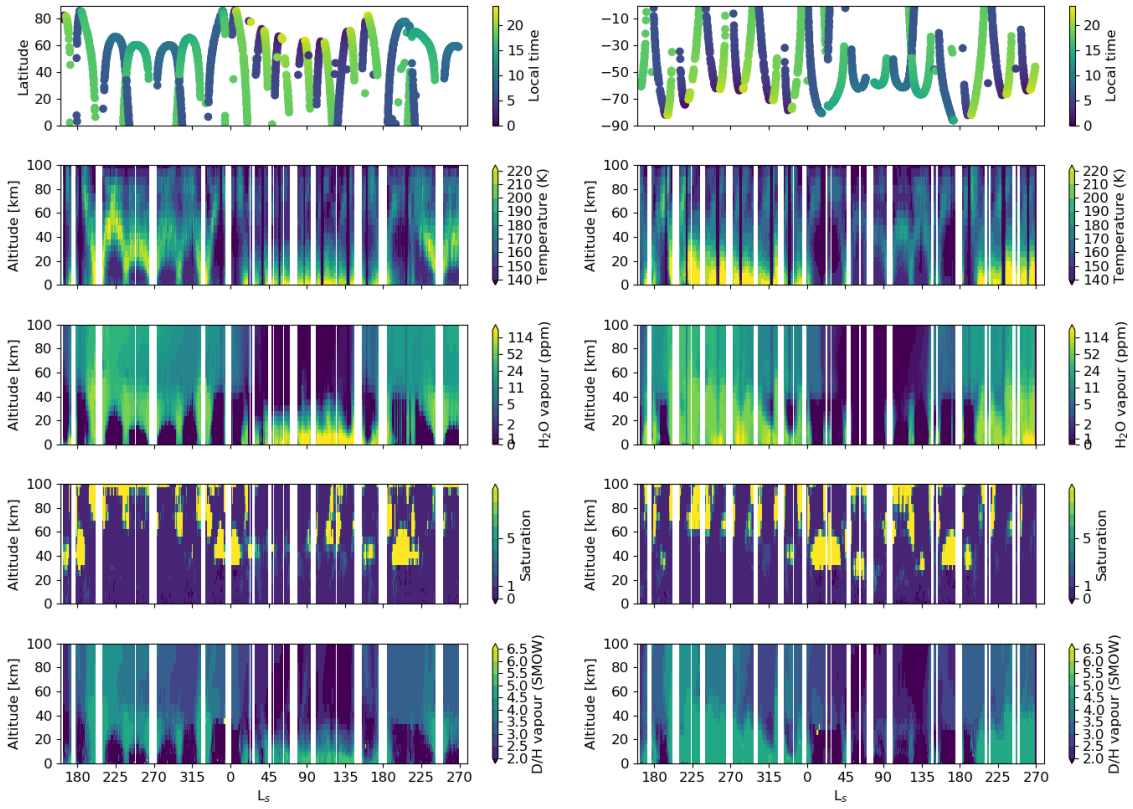

Figure 5.13: GCM climatology of the atmospheric parameters displayed simulating the same observational coverage as ACS solar occultation observations (Rossi et al., 2021). The panels show the values of the atmospheric parameters as a function of altitude and solar longitude for the northern (left) and southern (right) hemispheres. A) Distribution of ACS MIR solar occultation observations, with the local time represented by the colour bar. B) Atmospheric temperature. C) Water vapour volume mixing ratio. D) D/H ratio in water vapour.

Recently, Villanueva et al. (2021) measured the climatology of the H_2O abundance and the D/H ratio from solar occultation observations made by NOMAD during MY34. Although the observations made by NOMAD and ACS MIR are not simultaneous (see section 2.1), the observational coverage of both instruments is similar, as well as their sensitivity to H_2O and HDO. To first order, the variations of the water vapour mixing ratio and the D/H ratio follow similar trends. However, while the average D/H ratio measured by NOMAD lies within 6-7 VSMOW, our measurements typically reveal values of D/H of approximately 5 VSMOW. The source of this difference is currently unknown, although an in-depth cross comparison of the measurements made by both instruments will be performed in the future.

In the case of the evolution of the $^{18}O/^{16}O$ isotope ratio, variations appear to be milder than those found in the D/H ratio. During the SH summer, the $^{18}O/^{16}O$ isotope ratio lies within values of 1.1-1.3 VSMOW up to approximately 60 km. In MY35, the $^{18}O/^{16}O$ ratio appears to decrease towards lower values (0.5-1 VSMOW) above 30-40 km and 50-60 km altitude ranges for the northern and southern hemispheres, respectively, which resembles the behaviour of the D/H ratio above the hygropause. However, these points have larger uncertainties than those found below the hygropause. During the NH summer, the observations of the $^{18}O/^{16}O$ ratio indicate values ranging from 1-1.2 VSMOW, showing no evidence of strong fractionation, as opposed to the steady decrease observed in the D/H ratio. In the following section, we provide a more detailed analysis of the measurement error to estimate the statistical significance of the variations measured in the $^{18}O/^{16}O$ isotope ratio.

5.3.2 Estimation of the non-fractionated isotopic ratios

Understanding the variability of the isotopic ratios is essential to disentangle the values inferred from localised measurements, which are subject to climatological fractionating processes and the non-fractionated isotopic ratio representative of the whole atmospheric reservoir, which is important for understanding Mars' evolution. Figure 5.14 shows a histogram of the measured isotope ratios at all altitudes. The observed values of the D/H ratio show a large range of variability, varying from values as low as 1-2 to 5-6 VSMOW, while the variations in the $^{18}O/^{16}O$ are smaller, ranging from approximately 0.9 to 1.3 VSMOW. Typical uncertainties of the D/H ratio lie within 0.3-0.5 VSMOW, while those on the $^{18}O/^{16}O$ isotopic ratio range between 0.08 and 0.12 VSMOW.

In order to understand the nature of the observed variations in the isotopic ratios, their dependence on atmospheric temperature and water abundance is also shown in Figure 5.14. The variations in the D/H ratio are found to be positively correlated with those in the water vapour volume mixing ratio, with a Pearson correlation coefficient of 0.7 between D/H and $\log_{10}(H_2O)$. A logarithmic relation between D/H and water vapour abundance is predicted by the isotope fractionation during condensation (Montmessin et al., 2005), which appears therefore responsible for the observed variations. Similarly, the observed variations of the D/H ratio appear to be related to the atmospheric temperature: while the higher values of the D/H ratio (>4 VSMOW) are found in a wide range of temperatures (170-210 K), low

values of D/H (<3 VSMOW) are only measured for T<180 K. This correlation corroborates the hypothesis of the prominent role of condensation-induced fractionation, which is predicted to increase with decreasing temperatures (Krasnopolsky, 2015; Merlivat and Nief, 1967; Lamb et al., 2017).

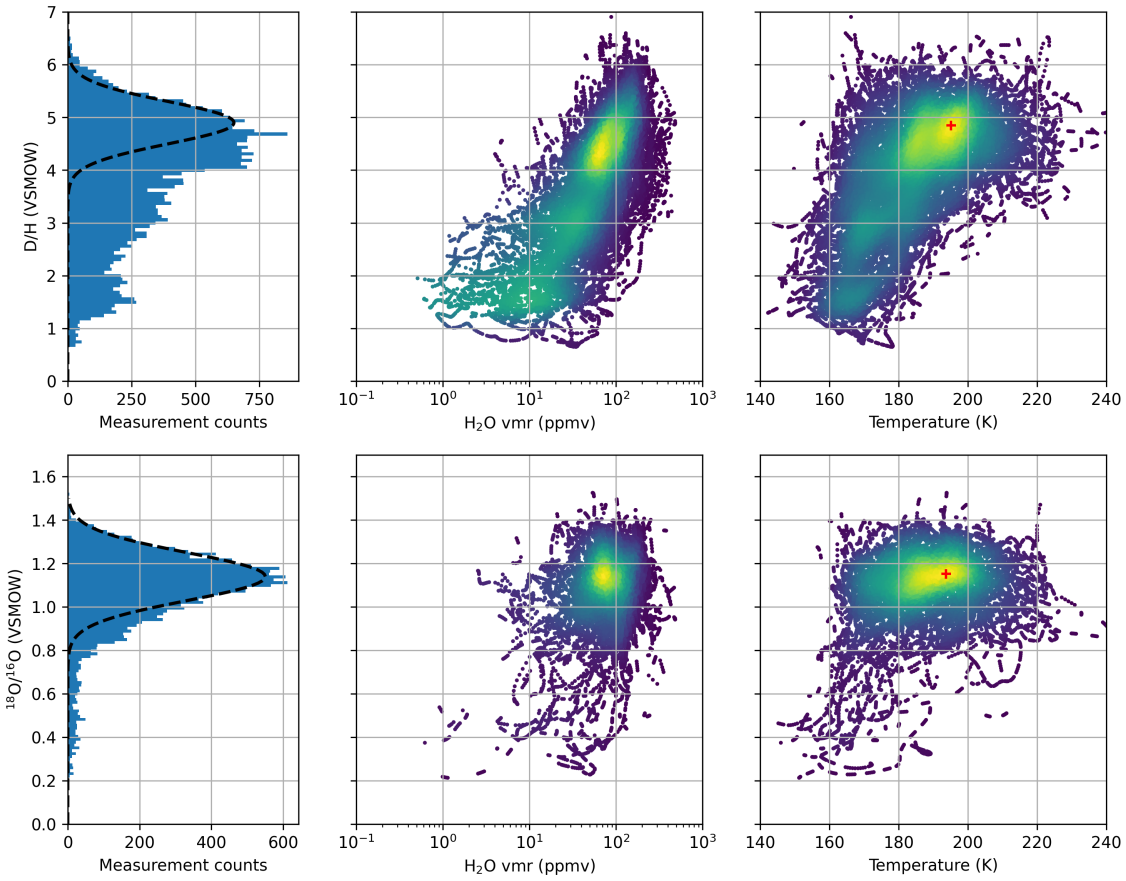

Figure 5.14: Histogram of the measured D/H and $^{18}O/^{16}O$ isotope ratios, as well as their relation with the water vapour mixing ratio and temperature. Only the points with uncertainties of D/H < 1 VSMOW and $^{18}O/^{16}O$ < 0.13 VSMOW are shown. The black dashed lines on the histogram plots represent typical measurement uncertainties, centred at D/H = 4.9 ± 0.4 VSMOW and $^{18}O/^{16}O$ = 1.14 ± 0.10 VSMOW. The colour of the points on the plots in the middle and right columns represents the density of measured points. The red cross in the temperature panels represents the most frequently measured value of the isotope ratios at temperatures >180 K, which we take as the average non-fractionated isotope ratios in the Martian atmosphere.

The estimation of the D/H ratio representative of the present-day Martian atmosphere requires the subtraction of climatological effects that impact the isotopic composition at certain times and locations. Climatological fractionation effects are expected to be minimum when observing high temperatures and water vapour abundances, when water is fully vaporised and free from condensation (Villanueva et al., 2015). Under these conditions, most of the

observations yield D/H ratios between 4 and 5 VSMOW. Larger values of the D/H ratio (5-6 VSMOW) are observed in certain instances. However, considering the typical statistical uncertainty of the measurements ($\sigma \sim 0.4$ VSMOW), which is highlighted in the histogram plot in Figure 5.14, it is not possible to determine whether the values of D/H > 5 VSMOW are real or an artefact due to the intrinsic measurement uncertainty. Considering the measurements with T > 180 K, the most frequently measured value is D/H $= 4.9 \pm 0.4$ VSMOW, which we take as the average non-fractionated isotope ratio in the Martian atmosphere.

In the case of the $^{18}O/^{16}O$, the range of observed variability is close to the uncertainty level in the measurements, which makes it impossible to disentangle potential variations of the $^{18}O/^{16}O$ isotope ratio in the Martian atmosphere from the statistical noise of the instrument. This is also highlighted in the histogram plot in Figure 5.14. In contrast to the measurements of the D/H ratio, no apparent correlation is found between the $^{18}O/^{16}O$ isotopic ratio, water abundance and temperature (see Figure 5.14). We do not observe either any correlation between the observed variations in D/H and those in the $^{18}O/^{16}O$ ratio (see Figure 5.15). A relation between the fractionation of these two isotope ratios is expected during condensation onto water ice clouds, typically following $\delta D = 8 \times \delta^{18}O$ on Earth (meteoric line), although the slope of this relation varies as a function of temperature, and also depending on the role of kinetic effects and supersaturation, as reviewed in section 1.1.5.2. Trendlines following different slopes are superimposed on the data in Figure 5.15. However, while expectations from condensation-induced fractionation predict a correlation between these parameters, this dependence cannot be robustly seen in the data because of the uncertainty exhibited by the measurement of the O isotope ratios being at least as large as any variation seen in the atmosphere.

From the measured $^{18}O/^{16}O$ isotope ratios throughout more than one Martian year, we estimate the $^{18}O/^{16}O$ isotope ratio representative of the Martian atmosphere to be 1.14 ± 0.08 VSMOW, where the uncertainty corresponds to the lower bound of the typical measured uncertainties. Within the observed variations, our results are consistent with the measurement made with the Sample Analysis at Mars (SAM) instrument on the Curiosity Rover, which revealed an enrichment of the $^{18}O/^{16}O$ isotope ratio of 1.08 ± 0.01 VSMOW (Webster et al., 2013). In addition, the results derived from the ACS MIR measurements made with secondary

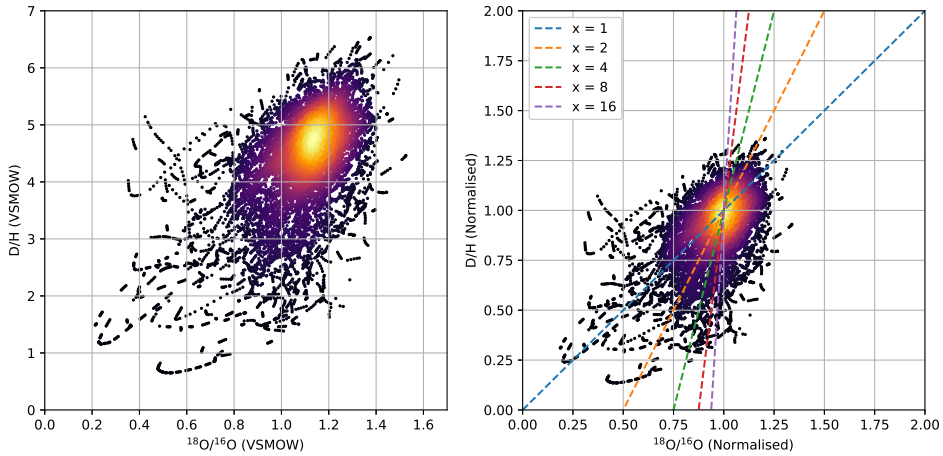

Figure 5.15: Left) Relation between the measured values of the D/H and $^{18}O/^{16}O$ isotope ratios in H_2O in units of VSMOW. Right) Relation between the measured values of the D/H and $^{18}O/^{16}O$ isotope ratios in H_2O normalised using D/H = 4.9 and $^{18}O/^{16}O$ = 1.14 VSMOW. The coloured straight lines represent the expected relation from condensation-induced fractionation with various slopes representing various cases of temperature and impact of kinetic fractionation.

grating position 4 can be compared with those derived from secondary grating position 5, which were described in the previous chapter. Both analyses yield mean $^{18}O/^{16}O$ values of 1.14 ± 0.08 and 1.20 ± 0.20 VSMOW, and are therefore consistent within the errorbars. Nevertheless, it must be noted that while the value derived from position 5 data relied on the analysis of eight solar occultation observations, the value derived in this chapter is obtained using more than 500 observations, and is therefore considered more accurate.

5.3.3 Implications to isotopic fractionation during atmospheric escape

Accurate estimations of the total amount of water vapour lost throughout Martian history from isotopic measurements require an understanding of the relative efficiency of the different isotopologues to escape into space, which is represented by the escape fractionation factor f (see equation 1.0.2). The first part of the escaping process of water into space starts with the photolysis of H_2O, giving rise to OH and H (see section 1.1.4). The isotopic ratio of the photolysis products can be estimated taking into account the isotopic ratio of the parent molecules (H_2O) and the relative photolysis rates of the different isotopes. From now on, the calculations regarding the isotopic ratios are going to be made for D/H, but it must be noted that they are analogous for the $^{18}O/^{16}O$ ratio. The D/H ratio of the photodissociation products can therefore be estimated using

$$(\mathrm{D/H})_{product}(z) = (\mathrm{D/H})_{parent}(z) \cdot \frac{J_{\mathrm{HDO}}}{J_{\mathrm{H_2O}}}(z) \tag{5.3.3}$$

where $(\mathrm{D/H})_{parent}$ represents the D/H ratio of the parent H_2O molecules and J_{HDO} and J_{H_2O} are the photolysis rates of HDO and H_2O in s^{-1}, respectively. Note that the D/H ratio of the parent molecules being photolysed might be different from the average D/H ratio of the bulk atmosphere if water vapour is fractionated in the lower atmosphere, leading to a localised enrichment or depletion with respect to the average lower atmosphere value. Therefore, the fractionation factor R relating the isotopic composition of the photolysis products and that of the bulk atmosphere can be calculated as

$$R(z) = \frac{(\mathrm{D/H})_{product}}{(\mathrm{D/H})_{bulk}} = \frac{(\mathrm{D/H})_{parent}(z)}{(\mathrm{D/H})_{bulk}} \cdot \frac{J_{\mathrm{HDO}}}{J_{\mathrm{H_2O}}}(z) \tag{5.3.4}$$

.

Therefore, the fractionation factor between the D/H ratio of the photolysis products and that representative of the bulk of the atmosphere is the combination of two factors:

- The fractionation between the D/H ratio of the atmospheric bulk representative of the Martian lower atmosphere, and the D/H ratio of the parent H_2O molecules, which might be subject to climatological fractionation processes occurring in the atmosphere. Given that the observed variations in the D/H ratio in H_2O appear to be consistent with the expectations from condensation-induced fractionation, this factor represents the effect that condensation processes have in fractionating the isotopic composition between the near-surface atmospheric reservoir and the photolysis products, and is given by

$$R_c(z) = \frac{(\mathrm{D/H})_{parent}(z)}{(\mathrm{D/H})_{bulk}}. \tag{5.3.5}$$

- The fractionation inherent in the photolysis of H_2O, which differentiates between the H_2O and HDO because of their different ultraviolet cross sections (Cheng et al., 1999) (see Figure 5.16). Therefore, the fractionation factor inherent in the photolysis mechanism is given by

$$R_p(z) = \frac{J_{\mathrm{HDO}}}{J_{\mathrm{H_2O}}}(z). \tag{5.3.6}$$

In order to estimate the efficiency of these processes to fractionate the isotopes during their photodissociation, the absorption cross-sections of H_2O and HDO are implemented in the photolysis model of the LMD-GCM (Cheng et al., 1999; Lefèvre et al., 2004). The middle panel in Figure 5.16 shows the photolysis rates of H_2O and HDO calculated for four different solar zenith angles (SZA = 0°, 30°, 60°, 85°), and at a Sun-Mars distance of 1.52 astronomical units (AU). As it was introduced in Chapter 1, the photolysis rates of HDO and H_2O at high altitudes are dominated by the absorption at wavelengths $\lambda < 180$ nm, which exhibit similar cross-sections, leading to little fractionation. At lower altitudes, the absorption by CO_2 becomes important, impeding photons with $\lambda < 180$ nm to penetrate to the lower altitudes. Instead, the photolysis of H_2O and HDO at lower altitudes is driven by photons with $\lambda > 180$ nm, which yield lower photolysis rates due the lower absorption cross-section at these wavelengths, but higher fractionation between the two isotopologues.

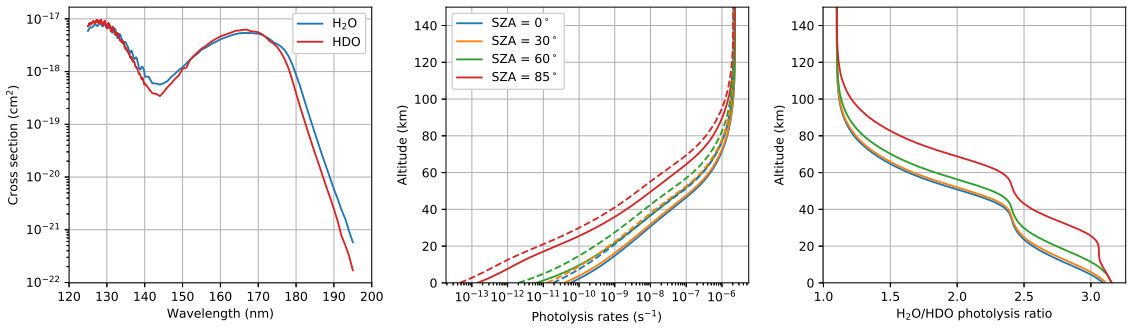

Figure 5.16: Calculation of the H_2O and HDO photolysis rates with the photolysis code of the LMD-GCM (Lefèvre et al., 2004). Left) UV absorption cross-sections of H_2O and HDO from Cheng et al. (1999); Chung et al. (2001); Mota et al. (2005). The cross-section of HDO is assumed to be the same as that of H_2O for wavelengths smaller than 125 nm, as there are no available cross-sections of HDO at these wavelengths. Middle) Photolysis rates J_{H_2O} (solid) and J_{HDO} (dashed) in s^{-1} at different solar zenith angles (SZA), calculated at a Sun-Mars distance of 1.52 AU. Right) Ratio of the H_2O/HDO photolysis rates as a function of SZA.

In order to get an insight into the importance of seasonal effects on the photolysis of water and its isotopic fractionation, the photolysis rates from the model at SZA = 60°, are scaled to the relevant Sun-Mars distance, and multiplied by the water vapour number densities retrieved from the ACS MIR spectra during the summer seasons in the southern and northern hemispheres (see Figure 5.17A). These estimated dissociation rates show very

different seasonal behaviours. During the SH summer, the stronger Hadley circulation allows water to rise into the middle atmosphere in both hemispheres, where photolysis increases, reaching a maximum of H_2O dissociation rates at approximately 50-60 km in the SH (10^4-10^5 cm^{-3} s^{-1}) and at about 40-50 km in the NH (10^3-10^4 cm^{-3} s^{-1}). On the other hand, during the NH summer the lower altitude of the hygropause confines water vapour to the near-surface, where photolysis is very inefficient, yielding maximum dissociation rates at 10 km ($\sim 10^3$ cm^{-3} s^{-1}). During this period, in the southern hemisphere, the photolysis rates are very low at all altitudes ($<10^2$ cm^{-3} s^{-1}) due to the low abundance of water vapour in the atmosphere, which condenses on the polar cap.

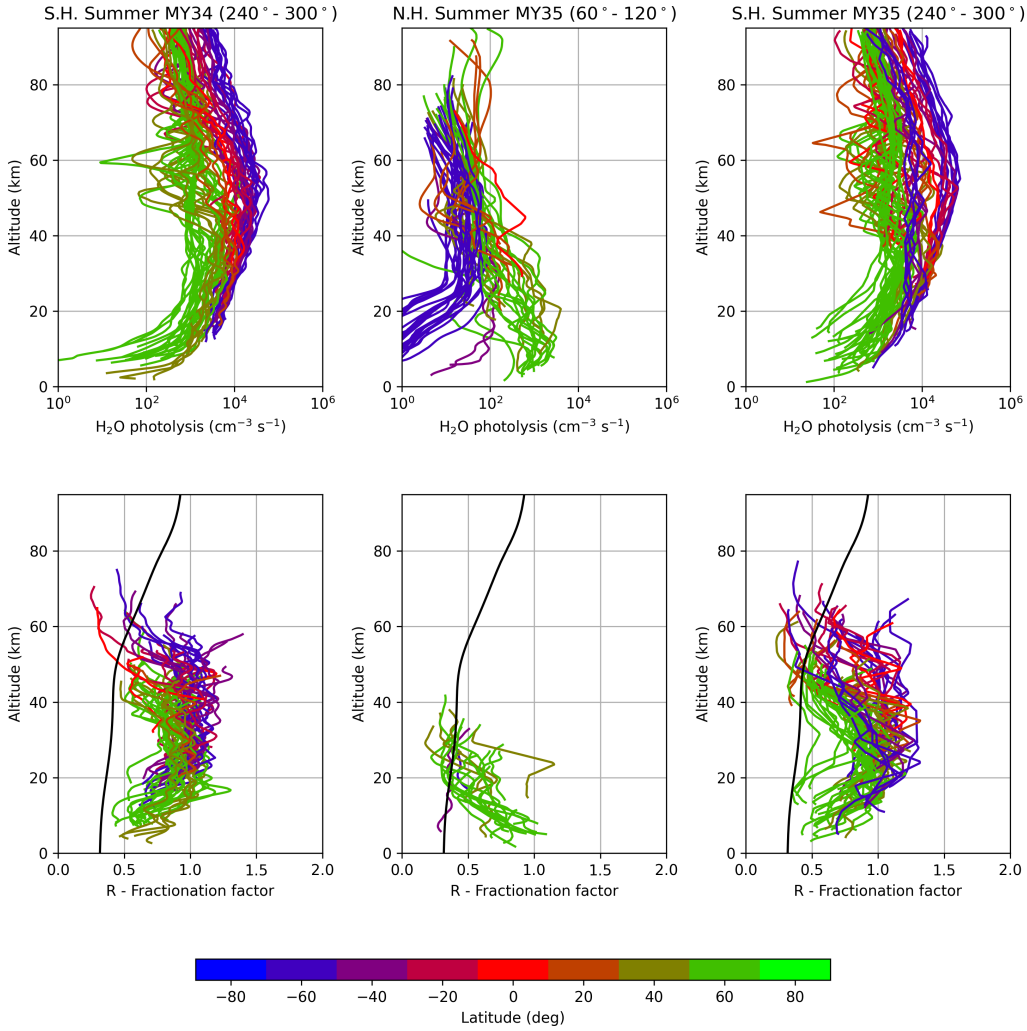

Figure 5.17: Comparison of the estimated impact of fractionation during photolysis for the perihelion and aphelion seasons during MY34 and MY35. The top panels show the estimated H_2O dissociation rates, with the colour of the lines representing the latitude of the observations. The bottom panels show the fractionation factor for the cases of photolysis-induced fractionation R_p (black line) and condensation-induced fractionation R_c (colour-coded lines).

Similarly, we calculate the fractionation factor R relating the D/H ratio in the photolysis products with respect to the mean D/H ratio representative of water in the lower atmosphere (see equation 5.3.3), taking into account the impact of both photolysis-induced fractionation R_p and condensation-induced fractionation R_c (see Figure 5.17). Our calculations show that during perihelion, at the altitudes at which photolysis is more efficient (40-60 km), while water vapour is still not affected by condensation ($R_c \sim 1$), the photolysis-induced fractionation factor is expected to be about $R_p \sim 0.4$-0.5. During aphelion, the role of condensation-induced fractionation increases with respect to perihelion ($R_c \sim 0.5$–0.7), as the decrease of the D/H ratio above the hygropause occurs at low altitudes. However, the role of photolysis-induced fractionation also increases during this period ($R_p \sim 0.3$–0.4), as the bulk of photolysis peaks closer to the surface, where the differences between the photolysis rates of H_2O and HDO are highest.

In order to estimate the total production of OH and H at the observed locations and times, we integrate the calculated photolysis rates shown in Figure 5.17 over the observed column. Figure 5.18 shows the evolution of the column-integrated photolysis rates for more than a full Martian year, revealing the perihelion season to be dominant in the photodissociation of water vapour, with rates approximately 100 times greater than those found close to aphelion. Photochemical models predict atomic H to quickly recombine in the lower atmosphere, while its chemical lifetime increases exponentially with altitude (González-Galindo et al., 2005). In fact, Chaffin et al. (2017) predicts that an increase of the water abundance of 80 ppmv at 60 km yields approximately an increase in the H escape flux of a factor of five in a timescale of days to weeks. In order to take into account the effect of the altitude at which photolysis occurs in the escape rates, we calculate the photolysis rates below and above 60 km, as it is shown in Figure 5.18c. Our calculations suggest that while the photolysis rates above 60 km are very low during aphelion (10^6-10^8 cm^{-2} s^{-1}), they would increase by approximately three orders of magnitude (10^9-10^{11} cm^{-2} s^{-1}) during perihelion. This increase in the photolysis rates during perihelion together with the intensified atmospheric circulation during this period can potentially transport substantial amounts of H to the upper atmosphere (Shaposhnikov et al., 2019; Neary et al., 2020). This result is consistent with measurements of the H and D Lyman-α brightness, representative of upper-atmospheric atomic H and D densities, which show peak values around perihelion (Bhattacharyya et al., 2015; Halekas, 2017; Clarke et al.,

2017).

Similarly, we calculate the column-integrated fractionation factors of D/H, as shown in Figure 5.18d. However, while the calculation of the photolysis-induced column-integrated fractionation factor can be performed using all observed altitudes, the condensation-induced fractionation factor can just be calculated using the altitudes at which the measurements are sensitive to HDO, and missing part of the observed column. Therefore, the condensation-induced fractionation factor is just shown when the atmospheric column density where the measurements are sensitive to HDO is at least 75% of the column density calculated using all observed altitudes. Our calculations show higher fractionation during the aphelion season ($R \sim 0.2$) as compared to perihelion ($R \sim 0.4$). However, while the most fractionating period appears to be the aphelion season, its contribution to the annual average is expected to be negligible, since the photolysis rates during this period are about 100 times lower than those during perihelion.

When calculating the relative contribution of photolysis-induced and condensation-induced fractionation, we observe that the former dominates the fractionation between water vapour and its dissociation products. During the aphelion season, the role of condensation-induced fractionation ($R_c \sim$ 0.4-0.6) increases with respect to perihelion ($R_c \sim$ 0.8-1.0), but so does the role of photolysis-induced fractionation, which is more fractionating in the aphelion season ($R_p \sim$ 0.3-0.5) as compared to perihelion ($R_p \sim$ 0.4-0.6). Besides, as was mentioned before, the contribution of the aphelion season to the annual average is expected to be minor, which strengthens the prevalent role of photolysis-induced fractionation in shaping the isotopic composition of the dissociation products.

It must be noted that the calculations of the fractionation factor R are representative of photolysis below ∼60 km, where the ACS MIR measurements are sensitive to HDO. At these altitudes, the formed H and D will not participate in the direct escape of these species in the upper atmosphere. Instead, most formed OH and H will ultimately recombine into H_2 and contribute to escape at much longer timescales (see section 1.1.4). Our calculations are consistent with the measurement of D/H in molecular hydrogen in the upper atmosphere, which was found to be approximately 2.5 times smaller than the D/H ratio in water ($R = 0.4$)

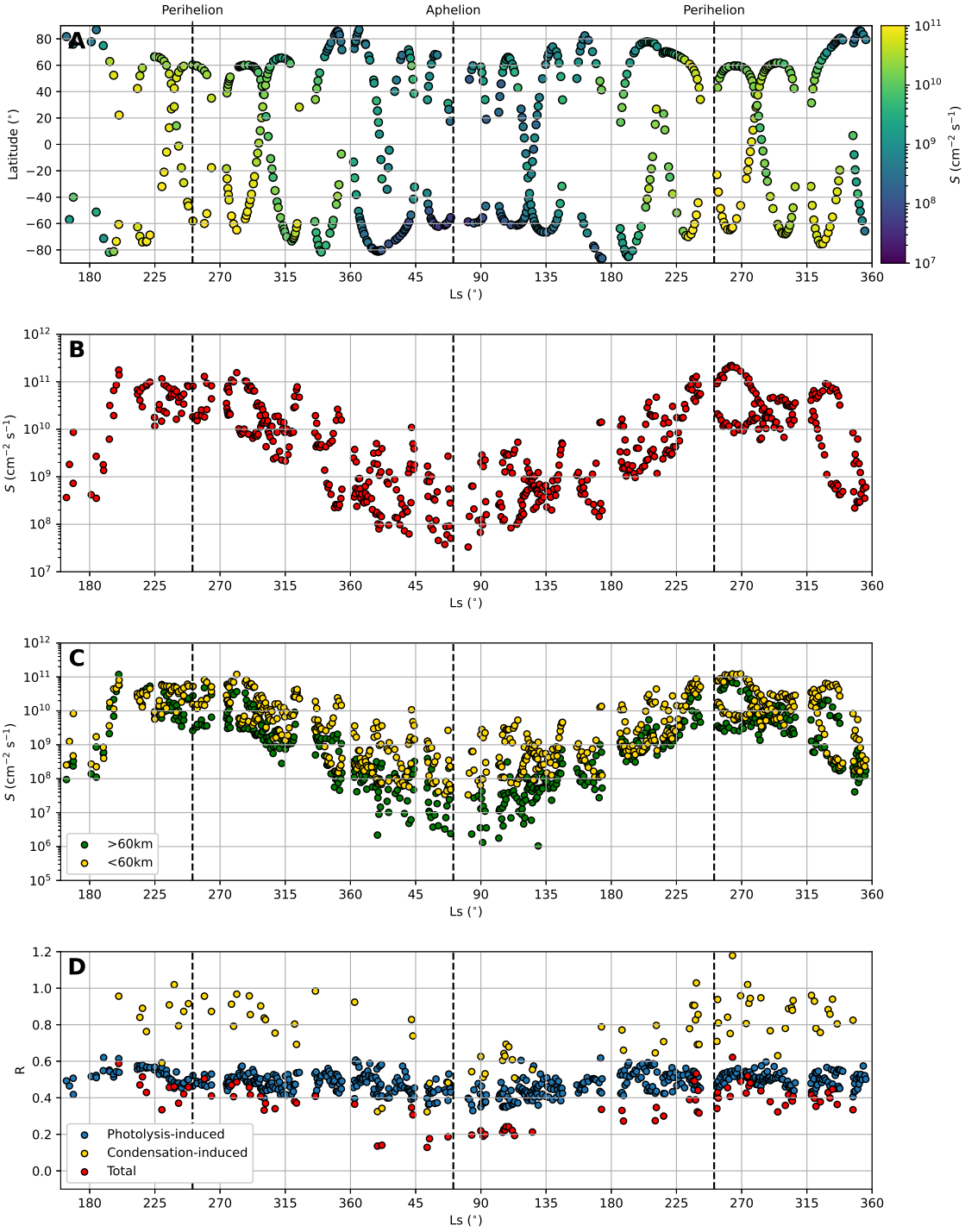

Figure 5.18: Evolution of the water vapour photolysis rates and D/H fractionation factor. A) Latitudinal coverage of the ACS MIR observations, with the colour of the points representing the column-integrated photolysis rate of H_2O. B) Column-integrated photolysis rate of H_2O. C) Column-integrated photolysis rates of H_2O above (green dots) and below (yellow dots) 60 km. D) Column-integrated fractionation factor R for the cases of photolysis-induced (blue dots) and condensation-induced (yellow dots) fractionation, as well as the combination of the two (red dots).

(Krasnopolsky, 2002). Further calculations will be needed to determine the relative impact of condensation and photolysis-induced fractionation above 60 km, where the direct photolysis of water can contribute to escape at short timescales. Our results provide new insights for resolving the old paradigm regarding the role of the different mechanisms in fractionating the D/H ratio of water vapour in the lower atmosphere and its dissociation products, leading to the enrichment of D/H in the atmosphere as it escapes into space.

Similarly, as for HDO, the $H_2^{18}O$ molecules are expected to have a different UV absorption cross-section than the $H_2^{16}O$ ones, which can impact the isotope composition of the dissociation products of water vapour and the efficiency of ^{18}O to escape into space. To our knowledge, there are no available cross-sections for $H_2^{18}O$. However, we can make some estimations on the relative fractionation of $^{18}O/^{16}O$ relative to D/H based on theoretical expectations. Miller and Yung (2000) predict most noticeable differences in the absorption cross-sections of $H_2^{18}O$ and $H_2^{16}O$ for wavelengths $\lambda > 180$ nm, similar to the H_2O-HDO dichotomies, as shown in Figures 1.14 and 5.16. However, while the enrichment function of the cross sections of $HD^{16}O$ over $H_2^{16}O$ ($\epsilon(\lambda) = (\sigma_{HDO}/\sigma_{H2O}$ - 1) $\cdot$ 100) is about ϵ = -60% for $\lambda > 180$ nm, it is only about ϵ = -2.5% in the case of $H_2^{18}O$. With this information, we can estimate that

$$\left(\frac{\sigma_{\mathrm{HDO}}}{\sigma_{\mathrm{H_2^{16}O}}} - 1\right) \cdot 100 = -60 \longrightarrow \frac{\sigma_{\mathrm{HDO}}}{\sigma_{\mathrm{H_2^{16}O}}} = 0.4 \tag{5.3.7}$$

$$\left(\frac{\sigma_{\mathrm{H_2^{18}O}}}{\sigma_{\mathrm{H_2^{16}O}}} - 1\right) \cdot 100 = -2.5 \longrightarrow \frac{\sigma_{\mathrm{H_2^{18}O}}}{\sigma_{\mathrm{H_2^{16}O}}} = 0.975 \tag{5.3.8}$$

If considering that most of the dissociation of water occurs during the perihelion, when the photolysis-induced fractionation factor for D/H is $R_p(\mathrm{D/H}) \sim 0.4$, then we can estimate that this factor will just be $R_p(^{18}O/^{16}O) \sim 0.975$ for $^{18}O/^{16}O$. These calculations reveal a much higher efficiency of of ^{18}O to be transferred to the dissociation products (OH and H) with respect to D.

The different relative efficiency of the isotopologues to be transferred to the photolysis products might explain the dichotomy between the large enrichment in the heavy isotope of the D/H ratio with respect to the primordial values (∼4.9 VSMOW) as opposed to the mild enrichment in the $^{18}O/^{16}O$ ratio (∼1.14 VSMOW): while ^{18}O is efficiently transferred

to the photolysis products of water vapour, HDO molecules are less efficiently photolysed, decreasing the D/H ratio of the lighter species that ultimately the escape to space. Potentially, this difference will make the escape fractionation factor of D/H lower than that of $^{18}O/^{16}O$. Therefore, as H and O escape from the Martian atmosphere, they will enrich more efficiently the D/H ratio than the $^{18}O/^{16}O$ ratio. Nevertheless, it must also be noted that, while the O isotopic composition of the atmosphere may be buffered by interactions with the O in the surface, atmospheric-surface interactions are expected to have a lower influence on the H isotopic composition of the atmosphere (Jakosky, 1991; Fox and Hać, 2010; Jakosky et al., 1994).

5.4 Summary

In the previous chapter, we analysed several ACS MIR observations made using secondary grating position 5 to constrain, for the first time, the vertical distribution of the oxygen isotopic composition of H_2O in the atmosphere of Mars. In this chapter, we have extended this analysis to more than a full Martian year of observations in order to understand how the isotopic composition of H_2O varies with altitude, season and location. However, in order to include D/H in our analysis, we have applied the retrieval scheme to ACS MIR observations made with secondary grating position 4, which allow the monitoring of the D/H and $^{18}O/^{16}O$ isotopic ratios.

Our retrievals have revealed a very different behaviour of the temperature and water cycles during the year. During the SH summer ($L_S = 270°$), which roughly coincides with perihelion ($L_S = 251°$), the greater heating by dust and proximity to the Sun increases the Hadley circulation, allowing warmer temperatures to expand to the middle atmosphere in both the northern and southern hemispheres. The warmer temperatures raise the hygropause level, allowing water vapour to migrate to the middle and upper atmospheres, reaching values greater than 50 ppmv as high as 100 km. In contrast, during the NH summer ($L_S = 90°$), which is closer to aphelion ($L_S = 71°$), water vapour is confined to the lowest scale heights, and the hygropause is set at an altitude of approximately 20 km.

We also found a very dynamic behaviour of the D/H ratio, varying from 1 to 6 VSMOW, with an average non-fractionated isotopic ratio of 4.9 ± 0.4 VSMOW. These variations in the D/H ratio are found to be correlated with those in the temperature and water vapour abundance fields, which reveal condensation-induced fractionation to be the main source of variations of D/H in the Martian atmosphere. In particular, we observe a decrease of the D/H ratio above the hygropause, which is predicted by the preferential condensation of HDO over H_2O during the formation of water ice cloud, and low values of D/H in the lowest observed altitudes during the winter seasons, which is also consistent with the expectations of condensation-induced fractionation onto the polar caps.

From the measured $^{18}O/^{16}O$ isotope ratios throughout more than one Martian year, we have estimated that the value representative of the Martian atmosphere is 1.14 ± 0.08 VSMOW. The observations show variations in the $^{18}O/^{16}O$ isotope ratio with a smaller amplitude than those found in D/H. However, these variations are close to the uncertainty level of the measurements, which means we cannot determine if the variations are real or just an artefact of the observations.

In order to get an insight of the role of water vapour in the production of atomic hydrogen and its relevance to hydrogen escape, we combined the retrieved ACS MIR vertical profiles with calculations of the photodissociation rates of H_2O calculated with the photolysis code of the LMD-GCM (Lefèvre et al., 2004). Our calculations reveal the perihelion season to be dominant in the dissociation of water vapour, with rates approximately 100 times greater than those found close to aphelion. In particular, the photolysis rates above 60 km increase by approximately three orders of magnitude with respect to aphelion, and could participate in the escape of hydrogen from the Martian atmosphere in short timescales.

We also calculated the fractionation factor R relating the average isotopic ratio of water in the lower atmosphere and the isotopic ratio of its photolysis products (OH and H). Our calculations suggest that while condensation-induced fractionation is the main driver of variations of D/H in water vapour, the differential photolysis of HDO and H_2O is a more important factor in determining the isotopic composition of the dissociation products. In particular, we estimated that the D/H ratio of the photolysis products would be approximately 2.0-2.5 times

lower than that of water in the lower atmosphere (D/H = 4.9 ± 0.4 VSMOW).

Similarly, we made some estimations of the corresponding $^{18}O/^{16}O$ isotope ratio in the dissociation products. Our calculations suggest that $^{18}O/^{16}O$ in the dissociation products is approximately 1.025 times smaller than that of water in the lower atmosphere ($^{18}O/^{16}O$ = 1.14 ± 0.08 VSMOW). This higher efficiency of ^{18}O to be transferred to the lighter species, as compared to D, can have implications for understanding the rates at which both $^{18}O/^{16}O$ and D/H in the atmosphere get enriched when these species escape into space.

In the next chapter, we also perform retrievals of ACS MIR observations made with secondary grating position 4, but using a spectral range suitable for the derivation of the isotopic ratios in CO_2.

Chapter 6

Isotopic composition of CO_2 from grating position 4

In the previous chapter, we explained how we used the ACS MIR measurements from secondary grating position 4 to constrain the variations of the D/H and $^{18}O/^{16}O$ isotopic ratios in water vapour, as well as their average non-fractionated values, which are relevant for the understanding of the evolution of water on Mars. In this chapter, we use a similar approach to characterise the isotopic composition of oxygen ($^{18}O/^{16}O$ and $^{17}O/^{16}O$) and carbon ($^{13}C/^{12}C$) in CO_2 in the Martian atmosphere. Precise measurements of the average isotopic ratios in CO_2 can help us understand the evolution of the Martian atmosphere. In addition, monitoring the variations of the isotopic ratios in CO_2 can provide an insight about the different processes that affect CO_2 at present. In order to perform this analysis, we also use ACS MIR measurements from secondary grating position 4, but now focusing in a spectral range between 3635 and 3682 cm^{-1}.

In section 6.1, we introduce the dataset selected for the retrieval of the isotope ratios of CO_2, focusing on the availability of observations that cover the desired spectral range. In section 6.2, we initially explain how the methodology presented in section 3.4 is applied to this dataset. However, due to some systematic behaviours in the retrievals, a slightly different approach employing simpler radiative transfer calculations is applied to these data. Section 6.3 presents the main results of the study, focusing the analysis on the identification of variations in the isotopic ratios of CO_2 in the atmosphere, the derivation of the average non-

fractionated isotope ratios representative of the Martian atmosphere, and the implications of the measurements on our understanding of the escape of carbon dioxide over history. Finally, in section 6.4 we summarise the findings derived from this analysis of the measurements.

The analysis described in this chapter of the thesis has been peer-reviewed and published in *Journal of Geophysical Research: Planets* (Alday et al., 2021b). Although that publication has a number of coauthors, all work presented in this chapter was performed by me, except for the calibration of the ACS MIR transmission spectra, which was performed by Alexander Trokhimovskiy at the Space Research Institute (IKI).

6.1 ACS MIR observational dataset

The observational dataset assembled for this study is similar to that used for the derivation of the isotopic ratios in water vapour (see Chapter 5), which includes ACS MIR observations made with secondary grating position 4. The data from this position includes ten diffraction orders (215-224) expanding over a wavenumber range between 3604 and 3769 cm^{-1}. This spectral range encompasses strong absorption by several isotopologues of CO_2 (see Figures 3.6 and 5.2). In particular, there are two very strong absorption bands of $^{12}C^{16}O_2$ centered at 3615 and 3715 cm^{-1}, respectively. Between these two absorption bands, in a spectral range from approximately 3640 to 3680 cm^{-1}, there is a spectral window in which absorption by $^{13}C^{16}O_2$, $^{18}O^{12}C^{16}O$ and $^{17}O^{12}C^{16}O$ is not contaminated by the much stronger absorption of the main isotopologue, which coincides with the spectral range sampled in diffraction orders 217, 218 and 219. Indeed, in this spectral region, the optical depth of the lines of the minor isotopologues is similar to that of the main isotopologue, as it is the edges of the strong absorption bands of $^{12}C^{16}O_2$ that are sampled (see Figure 6.1).

The analysis of the data for the derivation of the CO_2 isotopic ratios is therefore based on spectra measured with diffraction orders 217, 218 and 219. In particular, five different spectral windows are selected within these diffraction orders, encompassing measurable absorption lines by the four main isotopologues of carbon dioxide ($^{12}C^{16}O_2$, $^{13}C^{16}O_2$, $^{18}O^{12}C^{16}O$ and $^{17}O^{12}C^{16}O$). These diffraction orders are situated in the mid-to-upper parts of the detector frame in which the doubled image is perceived as two-peak absorption lines when using the

row corresponding to the centre of the stripe. In the case of using the slit edge this effect is minimised, at the expense of achieving a lower signal-to-noise ratio (see section 2.2.3). In this chapter, similar to how we derived H_2O isotopic ratios from secondary grating position 4, several rows from the detector frame are combined in order to increase the accuracy of the retrieved profiles and their associated uncertainties.

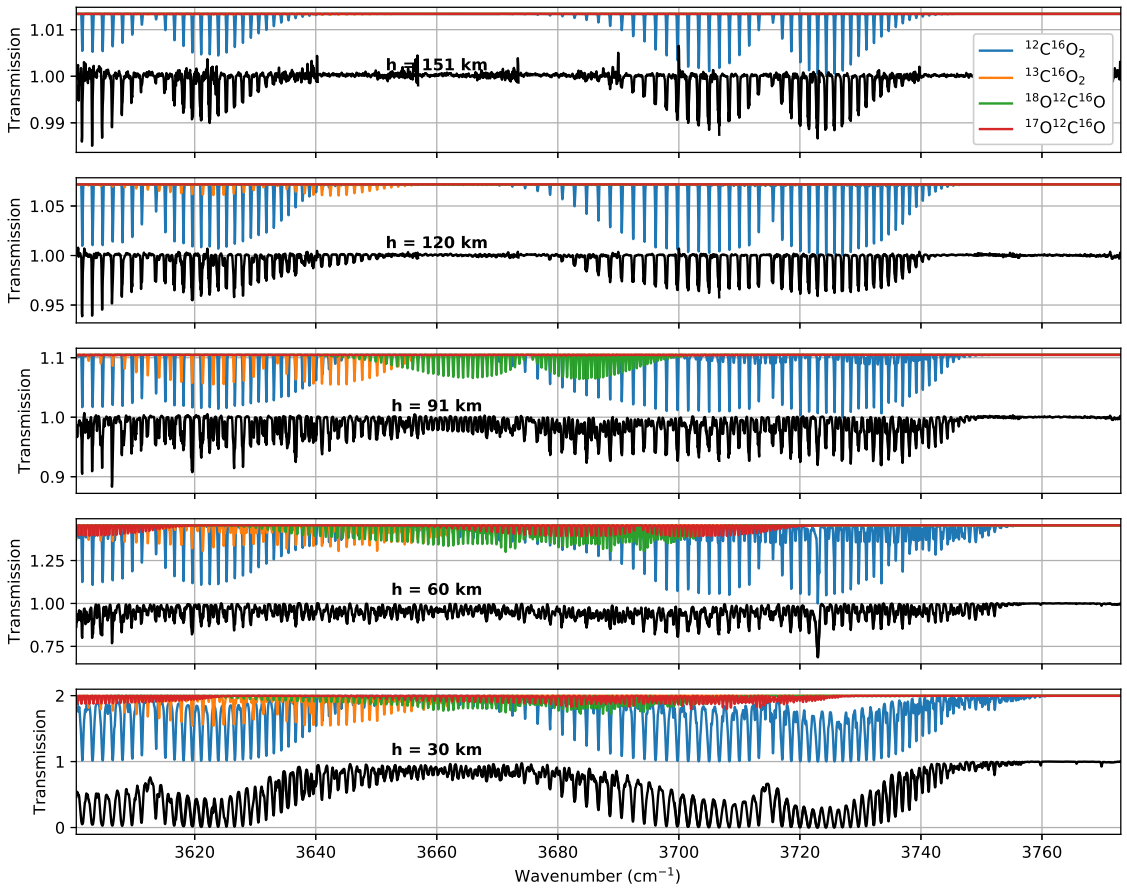

Figure 6.1: Example of an ACS MIR solar occultation in secondary grating position 4. The black lines show the measured spectra at five different tangent heights made during orbit 1849. The coloured and shifted lines represent synthetic spectra showing the contribution from different CO_2 isotopes to the spectrum.

We perform the analysis of the isotope ratios in CO_2 using all available secondary grating position 4 observations from the start of the science operations in March 2018 to the observations made in February 2021. However, during a substantial part of the science operations in this period, observations were made using partial framing, by which only the lower part of the detector frame was recorded and sent to Earth. While diffraction orders 223 and 224, used for the derivation of the H_2O isotope ratios, were situated in the lower part of the detector

and were available in all observations, diffraction orders 217, 218 and 219, which are more relevant to the analysis of the isotopic ratios of CO_2, were excluded when using partial framing. Figure 6.2 shows the evolution of the tangent latitude of the secondary grating position 4 solar occultations, highlighting the observations made using full and partial framing. The full-frame observations, required for the derivation of the CO_2 isotope ratios, are therefore divided in two periods, one covering the range L_S = 164-219° in MY34, and the second one covering the range L_S = 141-356° in MY35.

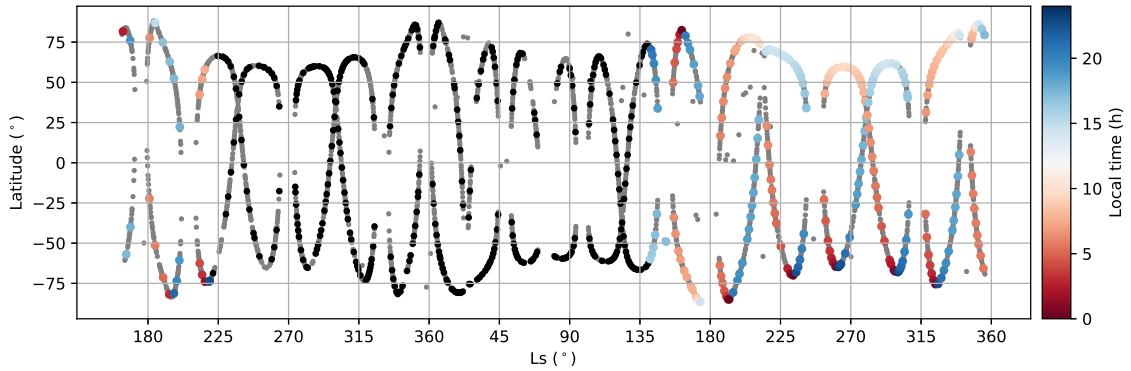

Figure 6.2: Observational coverage of ACS MIR full frame secondary grating position 4 solar occultation observations. The grey points show all available ACS MIR observations up to October 2020. The black points show ACS MIR grating position 4 observations made using partial framing, while the points following the colourbar, which indicates the local time of the occultation, are the points in which full frames were recorded.

6.2 Retrieval scheme

In this section, we present two different approaches used to derive the isotopic composition of CO_2 from ACS MIR secondary grating position 4 spectra. In the first method, we apply the full radiative transfer code presented in section 3.1, which was later applied for the analysis of ACS MIR spectra from secondary grating positions 4 and 5. After analysing the results, some systematic patterns observed in the results led to the development of the second method, which utilises simpler radiative transfer calculations, but can provide a more accurate understanding of the results.

6.2.1 Full radiative transfer approach

The retrieval scheme adopted for the derivation of the isotope ratios of carbon dioxide follows the same philosophy as that used for the characterisation of the isotopic composition of water

vapour from secondary grating positions 4 and 5 (see chapters 4 and 5). The analysis of the data is performed in two steps. First of all, vertical profiles of pressure and temperature are derived from $^{12}C^{16}O_2$ absorption in two spectral windows within diffraction orders 217 and 219 (see Table 6.1). Secondly, the pressure and temperature profiles are fixed, and the vertical profiles of the volume mixing ratio of the four main isotopologues of CO_2 are retrieved independently from all windows, using an *a priori* $^{12}C^{16}O_2$ volume mixing ratio from the Mars Climate Database (Forget et al., 1999) and the telluric isotope composition ($^{13}C/^{12}C$ = 1 VPDB; $^{18}O/^{16}O$ = 1 VSMOW; $^{17}O/^{16}O$ = 1 VSMOW). The rest of the minor isotopologues of carbon dioxide are also fixed and assumed to follow Earth-like fractionation.

Table 6.1: Summary of the spectral windows and retrieval scheme used to derive the pressure, temperature and carbon dioxide isotopic ratio profiles from secondary grating position 4.

Spectral Window	Diffraction Order	Wavenumber range (cm^{-1})	Retrieved Parameters
1	217	3634.5 - 3646.0	p, T ($^{12}C^{16}O_2$) $^{13}C^{16}O_2$
2	217	3646.0 - 3654.0	$^{12}C^{16}O_2$ $^{13}C^{16}O_2$ $^{18}O^{12}C^{16}O$
3	218	3652.5 - 3662.5	$^{13}C^{16}O_2$ $^{18}O^{12}C^{16}O$ $^{17}O^{12}C^{16}O$
4	218	3662.5 - 3672.0	$^{18}O^{12}C^{16}O$ $^{17}O^{12}C^{16}O$
5	219	3672.0 - 3682.0	p, T ($^{12}C^{16}O_2$) $^{18}O^{12}C^{16}O$ $^{17}O^{12}C^{16}O$

Figure 6.3 shows an example of the spectral fitting performed using this method during one solar occultation observation. The agreement between the measured spectra and the modelled one is very good, observing isotopic signatures up to approximately 120 km. The vertical profiles retrieved from each of the spectral windows are then combined using the procedure introduced in section 3.4.5. We find that, despite the good agreement found between the measurement and the retrieval best fit, the retrieved profiles from each of the spectral windows show some significant discrepancies, larger than the derived uncertainties (see Figure 6.4). In principle, the uncertainties associated to the averaged profiles include these discrep-

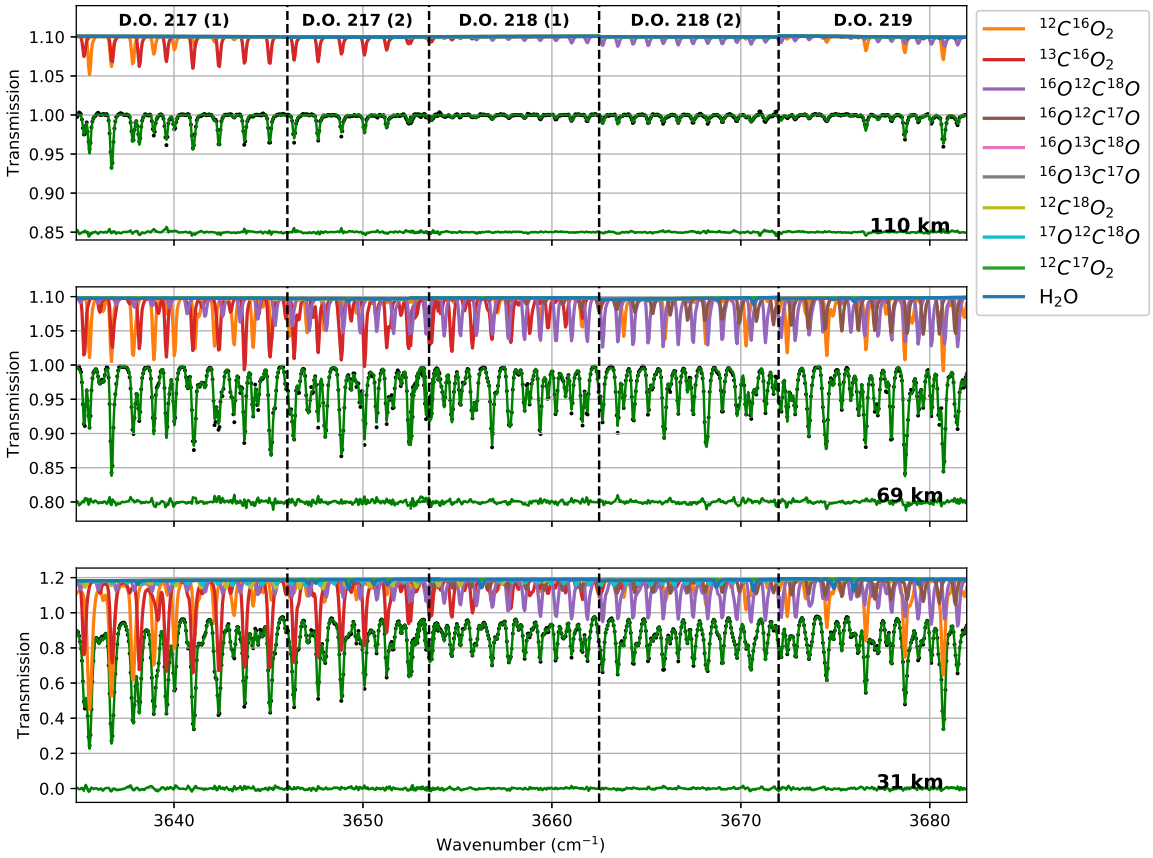

Figure 6.3: Measured spectra (black dots) and best fit to the data (green) at 30 (bottom), 70 (middle) and 110 (top) km for the ACS MIR grating position 4 observation made during orbit 1849. Residuals between the measured and modelled spectra, and the contribution from each gas to the spectra are also shown, including an offset for the clarity of the figure

ancies between spectral windows, which is desirable for the creation of data products with rigorous and reliable uncertainties. However, these large uncertainties impede the derivation of meaningful measurements of the isotopic ratios in CO_2.

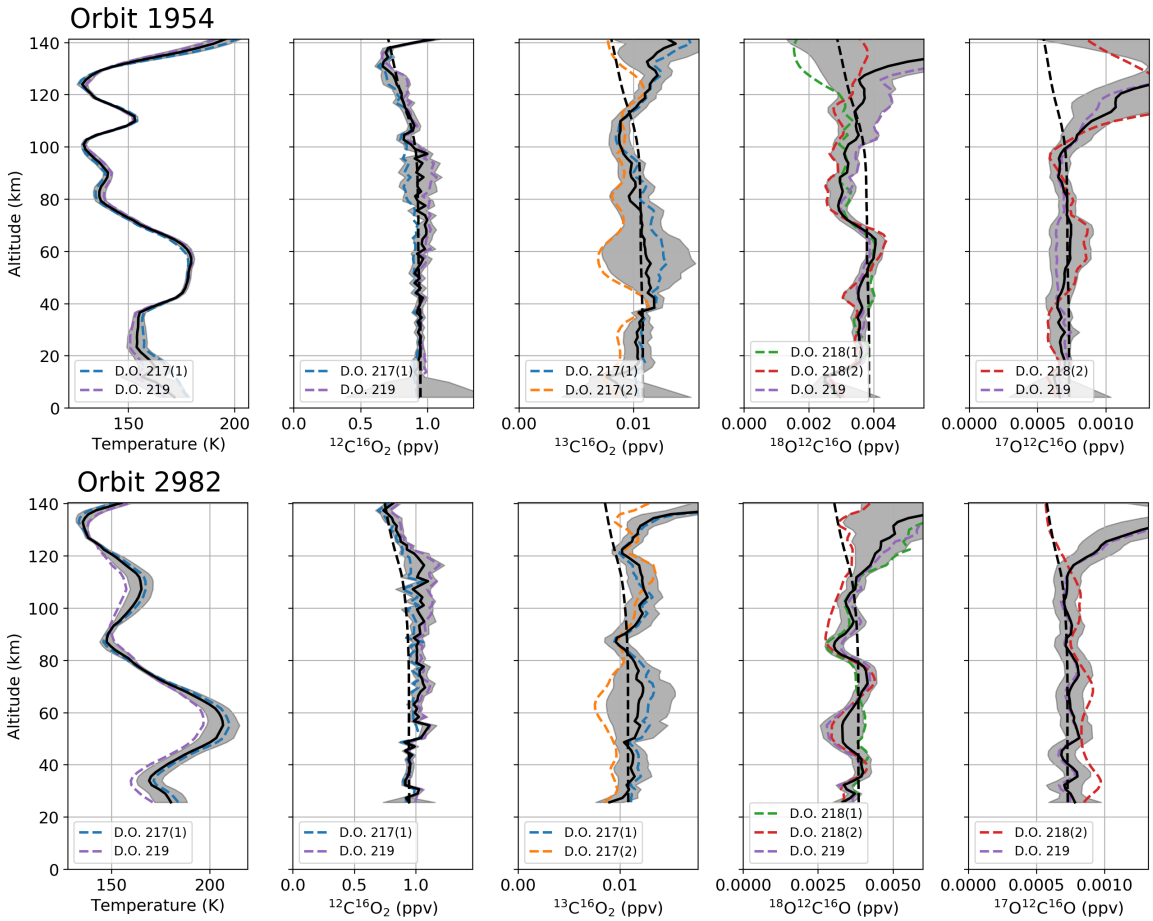

Figure 6.4: Retrieved vertical profiles of temperature and volume mixing ratios of $^{12}C^{16}O_2$, $^{13}C^{16}O_2$, $^{18}O^{12}C^{16}O$ and $^{17}O^{12}C^{16}O$, for the observations made in orbits 1954 (top) and 2982 (bottom). The retrieved profiles from several spectral windows are shown following the colour code in the legends. The black dashed line represents the a priori estimate, and the black solid line and shaded areas represent the averaged profiles and their uncertainties.

Analysing the results from the entire retrieved dataset, instead of focusing the results from each solar occultation observation independently, revealed that the discrepancies found between the different spectral windows are very similar in different observations, providing evidence of the clear systematic behaviour driving the retrievals (see Figure 6.5). This behaviour is especially interesting in the case of the $^{13}C^{16}O_2$ retrievals, which are performed in two spectral windows which belong to the same diffraction order and yet show discrepancies of approximately 40% at 60 km. The systematic behaviour of the retrievals is a sign that one

or more parameters are not being properly accounted for, and impedes the reliability of the results: if instead of having taken these spectral windows, we had chosen slightly different ones, the results would have changed drastically.

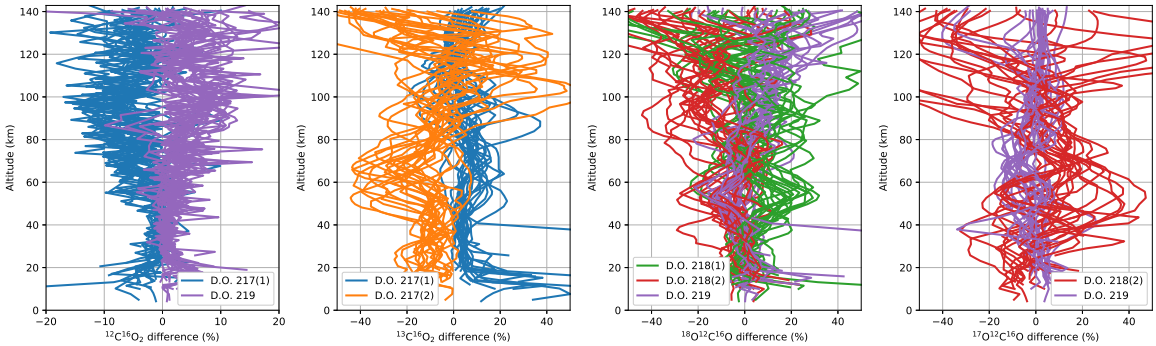

Figure 6.5: Difference between averaged profiles of $^{12}C^{16}O_2$, $^{13}C^{16}O_2$, $^{18}O^{12}C^{16}O$ and $^{17}O^{12}C^{16}O$ and the retrieved profiles from each of the spectral windows in units of percent.

With the purpose of understanding the systematic behaviour of the retrievals, a scheme employing simpler radiative transfer calculations was developed, which is explained in the next subsection.

6.2.2 Slant path approach

The radiative transfer calculations involved in the modelling of an atmosphere are complex, which makes it sometimes difficult to discern the impact of some of the assumptions involved in the calculations of the spectra. Aiming to identify the parameters sourcing the systematic behaviour of the retrievals, a simplified scheme was developed. This simplified scheme models the measured transmission spectra considering the absorption of a homogeneous path with constant pressure and temperature and a certain gaseous composition. The transmission spectrum forward model is calculated using the formulation presented in section 3.1, in which the tuning parameters are the pressure, temperature, line-of-sight density and volume mixing ratio of the different gases. Once computed, the modelled transmission spectrum is then convoluted with the ILS using the double Gaussian parameterisation for ACS MIR (see section 3.4.4).

Although the simplicity of this method is useful for getting an in-depth understanding of the sensitivity of the spectra to the atmospheric parameters, one must also understand its limitations. For example, considering a constant pressure and temperature along the line-of-

sight is unrealistic, as the path actually samples different atmospheric layers with different temperature and pressure. When assuming a constant pressure and temperature along the path, we are assuming that all absorption occurs at the tangent point, with no contribution from the other atmospheric layers. While it is true that most of the absorption occurs at the tangent point at a given tangent height due to the exponentially decreasing atmospheric density with altitude for weak lines, the sensitivity of the spectrum along the line-of-sight can be impacted when absorption lines are saturated (see section 3.1). As the absorption of carbon dioxide sampled by ACS MIR when using secondary grating position 4 is very strong, we only apply the slant path method at high altitudes. In addition, as the aim of this chapter is to retrieve isotope ratios, some of these assumptions will tend to average out.

In the next subsections, we present some tests aiming to understand and accurately model the radiative transfer calculations involved for the retrieval of the isotopic ratios of CO_2 from secondary grating position 4 spectra using the simplified slant path approach.

6.2.2.1 Sensitivity to temperature and pressure

In order to get an insight on the impact of some of the assumptions made in the calculations to the spectra, we first analyse the spectroscopic parameters of the absorption lines from the 2016 edition of the HITRAN database (Gordon et al., 2017). Figure 6.6 shows the line strengths of the four main isotopes of carbon dioxide within the spectral range covered by ACS MIR secondary grating position 4 at different temperatures. It must be noted that the line strengths in the HITRAN database are multiplied with the Earth's average isotopic abundance for each of the isotopologues. In this spectral range, we are essentially sampling the same energy transitions, but the change of one isotope by another shifts the wavenumber at which these transitions occur, so that the absorption band of $^{12}C^{16}O_2$ centred at 3715 cm^{-1} moves to 3635, 3675 and 3695 cm^{-1} for the $^{13}C^{16}O_2$, $^{18}O^{12}C^{16}O$ and $^{17}O^{12}C^{16}O$ isotopologues, respectively. In these, the absorption lines in the edges of the band show a strong dependence with temperature, while those close to the centre show a much milder dependence. In our region of interest for the derivation of the isotopic ratios in CO_2 (black dashed lines in Figure 6.6), the absorption lines of $^{12}C^{16}O_2$ in particular show a change of about two orders of magnitude in the line strengths over a temperature change of 100 K.

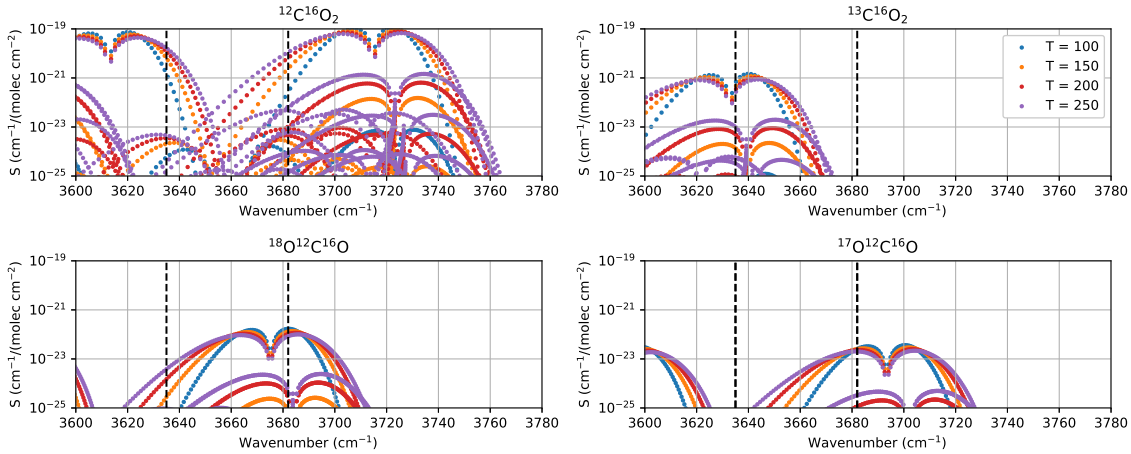

Figure 6.6: Line strength of the absorption lines at 100, 150, 200 and 250 K of the four main isotopologues of CO_2 within the spectral range covered by ACS MIR secondary grating position 4. The region between the black dashed lines shows the spectral region of interest for the derivation of the isotopic ratios in carbon dioxide.

In order to evaluate the effect of the temperature dependence of the absorption lines on the derived isotopic ratios, we perform a retrieval on a single ACS MIR spectrum using the slant path approach. In particular, we select the ACS MIR spectrum measured at an altitude of 100 km during orbit 1849, and we retrieve the fitting parameters (i.e., line-of-sight density, volume mixing ratio of $^{12}C^{16}O_2$, $^{13}C^{16}O_2$, $^{18}O^{12}C^{16}O$ and $^{17}O^{12}C^{16}O$, and parameters defining the ILS) using a grid of fixed temperatures and pressures, varying between 100–225 K and 10^{-5}–10^{-11} atm, respectively. These retrievals are performed independently using the spectral windows presented in Table 6.1. Figure 6.7 summarises the main results of this test, showing the good convergence that can be achieved between the modelled spectrum and the measurement using the slant path approach, and the strong dependence of the retrieved parameters with temperature. The retrieval of the $^{12}C^{16}O_2$ line-of-sight density, as could be anticipated from the analysis of Figure 6.6, shows a very strong dependence on the assumed temperature, suggesting that a small temperature bias will lead to a drastic change in the $^{12}C^{16}O_2$ density. In fact, the temperature dependence of $^{12}C^{16}O_2$ in the spectral windows in diffraction orders 217 and 219 is very similar, indicating that this bias would impact both windows similarly. In the case of the $^{13}C^{16}O_2$ and $^{18}O^{12}C^{16}O$ retrievals of line-of-sight density, these show in general a milder dependence with temperature, but this dependence is different in the several spectral windows. If there is a bias in temperature, the various spectral windows will be impacted differently, providing different results of the retrieved parameters. These results resemble the discrepancies observed in the retrieved profiles from the different spectral

windows when using the full radiative transfer calculations (see Figure 6.5), which might be caused by a small bias in the temperature field.

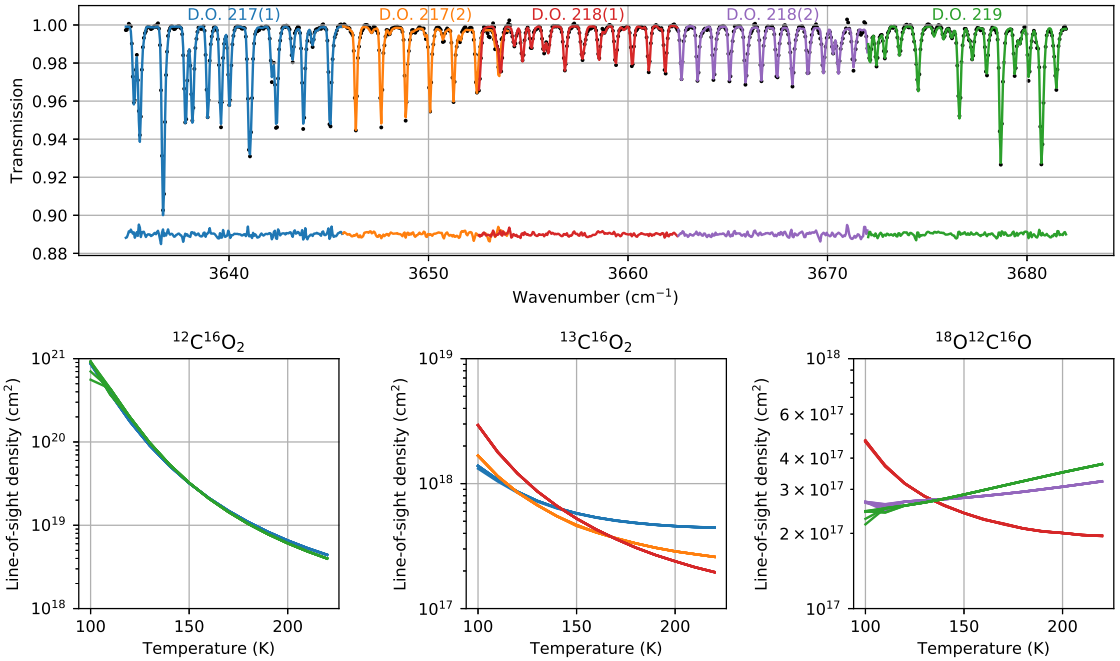

Figure 6.7: Top) ACS MIR measured spectrum at 100 km made during orbit 1849 (black dots) and best fit to the data, with each colour highlighting the spectral window used for each of the independent retrievals. The residuals between the best fit and the measured spectrum are also shown. Bottom) Retrieved line-of-sight densities of $^{12}C^{16}O_2$, $^{13}C^{16}O_2$ and $^{18}O^{12}C^{16}O$ as a function of assumed temperature along the homogeneous path with each colour corresponding to the retrieval performed in a specific spectral window. For each species, there are several lines of the same colour, which correspond to the different cases of assumed pressure.

In principle, the different temperature dependence of each of the spectral windows shows that the correct temperature is such that the densities retrieved from each of these are equal. Therefore, one may be able to retrieve the temperature in each individual spectrum making use of this behaviour. In order to evaluate this possibility, we perform the same retrieval as before, but now including the simultaneous fit of all spectral windows. In particular, we retrieve the atmospheric parameters (i.e., line-of-sight density, volume mixing ratio of $^{12}C^{16}O_2$, $^{13}C^{16}O_2$, $^{18}O^{12}C^{16}O$ and $^{17}O^{12}C^{16}O$) and the parameters defining the ILS, which are specific for each spectral window, over a grid of fixed temperatures and pressures varying between 100–225 K and 10^{-5}–10^{-11} atm, respectively. The results, summarised in Figure 6.8, show that there is a clear minimum of χ^2 between 130 and 140 K, showing that the measurement is best modelled when using a homogeneous path with a temperature in this range. On the other hand, changing the pressure over several orders of magnitude does not influence the level of

agreement between the model and the measurement, nor the other retrieved parameters. It is also observed in Figure 6.8 that the retrieved isotopic ratios are highly sensitive to the temperature of the homogeneous path, meaning that a small discrepancy in the temperature field will yield a strong bias in the derived ratios.

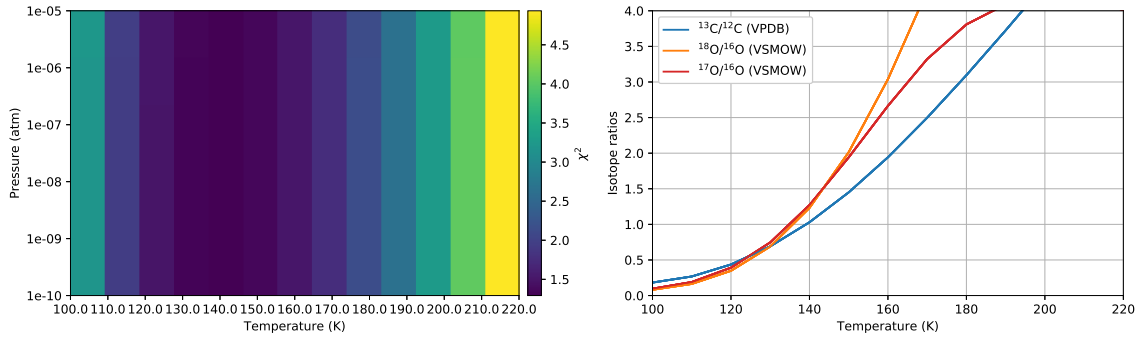

Figure 6.8: Results from the simultaneous retrieval of several spectral windows using the slant path approach. Left) Reduced χ^2 achieved for the different cases of pressure and temperature. Right) Derived isotopic ratios as a function of assumed temperature and pressure.

The dependence of the χ^2 as a function of the assumed temperature indicates that this parameter can be constrained from the data independently of the other retrieved atmospheric parameters. This method for retrieving the temperature field, which was already introduced in section 3.4.1, has its own advantages and disadvantages compared with the method used in the rest of this thesis (see Chapters 4, 5 and section 6.2.1), which relies on the assumption of hydrostatic equilibrium. In particular, while the hydrostatic method requires the simultaneous retrieval of the spectra measured all altitudes, the retrieval of the temperature from the partition functions can be performed independently at each tangent height. In addition, the hydrostatic method requires the assumption of a known CO_2 volume mixing ratio, which might not be accurately captured, especially at high altitudes, by the average climatology estimated with models (see sections 3.4.1 and 1.1.3). The main disadvantage of the temperature retrieval presented in this section is that it requires the analysis of many spectral lines in order to capture the full temperature dependence of the partition functions.

For the particular case of the retrievals of the CO_2 isotopes from secondary grating position 4, the retrievals using several spectral windows from different diffraction orders simultaneously are better behaved than those combining the parameters independently retrieved from each spectral window. One could implement this technique, together with the retrieval of the

temperature field from the partition functions, to the NEMESIS algorithm employing the full radiative transfer calculations. However, these retrievals cannot be easily implemented in practice due to the large number of spectral points that need to be simultaneously computed in each iteration, which is limited by the computational resources. Because of this reason, and given that at every tangent height all parameters can be accurately constrained, we perform the retrievals of the isotopic ratios in CO_2 using the slant path approach, which is described and validated in the next subsection. In addition, in Chapter 7.3, we provide some suggestions for future work that could allow the implementation of this technique to the full radiative transfer calculations.

6.2.2.2 Retrieval of vertical profiles

The experiments performed in the previous subsection reveal that the assumed temperature field has a strong impact on the retrieved parameters, and is possibly the source of systematic patterns found when using the full radiative transfer calculations (see section 6.2.1). However, these tests also reveal that when using all spectral windows at once, the retrievals are better behaved and the atmospheric temperature might be tuned to obtain the best agreement between the measurement and the modelled spectrum, which essentially means that temperature is a parameter that can be simultaneously constrained along with the line-of-sight densities of the different CO_2 isotopologues. In light of the results from these experiments, a new retrieval scheme was developed using the radiative transfer calculations in a homogeneous path, which simultaneously constrains the temperature, the line-of-sight density of $^{12}C^{16}O_2$, the $^{13}C/^{12}C$, $^{18}O/^{16}O$ and $^{17}O/^{16}O$ isotopic ratios, and the parameters defining the ILS for each of the spectral windows included.

This retrieval scheme is also performed using the optimal estimation framework (Rodgers, 2000), but instead of including all tangent heights simultaneously, the measurement acquisitions are retrieved one at a time. Once the retrievals are performed, one can access the retrieved parameters and corresponding uncertainties from the state vector $\mathbf{x}_n$ and the retrieved covariance matrix $\mathbf{S}_t$ (see equations 3.3.3 and 3.3.7). Usually, the retrieved uncertainties of each of the parameters are given by the elements of the diagonal of the covariance matrix, which represent the propagation of errors from the measurement to the retrieved parameters, assuming no correlation between the several parameters. In this specific case, given the strong

impact that temperature has on the retrieved gaseous densities (see Figure 6.8), this assumption is not very accurate, and one must take into account the error in the derived isotopic ratios resulting from the uncertainties in the temperature field. Mathematically, this can be expressed as

$$\sigma_{*R}^2 = \sigma_R^2 + \left(\frac{\partial R}{\partial T}\right)^2 \sigma_T^2 \tag{6.2.1}$$

where the first term represents the propagation of errors from the measurement to the retrieved isotope ratio R, given by the diagonal elements of the covariance matrix, and the second term represents the uncertainty in the ratios due to the uncertainty in the temperature field. One may assume that the relation between the retrieved temperature and isotopic ratios varies linearly for small changes in the temperature, so that

$$R(T) = A + B \cdot T \longrightarrow \frac{\partial R}{\partial T} = B. \tag{6.2.2}$$

The slope of this relation B is related to the Pearson correlation coefficient r_{xy} using

$$B = r_{RT} \cdot \frac{\sigma_R}{\sigma_T}. \tag{6.2.3}$$

The Pearson correlation coefficient is in turn related to the elements of the covariance matrix following

$$r_{RT} = \frac{\sigma_{RT}}{\sigma_R \cdot \sigma_T}, \tag{6.2.4}$$

where σ_{RT} is the covariance between the temperature and the isotopic ratio. Therefore, one may include this source of uncertainty in the isotopic ratios using

$$\sigma_{*R}^2 = \sigma_R^2 + \frac{\sigma_{RT}^2}{\sigma_T^2}. \tag{6.2.5}$$

In a more general definition, the error of any retrieved parameter, including its correlation with other variables, can be calculated following

$$\sigma_{*i}^2 = \sigma_i^2 + \sum_{\substack{j \\ i \neq j}}^{N_x} \frac{\sigma_{ij}^2}{\sigma_j^2}, \tag{6.2.6}$$

where N_x represents the number of elements in the state vector.

This retrieval scheme is applied individually to all acquisitions above 70 km in each solar occultation observation. The retrieved parameters from each individual acquisition are then merged together in order to build up the atmospheric vertical profiles. Figure 6.9 shows an example of the retrieved profiles using the slant path approach from the ACS MIR observation made during orbit 1849. This example shows that, despite the fact that all tangent heights are processed independently and no correlation is assumed between the parameters at different altitudes, the retrieved vertical profiles of temperature and the isotopic ratios show smooth variations, which is a sign of the good convergence and applicability of the approach.

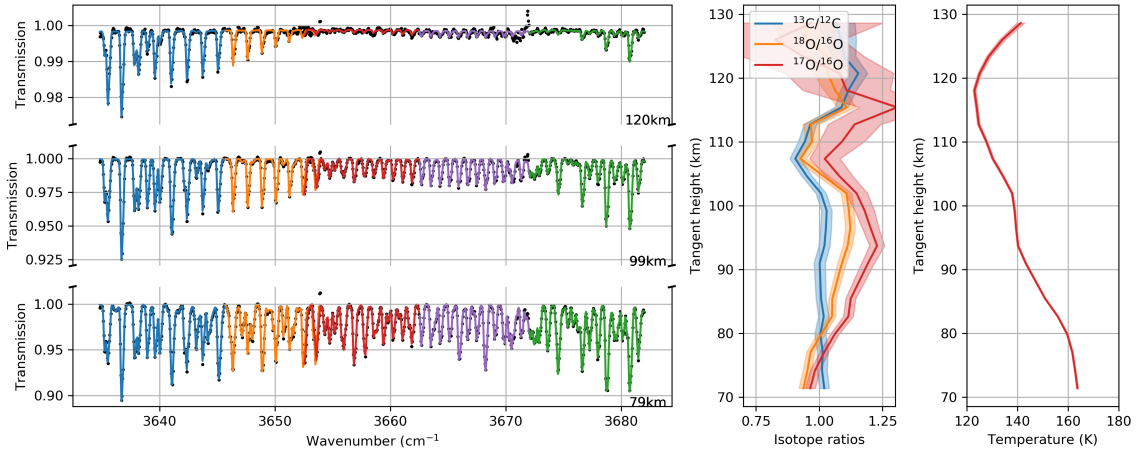

Figure 6.9: Summary of the retrieval of vertical profiles using the slant path approach. The left panels show the measured (black dots) and best fit spectrum (coloured lines) at three different altitudes, with the different colours representing the spectral windows that are chosen for optimising the ILS parameters. The panels on the right show the retrieved vertical profiles of the different isotopic ratios, as well as the temperature field.

In order to evaluate the impact of the row selection in the retrieved parameters, the retrievals are performed using six different spectral rows from the detector, which are later combined following the approach explained in section 3.4.5. Similarly as discussed for the retrieval of the H_2O isotopes from this grating position, the combination of different spectral rows from the detector is essential for the reliability of the results. Figure 6.10 shows three examples of how these profiles are combined, aiming to highlight the variability of cases that are found in these retrievals. In the first case, the retrieved profiles from the two detector rows look very much alike, yielding low uncertainties in the averaged profile. In the second case, while the temperature and isotope ratio profiles derived from the two rows follow similar trends, they

show differences greater than the estimated uncertainties, indicating the presence of systematic errors that are not accounted for in the retrievals. In the third example, the vertical profiles retrieved from the two detector rows show vast differences, which are too large to derive any conclusive information from them. These examples show that while the retrievals might have some unpredictable behaviours in some cases, the combination of different rows from the detector proves to be a reliable method for estimating the true uncertainty of the retrievals.

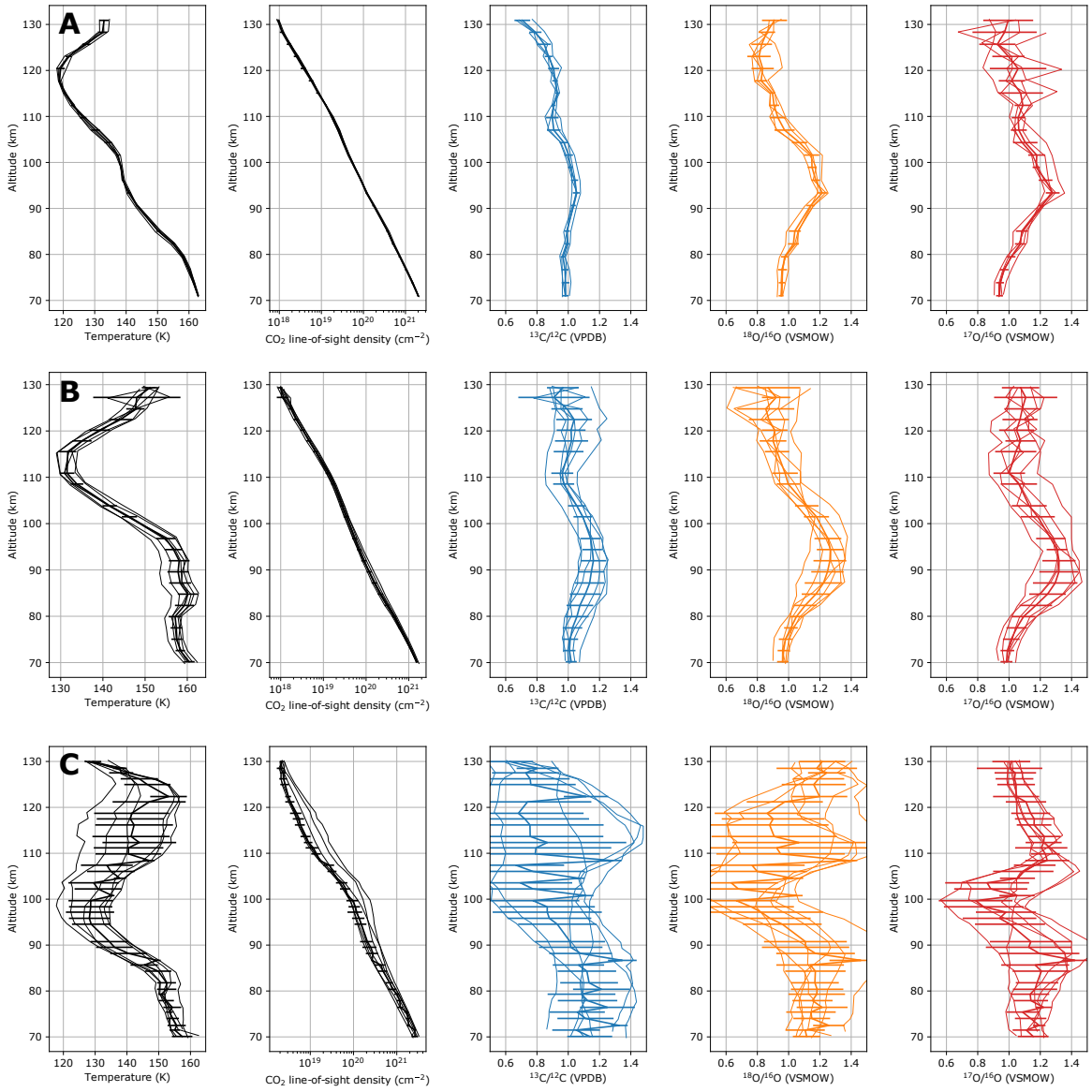

Figure 6.10: Combination of the retrieved vertical profiles from two different detector rows in secondary grating position 4. The three sets of panels show the retrieved vertical profiles of temperature (left), CO_2 line-of-sight density (middle) and the isotopic ratios (right) derived from six different detector rows (narrow lines), for the observations made during orbits 1849 (A), 2304 (B) and 10748 (C). The panels also show the averaged profiles and their corresponding uncertainties (thick lines) .

Finally, in order to validate retrievals made using the slant path approach, we compare the retrieved temperature profiles in this study with those retrieved from diffraction order 223 for the derivation of the isotopic ratios in H_2O, which relied on the assumption of the hydrostatic equilibrium equation (see Chapter 5). Figure 6.11 shows a comparison between the retrievals made with the two approaches, indicating a good agreement between the two. In particular, when calculating the differences derived from the whole dataset, we observe that they are of the order of 4 K. We take this small differences as proof of the good convergence achieved with both approaches. However, although this level of uncertainty is acceptable for most purposes, it can have a substantial impact in the measurement of the isotopic ratios of CO_2 from this spectral range. In particular, we estimate from the analysis shown in Figure 6.8 that a bias of 4 K in the temperature field would yield a systematic uncertainty of ∼20% in the isotopic ratios. It must be noted that the impact of temperature biases on the measurements of the isotope ratios made using the slant path approach is accounted for while calculating their uncertainties (see equation 6.2.6). Therefore, the retrieval scheme developed using the slant path approach can provide a good estimate of the temperature field at each altitude, as well as a realistic estimate of the uncertainties of the derived isotopic ratios in CO_2.

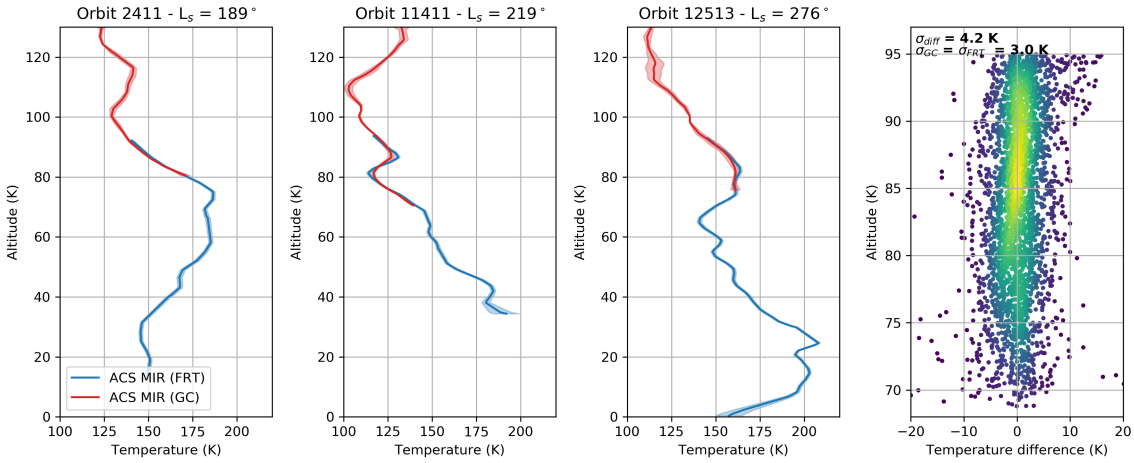

Figure 6.11: Comparison between the temperature retrievals made with the slant path approach in diffraction orders 217-219, and those made with the hydrostatic equilibrium approach from diffraction order 223. The three left panels show a comparison of the retrieved profiles in three different orbits during MY34 and MY35. The right panel shows the difference between the two approaches in the altitude region these retrievals overlap for all observations in the dataset. The standard deviation of the difference between the two approaches is 4.2 K. Assuming both approaches provide similar sensitivity, the uncertainty of each approach would be 3 K.

6.3 Results

The retrieval scheme based on the slant path approach is applied to all available solar occultation observations made with secondary grating position 4 in which the full frames were recorded, from the start of the science operations in March 2018 to February 2021 (see section 6.1). These retrievals allow the monitoring of the vertical profiles of temperature, line-of-sight CO_2 density and the isotopic ratios in CO_2 ($^{13}C/^{12}C$, $^{18}O/^{16}O$ and $^{17}O/^{16}O$) between 70 and 130 km. The results derived from the analysis of the ACS MIR secondary grating position 4 data are summarised in Figure 6.12, which shows the evolution or climatology of the retrieved atmospheric parameters. In the following subsections, these results are displayed in different manners to highlight the aspects of the data most relevant for the purposes of this thesis. In section 6.3.1, we analyse the evolution of the isotopic composition of CO_2 focusing on the understanding of the observed variations. Section 6.3.2 deals with the estimation of the average non-fractionated isotope ratios representative of CO_2 in the atmosphere of Mars, which must be accurately constrained to provide a meaningful understanding of evolution of the Martian atmosphere. Finally, in section 6.3.3 we discuss the importance of these measurements and findings to our understanding of the escape fractionation factor and the enrichment of the isotope ratios as the atmosphere escapes into space.

6.3.1 Variations of the isotope ratios in carbon dioxide

The evolution of the retrieved parameters in Figure 6.12 shows variations above the level of measured uncertainties, suggesting that these variations are not caused by the statistical error of the measurements, but by real processes in the atmosphere. To first order, the variations do not appear to follow any distinguishable patterns as a function of solar longitude or latitude, but they show repeatable patterns as a function of altitude.

Figure 6.13 shows the retrieved vertical profiles of the isotopic ratios of CO_2 from the whole dataset, as well as the average from these, which represents the altitude trends of the measured isotopic ratios. These trends indicate that above approximately 100 km, the $^{13}C/^{12}C$ and $^{18}O/^{16}O$ ratios show a steady decrease as a function of altitude. Below this altitude, the isotope ratios are approximately constant and consistent with Earth-like fractionation. In the case of the $^{17}O/^{16}O$ ratio, while the measurements below 100 km also show a consistent value

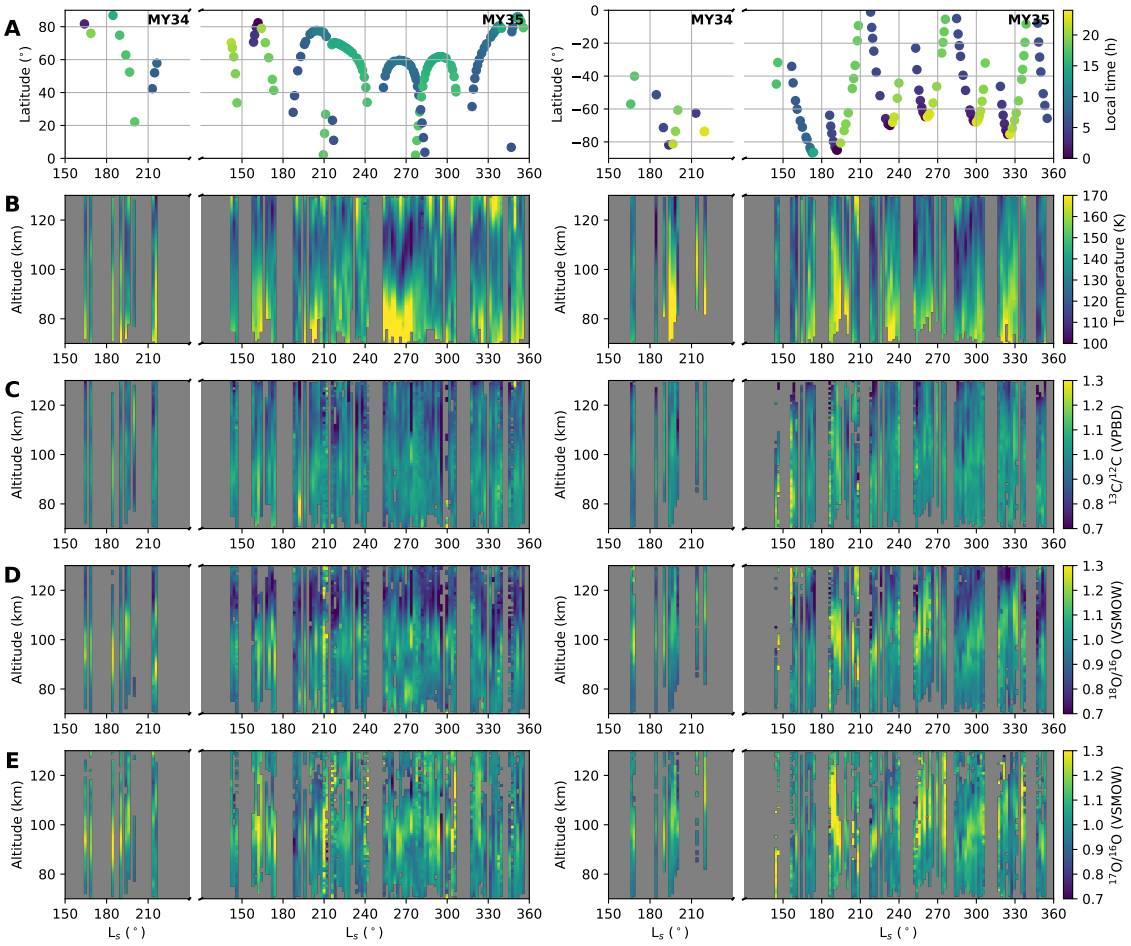

Figure 6.12: Climatology of the retrieved atmospheric parameters. The panels show the values of the retrieved parameters as a function of altitude and solar longitude for the northern (left) and southern (right) hemispheres. A) Distribution of ACS MIR solar occultation observations, with the local time represented by the colour bar. B) Atmospheric temperature. C) $^{13}C/^{12}C$ ratio in carbon dioxide with uncertainties lower than 0.15 VPDB. D) $^{18}O/^{16}O$ ratio in carbon dioxide with uncertainties lower than 0.15 VSMOW. E) $^{17}O/^{16}O$ ratio in carbon dioxide with uncertainties lower than 0.15 VSMOW.

with respect to Earth, the large uncertainties above this altitude impede to conclude if this isotope ratio also decreases with altitude. Such a decrease of the isotopic ratios with altitude is consistent with the expectations from the diffusive separation of the different isotopologues, which predict the density of each of these to decrease according to their own mass-dependent scale heights above the homopause (see equation 1.1.4). Slipski et al. (2018) constrained the altitude of the homopause in different seasons, local times and locations using the ratio of N_2 to Ar densities measured by NGIMS onboard MAVEN. These results show that the homopause is typically set at altitudes between 90 and 110 km, which agrees with the altitude at which we observe the decrease of the isotopic ratios.

Fractionation due to diffusive separation occurs because of the slightly different mass of the several isotopologues, which requires the variations of the isotope ratios to follow the expectations from mass-dependent fractionation (i.e., $\delta^{13}C \sim 0.5 \times \delta^{18}O$). Panel D in Figure 6.13 shows the values of the $^{13}C/^{12}C$ and $^{18}O/^{16}O$ isotope ratios measured above 100 km, which show a positive linear correlation with a Pearson correlation coefficient of 0.8. In order to calculate the slope of the correlation we perform a linear regression which suggests that the measurements follow fractionation given by $\delta^{13}C = 0.54 \times \delta^{18}O$, which is therefore in agreement with the expectations from mass-dependent fractionation. Therefore, we conclude that the decrease of the isotope ratios with altitude is most likely caused by the diffusive separation above the homopause.

A different pattern of variations of the isotopic ratios as a function of altitude is observed during the observations made in MY34 (see Figure 6.14). These observations, made shortly after the Autumn equinox in the northern hemisphere, show a significant increase of the oxygen isotope ratios ($^{18}O/^{16}O$ and $^{17}O/^{16}O$) of carbon dioxide from 0.9-1.0 VSMOW at 80 km, to 1.1-1.2 VSMOW at 95-105 km. This increase appears not to be followed, at least to the same extent, by the carbon isotopic ratio. This distinctive pattern in the oxygen isotopic ratios also appears in other occasions, although the retrieved profiles in these other periods look more scattered than those measured during MY34 (see Figure 6.12). In order to analyse the relative fractionation of the different isotopologues in these occasions, the measured isotope ratios in carbon dioxide are plotted against each other (see Panels D and E in Figure 6.14). This shows that, while the relation between $^{18}O/^{16}O$ and $^{13}C/^{12}C$ follows to first order the

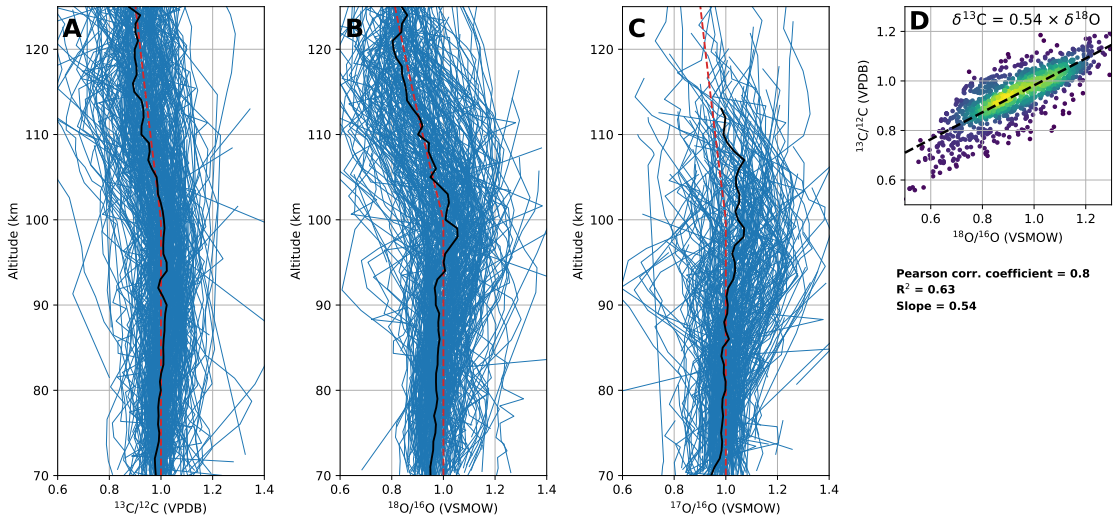

Figure 6.13: Altitude trends of the observed isotopic ratios. The blue lines represent all measured vertical profiles of $^{13}C/^{12}C$ (A), $^{18}O/^{16}O$ (B), and $^{17}O/^{16}O$ (C) with uncertainties lower than 0.075 VPDB and VSMOW. The solid black line is the averaged profile from all the observed profiles, which represents the altitude trends of the isotopic ratios. The red dashed line represents the expectations from diffusive separation assuming a constant temperature of 100 K and a homopause altitude of 100 km. (D) Correlation plot between the observed $^{13}C/^{12}C$ and $^{18}O/^{16}O$ isotopic ratios above 100 km, where the colour of the points represents the density of points. The black dashed line represents the best fit to this correlation using linear regression, showing that both isotopic ratios vary following approximately the expectations from mass-dependent fractionation ($\delta^{13}O \sim 0.5 \times \delta^{18}O$).

expectations from mass-dependent fractionation (δ^{13}C $\sim 0.5 \times \delta^{18}$O), both oxygen isotopic ratios appear to be equally enriched with respect to the standard (δ^{18}O $\sim \delta^{17}$O).

With this information, and without modelling constraints, it is difficult to attribute the observed fractionation to a specific atmospheric process. The ultraviolet photolysis cross-sections of the heavy isotopes of carbon dioxide are smaller than those of the main isotopologue, which would therefore deplete the photolysis products in the heavy isotopes, leaving the unphotolysed CO_2 relatively enriched in these (see section 1.1.5.2). However, based on the calculations of the cross-sections reported by Schmidt et al. (2013), photolysis would preferentially fractionate the ^{13}C/^{12}C ratio over both oxygen ratios, which would require δ^{13}C/δ^{18}O > 1. In addition, these calculations predict the oxygen ratios to follow mass-dependent fractionation, while the observed relation is close to unity (δ^{18}O $\sim \delta^{17}$O).

Oxygen isotope ratios in carbon dioxide in the Earth's stratosphere show a significant enrichment in the heavy isotopes (δ^{18}O $\sim$ 50 ‰) and not following the expectations from mass-dependent fractionation (Thiemens et al., 1995). The data measured by Thiemens et al.

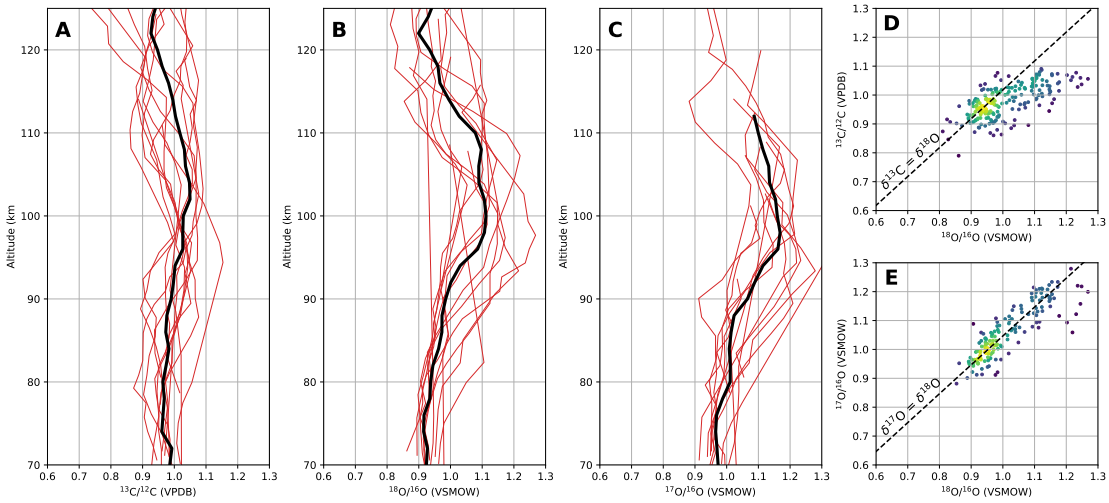

Figure 6.14: Altitude variations of the isotopic ratios in CO_2 during the observations made in MY34. The red lines represent the measured vertical profiles of $^{13}C/^{12}C$ (A), $^{18}O/^{16}O$ (B) and $^{17}O/^{16}O$ (C) with uncertainties lower than 0.075 VPDB and VSMOW. The solid black line is the averaged profile from all the observed profiles. The correlation plots between $^{13}C/^{12}C$, $^{18}O/^{16}O$ and $^{17}O/^{16}O$ (D,E) show that while the O isotopic ratios increase in the 90-110 km region with the same magnitude ($\delta^{18}O \sim \delta^{17}O$), this increase is not followed by the $^{13}C/^{12}C$ isotopic ratio ($\delta^{13}C < \delta^{18}O$).

(1995) suggest a relation between both isotope ratios to follow $\delta^{17}\mathrm{O} = 1.16 \times \delta^{18}\mathrm{O}$, although later studies have suggested that the slope could be even steeper, reaching values as high as 2.22 (Lämmerzahl et al., 2002; Wiegel et al., 2013). The mass-independent fractionation of stratospheric CO_2 appears to be a result of its interaction with other oxygen-bearing species (O_2 and O_3), and its relative enrichment depends on the relative mixing ratios of these (Shaheen et al., 2007; Wiegel et al., 2013). It must be noted that while O_3 and O_2 are very abundant in the Earth's stratosphere relative to CO_2, which can effectively enrich the isotopic ratios in CO_2, carbon dioxide is the major species in the atmosphere of Mars. Therefore, it seems implausible that these reactions are responsible for the observed increase in the isotopic ratios of CO_2.

6.3.2 Estimation of the non-fractionated isotope ratios

Estimations of the average non-fractionated isotopic ratios are essential for our understanding of the evolution of the atmosphere of Mars. In order to constrain these values, it is essential to understand how these relate to the isotopic ratios inferred from the measurements, which might be subject to fractionation processes in the atmosphere. Figure 6.15 shows a histogram of the isotope ratios in carbon dioxide and the corresponding uncertainties measured in the whole dataset, showing the points with uncertainties lower than 0.1 VPDB in the case of the

$^{13}C/^{12}C$, and 0.1 VSMOW in the case of $^{18}O/^{16}O$ and $^{17}O/^{16}O$.

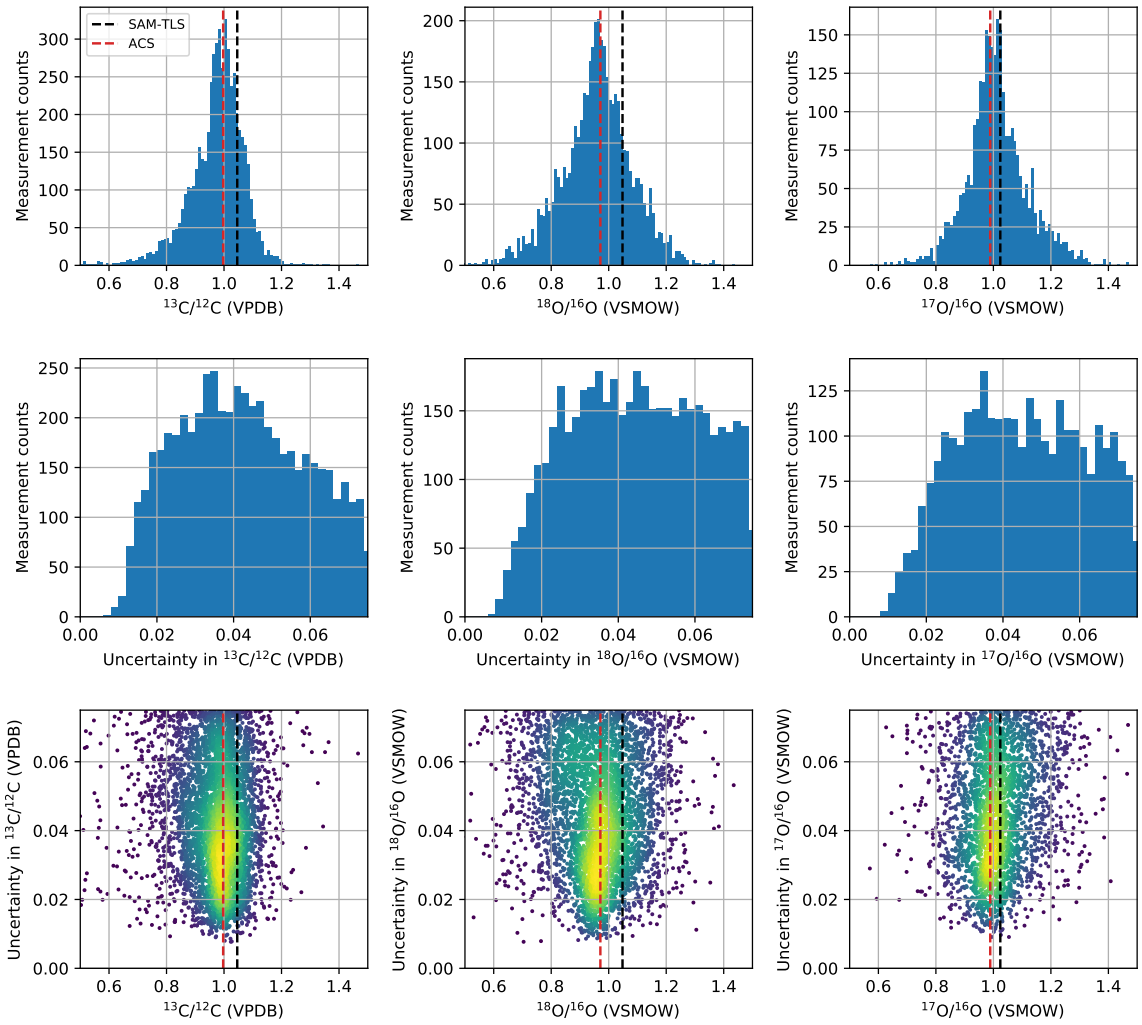

Figure 6.15: Histogram of the measured $^{13}C/^{12}C$, $^{18}O/^{16}O$ and $^{17}O/^{16}O$ isotopic ratios (top) and the retrieved uncertainties (middle). The bottom panel shows the relation between the measured values and the associated uncertainties, where the colour of the points represents the density of measured points. The black dashed lines in the bottom panels represent the value of the isotope ratios measured by Webster et al. (2013), while the red ones represent the values derived from the ACS dataset.

The observed values of the $^{13}C/^{12}C$ ratio show variations from approximately 0.7 to 1.2 VPDB. These variations are larger than the derived uncertainties, which most typically lie within 0.020 and 0.04 VPDB. The distribution of measured values resembles a Gaussian function centered at 1 VPDB, although a more quantitative analysis reveals that the observed distribution is not completely symmetrical, but slightly more populated in values $^{13}C/^{12}C <$ 1 VPDB. Averaging the observed distribution yields a mean value of $^{13}C/^{12}C = 0.973$ VPDB. While this value is representative of the average of our observations, it does not necessarily mean this is the average value of the isotopic ratio in the Martian atmosphere. Indeed, this

is most likely lower than the isotope ratio inferred for the lower atmosphere of Mars, since it includes the measurements made above the homopause, where the isotopic ratio starts to decrease due to diffusive separation (see Figure 6.13). Instead, we consider that a more accurate estimation of the isotopic ratio representative of the Martian atmosphere from the ACS MIR measurements is given by the mode of the distribution, which represents the most frequent measured value. In this case, we derive an isotopic ratio of $^{13}C/^{12}C = 0.997 \pm 0.037$ VPDB, where the error corresponds to the average of the measured uncertainties (see Figure 6.15).

A similar analysis can be carried out to estimate the average oxygen isotopic composition of carbon dioxide in the Martian atmosphere. The observed values of the $^{18}O/^{16}O$ ratio range from approximately 0.6 to 1.3 VSMOW, with an average ratio of $^{18}O/^{16}O = 0.979$ VSMOW. However, these values will also be influenced by fractionation processes, either enriching or depleting them in the heavy isotope with respect to the average (see Figures 6.13 and 6.14). If we again consider the mode of the distribution of measurements and uncertainties as a more reliable estimate of the average non-fractionated isotopic ratio, we derive $^{18}O/^{16}O = 0.971 \pm 0.038$ VSMOW. In this case, the mode of the distribution is lower than the average, opposite to the case of the $^{13}C/^{12}C$ ratio, due to the presence of highly enriching fractionation affecting mostly the $^{18}O/^{16}O$ and $^{17}O/^{16}O$ isotope ratios, but much more mildly the $^{13}C/^{12}C$ one.

Finally, the distribution of measured values of the $^{17}O/^{16}O$ ratio also appears to be asymmetrical, being more populated in values $^{17}O/^{16}O > 1$ VSMOW, due to the presence of isotopic fractionation (see Figure 6.14). The range of observed variability in this case expands from approximately 0.75 to 1.35 VSMOW, with an average value of 1.018 VSMOW. The mode of the distribution in this case is given by $^{17}O/^{16}O = 0.989 \pm 0.041$ VSMOW, which does not show any evidence of enrichment or depletion in the heavy isotope with respect to the standard.

The derived non-fractionated isotope ratios representative of the Martian atmosphere may be compared to those reported in other studies (see Table 6.2). In particular, special attention is given to the comparison with the measurements from the SAM-TLS instrument on the Curiosity Rover (Webster et al., 2013), which show the lowest uncertainties and are often used

as the isotopic ratios representative of the present-day atmospheric reservoir in evolutionary models (Hu et al., 2015; Jakosky, 2019). These measurements were made on various occasions (∼5 sols) during the first months of the mission operations, collecting gas samples in the late afternoon through shortly after midnight. The measurements revealed an enrichment in the heavy isotopes of carbon dioxide ($^{13}C/^{12}C = 1.046 \pm 0.004$ VPDB; $^{18}O/^{16}O = 1.048 \pm 0.005$ VSMOW; $^{17}O/^{16}O = 1.024 \pm 0.005$ VSMOW). While these results are nominally consistent with our measurements, our derived non-fractionated values do not show any evidence of enrichment in the heavy isotopes with respect to Earth. We suggest two possible scenarios to reconcile the measurements by the Curiosity Rover and those in this study:

- First of all, it must be noted that the measurements presented in this study are made at high altitudes (70-130 km), while those from the Curiosity Rover are made on the surface. The lower values of the isotope ratios observed with ACS MIR might be indicative of fractionation of the CO_2 isotopes between the lower and the upper atmospheres. However, it is not clear which processes could generate such depletion in the isotopic ratios. Condensation of CO_2 into ice clouds would preferentially deplete the atmosphere in the heavy isotopes, but this is expected to be very mild, especially for the carbon isotopes (Eiler et al., 2000). In addition, while formation of CO_2 ice clouds occurs sporadically in the Martian atmosphere (see section 1.1.3), the isotope ratios measured with ACS MIR are monitored for more than half of a Martian year, which makes unlikely the possibility of this mechanism to continuously fractionate the isotopes. Another mechanism potentially depleting the isotope ratios with altitude is due to diffusive separation above the homopause. The altitude at which the homopause is located is highly variable with season, latitude and local time, but typical values range close to 100 km (Slipski et al., 2018). In order to estimate the role of this mechanism in our derived averaged values, we calculate the mode of the distribution, but using only the measurements from 70 and 90 km. We find that the derived values do not change significantly, which means that diffusive separation cannot explain the discrepancy between the measurements of the Curiosity Rover and those presented in this study.

- Secondly, it must be noted that while measurements reveal the isotopic composition at a given location and time, these values are not necessarily representative of the atmosphere as a whole, since they might be fractionated by climatological processes. We

believe the continuous monitoring of the atmosphere included in our dataset, which allows averaging over hundreds of measurements spanning many locations and seasons, enables the derivation of the non-fractionated values. In that sense, although the measurements made by the Curiosity Rover are more precise, they are always made in the same location, at approximately the same local times, and covering only about 10% of a full Martian year. The contribution from seasonal cycling to these measurements is unknown, and so they might therefore not be representative of the whole atmosphere. Indeed, the measurements of Livengood et al. (2020) revealed high variability of the $^{18}O/^{16}O$ isotopic ratio, varying from $\delta^{18}O$ = -92 ± 23 ‰ to $\delta^{18}O$ = 71 ± 18 ‰ over a surface temperature increase from 266.9 to 275.4 K, which is most likely caused by an interaction between the surface and the atmosphere. This hypothesis is also supported by the values derived from different studies (see Table 6.2). Especially noticeable is the comparison between the measurements made by Phoenix (Niles et al., 2010) and Curiosity (Webster et al., 2013): while they provide similar uncertainties, the derived isotope ratios do not overlap, which might be indicative of isotopic fractionation in the atmosphere.

Table 6.2: Measured isotope ratios in CO_2 compared to previous studies, expressed as a deviation with respect to the VPDB and VSMOW standards, which are representative of Earth-like fractionation.

Reference	Method	δ^{13}**C (‰)**	δ^{18}**O (‰)**	δ^{17}**O (‰)**
Schrey et al. (1986)	Earth-based	-73 ± 58	-37 ± 121	-
Owen (1982)	Viking Lander	-11 ± 55	-2 ± 50	-
Krasnopolsky et al. (1996)	Earth-based	-60 ± 150	-130 ± 80	-
Encrenaz et al. (2005)	Earth-based	0 ± 110	-	-
Krasnopolsky et al. (2007)	Earth-based	-22 ± 20	18 ± 18	-
Niles et al. (2010)	Phoenix Lander	-2.5 ± 4.3	31.0 ± 5.7	-
Webster et al. (2013)	Curiosity Rover	46 ± 4	48 ± 5	24 ± 5
Livengood et al. (2020)	Earth-based	-	9 ± 14	-
This study	ExoMars TGO	-3 ± 37	-29 ± 38	-11 ± 41

Another interesting feature to examine is the comparison between the average oxygen isotopic ratios in carbon dioxide and water vapour, which have been continuously monitored using secondary grating position 4, and yielding values of $^{18}O/^{16}O$ (H_2O) = 1.140 ± 0.080 VSMOW and $^{18}O/^{16}O$ (CO_2) = 0.971 ± 0.038 VSMOW. Fractionation between the isotopic composition of these two species will occur if oxygen is exchanging between them. Based on the equilibrium fractionation of ^{18}O between CO_2 and H_2O derived by Urey (1947) from the

different binding energies, Jakosky (1991) suggests that the $^{18}O/^{16}O$ in CO_2 in the Martian atmosphere should be approximately 8% higher than that in H_2O. This equilibrium could be reached if for example liquid water was present in the near-surface layer, where CO_2 would be dissolved and would quickly exchange oxygen isotopes with the water. With the liquid water then exchanging with the gases in the atmosphere, the different oxygen-bearing species in the atmosphere would also reflect this equilibrium fractionation. Although liquid water is unstable under the present Martian conditions, it can be present occasionally as a transient phase (Martín-Torres et al., 2015). However, based on the measured isotope composition in both species, this type of equilibrium does not appear to be dominant on the Martian atmosphere. On the other hand, both species might find a photochemical equilibrium instead, in which oxygen isotopes are exchanged by the photochemical reactions occurring in the Martian atmosphere and which may ultimately lead to the preferential transfer of certain isotopes to a given species. For example, we estimated in Chapter 5 that the $^{18}O/^{16}O$ isotopic ratio in OH would be approximately 1.025 times smaller than that of H_2O, as a consequence of the preferential photodissociation of $H_2^{16}O$ over $H_2^{18}O$. Later on, this odd-hydrogen will recombine with CO to form CO_2 (McElroy and Donahue, 1972), which might result in the transfer of oxygen depleted in the heavy isotope from H_2O to CO_2. Although this example is most likely an oversimplification, the isotope ratios in different species might be used as tracers of photochemical reactions and might provide new insights about the chemistry of the Martian atmosphere.

6.3.3 Implications to isotopic fractionation during atmospheric escape

Accurate estimations of the amounts of oxygen and carbon lost to space throughout the Martian history require a very detailed understanding of the chemical and physical pathways by which these escape and how the several escape mechanisms differentiate between the different isotopologues. While this fractionation factor f (see equation 1.0.2) has been extensively studied for the case of water escape and the D/H ratio (e.g., Krasnopolsky (2002); Cangi et al. (2020)), there is much less information in the literature regarding the overall escape fractionation factor of the carbon and oxygen isotopologues (see section 1.1.5.2).

From our measurements, we estimate that the average isotopic ratios are $^{13}C/^{12}C = 0.997 \pm 0.037$ VPDB, $^{18}O/^{16}O = 0.971 \pm 0.038$ VSMOW and $^{17}O/^{16}O = 0.989 \pm 0.041$ VSMOW.

These isotopic ratios are lower than those measured at the surface by the Curiosity Rover. As discussed in the previous section, one possibility is that the measurements made by Curiosity are not representative of the overall atmosphere, but characteristic of the atmosphere at a particular time and location instead. However, if it is the case that the bulk atmosphere follows the isotopic composition measured by Curiosity, then our results depict fractionation between the isotopic composition of CO_2 in the lower and upper atmospheres, in which the fractionation factor would be given by

$$R(^{13}C/^{12}C) = \frac{(^{13}C/^{12}C)_{\text{upper}}}{(^{13}C/^{12}C)_{\text{lower}}} = \frac{0.997 \pm 0.037}{1.046 \pm 0.004} = 0.953 \pm 0.036, \tag{6.3.1}$$

$$R(^{18}O/^{16}O) = \frac{(^{18}O/^{16}O)_{\text{upper}}}{(^{18}O/^{16}O)_{\text{lower}}} = \frac{0.971 \pm 0.038}{1.048 \pm 0.005} = 0.926 \pm 0.037, \tag{6.3.2}$$

$$R(^{17}O/^{16}O) = \frac{(^{17}O/^{16}O)_{\text{upper}}}{(^{17}O/^{16}O)_{\text{lower}}} = \frac{0.989 \pm 0.041}{1.024 \pm 0.005} = 0.966 \pm 0.041. \tag{6.3.3}$$

These derived values suggest a higher fractionation for $^{18}O/^{16}O$ compared to $^{13}C/^{12}C$ and $^{17}O/^{16}O$, which could be the consequence of mass-dependent fractionation. However, in that case, the fractionation factor of the $^{13}C/^{12}C$ and $^{17}O/^{16}O$ ratios should be $R = 0.963$, which indeed agrees for the $^{13}C/^{12}C$ and $^{17}O/^{16}O$ ratios within the uncertainties.

It must be noted that this derived fractionation factor would represent just the first part of the overall escape fractionation factor, which takes into account all fractionating processes from the lower atmosphere until the isotopes escape into space (see equation 1.0.2). For example, if the main source of escape of carbon was the sputtering of CO_2 molecules at the exobase, which fractionate the atmosphere given the diffusive separation between the different isotopologues ($R \sim 0.83$), then the net escape fractionation factor would be given by $f = 0.953 \times 0.830 = 0.791$. Given this factor, considering the isotopic ratio measured by Webster et al. (2013), and considering a primordial isotopic ratio representative of the Martian mantle of $(^{13}C/^{12}C)_{\text{mantle}} = 0.975$ VPDB (Wright et al., 1986), then we can estimate that at least 30% of the carbon atmospheric reservoir has been lost to space throughout Martian history, following equation 1.0.1.

However, it must be noted that this ideal scenario is probably far from reality. Firstly, based on the discussion in the previous section, it is not clear whether the atmospheric reservoir is enriched on average in the heavy isotopes, as our measurements reveal non-fractionated isotopic ratios essentially consistent with the standards. In addition, the escape of carbon from the Martian atmosphere appears not to be dominated by sputtering, but by the photodissociation of CO and CO_2 instead (see section 1.1.4), which would yield different escape fractionation factors, and therefore different estimates of the amount of the initial carbon reservoir. In conclusion, more measurements of the isotope ratios and a better theoretical understanding of the escape fractionation factor are required to derive accurate estimations of the amount of carbon and oxygen lost to space throughout Martian history.

6.4 Summary

In the previous chapter, all ACS MIR observations made with secondary grating position 4 were analysed in order to constrain the isotopic composition of water vapour in the atmosphere of Mars. In this chapter, we have used the same observations made with secondary grating position 4, but now to monitor the isotopic composition of CO_2 in order to constrain the non-fractionated values of the isotope ratios as well as their seasonal and spatial variations. The dataset assembled for this study includes all observations made with secondary grating position 4 in which the full detector frames were recorded. This dataset includes 190 solar occultation observations divided in two time periods, one covering the range between L_S = 164-219° in MY34, and the second one covering the range L_S = 141-356° in MY35.

The spectral range sampled in these observations includes absorption lines of the different isotopologues of CO_2 which are very sensitive to the temperature field. In order to retrieve the temperature with very high accuracy in this spectral range, different spectral windows from several diffraction orders were combined, exploiting the temperature dependence of the absorption lines for the retrieval, rather than the assumption of hydrostatic equilibrium, which was exploited in the two previous chapters. The temperature profiles retrieved with this technique have been validated against those retrieved with the hydrostatic approach in Chapter 5, and showing an average difference of 4 K. In order to introduce these new requirements in the retrieval scheme a new formulation of the radiative transfer calculations

was implemented, which models each acquisition independently treating the absorption as if it occurs in a homogeneous path with constant pressure and temperature. Due to the simplicity of these calculations, this scheme can just be applied when the absorption lines are not saturated, which limits the vertical extent of its applicability. Therefore, the retrievals are just performed for the acquisitions made between 70 and 130 km above the Martian surface.

The measurements indicate variations of the isotope ratios of CO_2 above the level of the measured uncertainties, suggesting the variations are indeed caused by real fractionation processes in the atmosphere. In particular, two patterns are discerned from the observations. The first pattern observed is a steady decrease of the $^{13}C/^{12}C$ and $^{18}O/^{16}O$ isotopic ratios above approximately 100 km. Based on the altitude range at which the decrease occurs, and the fact that the carbon and oxygen isotope ratios vary following the expectations from mass-dependent fractionation ($\delta^{13}C \sim 0.5 \times \delta^{18}O$), we conclude that these variations are the result of the diffusive separation of the different isotopologues above the homopause. On the other hand, the second pattern seen at other times is a substantial increase of the oxygen isotopic ratios from approximately 1 VSMOW at 70-80 km to 1.2 VSMOW at 90-110 km, which is not followed, at least to the same extent, by the $^{13}C/^{12}C$ isotopic ratio. Interestingly, the variations in both oxygen isotope ratios do not follow the expectations from mass-dependent fractionation ($\delta^{17}O \sim \delta^{18}O$), which might be indicative of the nature of these. However, with no modelling input, we were not able to reach any conclusions about the nature of the process sourcing the observed fractionation.

Using the results from the whole measured dataset we derived the average non-fractionated values of the isotope ratios in CO_2 to be $^{13}C/^{12}C = 0.997 \pm 0.037$ VPDB, $^{18}O/^{16}O = 0.971 \pm 0.038$ VSMOW and $^{17}O/^{16}O = 0.989 \pm 0.041$ VSMOW, which are lower than those measured at the surface by the Curiosity Rover. We suggest two possible scenarios to reconcile both datasets. The first possibility is that the reported values of the isotope ratios in these two datasets might not be representative of the whole atmosphere, but characteristic of the isotopic composition of the atmosphere at a particular time and location. Based on the monitoring of the atmosphere we achieve with the ACS MIR measurements, which spans many locations and seasons, we consider our derived values to be representative of the whole atmospheric reservoir, at least in the altitude range between 70 and 130 km. However, the measurements

made by the Curiosity Rover are much constrained in terms of location, season, and local time sampling, which may therefore just represent the isotopic composition in those particular circumstances. The second possibility is that both datasets are indeed representative of the average atmosphere, but in different altitude ranges. In that case, both datasets would reveal a depletion of the isotopic ratios in the heavy isotopes from the near-surface to the upper atmosphere. This fractionation factor should therefore be taken into account when estimating the amount of atmosphere lost to space, including in addition all other processes that might fractionate them until they escape into space.

Chapter 7

Conclusions and future work

7.1 Overview and summary

Atmospheric isotope ratios in species such as H, O and C provide important constraints on the history of the Martian volatile system, revealing the impact of several processes that might fractionate them. In particular, the atmosphere of Mars is enriched in the heavy isotopes of several species with respect to Earth, which is understood as an evidence of atmospheric escape into space, suggesting that billion years ago Mars' atmosphere was much denser and warmer than it is today. This dense and warm atmosphere might have been able to sustain liquid water on the surface, which carved the Martian terrains and formed "aqueous minerals" on the surface that we observe today. Although all these clues point to the much more hospitable climate that Mars had in its history compared to present, it is still not well understood what the atmosphere was made of to generate sufficient greenhouse warming to sustain liquid water on the surface, especially since the Sun was less powerful than it is today. A thorough understanding of the isotope ratios in each species can help understand the evolution of the different reservoirs on Mars and get an insight of how its climate was in the past. However, understanding the history of atmospheric escape through the atmospheric isotopic composition not only requires very precise measurements at present, but also a very good understanding of how the escape rates differ for different isotopologues.

To this purpose, we monitor the isotope composition of water vapour and carbon dioxide in the Martian atmosphere using sensitive infrared measurements made by the Atmospheric Chemistry Suite (ACS) onboard the ExoMars Trace Gas Orbiter (TGO) (see Chapter 2). The

mid-infrared channel of ACS (MIR) is a cross-dispersion spectrometer designed to achieve high spectral resolution ($\lambda/\Delta\lambda \sim$ 30000-50000) in a portion of the spectral range ($\sim$0.15 μm) between 2.3 and 4.2 μm (2380 - 4347 cm^{-1}). ACS MIR probes the Martian atmosphere using solar occultation measurements in which the Sun is observed along the TGO's orbit during egresses or ingresses, allowing a sampling of the vertical dimension of the atmosphere. Solar occultations are especially suitable for the measurement of trace gases due to the high intensity of the light source (i.e., the Sun), which yields high signal-to-noise ratio, and the long optical path length, which results in an observed air mass about 10 times greater than when observing the nadir.

In this project, the NEMESIS radiative transfer and retrieval algorithm has been adapted to analyse the solar occultation observations made by ACS MIR (see Chapter 3). In particular, a retrieval scheme was developed to be applicable for the retrieval of any gaseous species, as well as the retrieval of pressure and temperature vertical profiles from the absorption of carbon dioxide. The simultaneous retrieval of the pressure and temperature profiles allows not only a precise modelling of the radiative transfer calculations, but also to understand how the isotopic ratios vary in context with other atmospheric parameters. The conceived scheme was also developed to model some of the particularities of the ACS MIR data, such as the instrument line shape, which has been modelled using a varying double Gaussian function.

The developed retrieval scheme has then been applied to analyse ACS MIR solar occultations observations aiming to constrain and understand the isotope ratios in H_2O and CO_2 and their potential variations. In Chapter 4, retrievals of eight secondary grating position 5 observations (3789 - 3987 cm^{-1}) made during the first months of operations revealed the vertical distribution of the oxygen isotopic composition of water vapour ($^{18}O/^{16}O$ and $^{17}O/^{16}O$) for the first time. In Chapter 5, observations made using secondary grating position 4 for more than a full Martian Year (MY) were analysed to understand the variability of the D/H and $^{18}O/^{16}O$ isotopic ratios in water vapour, as well as to constrain how these isotope ratios are fractionated during the photolysis of water vapour. Finally, Chapter 6 dealt with the analysis of secondary grating position 4 observations to constrain the oxygen and carbon isotopic composition of carbon dioxide ($^{13}C/^{12}C$, $^{18}O/^{16}O$ and $^{17}O/^{16}O$) in the upper atmosphere, aiming to understand if there is any isotopic fractionation between the lower and upper atmospheres.

In the next section, we summarise the main outcomes of our analysis of these data and relate them to the original scientific goals that were outlined at the beginning of this thesis (Chapter 1). Finally, in section 7.3, some suggestions for future work are outlined, focusing on the study of isotope ratios in the Martian atmosphere and suggestions for improvements in the retrieval techniques used for the analysis of the spectral measurements.

7.2 Conclusions

At the beginning of Chapter 1 of this thesis, we asked several research questions that we will now address based on the results presented in this thesis:

1) What is the non-fractionated isotope composition of H_2O and CO_2 in the Martian atmosphere?

Detailed knowledge of the isotope ratios in the present-day atmosphere is essential for our understanding of the evolution of the atmosphere of Mars, which requires very precise values of these quantities to estimate the amount of atmosphere that escaped to space throughout history. Isotope ratios inferred from localised measurements are subject to fractionation processes occurring in the present-day atmosphere. Therefore, in order to estimate the value of the isotope ratios representative of the Martian atmospheric reservoir outside of any fractionation processes, it is important to measure the isotope ratios in different instances. It must be noted that in this thesis the term non-fractionated isotopic ratios refers to the potential isotopic fractionation occurring in the present-day atmosphere, not to the fractionation of the present-day isotopic ratios relative to their primordial sources.

The isotopic composition of water vapour was constrained using observations from secondary grating positions 4 and 5. In the case of secondary grating position 4, the D/H and $^{18}O/^{16}O$ isotope ratios were monitored for more than a full Martian year (MY). A statistical analysis based on the continuous monitoring over different seasons, latitudes and time found the observed ratios to be consistent with fractionation from a source reservoir isotopic ratio of D/H = 4.9 ± 0.4 and $^{18}O/^{16}O$ = 1.14 ± 0.08 with respect to VSMOW. These values are generally in agreement with other observations made by ground-based or *in situ* means, consistent with the hypothesis that indeed a large amount of water escaped from the Martian

atmosphere throughout its history.

Observations made with secondary grating position 5 were used to constrain the oxygen isotopic ratios in water vapour, revealing $^{18}O/^{16}O = 1.20 \pm 0.20$ and $^{17}O/^{16}O = 1.23 \pm 0.25$ with respect to VSMOW. However, one must note that while more than 500 observations were used to derive the isotope ratios from grating position 4, only eight observations were used for the analysis of secondary grating position 5. Therefore, we take the value of the $^{18}O/^{16}O$ isotope ratio from secondary grating position 4 as a more reliable estimate of the isotopic ratio of the Martian atmospheric reservoir. An interesting result inferred from the analysis of grating position 5 data is that both oxygen isotope ratios are similarly enriched in the heavy isotope with respect to the standard, being nominally not consistent with the expectations from mass-dependent fractionation. This similar enrichment in both the $^{18}O/^{16}O$ and $^{17}O/^{16}O$ isotope ratios might therefore be indicative of the role of photochemical reactions with other oxygen-bearing species in the atmosphere.

The isotopic composition of carbon dioxide was constrained using ACS MIR observations from secondary grating position 4 between 70 and 130 km of altitude. These measurements reveal that the isotope composition of carbon dioxide shows much milder deviations with respect to Earth than the isotope ratios in water vapour ($^{13}C/^{12}C = 0.997 \pm 0.037$ VPDB, $^{18}O/^{16}O = 0.971 \pm 0.038$ VSMOW and $^{17}O/^{16}O = 0.989 \pm 0.041$ VSMOW). The derived isotopic ratios are lower than those measured at the surface by the Curiosity Rover, which are usually used as a reference for the average isotopic composition of the Martian atmosphere (Webster et al., 2013). These differences might be explained by two possible scenarios. On one hand, these datasets might not be representative of the whole Martian atmosphere, but characteristic of the atmosphere at particular times and locations instead. In this sense, while our derived values are based on a continuous monitoring of the atmosphere for more than half Martian Year, the measurements by the Curiosity Rover are much more limited in terms of location, season and local time coverage, and might be impacted by fractionation processes at those particular times and locations. On the other hand, both datasets might be representative of the average atmosphere but at different altitude ranges. In that case, the difference between the two measurements of the isotopic ratios might reveal fractionation between the lower and upper atmospheres.

Interestingly, the oxygen isotopic composition of water vapour ($^{18}O/^{16}O$ (H_2O) = 1.14 VSMOW) is more enriched in the heavy isotope than that of carbon dioxide ($^{18}O/^{16}O$ (CO_2) = 0.971 VSMOW), which might be indicative of the means by which these two species exchange oxygen between them. The relative enrichment of the isotopic ratio in water with respect to that in carbon dioxide might depict a photochemical equilibrium between these species, in which the different oxygen isotopes are subject to the photochemical reactions in the Martian atmosphere, and may ultimately lead to the preferential transfer of a certain isotope to a given species. For example, our estimations of the fractionation factor between H_2O and OH revealed the $^{18}O/^{16}O$ ratio in OH to be approximately 10% lower than that in H_2O. If this OH population later recombines with CO to form CO_2, the newly formed CO_2 molecules would be depleted in the $^{18}O/^{16}O$ ratio with respect to H_2O. Although the oxygen isotope equilibrium in the Martian atmosphere is most likely much more complex than this, this example highlights the possibility of the isotopic composition of different species to be used as tracers to get new insights about the chemistry of the Martian atmosphere.

2) Does the isotopic composition of atmospheric H_2O and CO_2 vary? If so, what are the main drivers of variation?

Understanding the variations in the isotope composition of the atmosphere is not only important in order to infer what the values of the isotopic ratios outside of any fractionation processes are, but also to use these as tracers of the interaction between different reservoirs or atmospheric processes occurring in the present-day atmosphere.

Variations in the isotopic composition of water vapour were measured using the ACS MIR secondary grating position 4 observations covering more than half of MY34 (L_S = 160-360°) and of MY35 (L_S = 0-356°), encompassing two perihelion and one aphelion seasons. The D/H ratio was observed to vary in a range between 1 and 6 VSMOW in correlation with the temperature and water abundance in the atmosphere, consistent with the expectations from condensation-induced fractionation. In particular, one of the main features observed in the variations of the D/H ratio is its decrease above the level of the hygropause, which confines most water and high values of the D/H in the atmospheric layers below the saturation level. It is observed that while high water vapour and D/H ratios expand up to 50-60 km during the perihelion season, these are confined in the lowest 20 km during aphelion, which

is consistent with the variations of the hygropause level in these seasons as a consequence of the eccentricity of Mars' orbit around the Sun and the intensified Hadley circulation during perihelion. All these clues (i.e., correlation between D/H, temperature and water mixing ratio, and the decrease of the D/H above the hygropause level) suggest that the main driver of variability of D/H in the atmosphere of Mars is the condensation of water onto ice in the polar caps and in clouds.

The $^{18}O/^{16}O$ isotope ratio in water vapour was observed to vary from 0.9 to 1.3 VSMOW. However, these variations are close to the uncertainty level of the measurement, which means it is not possible to conclude whether the variations are real or just statistical noise from the measurements. Variations caused by condensation-induced fractionation predict the $^{18}O/^{16}O$ ratio to follow similar trends as the D/H ratio but with a smaller amplitude. It is difficult to accurately predict how the variations in the two isotopic ratios are connected, since this factor not only depends on the temperature at which condensation occurs, but also on the impact of supersaturation and kinetic effects. However, one may expect the variations in $^{18}O/^{16}O$ to be approximately 4-15 times smaller, depending on the factors above mentioned (section 1.1.5.2). Similarly, variations of the $^{17}O/^{16}O$ isotopic ratio caused from condensation processes are expected to be approximately half of those in $^{18}O/^{16}O$, although this factor might be larger depending on the impact of kinetic effects. Given that the uncertainties in the O isotope ratios derived from the ACS MIR measurements are larger than the level of variations expected from these processes, the non-detection of variations in the O isotopic ratios does not disprove the hypothesis that these fractionation processes are occurring.

The variations of the isotopic ratios of CO_2 were also measured using ACS MIR solar occultations from secondary grating position 4 between 70 and 130 km above the Martian surface. In this case, we discerned two main types of variation in the vertical structure of the CO_2 isotope ratios. Firstly, we observe a steady decrease of the isotopic ratios with altitude above approximately 100 km. Based on the altitudes at which the decrease occurs and the fact that these variations follow the expectations from mass-dependent fractionation ($\delta^{13}C \sim 0.5 \times \delta^{18}O$) (section 1.1.5.2), we conclude that the observed decrease with altitude corresponds to fractionation above the homopause due to diffusive separation of the different isotopologues. The second discerned pattern of variations from the observations reveals an increase of the

oxygen isotope composition of CO_2 from ∼1 VSMOW at 70-80 km to ∼1.2 VSMOW at 90-110 km, which is not followed by an increase, at least of the same magnitude, of the $^{13}C/^{12}C$ isotopic ratio. The variations in the oxygen isotopic ratios are approximately of equal amplitude ($\delta^{17}O \sim \delta^{18}C$), while the fractionation of the carbon isotope ratio approximately follows the expectations from mass-dependent fractionation ($\delta^{13}C \sim 0.5 \times \delta^{18}O$). Based solely on this information, it is not clear which process may be the source of the variations. Photolysis of CO_2 molecules is expected to leave the remaining CO_2 population enriched in the heavy isotopes, but it would preferentially enrich the $^{13}C/^{12}C$ isotopic ratio and the oxygen isotopic ratios would be expected to be fractionated following mass-dependent fractionation (Schmidt et al., 2013). In the Earth's stratosphere, the oxygen isotope ratios of CO_2 also show variations not following the mass-dependent relation, which are caused by the isotope exchange with other oxygen-bearing species such as O_2 and O_3 (e.g., Wiegel et al. (2013)). However, while CO_2 is just a trace gas on Earth, it is the main constituent of the Martian atmosphere, and it is implausible that isotopic exchange with O_2 and O_3 can produce such large variations of the oxygen isotopic ratios of CO_2.

3) Are the different isotopes in H_2O and CO_2 fractionated as they are decomposed into lighter species, affecting the escape fractionation factor f?

Accurate estimates of the evolution and escape of the Martian atmosphere into space rely not only on a precise description of the present-day isotopic ratios, but also on the escape fractionation factor, which essentially determines the rate at which the isotope ratios are enriched in the heavy isotope as the atmosphere escapes into space. The escape fractionation factor relates the isotopic ratio of the escaping species (e.g., D/H of the escaping hydrogen flux) with that representative of the Martian atmospheric reservoir (e.g., average non-fractionated D/H of water vapour), and therefore takes into account any fractionation processes that might influence this ratio.

In the case of hydrogen, it mostly escapes the Martian atmosphere by means of thermal escape in the form of atomic hydrogen. Therefore, the first part of the escaping mechanism comprises the chemical and physical pathways by which hydrogen in water vapour is transformed into atomic hydrogen. In order to estimate how the D/H ratio is fractionated during this transformation, the retrieved water vapour and D/H profiles from secondary grating po-

sition 4 were combined with calculations of the photolysis rates of H_2O and HDO, enabling the estimation of the fractionation factor R between the D/H ratio of the photolysis products of water vapour (D/H in OH and H) and that representative of water vapour in the lower atmosphere (D/H = 4.9 ± 0.4 VSMOW). Our calculations revealed that the photodissociation of water vapour molecules is the most important mechanism for the production of atomic hydrogen, which showed very strong seasonal variations. In particular, the perihelion season was observed to be dominant in the annual production of atomic hydrogen, with rates being approximately 100 times higher than those found during aphelion. In addition, our calculations also suggested that the D/H fractionation between the photolysis products and water also varied with season. In particular, we estimated that while the photolysis products would be depleted in D/H by a factor of 2-2.5 during the perihelion ($R \sim 0.4$-0.5), this factor would increase up to 5-6 during the aphelion season ($R \sim 0.2$). However, as the photolysis of water vapour was found to be much more efficient during perihelion, the annual average of the fractionation factor is expected to be approximately $R \sim 0.4$-0.5. It must be noted that any other fractionation factors affecting the isotope ratios of the escaping hydrogen and deuterium must be accounted for (e.g., diffusive separation) in order to calculate the net escape fractionation factor. Our results provide new insights for resolving the old paradigm regarding the role of the different mechanisms to fractionate the D/H ratio of water vapour in the lower atmosphere and that of its dissociation products, leading to the enrichment of D/H in the atmosphere as it escapes into space.

In the case of oxygen, although the reactions by which it escapes from the Martian atmosphere are known, it is not clear whether the oxygen atoms that escape come primarily from CO_2 or H_2O, or some combination of both. Therefore, it is difficult to estimate how the oxygen isotopic ratios are fractionated from their main reservoirs (CO_2 and H_2O) until they escape the Martian atmosphere, mainly by the dissociative recombination of O_2^+. In the scenario that escaping oxygen comes only from one of these species:

- If the main source of escaping oxygen comes from H_2O, it is likely the escaping pathway encompasses the photolysis of H_2O. Similarly as was performed with the D/H ratio, we estimated that the $^{18}O/^{16}O$ isotopic ratio of OH would be depleted by a factor of 1.025 with respect to the isotopic ratio representative of water vapour in the atmosphere

($^{18}O/^{16}O$ = 1.14 ± 0.08 VSMOW), which is equivalent to a fractionation factor of R = 0.975. The escape fractionation factor would then need to account for all subsequent reactions occurring after the photodissociation of H_2O.

- On the other hand, if the main source of oxygen comes from CO_2, one would need to account for the potential fractionation of CO_2 isotopes between the lower and upper atmospheres ($R = 0.926 \pm 0.037$) if both measurements by the Curiosity Rover and ACS MIR are representative of the average atmosphere at different altitudes, as discussed earlier in this section. The calculation of the escape fractionation factor would then require the inclusion of any other fractionation occurring on top of this. As well as for the H_2O scenario, it is likely the escape pathways of oxygen encompass the photolysis of CO_2 molecules. The fractionation factor inherent in this mechanism was not calculated in this thesis, but is expected to be $R < 1$ based on the cross-sections calculated by Schmidt et al. (2013).

In the case of carbon, the derivation of the escape fractionation factor is not currently possible due to the absence of measurements constraining the role of the different mechanisms controlling its escape. If the escape of carbon was dominated by the sputtering of CO_2 molecules, the fractionation factor would be $f = 0.791$, the product of the fractionation factors relating the $^{13}C/^{12}C$ isotope ratios in the lower and upper atmospheres ($R = 0.953$) and the fractionation factor due to the diffusive separation between the different isotopologues (R = 0.83). In this scenario, we calculated that given the current isotopic ratio of the atmospheric reservoir and the primordial isotope ratio of the Martian mantle, at least 30% of the carbon atmospheric reservoir has been lost to space throughout Martian history. If the escape of carbon was dominated by the photodissociation of CO instead, the escape fractionation factor should account for the fractionation factor between the lower and upper atmospheres, the fractionation occurring due to the difference in cross-section between the $^{12}C^{16}O_2$ and $^{13}C^{16}O_2$ isotopologues, and the fractionation inherent in this escape mechanism (R = 0.6; Hu et al. (2015)). However, the most plausible scenario is that escape is driven by a combination of several mechanisms.

7.3 Future work

In this thesis, we have developed a retrieval scheme applicable to the retrieval of vertical profiles from solar occultation observations, which we have applied to study the isotopic composition of water vapour and carbon dioxide in the Martian atmosphere. However, there is still plenty of room for improvement on the techniques we use to retrieve the solar occultation measurements and there is still a long way to go before we fully understand the processes that shape the isotopic composition of the atmosphere. In this section, we provide some examples that could improve our understanding of these two topics.

7.3.1 Retrieval techniques

In the future, one might expect the different sources of data from planetary missions and ground-based observatories to improve over time in terms of data volume and resolution. In order to process the increased amount of observations, retrieval algorithms must improve accordingly in terms of retrieval speed and the use of computational resources. Here, we provide some examples of improvements that can be performed in the NEMESIS algorithm to improve its efficiency.

Increasing the retrieval speed

ACS MIR performs about ten solar occultations per day. Up to February 2021, ACS MIR made approximately 4500 solar occultations observations using several secondary grating positions. In this thesis, just a small part of the dataset has been processed. In order to be able to process this continuously-growing dataset, the retrieval algorithm must be as fast as possible. One way to increase the speed of the radiative transfer calculations and the retrieval algorithm is to parallelise the calculations.

One part of the code which could be optimised for increasing the speed of the algorithm is during the calculation of the Jacobian matrix $\mathbf{K}$, which represents the derivatives of transmission spectra at each wavenumber with respect to each of the elements in the state vector. For some parameters in the state vector, this derivative can be calculated analytically (e.g., volume mixing ratio of a certain gas), while others have to be calculated numerically (e.g., pressure and temperature from hydrostatic assumption or parameters describing the instru-

ment lineshape), but essentially all these calculations are independent from each other. In this thesis, a new scheme was implemented on the NEMESIS algorithm that allowed the calculation of the different derivatives defining the Jacobian matrix in parallel. This update of the code increased the speed of the code vastly, essentially by a factor given by the number of processors that could be used in parallel. However, the use of the computational resources can be further improved taking advantage of the analytical calculation of the derivative too, especially since most of the calculations can be calculated this way. This could be easily implemented in the NEMESIS algorithm by introducing a flag indicating whether the calculation of the derivative of that specific parameter of the state vector can be calculated analytically or numerically.

Secondly, the speed of the NEMESIS algorithm could be greatly improved if performing some of the radiative transfer calculations (forward model) in parallel. In particular, a major improvement of the algorithm may be achieved if parallelising the calculation of each of the spectral points. Currently, the calculation of the forward model is performed as follows: first, the wavenumbers at which the spectrum has to be computed are calculated; secondly, the radiance is calculated independently and in series for each of the wavenumbers; lastly, the spectrum is convolved with the instrument lineshape to model the characteristics of the instrument. Therefore, if the calculations of the spectrum are performed in parallel, the computational time to calculate the forward model would be reduced by a factor given by the number of processors that could be used in parallel.

Increasing the efficiency of memory usage

Another issue that was faced during the analysis of the ACS MIR solar occultation observations was related to the memory allocation of the retrievals. NEMESIS was developed to be applicable for the retrieval of any kind of observation (e.g., ground-based observations, solar occultations, exoplanet transits, etc.), which often have different computational requirements. In order to be applicable to any of these cases, NEMESIS was developed to be able to perform very diverse radiative transfer calculations (e.g., single and multiple scattering, absorption and emission, line-by-line, correlated-k, etc.). All these calculations are performed on arrays which are currently defined statically, which means that the program will allocate some memory to each array based on its maximum size defined prior to the compilation of

the code. If these sizes are very large for all arrays, then NEMESIS will not compile due to an overshoot of the allocatable memory.

For solar occultations, although some of these array sizes could be decreased, memory issues were faced due to the large number of spectral points that needed to be calculated in each occultation, as these observations essentially combine a large number of spectra at different tangent heights to build up the high-vertical-resolution profiles. In that sense, one of the implemented options was to select optimised spectral windows to reduce the number of spectral points in each tangent height. However, for certain purposes, like the retrieval of the temperature field from the temperature dependence of the absorption lines presented in Chapter 6, a large number of spectral points is required.

One way to optimise the memory usage of the algorithm and solve some of these problems is to define the array sizes dynamically, which means that the memory of the arrays will not be allocated when compiling the code, but when using the arrays instead. Therefore, if for example we do not require scattering calculations for our analysis, the arrays used for that part of the code will not be allocated any memory, leaving that memory for the usage of other arrays. In addition, dynamic arrays can also be deallocated if they are no longer required in the calculations, which provides further improvement of the efficiency of the memory usage.

7.3.2 Isotopic studies of the Martian atmosphere

D/H ratio

The relation of the D/H ratio and the escape of water throughout history needs to be further understood to provide reliable estimates of the size of the water reservoir on early Mars. In particular, it is important to properly understand the pathways by which hydrogen escapes, and how these fractionate the D/H ratio. Currently, the IUVS instrument onboard the MAVEN spacecraft monitors the Lyman-α brightness of atomic hydrogen and deuterium. To date, the analyses of these observations have only reported ratios of the Lyman-α emission of these two species due to the difference in optical thickness of the two, but a more detailed analysis can reveal the isotopic composition of the escaping hydrogen (Clarke et al., 2017; Mayyasi et al., 2019). This, in combination with the value of the non-fractionated D/H ratio in H_2O, can provide the direct sampling of the escape fractionation factor at present. Al-

though these measurements would greatly advance our understanding of the escape of water from the Martian atmosphere, they must be accompanied by models that can reproduce them and that can be able to extrapolate the escape fractionation factor to earlier epochs, when the processes governing the escape of hydrogen might have been different.

The isotopic ratios in water vapour may also be used to better understand the water cycle on Mars. In particular, our analysis of the ACS MIR measurements has shown that to first order, the variations observed in the D/H ratio in H_2O are caused by condensation-induced fractionation during the formation of water ice clouds and during the condensation onto the ice caps. A more detailed study of the condensation-induced fractionation of the D/H ratio can provide information about the microphysics governing the formation of water ice clouds on Mars. This analysis could provide new insights about our understanding of the high levels of supersaturation observed in the atmosphere even in the presence of clouds (Fedorova et al., 2020b). In addition, with improved accuracy in the measurements, this analysis could be further improved including simultaneous information of the $^{18}O/^{16}O$ isotopic ratio, which is more affected by the presence of kinetic fractionation effects and the supersaturation levels at which condensation occurs.

C and O isotope ratios

The relation of the isotopic ratios with the escape of carbon and oxygen is generally much more poorly understood than that of D/H and the escape of hydrogen.

First of all, it is crucial for our understanding of the evolution of the Martian atmosphere to accurately measure the non-fractionated values of the carbon and oxygen isotopic ratios representative of the present-day atmospheric reservoir. These measurements can be performed with the SAM-TLS instrument on the Curiosity Rover, and should aim to cover a broader seasonal and local time sampling in order to disentangle the values derived in localised measurements from the average non-fractionated value representative of the Martian atmosphere. In addition, the measurement of the non-fractionated values can be improved with measurements from the the ExoMars 2022 Surface Platform (Kazachok) to sample the atmosphere in different locations (Rodin et al., 2020).

Calculations of the carbon and oxygen escape fractionation factors still require a better understanding of the pathways and mechanisms by which these escape to space. In the case of carbon, models suggest that the photodissociation of CO is the one of the main processes governing its escape. The fractionation effect inherent in this mechanism was estimated by Hu et al. (2015), but CO was assumed to have the same isotopic composition as CO_2 in the near-surface atmosphere. ACS MIR measurements from secondary grating positions 6 and 7 encompass absorption lines of $^{12}C^{16}O$, $^{13}C^{16}O$ and $^{12}C^{18}O$, which therefore allow the measurement of the $^{13}C/^{12}C$ and $^{18}O/^{16}O$ isotope ratios in CO. Using the carbon isotopic ratios from CO and CO_2, and taking into account the fractionation factor inherent in the photodissociation of CO, one can estimate the net escape fractionation factor for carbon at present. However, as was mentioned for the D/H ratio, these measurements should be accompanied by modelling efforts to fully understand the relation between the isotopic ratios and escape in earlier epochs.

In addition, measurements by the NGIMS instrument onboard the MAVEN spacecraft have provided information about the isotopic composition of Ar from the Martian upper atmosphere (Jakosky et al., 2017). In principle, this instrument can also provide measurements of the isotopic ratios in CO_2, which can be used to validate our analysis of the ACS MIR measurements and better understand the fractionation between the lower and upper atmospheres. To our knowledge, this analysis of the isotope ratios has not been yet reported in the literature.

We believe these lines of future work will improve our understanding of the isotope composition of the atmosphere of Mars, its evolution throughout history, and ultimately about the habitability of the Red Planet in the past.

Bibliography

Alday, J., Trokhimovskiy, A., Irwin, P. G. J., Wilson, C. F., Montmessin, F., Lefévre, F., Fedorova, A. A., Belyaev, D. A., Olsen, K. S., Korablev, O., Vals, M., Rossi, L., Baggio, L., Bertaux, J.-L., Patrakeev, A., and Shakun, A. (2021a). Isotopic fractionation of water and its photolytic products in the atmosphere of Mars. *Nature Astronomy*.

Alday, J., Wilson, C. F., Irwin, P. G. J., Olsen, K. S., Baggio, L., Montmessin, F., Trokhimovskiy, A., Korablev, O., Fedorova, A. A., Belyaev, D. A., Grigoriev, A., Patrakeev, A., and Shakun, A. (2019). Oxygen isotopic ratios in Martian water vapour observed by ACS MIR on board the ExoMars Trace Gas Orbiter. *Astronomy & Astrophysics*, 630:A91.

Alday, J., Wilson, C. F., Irwin, P. G. J., Trokhimovskiy, A., Montmessin, F., Fedorova, A. A., Belyaev, D. A., Olsen, K. S., Korablev, O., Lefèvre, F., Braude, A. S., Baggio, L., Patrakeev, A., and Shakun, A. (2021b). Isotopic Composition of CO $_2$ in the Atmosphere of Mars: Fractionation by Diffusive Separation Observed by the ExoMars Trace Gas Orbiter. *Journal of Geophysical Research: Planets*, 126(12).

Alsaeed, N. R. and Jakosky, B. M. (2019). Mars Water and D/H Evolution From 3.3 Ga to Present. *Journal of Geophysical Research: Planets*, 124(12):3344–3353.

Aoki, S., Nakagawa, H., Sagawa, H., Giuranna, M., Sindoni, G., Aronica, A., and Kasaba, Y. (2015). Seasonal variation of the HDO/H2O ratio in the atmosphere of Mars at the middle of northern spring and beginning of northern summer. *Icarus*, 260:7–22.

Aoki, S., Sato, Y., Giuranna, M., Wolkenberg, P., Sato, T., Nakagawa, H., and Kasaba, Y. (2018). Mesospheric CO2 ice clouds on Mars observed by Planetary Fourier Spectrometer onboard Mars Express. *Icarus*, 302:175–190.

Aoki, S., Vandaele, A. C., Daerden, F., Villanueva, G. L., Liuzzi, G., Thomas, I. R., Erwin,

J. T., Trompet, L., Robert, S., Neary, L., Viscardy, S., Clancy, R. T., Smith, M. D., Lopez-Valverde, M. A., Hill, B., Ristic, B., Patel, M. R., Bellucci, G., Lopez-Moreno, J., and the NOMAD team (2019). Water Vapor Vertical Profiles on Mars in Dust Storms Observed by TGO/NOMAD. *Journal of Geophysical Research: Planets*, 124(12):3482–3497.

Baker, V. R., Strom, R. G., Gulick, V. C., Kargel, J. S., Komatsu, G., and Kale, V. S. (1991). Ancient oceans, ice sheets and the hydrological cycle on Mars. *Nature*, 352(6336):589–594.

Barabash, S., Fedorov, A., Lundin, R., and Sauvaud, J.-A. (2007). Martian Atmospheric Erosion Rates. *Science*, 315(5811):501–503.

Barkan, E. and Luz, B. (2005). High precision measurements of17O/16O and18O/16O ratios in H2O. *Rapid Communications in Mass Spectrometry*, 19(24):3737–3742.

Beale, C., Buzan, E., Boone, C., and Bernath, P. (2016). Near-global distribution of CO isotopic fractionation in the Earth's atmosphere. *Journal of Molecular Spectroscopy*, 323:59–66.

Benson, J. L., Kass, D. M., and Kleinböhl, A. (2011). Mars' north polar hood as observed by the Mars Climate Sounder. *Journal of Geophysical Research*, 116(E3):E03008.

Benson, J. L., Kass, D. M., Kleinböhl, A., McCleese, D. J., Schofield, J. T., and Taylor, F. W. (2010). Mars' south polar hood as observed by the Mars Climate Sounder. *Journal of Geophysical Research*, 115(E12):E12015.

Bertaux, J.-L. and Montmessin, F. (2001). Isotopic fractionation through water vapor condensation: The Deuteropause, a cold trap for deuterium in the atmosphere of Mars. *Journal of Geophysical Research: Planets*, 106(E12):32879–32884.

Bhattacharya, S. K., Savarino, J., and Thiemens, M. H. (2000). A new class of oxygen isotopic fractionation in photodissociation of carbon dioxide: Potential Implications for atmospheres of Mars and Earth. *Geophysical Research Letters*, 27(10):1459–1462.

Bhattacharyya, D., Clarke, J. T., Bertaux, J.-L., Chaufray, J.-Y., and Mayyasi, M. (2015). A strong seasonal dependence in the Martian hydrogen exosphere. *Geophysical Research Letters*, 42(20):8678–8685.

Bibring, J.-P., Langevin, Y., Poulet, F., Gendrin, A., Gondet, B., Berthé, M., Soufflot, A., Drossart, P., Combes, M., Bellucci, G., Moroz, V., Mangold, N., Schmitt, B., and OMEGA team, t. (2004). Perennial water ice identified in the south polar cap of Mars. *Nature*, 428(6983):627–630.

Bjoraker, G. L., Mumma, M. J., and Larson, H. P. (1989). Isotopic Abundance Ratios for Hydrogen and Oxygen in the Martian Atmosphere. In *Bulletin of the American Astronomical Society*, volume 21, page 991. Conference Name: Bulletin of the American Astronomical Society.

Bogard, D. D., Clayton, R. N., Marti, K., Owen, T., and Turner, G. (2001). Martian Volatiles: Isotopic Composition, Origin, and Evolution. In Kallenbach, R., Geiss, J., and Hartmann, W. K., editors, *Chronology and Evolution of Mars*, pages 425–458, Dordrecht. Springer Netherlands.

Boynton, W. V., Feldman, W. C., Squyres, S. W., Prettyman, T. H., Brückner, J., Evans, L. G., Reedy, R. C., Starr, R., Arnold, J. R., Drake, D. M., Englert, P. a. J., Metzger, A. E., Mitrofanov, I., Trombka, J. I., d'Uston, C., Wänke, H., Gasnault, O., Hamara, D. K., Janes, D. M., Marcialis, R. L., Maurice, S., Mikheeva, I., Taylor, G. J., Tokar, R., and Shinohara, C. (2002). Distribution of Hydrogen in the Near Surface of Mars: Evidence for Subsurface Ice Deposits. *Science*, 297(5578):81–85. Publisher: American Association for the Advancement of Science Section: Report.

Brinjikji, M. and Lyons, J. R. (2021). Mass-Independent Fractionation of Oxygen Isotopes in the Atmosphere. *Reviews in Mineralogy and Geochemistry*, 86(1):197–216.

Brown, L., Humphrey, C., and Gamache, R. (2007). CO2-broadened water in the pure rotation and ν2 fundamental regions. *Journal of Molecular Spectroscopy*, 246(1):1–21.

Cangi, E. M., Chaffn, M. S., and Deighan, J. (2020). Higher Martian atmospheric temperatures at all altitudes increase the D/H fractionation factor and water loss. *Journal of Geophysical Research: Planets*, 125(12):e2020JE006626.

Cappa, C. D., Hendricks, M. B., DePaolo, D. J., and Cohen, R. C. (2003). Isotopic fractionation of water during evaporation. *Journal of Geophysical Research: Atmospheres*, 108(D16). _eprint: https://agupubs.onlinelibrary.wiley.com/doi/pdf/10.1029/2003JD003597.

Carr, M. H. (1974). The role of lava erosion in the formation of lunar rilles and Martian channels. *Icarus*, 22(1):1–23.

Carr, M. H. (1995). The Martian drainage system and the origin of valley networks and fretted channels. *Journal of Geophysical Research*, 100(E4):7479.

Carr, M. H. and Clow, G. D. (1981). Martian channels and valleys: Their characteristics, distribution, and age. *Icarus*, 48(1):91–117.

Casado, M., Cauquoin, A., Landais, A., Israel, D., Orsi, A., Pangui, E., Landsberg, J., Kerstel, E., Prie, F., and Doussin, J.-F. (2016). Experimental determination and theoretical framework of kinetic fractionation at the water vapour–ice interface at low temperature. *Geochimica et Cosmochimica Acta*, 174:54–69.

Chaffin, M., Deighan, J., Schneider, N., and Stewart, A. (2017). Elevated atmospheric escape of atomic hydrogen from Mars induced by high-altitude water. *Nature Geoscience*, 10(3):174–178.

Chaffin, M. S., Chaufray, J.-Y., Stewart, I., Montmessin, F., Schneider, N. M., and Bertaux, J.-L. (2014). Unexpected variability of Martian hydrogen escape. *Geophysical Research Letters*, 41(2):314–320.

Cheng, B.-M., Chew, E. P., Liu, C.-P., Bahou, M., Lee, Y.-P., Yung, Y. L., and Gerstell, M. F. (1999). Photo-induced fractionation of water isotopomers in the Martian atmosphere. *Geophysical Research Letters*, 26(24):3657–3660.

Chung, C.-Y., Chew, E. P., Cheng, B.-M., Bahou, M., and Lee, Y.-P. (2001). Temperature dependence of absorption cross-section of H2O, HOD, and D2O in the spectral region 140–193nm. *Nuclear Instruments and Methods in Physics Research Section A: Accelerators, Spectrometers, Detectors and Associated Equipment*, 467-468:1572–1576.

Clancy, R., Grossman, A., Wolff, M., James, P., Rudy, D., Billawala, Y., Sandor, B., Lee, S., and Muhleman, D. (1996). Water Vapor Saturation at Low Altitudes around Mars Aphelion: A Key to Mars Climate? *Icarus*, 122(1):36–62.

Clancy, R. T. and Sandor, B. J. (1998). CO $_2$ ice clouds in the upper atmosphere of Mars. *Geophysical Research Letters*, 25(4):489–492.

Clancy, R. T., Wolff, M. J., Whitney, B. A., Cantor, B. A., and Smith, M. D. (2007). Mars equatorial mesospheric clouds: Global occurrence and physical properties from Mars Global Surveyor Thermal Emission Spectrometer and Mars Orbiter Camera limb observations. *Journal of Geophysical Research*, 112(E4):E04004.

Clarke, J., Mayyasi, M., Bhattacharyya, D., Schneider, N., Chaufray, J.-Y., Bertaux, J.-L., Chaffin, M., Jakosky, B., Deighan, J., Jain, S., McClintock, B., and Yelle, R. (2019). The D/H Ratio in the Martian Upper Atmosphere. In *EPSC-DPS2019*. Conference Name: EPSC-DPS Joint Meeting 2019.

Clarke, J. T., Mayyasi, M., Bhattacharyya, D., Schneider, N. M., McClintock, W. E., Deighan, J. I., Stewart, A. I. F., Chaufray, J., Chaffin, M. S., Jain, S. K., Stiepen, A., Crismani, M., Holsclaw, G. M., Montmessin, F., and Jakosky, B. M. (2017). Variability of D and H in the Martian upper atmosphere observed with the MAVEN IUVS echelle channel. *Journal of Geophysical Research: Space Physics*, 122(2):2336–2344.

Colaprete, A. and Toon, O. B. (2002). Carbon dioxide snow storms during the polar night on Mars. *Journal of Geophysical Research: Planets*, 107(E7):5–1–5–16. _eprint: https://agupubs.onlinelibrary.wiley.com/doi/pdf/10.1029/2001JE001758.

Connes, J., Connes, P., and Maillard, J. P. (1969). Atlas des spectres dans le proche infrarouge de Venus, Mars, Jupiter et Saturn. *Editions du Centre Nationale de la Recherche Scientifique*, page 471.

Costa, M. (2018). SPICE for ESA Planetary Missions: geometry and visualization support to studies, operations and data analysis within your reach. In *2018 SpaceOps Conference*, SpaceOps Conferences. American Institute of Aeronautics and Astronautics.

Cui, J., Wu, X. S., Gu, H., Jiang, F. Y., and Wei, Y. (2019). Photochemical escape of atomic C and N on Mars: clues from a multi-instrument MAVEN dataset. *Astronomy & Astrophysics*, 621:A23.

Dansgaard, W. (1964). Stable isotopes in precipitation. *Tellus*, 16(4):436–468.

Devi, V. M., Benner, D. C., Sung, K., Crawford, T. J., Gamache, R. R., Renaud, C. L., Smith, M. A. H., Mantz, A. W., and Villanueva, G. L. (2017a). Line parameters for CO2-

and self-broadening in the ν1 band of HD16O. *Journal of Quantitative Spectroscopy and Radiative Transfer*, 203:133–157.

Devi, V. M., Benner, D. C., Sung, K., Crawford, T. J., Gamache, R. R., Renaud, C. L., Smith, M. A. H., Mantz, A. W., and Villanueva, G. L. (2017b). Line parameters for CO2- and self-broadening in the ν3 band of HD16O. *Journal of Quantitative Spectroscopy and Radiative Transfer*, 203:158–174.

Devi, V. M., Benner, D. C., Sung, K., Crawford, T. J., Gamache, R. R., Renaud, C. L., Smith, M. A. H., Mantz, A. W., and Villanueva, G. L. (2017c). Line parameters for CO2 broadening in the ν2 band of HD16O. *Journal of Quantitative Spectroscopy and Radiative Transfer*, 187:472–488.

Eiler, J. M., Kitchen, N., and Rahn, T. A. (2000). Experimental constraints on the stable-isotope systematics of CO2 ice/vapor systems and relevance to the study of Mars. *Geochimica et Cosmochimica Acta*, 64(4):733–746.

Encrenaz, T., Bezard, B., Owen, T., Lebonnois, S., Lefevre, F., Greathouse, T., Richter, M., Lacy, J., Atreya, S., and Wong, A. (2005). Infrared imaging spectroscopy of Mars: H2O mapping and determination of CO2 isotopic ratios. *Icarus*, 179(1):43–54.

Encrenaz, T., Bézard, B., Greathouse, T., Richter, M., Lacy, J., Atreya, S., Wong, A., Lebonnois, S., Lefèvre, F., and Forget, F. (2004). Hydrogen peroxide on Mars: evidence for spatial and seasonal variations. *Icarus*, 170(2):424–429.

Encrenaz, T., DeWitt, C., Richter, M. J., Greathouse, T. K., Fouchet, T., Montmessin, F., Lefèvre, F., Bézard, B., Atreya, S. K., Aoki, S., and Sagawa, H. (2018). New measurements of D/H on Mars using EXES aboard SOFIA. *Astronomy & Astrophysics*, 612:A112.

Encrenaz, T., DeWitt, C., Richter, M. J., Greathouse, T. K., Fouchet, T., Montmessin, F., Lefèvre, F., Forget, F., Bézard, B., Atreya, S. K., Case, M., and Ryde, N. (2016). A map of D/H on Mars in the thermal infrared using EXES aboard SOFIA. *Astronomy & Astrophysics*, 586:A62.

Fanale, F. P. and Cannon, W. A. (1974). Exchange of adsorbed H $_2$ O and CO $_2$ between the regolith and atmosphere of Mars caused by changes in surface insolation. *Journal of Geophysical Research*, 79(24):3397–3402.

Fedorova, A., Montmessin, F., Korablev, O., Lefevre, F., Trokhimovskiy, A., and Bertaux, J. (2020a). Multi-annual monitoring of the water vapor vertical distribution on Mars by SPICAM on Mars Express. *Journal of Geophysical Research: Planets*, 126(1):e2020JE006616.

Fedorova, A. A., Montmessin, F., Korablev, O., Luginin, M., Trokhimovskiy, A., Belyaev, D. A., Ignatiev, N. I., Lefèvre, F., Alday, J., Irwin, P. G. J., Olsen, K. S., Bertaux, J.-L., Millour, E., Määttänen, A., Shakun, A., Grigoriev, A. V., Patrakeev, A., Korsa, S., Kokonkov, N., Baggio, L., Forget, F., and Wilson, C. F. (2020b). Stormy water on Mars: The distribution and saturation of atmospheric water during the dusty season. *Science*, 367(6475):297–300.

Feldman, W. C., Boynton, W. V., Tokar, R. L., Prettyman, T. H., Gasnault, O., Squyres, S. W., Elphic, R. C., Lawrence, D. J., Lawson, S. L., Maurice, S., McKinney, G. W., Moore, K. R., and Reedy, R. C. (2002). Global Distribution of Neutrons from Mars: Results from Mars Odyssey. *Science*, 297(5578):75–78. Publisher: American Association for the Advancement of Science Section: Report.

Feldman, W. C., Prettyman, T. H., Maurice, S., Plaut, J. J., Bish, D. L., Vaniman, D. T., Mellon, M. T., Metzger, A. E., Squyres, S. W., Karunatillake, S., Boynton, W. V., Elphic, R. C., Funsten, H. O., Lawrence, D. J., and Tokar, R. L. (2004). Global distribution of near-surface hydrogen on Mars. *Journal of Geophysical Research: Planets*, 109(E9). _eprint: https://agupubs.onlinelibrary.wiley.com/doi/pdf/10.1029/2003JE002160.

Forbes, J. M., Lemoine, F. G., Bruinsma, S. L., Smith, M. D., and Zhang, X. (2008). Solar flux variability of Mars' exosphere densities and temperatures. *Geophysical Research Letters*, 35(1):L01201.

Forget, F., Hansen, G. B., and Pollack, J. B. (1995). Low brightness temperatures of Martian polar caps: CO $_2$ clouds or low surface emissivity? *Journal of Geophysical Research*, 100(E10):21219.

Forget, F., Hourdin, F., Fournier, R., Hourdin, C., Talagrand, O., Collins, M., Lewis, S. R., Read, P. L., and Huot, J.-P. (1999). Improved general circulation models of the Martian atmosphere from the surface to above 80 km. *Journal of Geophysical Research: Planets*, 104(E10):24155–24175.

Forget, F., Montmessin, F., Bertaux, J.-L., González-Galindo, F., Lebonnois, S., Quémerais, E., Reberac, A., Dimarellis, E., and López-Valverde, M. A. (2009). Density and temperatures of the upper Martian atmosphere measured by stellar occultations with Mars Express SPICAM. *Journal of Geophysical Research*, 114(E1):E01004.

Formisano, V., Moroz, V., Amata, E., Baldetti, P., Bellucci, G., Chionchio, G., Matteuzzi, A., Orfei, R., Piccioni, G., Carusi, A., Coradini, A., Cerroni, P., Capaccioni, F., Adriani, A., Viterbini, M., Angrilli, F., Baglioni, P., Bianchini, G., Fanti, G., Bussoletti, E., Fonti, S., Mancini, D., Colangeli, L., Grigoriev, A., Moshkin, B., Zasova, L., Sanko, N., Nikolsky, Y., Gnedykh, V., Kiselev, A., Khatuntsev, I., Goncharov, S., Titov, D., Hirsh, H., Arnold, G., Orleansky, P., Combes, M., Michel, G., Rodrigo, R., Lopez Moreno, J. J., Rodriguez Gomez, J., and Olivares, I. (1993). Planetary Fourier spectrometer: An interferometer for atmospheric studies on board Mars 94 mission. *Il Nuovo Cimento C*, 16(5):575–588.

Fouchet, T. and Lellouch, E. (2000). Vapor Pressure Isotope Fractionation Effects in Planetary Atmospheres: Application to Deuterium. *Icarus*, 144(1):114–123.

Fox, J. L. and Bakalian, F. M. (2001). Photochemical escape of atomic carbon from Mars. *Journal of Geophysical Research: Space Physics*, 106(A12):28785–28795.

Fox, J. L. and Hać, A. (1999). Velocity distributions of C atoms in CO^+ dissociative recombination: Implications for photochemical escape of C from Mars. *Journal of Geophysical Research: Space Physics*, 104(A11):24729–24737.

Fox, J. L. and Hać, A. (2010). Isotope fractionation in the photochemical escape of O from Mars. *Icarus*, 208(1):176–191.

Gamache, R. R., Farese, M., and Renaud, C. L. (2016). A spectral line list for water isotopologues in the 1100–4100 cm1 region for application to CO2-rich planetary atmospheres. *Journal of Molecular Spectroscopy*, 326:144–150.

Gamache, R. R., Roller, C., Lopes, E., Gordon, I. E., Rothman, L. S., Polyansky, O. L., Zobov, N. F., Kyuberis, A. A., Tennyson, J., Yurchenko, S. N., Császár, A. G., Furtenbacher, T., Huang, X., Schwenke, D. W., Lee, T. J., Drouin, B. J., Tashkun, S. A., Perevalov, V. I., and Kochanov, R. V. (2017). Total internal partition sums for 166 isotopologues of 51 molecules

important in planetary atmospheres: Application to HITRAN2016 and beyond. *Journal of Quantitative Spectroscopy and Radiative Transfer*, 203:70–87.

Gamache, R. R. and Vispoel, B. (2018). On the temperature dependence of half-widths and line shifts for molecular transitions in the microwave and infrared regions. *Journal of Quantitative Spectroscopy and Radiative Transfer*, 217:440–452.

Geiger, B., Muñoz, C., Cardesin Moinelo, A., Frew, D., Aberasturi Vega, M., Ashman, M., Garcia Beteta, J. J., Muñoz, M., Costa, M., Metcalfe, L., and Svedhem, H. (2018). Long Term Planning for the ExoMars Trace Gas Orbiter Mission: Opportunity Analysis and Observation Scheduling. In *2018 SpaceOps Conference*, SpaceOps Conferences. American Institute of Aeronautics and Astronautics.

Gierasch, P. J. and Goody, R. M. (1972). The Effect of Dust on the Temperature of the Martian Atmosphere. *Journal of the Atmospheric Sciences*, 29(2):400–402.

Giuranna, M., Wolkenberg, P., Grassi, D., Aronica, A., Aoki, S., Scaccabarozzi, D., Saggin, B., and Formisano, V. (2019). The current weather and climate of Mars: 12 years of atmospheric monitoring by the Planetary Fourier Spectrometer on Mars Express. *Icarus*, page 113406.

Gkouvelis, L., Gérard, J., González-Galindo, F., Hubert, B., and Schneider, N. M. (2020). Isobar Altitude Variations in the Upper Mesosphere Observed With IUVS-MAVEN in Response to Martian Dust Storms. *Geophysical Research Letters*, 47(12).

González-Galindo, F., López-Valverde, M. A., Coll, M. A. i., and Forget, F. (2005). Extension of a Martian general circulation model to thermospheric altitudes: UV heating and photochemical models. *Journal of Geophysical Research: Planets*, 110(E9). _eprint: https://agupubs.onlinelibrary.wiley.com/doi/pdf/10.1029/2004JE002312.

Gordon, I., Rothman, L., Hill, C., Kochanov, R., Tan, Y., Bernath, P., Birk, M., Boudon, V., Campargue, A., Chance, K., Drouin, B., Flaud, J.-M., Gamache, R., Hodges, J., Jacquemart, D., Perevalov, V., Perrin, A., Shine, K., Smith, M.-A., Tennyson, J., Toon, G., Tran, H., Tyuterev, V., Barbe, A., Császár, A., Devi, V., Furtenbacher, T., Harrison, J., Hartmann, J.-M., Jolly, A., Johnson, T., Karman, T., Kleiner, I., Kyuberis, A., Loos, J., Lyulin, O., Massie, S., Mikhailenko, S., Moazzen-Ahmadi, N., Müller, H., Naumenko, O., Nikitin,

A., Polyansky, O., Rey, M., Rotger, M., Sharpe, S., Sung, K., Starikova, E., Tashkun, S., Auwera, J. V., Wagner, G., Wilzewski, J., Wcisło, P., Yu, S., and Zak, E. (2017). The HITRAN2016 molecular spectroscopic database. *Journal of Quantitative Spectroscopy and Radiative Transfer*, 203:3–69.

Gough, D. O. (1981). Solar interior structure and luminosity variations. *Solar Physics*, 74(1):21–34.

Greeley, R. and Schneid, B. D. (1991). Magma Generation on Mars: Amounts, Rates, and Comparisons with Earth, Moon, and Venus. *Science*, 254(5034):996–998. Publisher: American Association for the Advancement of Science.

Grott, M., Morschhauser, A., Breuer, D., and Hauber, E. (2011). Volcanic outgassing of CO2 and H2O on Mars. *Earth and Planetary Science Letters*, 308(3):391–400.

Gröller, H., Lichtenegger, H., Lammer, H., and Shematovich, V. (2014). Hot oxygen and carbon escape from the martian atmosphere. *Planetary and Space Science*, 98:93–105.

Haberle, R. M., Catling, D. C., Carr, M. H., and Zahnle, K. J. (2017). The Early Mars Climate System. In Haberle, R. M., Clancy, R. T., Forget, F., Smith, M. D., and Zurek, R. W., editors, *The Atmosphere and Climate of Mars*, pages 526–568. Cambridge University Press, Cambridge.

Haberle, R. M., Forget, F., Colaprete, A., Schaeffer, J., Boynton, W. V., Kelly, N. J., and Chamberlain, M. A. (2008). The effect of ground ice on the Martian seasonal CO2 cycle. *Planetary and Space Science*, 56(2):251–255.

Halekas, J. S. (2017). Seasonal variability of the hydrogen exosphere of Mars: Mars Hydrogen. *Journal of Geophysical Research: Planets*, 122(5):901–911.

Hansen, G. B. (1997). The infrared absorption spectrum of carbon dioxide ice from 1.8 to 333 µm. *Journal of Geophysical Research: Planets*, 102(E9):21569–21587.

Harri, A.-M., Genzer, M., Kemppinen, O., Kahanpää, H., Gomez-Elvira, J., Rodriguez-Manfredi, J. A., Haberle, R., Polkko, J., Schmidt, W., Savijärvi, H., Kauhanen, J., Atlaskin, E., Richardson, M., Siili, T., Paton, M., de la Torre Juarez, M., Newman, C., Rafkin, S., Lemmon, M. T., Mischna, M., Merikallio, S., Haukka, H., Martin-Torres, J.,

Zorzano, M.-P., Peinado, V., Urqui, R., Lapinette, A., Scodary, A., Mäkinen, T., Vazquez, L., Rennó, N., and the REMSMSL Science Team (2014). Pressure observations by the Curiosity rover: Initial results: MSL PRESSURE OBSERVATIONS: INITIAL RESULTS. *Journal of Geophysical Research: Planets*, 119(1):82–92.

Hartogh, P., Jarchow, C., Lellouch, E., de Val-Borro, M., Rengel, M., Moreno, R., Medvedev, A. S., Sagawa, H., Swinyard, B. M., Cavalié, T., Lis, D. C., Błęcka, M. I., Banaszkiewicz, M., Bockelée-Morvan, D., Crovisier, J., Encrenaz, T., Küppers, M., Lara, L.-M., Szutowicz, S., Vandenbussche, B., Bensch, F., Bergin, E. A., Billebaud, F., Biver, N., Blake, G. A., Blommaert, J. A. D. L., Cernicharo, J., Decin, L., Encrenaz, P., Feuchtgruber, H., Fulton, T., de Graauw, T., Jehin, E., Kidger, M., Lorente, R., Naylor, D. A., Portyankina, G., Sánchez-Portal, M., Schieder, R., Sidher, S., Thomas, N., Verdugo, E., Waelkens, C., Whyborn, N., Teyssier, D., Helmich, F., Roelfsema, P., Stutzki, J., LeDuc, H. G., and Stern, J. A. (2010). *Herschel* /HIFI observations of Mars: First detection of O $_2$ at submillimetre wavelengths and upper limits on HCl and H $_2$ O $_2$. *Astronomy and Astrophysics*, 521:L49.

Hase, F., Wallace, L., McLeod, S. D., Harrison, J. J., and Bernath, P. F. (2010). The ACE-FTS atlas of the infrared solar spectrum. *Journal of Quantitative Spectroscopy and Radiative Transfer*, 111(4):521–528.

Hayne, P. O., Paige, D. A., and Heavens, N. G. (2014). The role of snowfall in forming the seasonal ice caps of Mars: Models and constraints from the Mars Climate Sounder. *Icarus*, 231:122–130.

Hayne, P. O., Paige, D. A., Schofield, J. T., Kass, D. M., Kleinböhl, A., Heavens, N. G., and McCleese, D. J. (2012). Carbon dioxide snow clouds on Mars: South polar winter observations by the Mars Climate Sounder: POLAR SNOW CLOUDS ON MARS. *Journal of Geophysical Research: Planets*, 117(E8):n/a–n/a.

Head, J. W., Hiesinger, H., Ivanov, M. A., Kreslavsky, M. A., Pratt, S., and Thomson, B. J. (1999). Possible Ancient Oceans on Mars: Evidence from Mars Orbiter Laser Altimeter Data. *Science*, 286(5447):2134–2137. Publisher: American Association for the Advancement of Science Section: Report.

Heavens, N. G., Kleinböhl, A., Chaffin, M. S., Halekas, J. S., Kass, D. M., Hayne, P. O.,

McCleese, D. J., Piqueux, S., Shirley, J. H., and Schofield, J. T. (2018). Hydrogen escape from Mars enhanced by deep convection in dust storms. *Nature Astronomy*, 2(2):126–132.

Hess, S. L., Henry, R. M., Leovy, C. B., Ryan, J. A., and Tillman, J. E. (1977). Meteorological results from the surface of Mars: Viking 1 and 2. *Journal of Geophysical Research*, 82(28):4559–4574.

Hu, R. (2019). Predicted diurnal variation of the deuterium to hydrogen ratio in water at the surface of Mars caused by mass exchange with the regolith. *Earth and Planetary Science Letters*, 519:192–201.

Hu, R., Kass, D. M., Ehlmann, B. L., and Yung, Y. L. (2015). Tracing the fate of carbon and the atmospheric evolution of Mars. *Nature Communications*, 6(1):10003.

Irwin, P., Teanby, N., de Kok, R., Fletcher, L., Howett, C., Tsang, C., Wilson, C., Calcutt, S., Nixon, C., and Parrish, P. (2008). The NEMESIS planetary atmosphere radiative transfer and retrieval tool. *Journal of Quantitative Spectroscopy and Radiative Transfer*, 109(6):1136–1150.

Irwin, P. G., Toledo, D., Garland, R., Teanby, N. A., Fletcher, L. N., Orton, G. S., and Bézard, B. (2019). Probable detection of hydrogen sulphide (H2S) in Neptune's atmosphere. *Icarus*, 321:550–563.

Jakosky, B. (1997). Evolution of the Martian atmosphere. *Advances in Space Research*, 19(8):1289.

Jakosky, B., Brain, D., Chaffin, M., Curry, S., Deighan, J., Grebowsky, J., Halekas, J., Leblanc, F., Lillis, R., Luhmann, J., Andersson, L., Andre, N., Andrews, D., Baird, D., Baker, D., Bell, J., Benna, M., Bhattacharyya, D., Bougher, S., Bowers, C., Chamberlin, P., Chaufray, J.-Y., Clarke, J., Collinson, G., Combi, M., Connerney, J., Connour, K., Correira, J., Crabb, K., Crary, F., Cravens, T., Crismani, M., Delory, G., Dewey, R., DiBraccio, G., Dong, C., Dong, Y., Dunn, P., Egan, H., Elrod, M., England, S., Eparvier, F., Ergun, R., Eriksson, A., Esman, T., Espley, J., Evans, S., Fallows, K., Fang, X., Fillingim, M., Flynn, C., Fogle, A., Fowler, C., Fox, J., Fujimoto, M., Garnier, P., Girazian, Z., Groeller, H., Gruesbeck, J., Hamil, O., Hanley, K., Hara, T., Harada, Y., Hermann, J., Holmberg, M., Holsclaw, G., Houston, S., Inui, S., Jain, S., Jolitz, R., Kotova, A., Kuroda, T., Larson,

D., Lee, Y., Lee, C., Lefevre, F., Lentz, C., Lo, D., Lugo, R., Ma, Y.-J., Mahaffy, P., Marquette, M., Matsumoto, Y., Mayyasi, M., Mazelle, C., McClintock, W., McFadden, J., Medvedev, A., Mendillo, M., Meziane, K., Milby, Z., Mitchell, D., Modolo, R., Montmessin, F., Nagy, A., Nakagawa, H., Narvaez, C., Olsen, K., Pawlowski, D., Peterson, W., Rahmati, A., Roeten, K., Romanelli, N., Ruhunusiri, S., Russell, C., Sakai, S., Schneider, N., Seki, K., Sharrar, R., Shaver, S., Siskind, D., Slipski, M., Soobiah, Y., Steckiewicz, M., Stevens, M., Stewart, I., Stiepen, A., Stone, S., Tenishev, V., Terada, N., Terada, K., Thiemann, E., Tolson, R., Toth, G., Trovato, J., Vogt, M., Weber, T., Withers, P., Xu, S., Yelle, R., Yiğit, E., and Zurek, R. (2018). Loss of the Martian atmosphere to space: Present-day loss rates determined from MAVEN observations and integrated loss through time. *Icarus*, 315:146–157.

Jakosky, B. M. (1991). Mars volatile evolution: Evidence from stable isotopes. *Icarus*, 94(1):14–31.

Jakosky, B. M. (2019). The CO2 inventory on Mars. *Planetary and Space Science*, 175:52–59.

Jakosky, B. M. and Farmer, C. B. (1982). The seasonal and global behavior of water vapor in the Mars atmosphere: Complete global results of the Viking Atmospheric Water Detector Experiment. *Journal of Geophysical Research*, 87(B4):2999.

Jakosky, B. M., Pepin, R. O., Johnson, R. E., and Fox, J. (1994). Mars Atmospheric Loss and Isotopic Fractionation by Solar-Wind-Induced Sputtering and Photochemical Escape. *Icarus*, 111(2):271–288.

Jakosky, B. M., Slipski, M., Benna, M., Mahaffy, P., Elrod, M., Yelle, R., Stone, S., and Alsaeed, N. (2017). Mars' atmospheric history derived from upper-atmosphere measurements of ^{38}Ar/^{36}Ar. *Science*, 355(6332):1408–1410.

Jiang, F. Y., Yelle, R. V., Jain, S. K., Cui, J., Montmessin, F., Schneider, N. M., Deighan, J., Gröller, H., and Verdier, L. (2019). Detection of Mesospheric CO $_2$ Ice Clouds on Mars in Southern Summer. *Geophysical Research Letters*, 46(14):7962–7971.

Johnson, S. S., Mischna, M. A., Grove, T. L., and Zuber, M. T. (2008). Sulfur-induced greenhouse warming on early Mars. *Journal of Geophysical Research*, 113(E8):E08005.

Jouzel, J. and Merlivat, L. (1984). Deuterium and oxygen 18 in precipitation: Modeling of the isotopic effects during snow formation. *Journal of Geophysical Research*, 89(D7):11749.

Kaplan, L. D., Connes, J., and Connes, P. (1969). Carbon Monoxide in the Martian Atmosphere. *The Astrophysical Journal Letters*, 157:L187.

Kasting, J. F. (1991). CO2 condensation and the climate of early Mars. *Icarus*, 94(1):1–13.

Kelly, N. J., Boynton, W. V., Kerry, K., Hamara, D., Janes, D., Reedy, R. C., Kim, K. J., and Haberle, R. M. (2007). Seasonal polar carbon dioxide frost on Mars: CO $_2$ mass and columnar thickness distribution. *Journal of Geophysical Research*, 112(E3):E03S07.

Khayat, A. S., Villanueva, G. L., Smith, M. D., and Guzewich, S. D. (2019). IRTF/CSHELL mapping of atmospheric HDO, H2O and D/H on Mars during northern summer. *Icarus*, 330:204–216.

Kieffer, H. H. (1979). Mars south polar spring and summer temperatures: A residual CO $_2$ frost. *Journal of Geophysical Research*, 84(B14):8263.

Kleinböhl, A., Schofield, J. T., Kass, D. M., Abdou, W. A., Backus, C. R., Sen, B., Shirley, J. H., Lawson, W. G., Richardson, M. I., Taylor, F. W., Teanby, N. A., and McCleese, D. J. (2009). Mars Climate Sounder limb profile retrieval of atmospheric temperature, pressure, and dust and water ice opacity: MCS RETRIEVALS. *Journal of Geophysical Research: Planets*, 114(E10):n/a–n/a.

Korablev, O., Bertaux, J.-L., Fedorova, A., Fonteyn, D., Stepanov, A., Kalinnikov, Y., Kiselev, A., Grigoriev, A., Jegoulev, V., Perrier, S., Dimarellis, E., Dubois, J. P., Reberac, A., Ransbeeck, E. V., Gondet, B., Montmessin, F., and Rodin, A. (2006). SPICAM IR acousto-optic spectrometer experiment on Mars Express. *Journal of Geophysical Research: Planets*, 111(E9). _eprint: https://agupubs.onlinelibrary.wiley.com/doi/pdf/10.1029/2006JE002696.

Korablev, O., Montmessin, F., Trokhimovskiy, A., Fedorova, A. A., Shakun, A. V., Grigoriev, A. V., Moshkin, B. E., Ignatiev, N. I., Forget, F., Lefèvre, F., Anufreychik, K., Dzuban, I., Ivanov, Y. S., Kalinnikov, Y. K., Kozlova, T. O., Kungurov, A., Makarov, V., Martynovich, F., Maslov, I., Merzlyakov, D., Moiseev, P. P., Nikolskiy, Y., Patrakeev, A., Patsaev, D.,

Santos-Skripko, A., Sazonov, O., Semena, N., Semenov, A., Shashkin, V., Sidorov, A., Stepanov, A. V., Stupin, I., Timonin, D., Titov, A. Y., Viktorov, A., Zharkov, A., Altieri, F., Arnold, G., Belyaev, D. A., Bertaux, J. L., Betsis, D. S., Duxbury, N., Encrenaz, T., Fouchet, T., Gérard, J.-C., Grassi, D., Guerlet, S., Hartogh, P., Kasaba, Y., Khatuntsev, I., Krasnopolsky, V. A., Kuzmin, R. O., Lellouch, E., Lopez-Valverde, M. A., Luginin, M., Määttänen, A., Marcq, E., Martin Torres, J., Medvedev, A. S., Millour, E., Olsen, K. S., Patel, M. R., Quantin-Nataf, C., Rodin, A. V., Shematovich, V. I., Thomas, I., Thomas, N., Vazquez, L., Vincendon, M., Wilquet, V., Wilson, C. F., Zasova, L. V., Zelenyi, L. M., and Zorzano, M. P. (2018). The Atmospheric Chemistry Suite (ACS) of Three Spectrometers for the ExoMars 2016 Trace Gas Orbiter. *Space Science Reviews*, 214(1):7.

Korablev, O., Olsen, K. S., Trokhimovskiy, A., Lefèvre, F., Montmessin, F., Fedorova, A. A., Toplis, M. J., Alday, J., Belyaev, D. A., Patrakeev, A., Ignatiev, N. I., Shakun, A. V., Grigoriev, A. V., Baggio, L., Abdenour, I., Lacombe, G., Ivanov, Y. S., Aoki, S., Thomas, I. R., Daerden, F., Ristic, B., Erwin, J. T., Patel, M., Bellucci, G., Lopez-Moreno, J.-J., and Vandaele, A. C. (2021). Transient HCl in the atmosphere of Mars. *Science Advances*, 7(7):eabe4386.

Korablev, O., Vandaele, A. C., Montmessin, F., Fedorova, A. A., Trokhimovskiy, A., Forget, F., Lefèvre, F., Daerden, F., Thomas, I. R., Trompet, L., Erwin, J. T., Aoki, S., Robert, S., Neary, L., Viscardy, S., Grigoriev, A. V., Ignatiev, N. I., Shakun, A., Patrakeev, A., Belyaev, D. A., Bertaux, J.-L., Olsen, K. S., Baggio, L., Alday, J., Ivanov, Y. S., Ristic, B., Mason, J., Willame, Y., Depiesse, C., Hetey, L., Berkenbosch, S., Clairquin, R., Queirolo, C., Beeckman, B., Neefs, E., Patel, M. R., Bellucci, G., López-Moreno, J.-J., Wilson, C. F., Etiope, G., Zelenyi, L., Svedhem, H., and Vago, J. L. (2019). No detection of methane on Mars from early ExoMars Trace Gas Orbiter observations. *Nature*, 568(7753):517–520.

Korablev, O. I., Bertaux, J.-L., and Vinogradov, I. I. (2002). Compact high-resolution IR spectrometer for atmospheric studies. In *Infrared Spaceborne Remote Sensing X*, volume 4818, pages 272–281. International Society for Optics and Photonics.

Korablev, O. I., Grigoriev, A. V., Moshkin, B. E., Patsaev, D. V., Makarov, V. S., Maksimenko, S. V., Grechnev, K. V., Kotlov, V. I., Zasova, L. V., Shakun, A. V., Fedorova, A. A., Terentiev, A. I., Ekonomov, A. P., Khatuntsev, I. V., Mayorov, B. S., Nikolsky,

Y. V., Maslov, I. A., Gvozdev, A. B., Montmessin, F., and Kuzmin, R. O. (2009). The AOST miniature Fourier spectrometer for space studies. *Journal of Optical Technology*, 76(2):75.

Krasnopolsky, V. (2000). On the Deuterium Abundance on Mars and Some Related Problems. *Icarus*, 148(2):597–602.

Krasnopolsky, V., Mumma, M., Bjoraker, G., and Jennings, D. (1996). Oxygen and Carbon Isotope Ratios in Martian Carbon Dioxide: Measurements and Implications for Atmospheric Evolution. *Icarus*, 124(2):553–568.

Krasnopolsky, V. A. (2002). Mars' upper atmosphere and ionosphere at low, medium, and high solar activities: Implications for evolution of water. *Journal of Geophysical Research: Planets*, 107(E12):11–1.

Krasnopolsky, V. A. (2015). Variations of the HDO/H2O ratio in the martian atmosphere and loss of water from Mars. *Icarus*, 257:377–386.

Krasnopolsky, V. A. (2019). Photochemistry of water in the martian thermosphere and its effect on hydrogen escape. *Icarus*, 321:62–70.

Krasnopolsky, V. A., Bjoraker, G. L., Mumma, M. J., and Jennings, D. E. (1997). High-resolution spectroscopy of Mars at 3.7 and 8 μm: A sensitive search for H $_2$ O $_2$, H $_2$ CO, HCl, and CH $_4$, and detection of HDO. *Journal of Geophysical Research: Planets*, 102(E3):6525–6534.

Krasnopolsky, V. A. and Feldman, P. D. (2001). Detection of Molecular Hydrogen in the Atmosphere of Mars. *Science*, 294(5548):1914.

Krasnopolsky, V. A., Maillard, J. P., Owen, T. C., Toth, R. A., and Smith, M. D. (2007). Oxygen and carbon isotope ratios in the martian atmosphere. *Icarus*, 192(2):396–403.

Krasnopolsky, V. A., Mumma, M. J., and Gladstone, G. R. (1998). Detection of Atomic Deuterium in the Upper Atmosphere of Mars. *Science*, 280(5369):1576–1580.

Kurokawa, H., Sato, M., Ushioda, M., Matsuyama, T., Moriwaki, R., Dohm, J., and Usui, T. (2014). Evolution of water reservoirs on Mars: Constraints from hydrogen isotopes in martian meteorites. *Earth and Planetary Science Letters*, 394:179–185.

Lamb, K. D., Clouser, B. W., Bolot, M., Sarkozy, L., Ebert, V., Saathoff, H., Möhler, O., and Moyer, E. J. (2017). Laboratory measurements of HDO/H $_2$ O isotopic fractionation during ice deposition in simulated cirrus clouds. *Proceedings of the National Academy of Sciences*, 114(22):5612–5617.

Landais, A., Barkan, E., and Luz, B. (2008). Record of $\backslash delta\ ^{18}$ O and ^{17} O-excess in ice from Vostok Antarctica during the last 150,000 years. *Geophysical Research Letters*, 35(2):L02709.

Lasue, J., Mangold, N., Hauber, E., Clifford, S., Feldman, W., Gasnault, O., Grima, C., Maurice, S., and Mousis, O. (2013). Quantitative Assessments of the Martian Hydrosphere. *Space Science Reviews*, 174(1-4):155–212.

Leblanc, F. (2002). Role of molecular species in pickup ion sputtering of the Martian atmosphere. *Journal of Geophysical Research*, 107(E2):5010.

Lefèvre, F. and Krasnopolsky, V. (2017). Atmospheric Photochemistry. In Haberle, R. M., Clancy, R. T., Forget, F., Smith, M. D., and Zurek, R. W., editors, *The Atmosphere and Climate of Mars*, pages 405–432. Cambridge University Press, Cambridge.

Lefèvre, F., Lebonnois, S., Montmessin, F., and Forget, F. (2004). Three-dimensional modeling of ozone on Mars. *Journal of Geophysical Research: Planets*, 109(E7). _eprint: https://agupubs.onlinelibrary.wiley.com/doi/pdf/10.1029/2004JE002268.

Liang, M.-C., Blake, G. A., and Yung, Y. L. (2004). A semianalytic model for photo-induced isotopic fractionation in simple molecules. *Journal of Geophysical Research: Atmospheres*, 109(D10). _eprint: https://agupubs.onlinelibrary.wiley.com/doi/pdf/10.1029/2004JD004539.

Livengood, T. A., Kostiuk, T., Hewagama, T., Smith, R. L., Fast, K. E., Annen, J. N., and Delgado, J. D. (2020). Evidence for diurnally varying enrichment of heavy oxygen in Mars atmosphere. *Icarus*, 335:113387.

Lo, D. Y., Yelle, R. V., and Lillis, R. J. (2020). Carbon photochemistry at Mars: Updates with recent data. *Icarus*, 352:114001.

Lu, Z., Chang, Y. C., Yin, Q.-Z., Ng, C. Y., and Jackson, W. M. (2014). Evidence for direct molecular oxygen production in CO $_2$ photodissociation. *Science*, 346(6205):61–64.

Luginin, M., Fedorova, A., Ignatiev, N., Trokhimovskiy, A., Shakun, A., Grigoriev, A., Patrakeev, A., Montmessin, F., and Korablev, O. (2020). Properties of Water Ice and Dust Particles in the Atmosphere of Mars During the 2018 Global Dust Storm as Inferred From the Atmospheric Chemistry Suite. *Journal of Geophysical Research: Planets*, 125(11):e2020JE006419.

Luz, B., Barkan, E., Yam, R., and Shemesh, A. (2009). Fractionation of oxygen and hydrogen isotopes in evaporating water. *Geochimica et Cosmochimica Acta*, 73(22):6697–6703.

Lämmerzahl, P., Röckmann, T., Brenninkmeijer, C. A. M., Krankowsky, D., and Mauersberger, K. (2002). Oxygen isotope composition of stratospheric carbon dioxide. *Geophysical Research Letters*, 29(12):23–1–23–4. _eprint: https://agupubs.onlinelibrary.wiley.com/doi/pdf/10.1029/2001GL014343.

Madeleine, J.-B., Forget, F., Millour, E., Montabone, L., and Wolff, M. J. (2011). Revisiting the radiative impact of dust on Mars using the LMD Global Climate Model. *Journal of Geophysical Research*, 116(E11):E11010.

Mahaffy, P. R., Webster, C. R., Atreya, S. K., Franz, H., Wong, M., Conrad, P. G., Harpold, D., Jones, J. J., Leshin, L. A., Manning, H., Owen, T., Pepin, R. O., Squyres, S., Trainer, M., MSL Science Team, Kemppinen, O., Bridges, N., Johnson, J. R., Minitti, M., Cremers, D., Bell, J. F., Edgar, L., Farmer, J., Godber, A., Wadhwa, M., Wellington, D., McEwan, I., Newman, C., Richardson, M., Charpentier, A., Peret, L., King, P., Blank, J., Weigle, G., Schmidt, M., Li, S., Milliken, R., Robertson, K., Sun, V., Baker, M., Edwards, C., Ehlmann, B., Farley, K., Griffes, J., Grotzinger, J., Miller, H., Newcombe, M., Pilorget, C., Rice, M., Siebach, K., Stack, K., Stolper, E., Brunet, C., Hipkin, V., Leveille, R., Marchand, G., Sanchez, P. S., Favot, L., Cody, G., Steele, A., Fluckiger, L., Lees, D., Nefian, A., Martin, M., Gailhanou, M., Westall, F., Israel, G., Agard, C., Baroukh, J., Donny, C., Gaboriaud, A., Guillemot, P., Lafaille, V., Lorigny, E., Paillet, A., Perez, R., Saccoccio, M., Yana, C., Armiens-Aparicio, C., Rodriguez, J. C., Blazquez, I. C., Gomez, F. G., Gomez-Elvira, J., Hettrich, S., Malvitte, A. L., Jimenez, M. M., Martinez-Frias, J., Martin-Soler, J., Martin-Torres, F. J., Jurado, A. M., Mora-Sotomayor, L., Caro, G. M.,

Lopez, S. N., Peinado-Gonzalez, V., Pla-Garcia, J., Manfredi, J. A. R., Romeral-Planello, J. J., Fuentes, S. A. S., Martinez, E. S., Redondo, J. T., Urqui-O'Callaghan, R., Mier, M.-P. Z., Chipera, S., Lacour, J.-L., Mauchien, P., Sirven, J.-B., Fairen, A., Hayes, A., Joseph, J., Sullivan, R., Thomas, P., Dupont, A., Lundberg, A., Melikechi, N., Mezzacappa, A., DeMarines, J., Grinspoon, D., Reitz, G., Prats, B., Atlaskin, E., Genzer, M., Harri, A.-M., Haukka, H., Kahanpaa, H., Kauhanen, J., Kemppinen, O., Paton, M., Polkko, J., Schmidt, W., Siili, T., Fabre, C., Wray, J., Wilhelm, M. B., Poitrasson, F., Patel, K., Gorevan, S., Indyk, S., Paulsen, G., Gupta, S., Bish, D., Schieber, J., Gondet, B., Langevin, Y., Geffroy, C., Baratoux, D., Berger, G., Cros, A., d'Uston, C., Forni, O., Gasnault, O., Lasue, J., Lee, Q.-M., Maurice, S., Meslin, P.-Y., Pallier, E., Parot, Y., Pinet, P., Schroder, S., Toplis, M., Lewin, E., Brunner, W., Heydari, E., Achilles, C., Oehler, D., Sutter, B., Cabane, M., Coscia, D., Israel, G., Szopa, C., Dromart, G., Robert, F., Sautter, V., Le Mouelic, S., Mangold, N., Nachon, M., Buch, A., Stalport, F., Coll, P., Francois, P., Raulin, F., Teinturier, S., Cameron, J., Clegg, S., Cousin, A., DeLapp, D., Dingler, R., Jackson, R. S., Johnstone, S., Lanza, N., Little, C., Nelson, T., Wiens, R. C., Williams, R. B., Jones, A., Kirkland, L., Treiman, A., Baker, B., Cantor, B., Caplinger, M., Davis, S., Duston, B., Edgett, K., Fay, D., Hardgrove, C., Harker, D., Herrera, P., Jensen, E., Kennedy, M. R., Krezoski, G., Krysak, D., Lipkaman, L., Malin, M., McCartney, E., McNair, S., Nixon, B., Posiolova, L., Ravine, M., Salamon, A., Saper, L., Stoiber, K., Supulver, K., Van Beek, J., Van Beek, T., Zimdar, R., French, K. L., Iagnemma, K., Miller, K., Summons, R., Goesmann, F., Goetz, W., Hviid, S., Johnson, M., Lefavor, M., Lyness, E., Breves, E., Dyar, M. D., Fassett, C., Blake, D. F., Bristow, T., DesMarais, D., Edwards, L., Haberle, R., Hoehler, T., Hollingsworth, J., Kahre, M., Keely, L., McKay, C., Wilhelm, M. B., Bleacher, L., Brinckerhoff, W., Choi, D., Dworkin, J. P., Eigenbrode, J., Floyd, M., Freissinet, C., Garvin, J., Glavin, D., Jones, A., Martin, D. K., McAdam, A., Pavlov, A., Raaen, E., Smith, M. D., Stern, J., Tan, F., Meyer, M., Posner, A., Voytek, M., Anderson, R. C., Aubrey, A., Beegle, L. W., Behar, A., Blaney, D., Brinza, D., Calef, F., Christensen, L., Crisp, J. A., DeFlores, L., Ehlmann, B., Feldman, J., Feldman, S., Flesch, G., Hurowitz, J., Jun, I., Keymeulen, D., Maki, J., Mischna, M., Morookian, J. M., Parker, T., Pavri, B., Schoppers, M., Sengstacken, A., Simmonds, J. J., Spanovich, N., Juarez, M. d. l. T., Vasavada, A. R., Yen, A., Archer, P. D., Cucinotta, F., Ming, D.,

Morris, R. V., Niles, P., Rampe, E., Nolan, T., Fisk, M., Radziemski, L., Barraclough, B., Bender, S., Berman, D., Dobrea, E. N., Tokar, R., Vaniman, D., Williams, R. M. E., Yingst, A., Lewis, K., Cleghorn, T., Huntress, W., Manhes, G., Hudgins, J., Olson, T., Stewart, N., Sarrazin, P., Grant, J., Vicenzi, E., Wilson, S. A., Bullock, M., Ehresmann, B., Hamilton, V., Hassler, D., Peterson, J., Rafkin, S., Zeitlin, C., Fedosov, F., Golovin, D., Karpushkina, N., Kozyrev, A., Litvak, M., Malakhov, A., Mitrofanov, I., Mokrousov, M., Nikiforov, S., Prokhorov, V., Sanin, A., Tretyakov, V., Varenikov, A., Vostrukhin, A., Kuzmin, R., Clark, B., Wolff, M., McLennan, S., Botta, O., Drake, D., Bean, K., Lemmon, M., Schwenzer, S. P., Anderson, R. B., Herkenhoff, K., Lee, E. M., Sucharski, R., Hernandez, M. A. d. P., Avalos, J. J. B., Ramos, M., Kim, M.-H., Malespin, C., Plante, I., Muller, J.-P., Navarro-Gonzalez, R., Ewing, R., Boynton, W., Downs, R., Fitzgibbon, M., Harshman, K., Morrison, S., Dietrich, W., Kortmann, O., Palucis, M., Sumner, D. Y., Williams, A., Lugmair, G., Wilson, M. A., Rubin, D., Jakosky, B., Balic-Zunic, T., Frydenvang, J., Jensen, J. K., Kinch, K., Koefoed, A., Madsen, M. B., Stipp, S. L. S., Boyd, N., Campbell, J. L., Gellert, R., Perrett, G., Pradler, I., VanBommel, S., Jacob, S., Rowland, S., Atlaskin, E., Savijarvi, H., Boehm, E., Bottcher, S., Burmeister, S., Guo, J., Kohler, J., Garcia, C. M., Mueller-Mellin, R., Wimmer-Schweingruber, R., Bridges, J. C., McConnochie, T., Benna, M., Bower, H., Brunner, A., Blau, H., Boucher, T., Carmosino, M., Elliott, H., Halleaux, D., Renno, N., Elliott, B., Spray, J., Thompson, L., Gordon, S., Newsom, H., Ollila, A., Williams, J., Vasconcelos, P., Bentz, J., Nealson, K., Popa, R., Kah, L. C., Moersch, J., Tate, C., Day, M., Kocurek, G., Hallet, B., Sletten, R., Francis, R., McCullough, E., Cloutis, E., ten Kate, I. L., Kuzmin, R., Arvidson, R., Fraeman, A., Scholes, D., Slavney, S., Stein, T., Ward, J., Berger, J., and Moores, J. E. (2013). Abundance and Isotopic Composition of Gases in the Martian Atmosphere from the Curiosity Rover. *Science*, 341(6143):263–266.

Mahata, S. and Bhattacharya, S. (2009a). Temperature dependence of isotopic fractionation in CO2 photolysis. *Chemical Physics Letters*, 477(1-3):52–56.

Mahata, S. and Bhattacharya, S. K. (2009b). Anomalous enrichment of O17 and C13 in photodissociation products of CO2: Possible role of nuclear spin. *The Journal of Chemical Physics*, 130(23):234312.

Mahieux, A., Vandaele, A. C., Neefs, E., Robert, S., Wilquet, V., Drummond, R., Federova,

A., and Bertaux, J. L. (2010). Densities and temperatures in the Venus mesosphere and lower thermosphere retrieved from SOIR on board Venus Express: Retrieval technique. *Journal of Geophysical Research*, 115(E12):E12014.

Mahieux, A., Vandaele, A. C., Robert, S., Wilquet, V., Drummond, R., Montmessin, F., and Bertaux, J. L. (2012). Densities and temperatures in the Venus mesosphere and lower thermosphere retrieved from SOIR on board Venus Express: Carbon dioxide measurements at the Venus terminator: CO $_2$ MEASUREMENTS AT THE VENUS TERMINATOR. *Journal of Geophysical Research: Planets*, 117(E7):n/a–n/a.

Majoube, M. (1970). Fractionation Factor of 18O between Water Vapour and Ice. *Nature*, 226(5252):1242–1242.

Majoube, M. (1971). Fractionnement en oxygène 18 et en deutérium entre l'eau et sa vapeur. *Journal de Chimie Physique*, 68:1423–1436. Publisher: EDP Sciences.

Maltagliati, L., Montmessin, F., Fedorova, A., Korablev, O., Forget, F., and Bertaux, J.-L. (2011). Evidence of Water Vapor in Excess of Saturation in the Atmosphere of Mars. *Science*, 333(6051):1868–1871.

Martín-Torres, F. J., Zorzano, M.-P., Valentín-Serrano, P., Harri, A.-M., Genzer, M., Kemppinen, O., Rivera-Valentin, E. G., Jun, I., Wray, J., Bo Madsen, M., Goetz, W., McEwen, A. S., Hardgrove, C., Renno, N., Chevrier, V. F., Mischna, M., Navarro-González, R., Martínez-Frías, J., Conrad, P., McConnochie, T., Cockell, C., Berger, G., R. Vasavada, A., Sumner, D., and Vaniman, D. (2015). Transient liquid water and water activity at Gale crater on Mars. *Nature Geoscience*, 8(5):357–361.

Mauersberger, K. (1981). Measurement of heavy ozone in the stratosphere. *Geophysical Research Letters*, 8(8):935–937.

Mayyasi, M., Clarke, J., Bhattacharyya, D., Chaufray, J. Y., Benna, M., Mahaffy, P., Stone, S., Yelle, R., Thiemann, E., Chaffin, M., Deighan, J., Jain, S., Schneider, N., and Jakosky, B. (2019). Seasonal Variability of Deuterium in the Upper Atmosphere of Mars. *Journal of Geophysical Research: Space Physics*, 124(3):2152–2164.

McCleese, D. J., Heavens, N. G., Schofield, J. T., Abdou, W. A., Bandfield, J. L., Calcutt, S. B., Irwin, P. G. J., Kass, D. M., Kleinböhl, A., Lewis, S. R., Paige, D. A., Read, P. L.,

Richardson, M. I., Shirley, J. H., Taylor, F. W., Teanby, N., and Zurek, R. W. (2010). Structure and dynamics of the Martian lower and middle atmosphere as observed by the Mars Climate Sounder: Seasonal variations in zonal mean temperature, dust, and water ice aerosols. *Journal of Geophysical Research*, 115(E12):E12016.

McConnochie, T., Bell III, J., Savransky, D., Wolff, M., Toigo, A., Wang, H., Richardson, M., and Christensen, P. (2010). THEMIS-VIS observations of clouds in the martian mesosphere: Altitudes, wind speeds, and decameter-scale morphology. *Icarus*, 210(2):545–565.

McElroy, M. B. (1972). Mars: An Evolving Atmosphere. *Science*, 175(4020):443–445.

McElroy, M. B. and Donahue, T. M. (1972). Stability of the Martian Atmosphere. *Science*, 177(4053):986–988.

Merlivat, L. (1978). Molecular diffusivities of H[sub 2] [sup 16]O, HD[sup 16]O, and H[sub 2] [sup 18]O in gases. *The Journal of Chemical Physics*, 69(6):2864.

Merlivat, L. and Nief, G. (1967). Fractionnement isotopique lors des changements d'état solide-vapeur et liquide-vapeur de l'eau à des températures inférieures à 0°C. *Tellus*, 19(1):122–127.

Milkovich, S. M. and Head, J. W. (2005). North polar cap of Mars: Polar layered deposit characterization and identification of a fundamental climate signal. *Journal of Geophysical Research: Planets*, 110(E1). _eprint: https://agupubs.onlinelibrary.wiley.com/doi/pdf/10.1029/2004JE002349.

Miller, C. E. and Yung, Y. L. (2000). Photo-induced isotopic fractionation. *Journal of Geophysical Research: Atmospheres*, 105(D23):29039–29051.

Mitrofanov, I., Malakhov, A., Bakhtin, B., Golovin, D., Kozyrev, A., Litvak, M., Mokrousov, M., Sanin, A., Tretyakov, V., Vostrukhin, A., Anikin, A., Zelenyi, L. M., Semkova, J., Malchev, S., Tomov, B., Matviichuk, Y., Dimitrov, P., Koleva, R., Dachev, T., Krastev, K., Shvetsov, V., Timoshenko, G., Bobrovnitsky, Y., Tomilina, T., Benghin, V., and Shurshakov, V. (2018). Fine Resolution Epithermal Neutron Detector (FREND) Onboard the ExoMars Trace Gas Orbiter. *Space Science Reviews*, 214(5):86.

Montmessin, F. (2002). New insights into Martian dust distribution and water-ice cloud microphysics. *Journal of Geophysical Research*, 107(E6):5037.

Montmessin, F., Bertaux, J.-L., Quémerais, E., Korablev, O., Rannou, P., Forget, F., Perrier, S., Fussen, D., Lebonnois, S., Rébérac, A., and Dimarellis, E. (2006a). Subvisible CO2 ice clouds detected in the mesosphere of Mars. *Icarus*, 183(2):403–410.

Montmessin, F., Forget, F., Rannou, P., Cabane, M., and Haberle, R. M. (2004). Origin and role of water ice clouds in the Martian water cycle as inferred from a general circulation model. *Journal of Geophysical Research: Planets*, 109(E10):E10004.

Montmessin, F., Fouchet, T., and Forget, F. (2005). Modeling the annual cycle of HDO in the Martian atmosphere. *Journal of Geophysical Research: Planets*, 110(E3):E03006.

Montmessin, F., Gondet, B., Bibring, J.-P., Langevin, Y., Drossart, P., Forget, F., and Fouchet, T. (2007). Hyperspectral imaging of convective CO $_2$ ice clouds in the equatorial mesosphere of Mars. *Journal of Geophysical Research*, 112(E11):E11S90.

Montmessin, F., Quémerais, E., Bertaux, J. L., Korablev, O., Rannou, P., and Lebonnois, S. (2006b). Stellar occultations at UV wavelengths by the SPICAM instrument: Retrieval and analysis of Martian haze profiles. *Journal of Geophysical Research*, 111(E9):E09S09.

Moores, J. E., Smith, P. H., and Boynton, W. V. (2011). Adsorptive fractionation of HDO on JSC MARS-1 during sublimation with implications for the regolith of Mars. *Icarus*, 211(2):1129–1149.

Mota, R., Parafita, R., Giuliani, A., Hubin-Franskin, M.-J., Lourenço, J., Garcia, G., Hoffmann, S., Mason, N., Ribeiro, P., Raposo, M., and Limão-Vieira, P. (2005). Water VUV electronic state spectroscopy by synchrotron radiation. *Chemical Physics Letters*, 416(1-3):152–159.

Mumma, M. J., Novak, R. E., DiSanti, M. A., Bonev, B., Russo, N. D., and Magee-Sauer, K. (2003). SEASONAL MAPPING OF HDO and H2O IN THE MARTIAN ATMOSPHERE. page 3.

Mumma, M. J., Novak, R. E., DiSanti, M. A., Bonev, B. P., and Dello Russo, N. (2004). Detection and Mapping of Methane and Water on Mars. In *AAS/Division for Planetary Sciences Meeting Abstracts #36*, volume 36, page 26.02.

Murchie, S. L., Mustard, J. F., Ehlmann, B. L., Milliken, R. E., Bishop, J. L., McKeown, N. K., Noe Dobrea, E. Z., Seelos, F. P., Buczkowski, D. L., Wiseman, S. M., Arvidson, R. E., Wray, J. J., Swayze, G., Clark, R. N., Des Marais, D. J., McEwen, A. S., and Bibring, J.-P. (2009). A synthesis of Martian aqueous mineralogy after 1 Mars year of observations from the Mars Reconnaissance Orbiter. *Journal of Geophysical Research*, 114:E00D06.

Määttänen, A., Montmessin, F., Gondet, B., Scholten, F., Hoffmann, H., González-Galindo, F., Spiga, A., Forget, F., Hauber, E., Neukum, G., Bibring, J.-P., and Bertaux, J.-L. (2010). Mapping the mesospheric CO2 clouds on Mars: MEx/OMEGA and MEx/HRSC observations and challenges for atmospheric models. *Icarus*, 209(2):452–469.

Nair, H., Allen, M., Anbar, A. D., Yung, Y. L., and Clancy, R. (1994). A Photochemical Model of the Martian Atmosphere. *Icarus*, 111(1):124–150.

Neary, L., Daerden, F., Aoki, S., Whiteway, J., Clancy, R. T., Smith, M., Viscardy, S., Erwin, J., Thomas, I. R., Villanueva, G., Liuzzi, G., Crismani, M., Wolff, M., Lewis, S. R., Holmes, J. A., Patel, M. R., Giuranna, M., Depiesse, C., Piccialli, A., Robert, S., Trompet, L., Willame, Y., Ristic, B., and Vandaele, A. C. (2020). Explanation for the increase in high-altitude water on Mars observed by NOMAD during the 2018 global dust storm. *Geophysical Research Letters*, 47(7):e2019GL084354.

Nevejans, D., Neefs, E., Van Ransbeeck, E., Berkenbosch, S., Clairquin, R., De Vos, L., Moelans, W., Glorieux, S., Baeke, A., Korablev, O., Vinogradov, I., Kalinnikov, Y., Bach, B., Dubois, J.-P., and Villard, E. (2006). Compact high-resolution spaceborne echelle grating spectrometer with acousto-optical tunable filter based order sorting for the infrared domain from 22 to 43 µm. *Applied Optics*, 45(21):5191.

Nier, A. O. and McElroy, M. B. (1977). Composition and structure of Mars' Upper atmosphere: Results from the neutral mass spectrometers on Viking 1 and 2. *Journal of Geophysical Research*, 82(28):4341–4349.

Nier, A. O., McElroy, M. B., and Yung, Y. L. (1976). Isotopic Composition of the Martian Atmosphere. *Science*, 194(4260):68–70. Publisher: American Association for the Advancement of Science.

Niles, P. B., Boynton, W. V., Hoffman, J. H., Ming, D. W., and Hamara, D. (2010). Stable Isotope Measurements of Martian Atmospheric CO $_2$ at the Phoenix Landing Site. *Science*, 329(5997):1334–1337.

Novak, R., Mumma, M., and Villanueva, G. (2011). Measurement of the isotopic signatures of water on Mars; Implications for studying methane. *Planetary and Space Science*, 59(2-3):163–168.

Olsen, K. S., Lefèvre, F., Montmessin, F., Fedorova, A. A., Trokhimovskiy, A., Baggio, L., Korablev, O., Alday, J., Wilson, C. F., Forget, F., Belyaev, D. A., Patrakeev, A., Grigoriev, A. V., and Shakun, A. (2021). The vertical structure of CO in the Martian atmosphere from the ExoMars Trace Gas Orbiter. *Nature Geoscience*, 14:67–71.

Olsen, K. S., Lefèvre, F., Montmessin, F., Trokhimovskiy, A., Baggio, L., Fedorova, A., Alday, J., Lomakin, A., Belyaev, D. A., Patrakeev, A., Shakun, A., and Korablev, O. (2020). First detection of ozone in the mid-infrared at Mars: implications for methane detection. *Astronomy & Astrophysics*, 639:A141.

Owen, T. (1982). The composition of the martian atmosphere. *Advances in Space Research*, 2(2):75–80.

Owen, T., Biemann, K., Rushneck, D. R., Biller, J. E., Howarth, D. W., and Lafleur, A. L. (1977). The composition of the atmosphere at the surface of Mars. *Journal of Geophysical Research*, 82(28):4635–4639.

Owen, T., Maillard, J. P., de Bergh, C., and Lutz, B. L. (1988). Deuterium on Mars: The Abundance of HDO and the Value of D/H. *Science*, 240(4860):1767–1767.

Parkinson, T. D. and Hunten, D. M. (1972). Spectroscopy and Acronomy of O2 on Mars. *Journal of the Atmospheric Sciences*, 29(7):1380–1390.

Perrier, S., Bertaux, J. L., Lefèvre, F., Lebonnois, S., Korablev, O., Fedorova, A., and Montmessin, F. (2006). Global distribution of total ozone on Mars from SPICAM/MEX UV measurements. *Journal of Geophysical Research*, 111(E9):E09S06.

Pettengill, G. H. and Ford, P. G. (2000). Winter clouds over the North Martian Polar Cap. *Geophysical Research Letters*, 27(5):609–612.

Piqueux, S., Kleinböhl, A., Hayne, P. O., Kass, D. M., Schofield, J. T., and McCleese, D. J. (2015). Variability of the martian seasonal CO2 cap extent over eight Mars Years. *Icarus*, 251:164–180.

Pollack, J., Kasting, J., Richardson, S., and Poliakoff, K. (1987). The case for a wet, warm climate on early Mars. *Icarus*, 71(2):203–224.

Quémerais, E., Bertaux, J.-L., Korablev, O., Dimarellis, E., Cot, C., Sandel, B. R., and Fussen, D. (2006). Stellar occultations observed by SPICAM on Mars Express. *Journal of Geophysical Research*, 111(E9):E09S04.

Rahn, T. and Eiler, J. (2001). Experimental constraints on the fractionation of 13C/12C and 18O/16O ratios due to adsorption of CO2 on mineral substrates at conditions relevant to the surface of Mars. *Geochimica et Cosmochimica Acta*, 65(5):839–846.

Read, P. L., Lewis, S. R., and Mulholland, D. P. (2015). The physics of Martian weather and climate: a review. *Reports on Progress in Physics*, 78(12):125901.

Rodgers, C. D. (2000). *Inverse Methods for Atmospheric Sounding: Theory and Practice*, volume 2 of *Series on Atmospheric, Oceanic and Planetary Physics*. World Scientific.

Rodin, A., Vinogradov, I., Zenevich, S., Spiridonov, M., Gazizov, I., Kazakov, V., Meshcherinov, V., Golovin, I., Kozlova, T., Lebedev, Y., Malashevich, S., Nosov, A., Roste, O., Venkstern, A., Klimchuk, A., Semenov, V., Barke, V., Durry, G., Ghysels-Dubois, M., Tepteeva, E., and Korablev, O. (2020). Martian Multichannel Diode Laser Spectrometer (M-DLS) for In-Situ Atmospheric Composition Measurements on Mars Onboard ExoMars-2022 Landing Platform. *Applied Sciences*, 10(24):8805.

Rossi, L., Vals, M., Montmessin, F., Forget, F., Millour, E., Fedorova, A., Trokhimovskiy, A., and Korablev, O. (2021). The effect of the Martian 2018 global dust storm on HDO as predicted by a Mars Global Climate Model. *submitted to Geophysical Research Letters*.

Régalia, L., Cousin, E., Gamache, R., Vispoel, B., Robert, S., and Thomas, X. (2019). Laboratory measurements and calculations of line shape parameters of the H2O–CO2 collision system. *Journal of Quantitative Spectroscopy and Radiative Transfer*, 231:126–135.

Sagan, C., Toon, O. B., and Gierasch, P. J. (1973). Climatic Change on Mars. *Science*, 181(4104):1045–1049.

Schmidt, J. A., Johnson, M. S., and Schinke, R. (2013). Carbon dioxide photolysis from 150 to 210 nm: Singlet and triplet channel dynamics, UV-spectrum, and isotope effects. *Proceedings of the National Academy of Sciences*, 110(44):17691–17696.

Schorghofer, N. and Forget, F. (2012). History and anatomy of subsurface ice on Mars. *Icarus*, 220(2):1112–1120.

Schrey, U., Rothermel, H., Kaufl, H. U., and Drapatz, S. (1986). Determination of the C-12/C-13 and O-16/O-18 ratio in the Martian atmosphere by 10 micron heterodyne spectroscopy. *Astronomy and Astrophysics*, 155:200–204.

Sefton-Nash, E., Teanby, N., Montabone, L., Irwin, P., Hurley, J., and Calcutt, S. (2013). Climatology and first-order composition estimates of mesospheric clouds from Mars Climate Sounder limb spectra. *Icarus*, 222(1):342–356.

Shaheen, R., Janssen, C., and Röckmann, T. (2007). Investigations of the photochemical isotope equilibrium between O₂, CO₂ and O₃. *Atmospheric Chemistry and Physics*, 7(2):495–509.

Shaposhnikov, D. S., Medvedev, A. S., Rodin, A. V., and Hartogh, P. (2019). Seasonal Water "Pump" in the Atmosphere of Mars: Vertical Transport to the Thermosphere. *Geophysical Research Letters*, 46(8):4161–4169.

Sindoni, G., Formisano, V., and Geminale, A. (2011). Observations of water vapour and carbon monoxide in the Martian atmosphere with the SWC of PFS/MEX. *Planetary and Space Science*, 59(2-3):149–162.

Slipski, M., Jakosky, B., Benna, M., Elrod, M., Mahaffy, P., Kass, D., Stone, S., and Yelle, R. (2018). Variability of Martian Turbopause Altitudes. *Journal of Geophysical Research: Planets*, 123(11):2939–2957.

Smith, M. D. (2002). The annual cycle of water vapor on Mars as observed by the Thermal Emission Spectrometer: MARS WATER VAPOR. *Journal of Geophysical Research: Planets*, 107(E11):25–1–25–19.

Smith, M. D. (2004). Interannual variability in TES atmospheric observations of Mars during 1999–2003. *Icarus*, 167(1):148–165.

Smith, M. D. (2019). THEMIS Observations of the 2018 Mars Global Dust Storm. *Journal of Geophysical Research: Planets*, 124(11):2929–2944.

Smith, M. D., Bougher, S. W., Encrenaz, T., Forget, F., and Kleinböhl, A. (2017). Thermal Structure and Composition. In Haberle, R. M., Clancy, R. T., Forget, F., Smith, M. D., and Zurek, R. W., editors, *The Atmosphere and Climate of Mars*, pages 42–75. Cambridge University Press, Cambridge.

Smith, M. D., Daerden, F., Neary, L., and Khayat, A. (2018). The climatology of carbon monoxide and water vapor on Mars as observed by CRISM and modeled by the GEM-Mars general circulation model. *Icarus*, 301:117–131.

Smith, M. D., Pearl, J. C., Conrath, B. J., and Christensen, P. R. (2001). Thermal Emission Spectrometer results: Mars atmospheric thermal structure and aerosol distribution. *Journal of Geophysical Research: Planets*, 106(E10):23929–23945.

Smith, M. D., Wolff, M. J., Clancy, R. T., and Murchie, S. L. (2009). Compact Reconnaissance Imaging Spectrometer observations of water vapor and carbon monoxide. *Journal of Geophysical Research*, 114:E00D03.

Smith, M. D., Wolff, M. J., Lemmon, M. T., Spanovich, N., Banfield, D., Budney, C. J., Clancy, R. T., Ghosh, A., Landis, G. A., Smith, P., Whitney, B., Christensen, P. R., and Squyres, S. W. (2004). First Atmospheric Science Results from the Mars Exploration Rovers Mini-TES. *Science*, 306(5702):1750–1753.

Stcherbinine, A., Vincendon, M., Montmessin, F., Wolff, M. J., Korablev, O., Fedorova, A., Trokhimovskiy, A., Patrakeev, A., Lacombe, G., Baggio, L., and Shakun, A. (2020). Martian Water Ice Clouds During the 2018 Global Dust Storm as Observed by the ACS-MIR Channel Onboard the Trace Gas Orbiter. *Journal of Geophysical Research: Planets*, 125(3).

Stone, S. W., Yelle, R. V., Benna, M., Lo, D. Y., Elrod, M. K., and Mahaffy, P. R. (2020). Hydrogen escape from Mars is driven by seasonal and dust storm transport of water. *Science*, 370(6518):824–831.

Sánchez-Lavega, A., Río-Gaztelurrutia, T., Hernández-Bernal, J., and Delcroix, M. (2019). The Onset and Growth of the 2018 Martian Global Dust Storm. *Geophysical Research Letters*, 46(11):6101–6108.

Temel, O., Karatekin, O., Gloesener, E., Mischna, M. A., and van Beeck, J. (2019). Atmospheric transport of subsurface, sporadic, time-varying methane releases on Mars. *Icarus*, 325:39–54.

Thiemens, M. H. (1999). Mass-Independent Isotope Effects in Planetary Atmospheres and the Early Solar System. *Science*, 283(5400):341–345.

Thiemens, M. H. and Heidenreich, J. E. (1983). The Mass-Independent Fractionation of Oxygen: A Novel Isotope Effect and Its Possible Cosmochemical Implications. *Science*, 219(4588):1073–1075.

Thiemens, M. H., Jackson, T., Zipf, E. C., Erdman, P. W., and van Egmond, C. (1995). Carbon Dioxide and Oxygen Isotope Anomalies in the Mesosphere and Stratosphere. *Science*, 270(5238):969–972.

Thomas, N., Cremonese, G., Ziethe, R., Gerber, M., Brändli, M., Bruno, G., Erismann, M., Gambicorti, L., Gerber, T., Ghose, K., Gruber, M., Gubler, P., Mischler, H., Jost, J., Piazza, D., Pommerol, A., Rieder, M., Roloff, V., Servonet, A., Trottmann, W., Uthaicharoenpong, T., Zimmermann, C., Vernani, D., Johnson, M., Pelò, E., Weigel, T., Viertl, J., De Roux, N., Lochmatter, P., Sutter, G., Casciello, A., Hausner, T., Ficai Veltroni, I., Da Deppo, V., Orleanski, P., Nowosielski, W., Zawistowski, T., Szalai, S., Sodor, B., Tulyakov, S., Troznai, G., Banaskiewicz, M., Bridges, J. C., Byrne, S., Debei, S., El-Maarry, M. R., Hauber, E., Hansen, C. J., Ivanov, A., Keszthelyi, L., Kirk, R., Kuzmin, R., Mangold, N., Marinangeli, L., Markiewicz, W. J., Massironi, M., McEwen, A. S., Okubo, C., Tornabene, L. L., Wajer, P., and Wray, J. J. (2017). The Colour and Stereo Surface Imaging System (CaSSIS) for the ExoMars Trace Gas Orbiter. *Space Science Reviews*, 212(3-4):1897–1944.

Tillman, J. E., Johnson, N. C., Guttorp, P., and Percival, D. B. (1993). The Martian annual atmospheric pressure cycle: Years without great dust storms. *Journal of Geophysical Research*, 98(E6):10963.

Trokhimovskiy, A., Fedorova, A., Korablev, O., Montmessin, F., Bertaux, J.-L., Rodin, A., and Smith, M. D. (2015). Mars' water vapor mapping by the SPICAM IR spectrometer: Five martian years of observations. *Icarus*, 251:50–64.

Trokhimovskiy, A., Fedorova, A. A., Olsen, K. S., Alday, J., Lefèvre, F., Korablev, O. I., Montmessin, F., Patrakeev, A., Belyaev, D. A., and Shakun, A. (2021). The Chlorine Isotope Composition of HCl in the atmosphere of Mars. *submitted to Astronomy & Astrophysics*.

Trokhimovskiy, A., Perevalov, V., Korablev, O., Fedorova, A. F., Olsen, K. S., Bertaux, J.-L., Patrakeev, A., Shakun, A., Montmessin, F., Lefèvre, F., and Lukashevskaya, A. (2020). First observation of the magnetic dipole CO $_2$ absorption band at 3.3 *textmu* m in the atmosphere of Mars by the ExoMars Trace Gas Orbiter ACS instrument. *Astronomy & Astrophysics*, 639:A142.

Urey, H. C. (1947). The thermodynamic properties of isotopic substances. *Journal of the Chemical Society (Resumed)*, page 562.

Usui, T., Alexander, C. M. O., Wang, J., Simon, J. I., and Jones, J. H. (2012). Evidence from Olivine-Hosted Melt Inclusions that the Martian Mantle has a Chondritic D/H Ratio and that Some Young Basalts have Assimilated Old Crust. In *Lunar and Planetary Science Conference*, volume 43, page 1341. Conference Name: Lunar and Planetary Science Conference.

Vago, J., Witasse, O., Svedhem, H., Baglioni, P., Haldemann, A., Gianfiglio, G., Blancquaert, T., McCoy, D., and de Groot, R. (2015). ESA ExoMars program: The next step in exploring Mars. *Solar System Research*, 49(7):518–528.

Van Hook, W. A. (1968). Vapor pressures of the isotopic waters and ices. *The Journal of Physical Chemistry*, 72(4):1234–1244.

Vandaele, A. C., Korablev, O., Daerden, F., Aoki, S., Thomas, I. R., Altieri, F., López-Valverde, M., Villanueva, G., Liuzzi, G., Smith, M. D., Erwin, J. T., Trompet, L., Fedorova, A. A., Montmessin, F., Trokhimovskiy, A., Belyaev, D. A., Ignatiev, N. I., Luginin, M., Olsen, K. S., Baggio, L., Alday, J., Bertaux, J.-L., Betsis, D., Bolsée, D., Clancy, R. T., Cloutis, E., Depiesse, C., Funke, B., Garcia-Comas, M., Gérard, J.-C., Giuranna, M.,

Gonzalez-Galindo, F., Grigoriev, A. V., Ivanov, Y. S., Kaminski, J., Karatekin, O., Lefèvre, F., Lewis, S., López-Puertas, M., Mahieux, A., Maslov, I., Mason, J., Mumma, M. J., Neary, L., Neefs, E., Patrakeev, A., Patsaev, D., Ristic, B., Robert, S., Schmidt, F., Shakun, A., Teanby, N. A., Viscardy, S., Willame, Y., Whiteway, J., Wilquet, V., Wolff, M. J., Bellucci, G., Patel, M. R., López-Moreno, J.-J., Forget, F., Wilson, C. F., Svedhem, H., Vago, J. L., and Rodionov, D. (2019). Martian dust storm impact on atmospheric H2O and D/H observed by ExoMars Trace Gas Orbiter. *Nature*, 568(7753):521–525.

Vandaele, A. C., Patel, M. R., Bellucci, G., Daerden, F., Ristic, B., Robert, S., Thomas, I. R., Wilquet, V., Allen, M., Alonso-Rodrigo, G., Altieri, F., Aoki, S., Bolsée, D., Clancy, T., Cloutis, E., Depiesse, C., Drummond, R., Fedorova, A., Formisano, V., Funke, B., González-Galindo, F., Geminale, A., Gérard, J.-C., Giuranna, M., Hetey, L., Ignatiev, N., Kaminski, J., Karatekin, O., Kasaba, Y., Leese, M., Lefèvre, F., Lewis, S. R., López-Puertas, M., López-Valverde, M., Mahieux, A., Mason, J., McConnell, J., Mumma, M., Neary, L., Neefs, E., Renotte, E., Rodriguez-Gomez, J., Sindoni, G., Smith, M., Stiepen, A., Trokhimovsky, A., Vander Auwera, J., Villanueva, G., Viscardy, S., Whiteway, J., Willame, Y., and Wolff, M. (2018). NOMAD, an Integrated Suite of Three Spectrometers for the ExoMars Trace Gas Mission: Technical Description, Science Objectives and Expected Performance. *Space Science Reviews*, 214(5):80.

Villanueva, G. L., Liuzzi, G., Crismani, M. M. J., Aoki, S., Vandaele, A. C., Daerden, F., Smith, M. D., Mumma, M. J., Knutsen, E. W., Neary, L., Viscardy, S., Thomas, I. R., Lopez-Valverde, M. A., Ristic, B., Patel, M. R., Holmes, J. A., Bellucci, G., Lopez-Moreno, J. J., and NOMAD team (2021). Water heavily fractionated as it ascends on Mars as revealed by ExoMars/NOMAD. *Science Advances*, 7(7):eabc8843.

Villanueva, G. L., Mumma, M. J., Novak, R. E., Kaufl, H. U., Hartogh, P., Encrenaz, T., Tokunaga, A., Khayat, A., and Smith, M. D. (2015). Strong water isotopic anomalies in the martian atmosphere: Probing current and ancient reservoirs. *Science*, 348(6231):218–221.

Vincendon, M., Pilorget, C., Gondet, B., Murchie, S., and Bibring, J.-P. (2011). New near-IR observations of mesospheric CO $_2$ and H $_2$ O clouds on Mars. *Journal of Geophysical Research*, 116:E00J02.

Warren, S. G. and Brandt, R. E. (2008). Optical constants of ice from the ultraviolet to the microwave: A revised compilation. *Journal of Geophysical Research*, 113(D14):D14220.

Webster, C. R., Mahaffy, P. R., Atreya, S. K., Moores, J. E., Flesch, G. J., Malespin, C., McKay, C. P., Martinez, G., Smith, C. L., Martin-Torres, J., Gomez-Elvira, J., Zorzano, M.-P., Wong, M. H., Trainer, M. G., Steele, A., Archer, D., Sutter, B., Coll, P. J., Freissinet, C., Meslin, P.-Y., Gough, R. V., House, C. H., Pavlov, A., Eigenbrode, J. L., Glavin, D. P., Pearson, J. C., Keymeulen, D., Christensen, L. E., Schwenzer, S. P., Navarro-Gonzalez, R., Pla-García, J., Rafkin, S. C. R., Vicente-Retortillo, A., Kahanpää, H., Viudez-Moreiras, D., Smith, M. D., Harri, A.-M., Genzer, M., Hassler, D. M., Lemmon, M., Crisp, J., Sander, S. P., Zurek, R. W., and Vasavada, A. R. (2018). Background levels of methane in Mars' atmosphere show strong seasonal variations. *Science*, 360(6393):1093–1096. Publisher: American Association for the Advancement of Science Section: Report.

Webster, C. R., Mahaffy, P. R., Flesch, G. J., Niles, P. B., Jones, J. H., Leshin, L. A., Atreya, S. K., Stern, J. C., Christensen, L. E., Owen, T., Franz, H., Pepin, R. O., Steele, A., and the MSL Science Team (2013). Isotope Ratios of H, C, and O in CO2 and H2O of the Martian Atmosphere. *Science*, 341(6143):260–263.

Wiegel, A. A., Cole, A. S., Hoag, K. J., Atlas, E. L., Schauffler, S. M., and Boering, K. A. (2013). Unexpected variations in the triple oxygen isotope composition of stratospheric carbon dioxide. *Proceedings of the National Academy of Sciences*, 110(44):17680–17685.

Wilzewski, J. S., Gordon, I. E., Kochanov, R. V., Hill, C., and Rothman, L. S. (2016). H 2 , He, and CO 2 line-broadening coefficients, pressure shifts and temperature-dependence exponents for the HITRAN database. Part 1: SO 2 , NH 3 , HF, HCl, OCS and C 2 H 2. *Journal of Quantitative Spectroscopy and Radiative Transfer*, 168:193–206.

Wolff, M. J., Smith, M. D., Clancy, R. T., Spanovich, N., Whitney, B. A., Lemmon, M. T., Bandfield, J. L., Banfield, D., Ghosh, A., Landis, G., Christensen, P. R., Bell, J. F., and Squyres, S. W. (2006). Constraints on dust aerosols from the Mars Exploration Rovers using MGS overflights and Mini-TES: DUST PROPERTIES-MER-MGS OVERFLIGHTS. *Journal of Geophysical Research: Planets*, 111(E12):n/a–n/a.

Wordsworth, R., Forget, F., Millour, E., Head, J., Madeleine, J.-B., and Charnay, B. (2013).

Global modelling of the early martian climate under a denser CO2 atmosphere: Water cycle and ice evolution. *Icarus*, 222(1):1–19.

Wright, I., Carr, R., and Pillinger, C. (1986). Carbon abundance and isotopic studies of Shergotty and other shergottite meteorites. *Geochimica et Cosmochimica Acta*, 50(6):983–991.

Young, L. (1971). Interpretation of high resolution spectra of Mars—II calculations of CO2 abundance, rotational temperature and surface pressure. *Journal of Quantitative Spectroscopy and Radiative Transfer*, 11(7):1075–1086.

Yung, Y. L., DeMore, W. B., and Pinto, J. P. (1991). Isotopic exchange between carbon dioxide and ozone via O(^{1} D) in the stratosphere. *Geophysical Research Letters*, 18(1):13–16.

Yung, Y. L. and Pinto, J. P. (1978). Primitive atmosphere and implications for the formation of channels on Mars. *Nature*, 273(5665):730–732.

Yung, Y. L., Wen, J.-S., Moses, J. I., Landry, B. M., Allen, M., and Hsu, K.-J. (1989). Hydrogen and deuterium loss from the terrestrial atmosphere: A quantitative assessment of nonthermal escape fluxes. *Journal of Geophysical Research: Atmospheres*, 94(D12):14971–14989.

Yung, Y. L., Wen, J.-S., Pinto, J. P., Allen, M., Pierce, K. K., and Paulson, S. (1988). HDO in the Martian atmosphere: Implications for the abundance of crustal water. *Icarus*, 76(1):146–159.

Zent, A. P., Haberle, R. M., Houben, H. C., and Jakosky, B. M. (1993). A coupled subsurface-boundary layer model of water on Mars. *Journal of Geophysical Research: Planets*, 98(E2):3319–3337.

Zuber, M. T. (1998). Observations of the North Polar Region of Mars from the Mars Orbiter Laser Altimeter. *Science*, 282(5396):2053–2060.